THE UNIVERSITY OF TEXAS AT AUSTIN
CENTER FOR TRANSPORTATION RESEARCH

Geosynthetic-stabilized Roadways for Base Course Reduction

Jorge Zornberg
Subramanian Sankaranarayanan
Hossein Roodi
Vinay Kumar Vasanthkumar
Calvin Blake
Abed Mikati
Yagizer Yalcin

August 2023

Published January 2025

https://library.ctr.utexas.edu/ctr-publications/5-4829-05-1.pdf

Technical Report Documentation Page

1. Report No. FHWA/TX-24/5-4829-05-1	2. Government Accession No.	3. Recipient's Catalog No.
4. Title and Subtitle Geosynthetic-stabilized Roadways for Base Course Reduction		5. Report Date Submitted: July 2023
		6. Performing Organization Code
7. Author(s) Jorge Zornberg. PhD, PE (ORCID: 0000-0002-6307-1047) Subramanian Sankaranarayanan, PhD Gholam Hossein Roodi, PhD Vinay Kumar Vasanthkumar, PhD Yağizer Yalçin Calvin Blake, PhD Abdurrahman Almikati, PhD		8. Performing Organization Report No. 5-4829-05-1
9. Performing Organization Name and Address Center for Transportation Research The University of Texas at Austin 3925 W. Braker Lane, 4th Floor Austin, TX 78759		10. Work Unit No. (TRAIS)
		11. Contract or Grant No. 5-4829-05
12. Sponsoring Agency Name and Address Texas Department of Transportation Research and Technology Implementation Division 125 E. 11th Street Austin, TX 78701		13. Type of Report and Period Covered Technical Report April 2018 – July 2023
		14. Sponsoring Agency Code
15. Supplementary Notes Project performed in cooperation with the Texas Department of Transportation and the Federal Highway Administration.		

16. Abstract

This project includes the instrumentation and post-construction monitoring of pavement test sections that incorporate geogrids for base stabilization along IH10 frontage roads east of San Antonio. Specifically, and as part of a full-depth frontage road rehabilitation, the test sections were constructed with an unbound aggregate base layer stabilized with three different geogrids, as well as control sections, which were instrumented extensively. The pavement materials and geogrids were characterized in the laboratory and field through a number of different methods. Post-construction, the pavement layers were characterized periodically, at six-to-12-month intervals, in addition to long-term monitoring ionvolving sensors under environmental and traffic loads. Characterization test results indicated that the stabilized sections showed a time-dependent improvement in performance due to the increasing mobilization of the geogrids. The long-term sensor data also showed that, upon application of known traffic loads, the strains in the stabilized sections were significantly lower than those in the control section, thereby quantifying the lateral restraint provided by the various geogrids. Recommendations for continued long-term monitoring and testing, in addition to experimental programs, are provided to facilitate further understanding of the mechanisms involved in geogrid stabilization and the differentiation among the performance of various geogrid types.

17. Key Words Geosynthetics, Geogrids, Stabilization, Base layer, Unbound Aggregates, Field Monitoring, Instrumentation.		18. Distribution Statement No restrictions. This document is available to the public through the National Technical Information Service, Alexandria, Virginia 22312; www.ntis.gov.	
19. Security Classif. (of report) Unclassified	20. Security Classif. (of this page) Unclassified	21. No. of pages TBD [Total count excl. cover]	22. Price

Form DOT F 1700.7 (8-72) Reproduction of completed page authorized

THE UNIVERSITY OF TEXAS AT AUSTIN
CENTER FOR TRANSPORTATION RESEARCH

Geosynthetic-stabilized Roadways for Base Course Reduction

Jorge Zornberg. PhD, PE
Subramanian Sankaranarayanan, PhD
Gholam Hossein Roodi, PhD
Vinay Kumar Vasanthkumar, PhD
Yağizer Yalçin
Calvin Blake, PhD
Abdurrahman Almikati, PhD

Center for Transportation Research
The University of Texas at Austin
3925 W. Braker Lane, 4th floor
Austin, TX 78759

http://ctr.utexas.edu/

Disclaimers

Author's Disclaimer: The contents of this report reflect the views of the authors, who are responsible for the facts and the accuracy of the data presented herein. The contents do not necessarily reflect the official view or policies of the Federal Highway Administration or the Texas Department of Transportation (TxDOT). This report does not constitute a standard, specification, or regulation.

Patent Disclaimer: There was no invention or discovery conceived or first actually reduced to practice in the course of or under this contract, including any art, method, process, machine manufacture, design or composition of matter, or any new useful improvement thereof, or any variety of plant, which is or may be patentable under the patent laws of the United States of America or any foreign country.

Engineering Disclaimer

NOT INTENDED FOR CONSTRUCTION, BIDDING, OR PERMIT PURPOSES.

Project Engineer: Jorge G. Zornberg, Ph.D., P.E.
Professional Engineer License State and Number: California No. C 056325
P.E. Designation: Research Supervisor

Acknowledgments

Table of Contents

List of Tables

List of Figures

Chapter 1. Introduction

1.1. Background

Mechanical stabilization of unbound aggregate base layers in flexible pavements using tension-resistant materials (steel mesh, polymeric grids, and fabrics) has been studied for nearly five decades. Stabilization of the base is the application of the stiffening function that a geogrid provides when mechanically coupled (through friction and interlocking) with the unbound aggregates whereby the tensile stiffness of the geogrid stiffens the aggregate matrix against lateral spreading when subject to vertical stresses (Zornberg, 2017). Early full-scale laboratory and field studies (Bender and Barenberg, 1978; Brown et al., 1982; Halliday and Potter, 1984; Kinney and Barenberg, 1982; Ruddock et al., 1982; Webster and Watkins, 1977) indicated that the use of geosynthetics to stabilize the unbound layers could result in improved performance of flexible pavements in terms of rutting and fatigue cracking.

The primary objective of this project is to evaluate the performance of geosynthetic-reinforced base roadway sections constructed with reduced base thickness and provide evidence on the efficiency of this technique. The focus of the project is on supporting TxDOT on the ongoing reconstruction of segments of IH10 near San Antonio, designing pavement test sections using all classes of geogrids, designing instrumentation and monitoring plans for pavement test sections, supporting TxDOT on procurement, testing, and installation of sensors, and collecting and interpreting performance data (collected by sensors and other components of the monitoring program) from the pavement test section.

The project involved the instrumentation of 4 test sections (one control and three with stabilized unbound aggregate base) with sensors to measure the response of the pavement layers under various conditions ranging from active traffic loading using vehicular traffic, to impact loads from falling weight deflectometer, to long-term response to passive traffic loading from public vehicles.

1.2. Value of Research

The research team considered qualitative and economic benefits of research according to Table 1 shown below. The functional areas listed in this table were identified by the sponsoring agency to be specifically considered for Project 5-4829-05.

Table 1. Applicable focus areas for Value of Research (VoR) for Project 5-4829-05

Selection	Benefit Areas	QUAL	ECON	Both	TxDOT	State	Both
X	Level of Knowledge	X			X		
X	Management and Policy	X			X		
X	Increased Service Life		X		X		
X	Improved Productivity and Work Efficiency		X		X		
X	Expedited Project Delivery		X		X		
X	Reduced Construction, Operations, and Maintenance Cost		X			X	
X	Infrastructure Condition		X				X
X	Engineering Design Development/ Improvement			X			X
X	Safety			X			X

1.2.1. Qualitative Benefits

Functional Area 1: Level of Knowledge

The outcomes of this project will provide valuable data relevant to the performance under traffic and environmental loads of geosynthetic-stabilized roadways with reduced base thickness. This information will include deformation data in the hot mix asphalt layer, deformation data of the base course layer, moisture data in the subgrade, rutting and vertical movement data of the road surface, stiffness data of various roadway layers, and pavement surface distress data. This information will be collected over a long period of time and for control pavement test sections (i.e., sections without geosynthetic) as well as pavement test sections that will be constructed using three different classes of geogrid (i.e., geogrid types I, II and II per TxDOT specifications). Interpretation of this data will be particularly useful in the future design of geosynthetic-stabilized roadways. Specifically, the outcomes of this project will provide insight on the following aspects of the future design:

1. Benefits from geosynthetic stabilization of base course in roadways subjected to traffic loads.

2. Benefits from geosynthetic stabilization of base course in roadways subjected to environmental loads.

3. Structural benefits in the hot mix asphalt layer from geosynthetic stabilization of base course

4. Structural benefits in the base course from geosynthetic stabilization of the base course

5. Difference between the expected benefits from various types of geogrids

6. Correlation of moisture migration in the subgrade layer and environmental conditions of the road with the development of environmental longitudinal cracks

Functional Area 2: Management and Policy

The outcomes of this project will significantly affect TxDOT managers and policy makers in making critical decisions to adopt geosynthetic stabilization as one of the primary solutions to problems caused by traffic and environmental loads. More specifically, documentation and interpretation of the performance of the pavement test sections in this project will help TxDOT to determine economic and mechanical advantages and disadvantages of using geosynthetic stabilization while reducing the thickness of the base layer. This insight will be crucial in the future decision-making of TxDOT managers and policy makers to adopt (or not) geosynthetic-stabilized reduced base thickness roadways.

Functional Area 3: Engineering Design Development & Improvement

In the absence of a proper design procedure for geosynthetic-stabilized roadways, TxDOT and other U.S. State Departments of Transportation have often relied on design recommendations provided by geosynthetic manufacturers. This project will provide valuable information to advance current TxDOT design procedures to include geosynthetic stabilization of the base. The adoption of such design will be advantageous in all districts of Texas and will also reduce reliance of TxDOT on empirical and/or non-verified designs that may otherwise suggested by geosynthetic manufacturers.

Functional Area 4: Safety

A substantial proportion of road accidents occur in work zones during roadway construction. A longer construction period will expose construction laborers, road engineers, TxDOT personnel, motorists and pedestrians alike to costly accidents. Adoption of geosynthetic-stabilized roadways with reduced base thickness will significantly reduce construction time because the duration of construction for geosynthetic installation is considerably shorter than that for a section of the base layer (including the time required for transport, spreading, conditioning, compaction, etc.). Furthermore, because the volume of geosynthetic materials required is significantly smaller than the base course granular materials needed for the same section, substantially fewer trips (and trucks) will be needed to transport the materials to the work zone. Fewer trucks within the transportation network will reduce the overall chance of accidents and improve roadway safety.

1.2.2. Economic Benefits

Economic benefits are expected to realize in the following functional areas:

Increased Service Life

Improved Productivity and Work Efficiency

Expedited Project Delivery

Reduced Construction, Operations, and Maintenance Costs

Infrastructure Conditions

Engineering Design Development/Improvement

Safety

Although each factor will provide individual economic benefits, the financial calculations conducted as part of this report was aimed at evaluating the most important economic benefit that may overshadow other marginal benefits.

Assumptions
Since the focus of this project is on the use of a reduced base thickness while installing geogrids, it was envisioned that the most significant change in TxDOT construction approach after completion of this project would be adoption of geosynthetic-stabilized reduced base thickness roadways as a common design and construction practice. Therefore, the most important economic benefit would be expected to result from replacing a portion of the granular base layer by the geosynthetic layer. The main assumptions adopted to calculate this benefit are as follows:

- Use of geosynthetics can result in a reduction of 10 to 20 % in base thickness.

- TxDOT adopts the new approach (i.e., replacing 10 to 20 % of the base course with a geosynthetic layer) only in highway construction projects.

- TxDOT adopts the new approach in all highway construction projects involving flexible base construction, independent of the type of flexible base.

- The economic benefit from this project will be realized in the fourth (i.e., last) year of the project, when the accumulated performance data will provide TxDOT compelling evidence on the suitability of this technique.

- An expected value duration of 15 years from the beginning of the project was adopted.

- A discount rate of 5% was adopted.

- Calculations were conducted based on TxDOT project letting and bids information over a 12-month period ending on May 31, 2018.

To best estimate the economic benefits detailed above, the TxDOT statewide average low bid unit price website was heavily utilized. Specifically, using information published over a 12-month period as of May 31, 2018, annual costs for construction of flexible base roads were estimated. Detailed calculations of the economic benefit are presented in the subsequent section.

Calculations

The total 12-month cost of various types and thicknesses of compacted-in-place flexible base in TxDOT highway construction projects was found as follows:

Total cost of flexible base construction = $56,470,666 + $77,915,288 = **$134,385,954**

Assuming a 10 to 20% reduction in base thickness due to the use of a geosynthetic reinforcement, the total annual saving was estimated as follows:

Total estimated savings due to reduced base thickness = **$13,438,595** to **$26,877,191**

Using the TxDOT statewide average low bid unit price website for the past 12 months, it was found that the average bid price for a square yard of geogrid for base stabilization ranged from approximately $1 to $2.70. The total square yardage of flexible base construction was then estimated as follows:

Total flexible base construction = 4,874,159 sy + 1,846,841 cy / 0.4 y = **9,491,260 sy**

In this estimation, an average thickness of 0.4 yard (14.5 inch) was assumed for the flexible base volume that was available by cubic yard.

The total additional cost for procurement and installation of the geogrid was then estimated to vary in the following range:

Total estimated cost of geogrids = 9,491,260 sy × $1 ~ $2.70 = **$9,491,261** to **$25,626,404**

Therefore, the expected annual benefit for adopting geosynthetic-reinforced reduced base roadways is expected to be in the following range:

Scenario 1:

= **$13,438,595** (savings) - $9,491,261 (additional cost) = **$3,947,335** (benefit) per year

Scenario 2:

= **$26,877,191** (savings) - **$25,626,404** (additional cost) = **$1,250,787** (benefit) per year

Note that Scenario 1 assumes a 10% reduction in base thickness and cheaper geogrid (i.e., $1/sy), and Scenario 2 assumes a 20% reduction in base thickness and a more expensive geogrid (i.e., $2.70/sy).

1.2.3. Net Present Value

The calculations presented in the previous section were used in the RTI VoR template to compute the net present value. As previously stated, this analysis was conducted assuming a 5% discount rate and a 15-year expected value duration. Figure 1 and Figure 2 show the completed VoR templates for the two previously described scenarios. The estimated net present value of this research was found to range from approximately $10 to $30 million and the cost benefit ratio of investing in this project was estimated to range from 18 to 60.

Project #	5-4829-05		
Project Name:	IMPLEMENTATION OF GEOSYNTHETIC-STABILIZED ROADWAYS FOR BASE COURSE REDUCTION: FIELD MONITORING AND DESIGN RECOMMENDATIONS		
Agency:	University of Texas (CTR)	Project Budget	$ 524,729
Project Duration (Yrs)	4.0	Exp. Value (per Yr)	$ 1,250,787
Expected Value Duration (Yrs)	15	Discount Rate	5%

Economic Value

Total Savings:	$ 15,210,774.58	Net Present Value (NPV):	$ 9,684,373
Payback Period (Yrs):	0.419519	Cost Benefit Ratio (CBR, $1 : $___):	$ 18

Years	Expected Value
0	-$131,182
1	-$131,182
2	-$131,182
3	$1,119,605
4	$1,250,787
5	$1,250,787
6	$1,250,787
7	$1,250,787
8	$1,250,787
9	$1,250,787
10	$1,250,787
11	$1,250,787
12	$1,250,787
13	$1,250,787
14	$1,250,787
15	$1,250,787
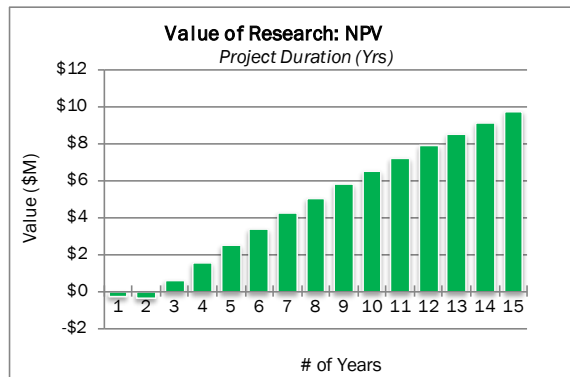
Value of Research: NPV
Project Duration (Yrs)

Variable Justification

See technical memorandum 1 for full description of input variables that led to the expected annual value.

Years	Expected Value	Expected Value	Expected Value	NPV
0	-$131,182	-$131,182	-$0.13	-$0.12
1	-$131,182	-$262,365	-$0.26	-$0.24
2	-$131,182	-$393,547	-$0.39	-$0.36
3	$1,119,605	$726,058	$0.73	$0.56
4	$1,250,787	$1,976,845	$1.98	$1.54
5	$1,250,787	$3,227,632	$3.23	$2.48
6	$1,250,787	$4,478,419	$4.48	$3.37
7	$1,250,787	$5,729,207	$5.73	$4.21
8	$1,250,787	$6,979,994	$6.98	$5.02
9	$1,250,787	$8,230,781	$8.23	$5.79
10	$1,250,787	$9,481,568	$9.48	$6.52
11	$1,250,787	$10,732,355	$10.73	$7.21
12	$1,250,787	$11,983,142	$11.98	$7.88
13	$1,250,787	$13,233,929	$13.23	$8.51
14	$1,250,787	$14,484,716	$14.48	$9.11
15	$1,250,787	$15,735,504	$15.74	$9.68

Figure 1. Results from completed VoR template in Scenario 1

25

	Project #	5-4829-05
	Project Name:	IMPLEMENTATION OF GEOSYNTHETIC-STABILIZED ROADWAYS FOR BASE COURSE REDUCTION: FIELD MONITORING AND DESIGN RECOMMENDATIONS
	Agency:	University of Texas (CTR)
	Project Duration (Yrs)	4.0
	Expected Value Duration (Yrs)	15

	Project Budget	$ 524,729
	Exp. Value (per Yr)	$ 3,947,335
	Discount Rate	5%

Economic Value

Total Savings:	$ 50,265,893.95	Net Present Value (NPV):	$ 31,565,567
Payback Period (Yrs):	0.132932	Cost Benefit Ratio (CBR, $1 : $___):	$ 60

Years	Expected Value
0	-$131,182
1	-$131,182
2	-$131,182
3	$3,816,153
4	$3,947,335
5	$3,947,335
6	$3,947,335
7	$3,947,335
8	$3,947,335
9	$3,947,335
10	$3,947,335
11	$3,947,335
12	$3,947,335
13	$3,947,335
14	$3,947,335
15	$3,947,335
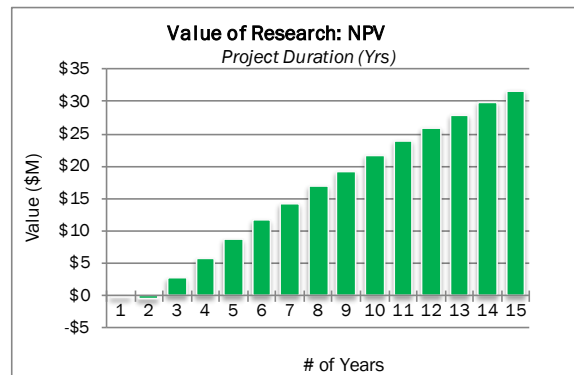
Value of Research: NPV
Project Duration (Yrs)

Variable Justification

See technical memorandum 1 for full description of input variables that led to the expected annual value.

Years	Expected Value	Expected Value	Expected Value	NPV
0	-$131,182	-$131,182	-$0.13	-$0.12
1	-$131,182	-$262,365	-$0.26	-$0.24
2	-$131,182	-$393,547	-$0.39	-$0.36
3	$3,816,153	$3,422,606	$3.42	$2.78
4	$3,947,335	$7,369,941	$7.37	$5.88
5	$3,947,335	$11,317,275	$11.32	$8.82
6	$3,947,335	$15,264,610	$15.26	$11.63
7	$3,947,335	$19,211,945	$19.21	$14.30
8	$3,947,335	$23,159,280	$23.16	$16.84
9	$3,947,335	$27,106,614	$27.11	$19.27
10	$3,947,335	$31,053,949	$31.05	$21.57
11	$3,947,335	$35,001,284	$35.00	$23.77
12	$3,947,335	$38,948,619	$38.95	$25.86
13	$3,947,335	$42,895,953	$42.90	$27.86
14	$3,947,335	$46,843,288	$46.84	$29.76
15	$3,947,335	$50,790,623	$50.79	$31.57

Figure 2. Results from completed VoR template in Scenario 2

26

1.2.4. Discussion

The VoR estimate presented above was developed based on a preliminary understanding of the VoR functional areas and previously listed assumptions. Final values may not reflect actual savings that will be realized by TxDOT. A better understanding of the functional areas and economic benefits of the research was developed as the project progressed.

1.3. Organization of the Report

This report is organized into eight chapters.

Chapter 1 provides a brief overview of geosynthetic stabilization of roadways and instrumentation of pavement structures, followed by a Value of Research report and a brief description of the organization of the report.

Chapter 2 explains the design of the various test sections with and without geogrids for base stabilization. It details the layout of the various instrumented and non-instrumented test sections and their locations along the frontage roads of IH10, east of San Antonio. It also summarizes the instrumentation plan adopted in the instrumented test sections, and explains the protocols adopted for monitoring the various test sections.

Chapter 3 explains the characterization of the unbound aggregate layers used in the test sections. In particular, the Cemex Flexible Base Gravel used, existing subgrade conditions and geogrids used in the stabilized test sections are characterized through various tests and in-situ measurements. The battery of laboratory tests conducted on the base and corresponding results are presented. The in-situ conditions of the subgrade, evaluated via an extensive boring and logging program, along with the subgrade PVR are shown. Finally, the mechanical, index and interaction properties of the geogrids used in the stabilized test sections are also summarized.

Chapter 4 covers the actual instrumentation of the test sections with various sensors such as asphalt strain gauges, thermocouples, soil extensometers, geophones, linear potentiometers and moisture sensors. The chapter goes over the as-built instrumentation layout, specifications of the various sensors and materials used, and actual installation protocols used to instrument the pavement sections.

Chapter 5 summarizes the various forms of testing conducted at different stages in the life cycle of the pavement. Testing included stiffness characterization tests to evaluate the as-built properties of the various pavement layers during and after construction; a passive evaluation conducted using GPR to assess layer uniformity; and total stational surveys for surface movements. Finally, the active loading campaigns designed to assess the response of the installed sensors under traffic loading are also covered.

Chapter 6 details the passive monitoring of the installed sensors to assess the long-term performance of the instrumented and non-instrumented pavement test sections. The various sensors from which the long-term data was collected and the status of the data collection from those sensors are summarized.

Chapter 7 provides the results of the analysis of the data from the sensors in various configurations. The subsurface characterization of the as-built pavement layers is presented through the results of stiffness characterization tests. Properties were determined during construction and with time after construction to assess pavement long-term performance. Pavement performance was assessed through long-term monitoring results collected by various sensors. Additionally, the actual performance under traffic and impact loads was assessed by analyzing the data collected from sensors under dynamic conditions.

Chapter 8 outlines the key conclusions drawn from this study.

Chapter 2. Design of the IH10 Field Test Sections

2.1. Introduction to Design of IH10 Field Test Sections

This chapter summarizes the design of a comprehensive field evaluation program to complement the construction of geosynthetic-stabilized unbound base course test sections along IH10. The activities conducted can be grouped into the following three categories, which are subsequently discussed: 1) determination of the layout of the test sections; 2) design of the instrumentation plan; and 3) determination of protocols for monitoring and data collection.

2.2. Determination of Layout of Test Sections

For consistency in construction and performance evaluations, test section construction was proposed at one location on relatively straight and flat sections of the eastbound frontage road, preferably far from intersections. As illustrated in Figure 3, each test section was initially proposed for construction in both lanes for a total length of 1,000 ft, with the reinforced and control (unreinforced) sections alternating in adjacent lanes in two 500-ft-long sections.
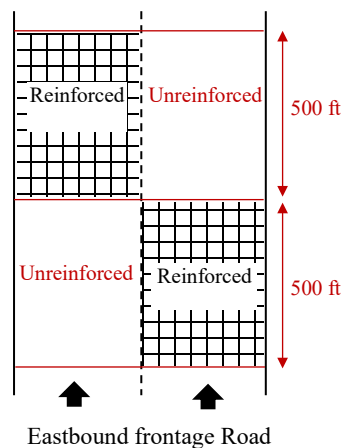
Figure 3. Schematic of the proposed layout for each test section

However, after collection of additional subgrade soil data and following a careful review of construction phases and close collaboration with TxDOT representatives, CEC site engineers, and representatives from the construction company involved, the aforementioned design changed several times. As presented in Figure 4, it was ultimately decided that the test sections would be constructed at two locations. This decision was made to avoid intersections and areas with changes in the number of traffic lanes and to allow construction on subgrade with the most uniform soil characteristics.

29
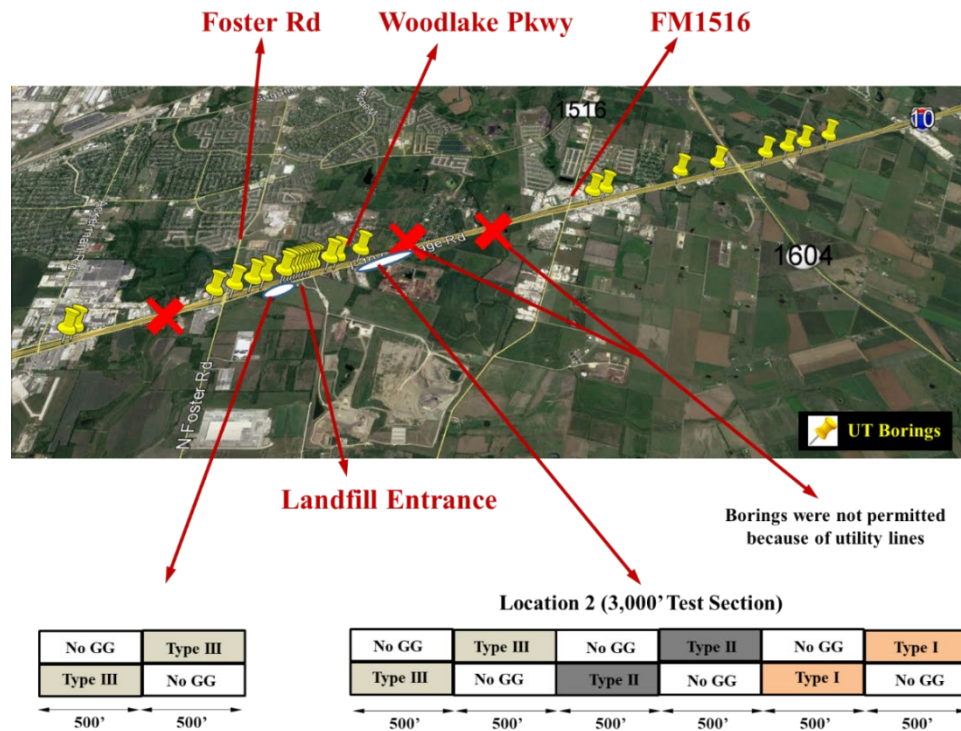
Figure 4. General view of the two locations selected for construction of test sections.

Location 1 was selected right before the entrance to the Republic Services Tessman Road Landfill (Figure 4). This allows evaluation of test section performance under the heavy traffic into the landfill. Intensive boring data at spacings of less than 200 feet confirmed uniform subgrade soil characteristics in this area. Four 500-ft-long test sections were considered at this location including two control and two geosynthetic-stabilized sections using geogrid type III (Figure 5).
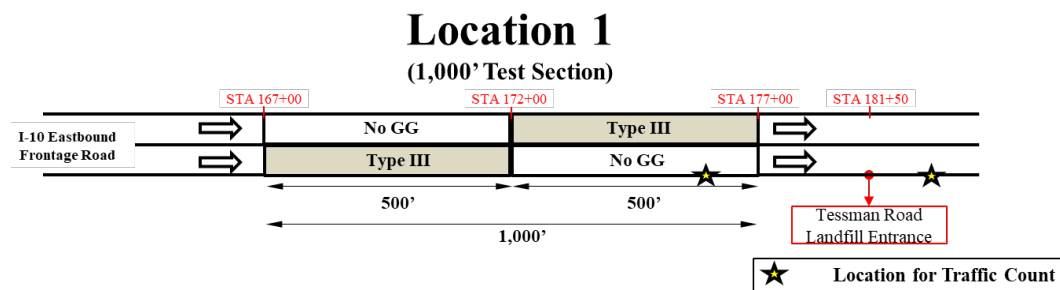
Figure 5. Location 1 for test sections

Location 2 was suggested to extend from slightly before the New Earth Compost Facility (located east of the intersection with Woodlake Pkwy) to after (Figure 4). This location was

selected to avoid ramps and change lanes from the cross-over intersection with Woodlake Pkwy. The initial test section design for this location is presented in Figure 4. However, these test sections were ultimately split: part 1 was to be constructed before the compost facility and part 2 after it. All three geogrid types (i.e., types I, II and III) were considered for side-by-side construction with the control sections for parts 1 and 2. An additional section per part was suggested in which the lanes for the control and type III geogrid sections were flipped (Figure 6). The initial test section lengths proposed were 250 ft for part 1 and 400 ft for part 2 (Figure 6), though different lengths for both parts were subsequently proposed based on the following considerations:

- Locating all of part 1 before the end of the compost facility and all of part 2 after the compost facility. This design was suggested to consider the effect of the difference in traffic weight going into and coming out of the compost facility.

- Avoiding starting part 1 at the Woodlake Pkwy cross-over ramp. This design was suggested to limit the west end of part 1 and reduce its section length from the initially designed 500 ft to the existing 250 ft.

- Avoiding construction of part 2 at the section where an additional traffic lane joins the frontage road. Because a traffic lane enters from the main lanes to the frontage road approximately 1,800 ft following the compost facility, the length of the part 2 test sections was reduced from the initially designed 500 ft to 400 ft, as presented in Figure 6. However, this length was also changed in the final design as explained next.
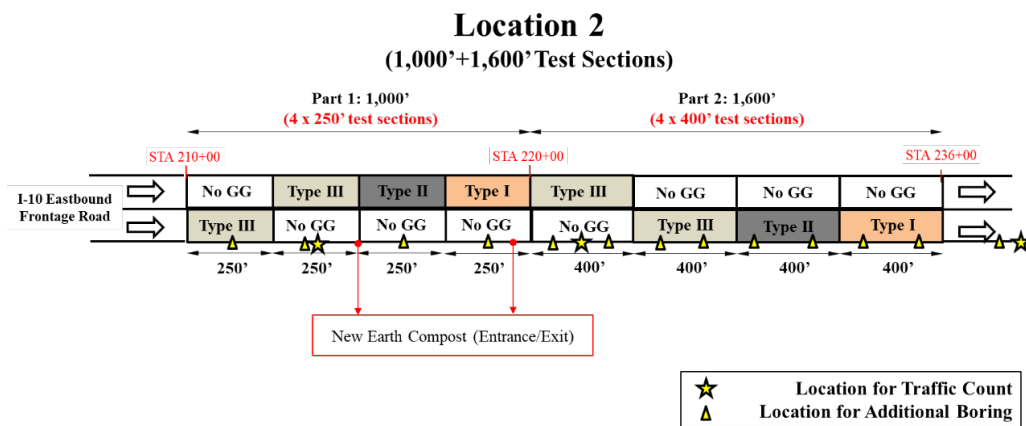
Figure 6. Location 2 for test sections (initial design)

As presented in Figure 7, the length of the part 2 test sections was later changed to address two concerns:

31

- Additional data collected from the subgrade soil indicated chances of a change in the subgrade soil characteristics starting 1,800 ft east of the compost facility.

- Evaluation of the construction phases for the eastbound frontage road indicated that 400-ft-long test sections may be constructed in two different phases at three-to-four-month construction intervals.

- Therefore, the final test section length of location 2 – part 2 was 250 ft (Figure 7).
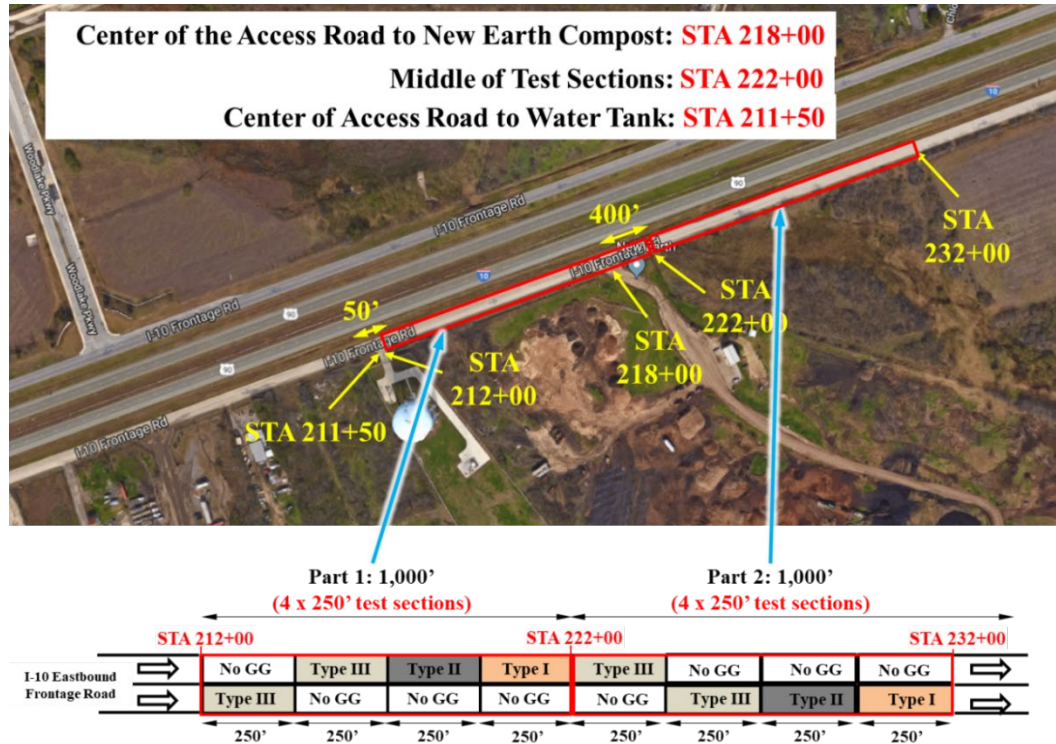
Figure 7. Location 2 for test sections (final design)

General characteristics of the test sections are summarized in Table 2.

Table 2. Characteristics of experimental test sections in IH10

	Number of test sections	Test section length (ft)	Location	Geosynthetic type	Geosynthetic manufacturer	Geosynthetic position
Location 1	4	500	Eastbound frontage road STA 167+00 to 177+00	Type III	Tensar Inc.	At subgrade-sub-base interface
Location 2 – Part 1	8	250	Eastbound frontage road STA 212+00 to 222+00	Types I, II, III	Tensar Inc.	At subgrade-sub-base interface
Location 2 – Part 2	8	250	Eastbound frontage road STA 222+00 to 232+00	Types I, II, III	Tensar Inc.	At subgrade-sub-base interface

2.3. Design of Instrumentation Plan

Three main types of sensors have been considered for installation within the hot mix asphalt, granular base and subgrade soil. The general location of the sensors is shown in the frontage road profile sketch in Figure 8. Sensors were installed in at least one of the various types of geosynthetic-stabilized test section repeat configurations and at least one of the control section repeat configurations. Characteristics of each sensor type along with their installation locations will be discussed next.
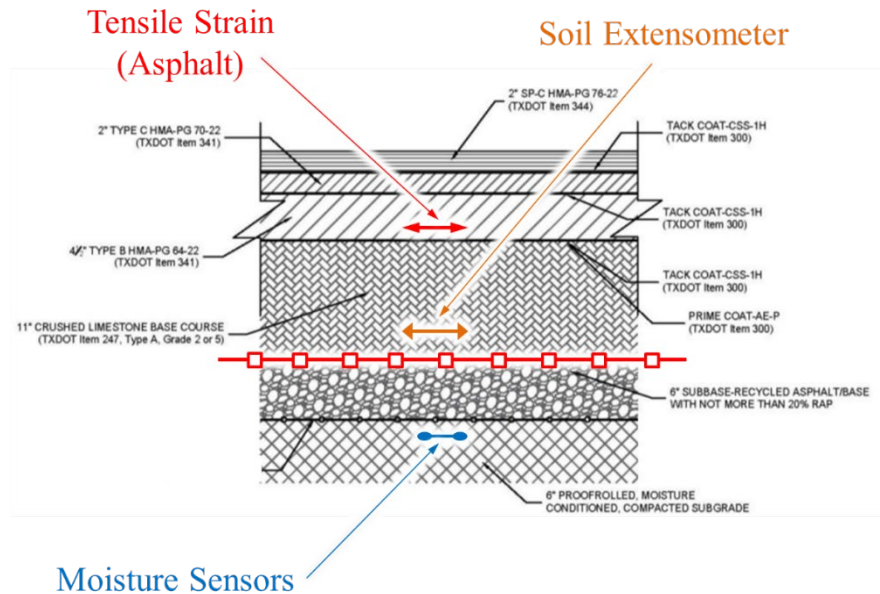
Figure 8. Main types and general locations of sensors

2.3.1. Asphalt Strain Gauges

Asphalt strain gauges will be installed in the hot mix asphalt to measure tensile strains. Comparisons between the tensile strains measured in the reinforced and unreinforced sections highlights the benefits of geosynthetics in reducing the accumulated strains induced by traffic loads or environmental changes. Figure 9 provides a picture of an asphalt strain gauge used in this project. UT team members have extensive experience using these strain gauges in the laboratory as well as in a field section in the Austin District. A total of 20 sensors were acquired, tested and calibrated at the UT lab.

The final design for the number and layout of asphalt strain gauges was discussed among the team members to optimize their use and the data collected. One potential layout is presented in Figure 10. The asphalt strain gauges were planned for installation in two directions including traffic (or longitudinal) and transverse directions. They will record tensile strains in the hot mix asphalt layer in directions parallel and perpendicular to traffic. Asphalt strain gauges will be used in the wheel paths as well as between two wheel paths.
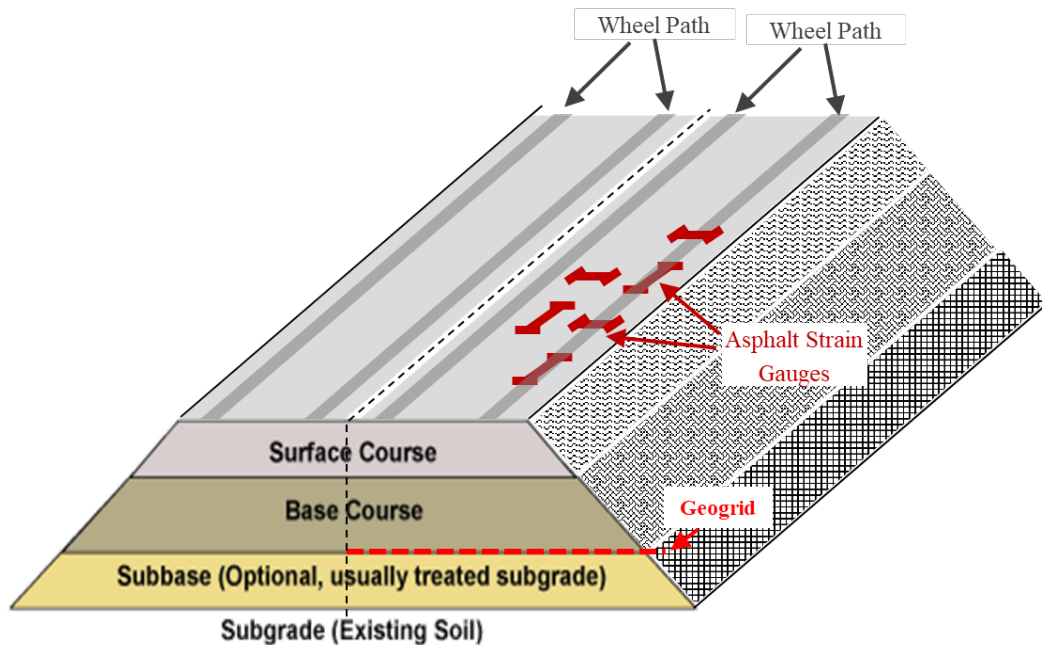
Figure 10. General layout for asphalt strain gauges

2.3.2. Soil Extensometers

Soil extensometers will be used within the base layer to measure relative displacements (strain) in the base course in the lateral direction. This information will be used to explore the effect of the geosynthetic on lateral spreading of the base aggregate, which is expected to be the main mechanism resulting in degradation of the base course. The geosynthetic layer is expected to delay degradation of the base layer through a mechanism referred to as lateral restraint. As part of this mechanism, the interaction between the geosynthetic and aggregate maintains confinement of the base layer and delays lateral spreading of the base.

Figure 11 presents images of the soil extensometer and data logger considered for this project. In the H-shaped sensor, a displacement transducer is incorporated between two metal L-shaped

flanges, which can easily move to retract or protract the H-shaped sensor. The displacement transducer then records the relative displacement between the two flanges.
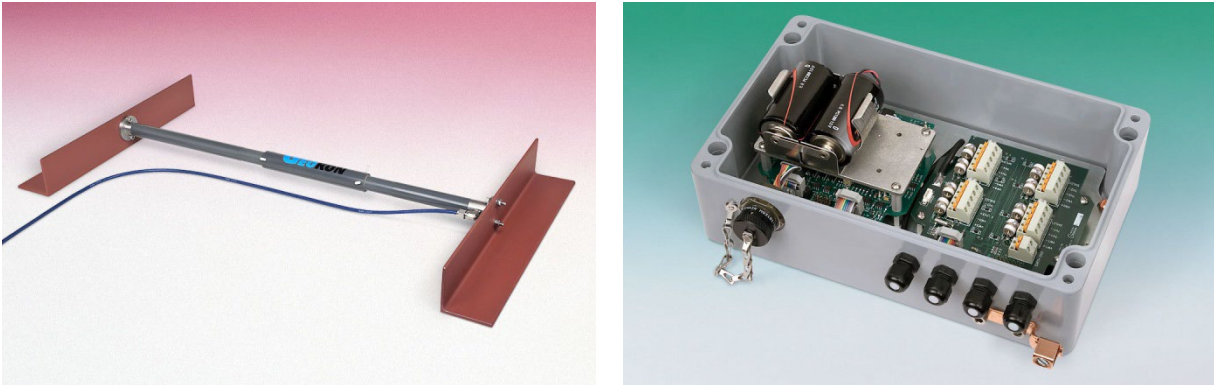
Figure 11. Soil extensometer and data logger to be used in IH10 instrumentation plan

Since prior experience with this type of sensor has been limited, a comprehensive evaluation program of these sensors was conducted at the UT lab. Specifically, a prototype sensor was purchased and used under various loading scenarios to investigate its performance. The number and layout of sensors was finalized following the laboratory investigation. Additionally, soil extensometers will be complemented by linear potentiometers to record additional data from horizontal movement of the base course. An example of a linear potentiometer is presented in Figure 12.

Figure 12. Linear potentiometer to be used in IH10 instrumentation plan

2.3.3. Temperature Sensors

Temperature sensors will be used to record the hot mix asphalt temperature. This data is important because properties of the viscoelastic hot mix asphalt layer are sensitive to

temperature. The hot mix asphalt temperature data will also be used to evaluate the data recorded by asphalt strain gauges to determine the potential effect thermally induced strains have on the recorded data. A picture of the thermocouple used in IH10 test sections is presented in Figure 13.

Figure 13. Temperature sensor to be used in IH10 instrumentation plan

2.3.4. Moisture Sensors

Change in the moisture content of subgrade soil will be monitored by installation of vertical and horizontal arrays of moisture sensors within the subgrade. Moisture migration in the natural ground is an important source of swelling and shrinkage of expansive clay subgrades. Swelling and shrinkage of expansive subgrades will eventually result damages in the pavement structure in form of longitudinal vertical cracks.

As part of the monitoring program proposed for this project, moisture sensors will be installed in the subgrade soil in horizontal and vertical arrays to measure changes in moisture content over time. An example moisture sensor along with a typical layout of the sensors in the subgrade soil are presented in Figure 14 and Figure 15.

Figure 14. Moisture sensor to be used in IH10 instrumentation plan

TDR 315L Sensors: 9
Datasnaps DAQ: 3

Centerline

4 ft   4 ft   3 ft   3 ft

1 ft

2 ft

Starting at 1 ft below the base-subgrade interface, at 2 ft spacing

2 ft
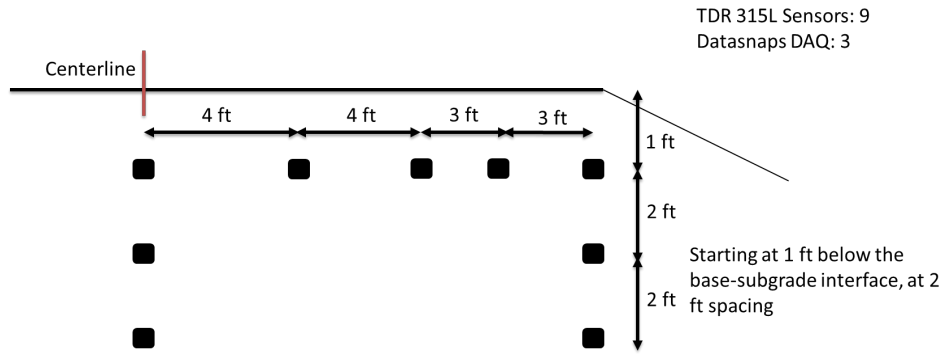
Figure 15. A typical layout for moisture sensors to be installed in IH10

2.3.5. Data Acquisition System

Several alternatives were evaluated for the data acquisition systems. Specifically, as presented in Figure 16, individual data loggers were considered for each moisture sensor. Various data loggers were evaluated for soil extensometers, linear potentiometers, temperature sensors and asphalt strain gauges. The focus of this evaluation was identifying a data logger that can simultaneously support various types of sensors and has the required number of channels. The frequency of reading and noise level among various data loggers were also evaluated to determine the suitability of each data logger for the type of data to be recorded by each sensor. Figure 17 presents the various data loggers evaluated.
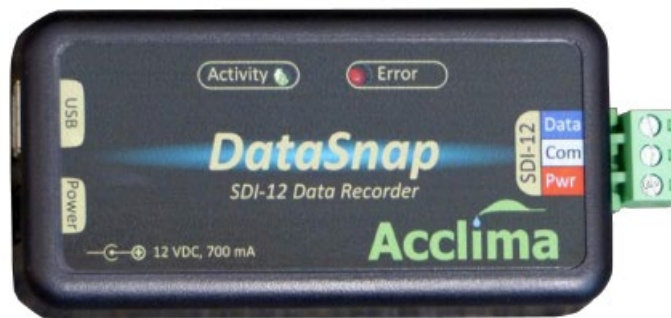
Figure 16. Data logger to be used for moisture sensors

Figure 17. Data loggers that have been evaluated for soil extensometers, linear potentiometers, thermocouples, and asphalt strain gauges

2.3.6. Power Supply

After evaluating various alternatives for the power supply, a solar panel system (including a solar panel, battery and charge controller) was selected to provide power for each instrumented section. This decision was made considering the large number of sensors, high frequency of sensor readings and long monitoring period. A secure roadside location will be selected for installation of the solar panel and charge controller. The battery will be placed in the ground box close to the data actuations system.

2.3.7. Location for Installation of Sensors

To minimize effects from variations in traffic, subgrade soils and construction activities, the instrumented sections were selected from nearby test sections. This selection will also facilitate installation and maintenance of the sensors and future monitoring activities. As presented in Figure 18, tentative locations for sensor installation were selected as the middle of the outside lanes in the test sections at location 2 – part 2.
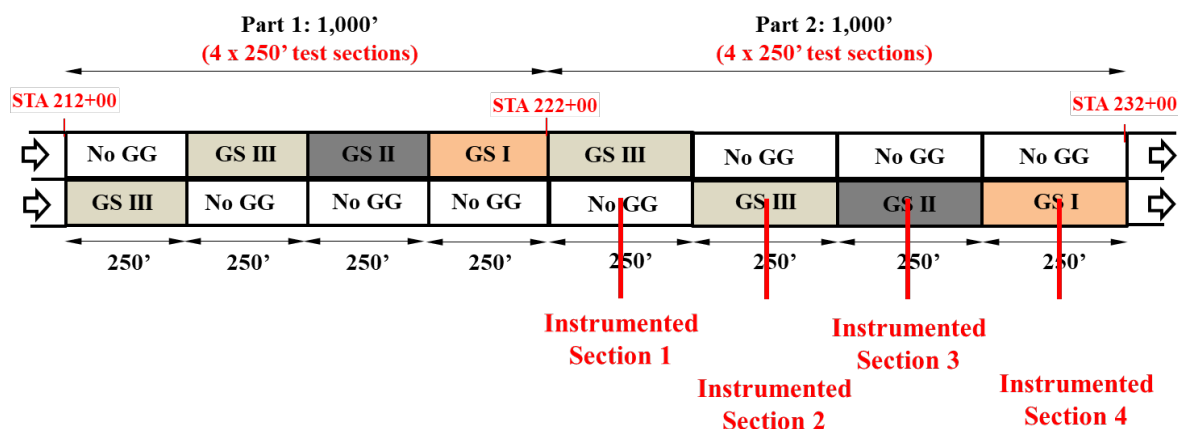
Figure 18. Tentative location for instrumented sections

Main characteristics of the instrumentation plan are summarized in Table 3.

Table 3. Characteristics of instrumentation plan for test sections in IH10

Sensor type	Potential vendor and model	Potential number of instrumented sections	Location of instrumented sections	Potential number of sensors per section	Pavement layer
Asphalt strain gauge	CTL – ASG 152	4 to 5	Location 2 – Part 2	4	Hot mix asphalt layer
Soil extensometer	Geokon Model 4435	4 to 5	Location 2 – Part 2	2	Base course
Linear potentiometer	UniMeasure LX-PA	4 to 5	Location 2 – Part 2	10	Base course
Temperature sensors	Omega Thermocouple 5TC	4 to 5	Location 2 – Part 2	1	Hot mix asphalt layer
Moisture sensors	Acclima TDR	4 to 5	Location 2 – Part 2	10	Subgrade soil
Data acquisition system 1 (for asphalt strain gauges, soil extensometer, linear potentiometer, and thermocouple)	DATAQ / Omega / Geokon	4 to 5	Location 2 – Part 2	TBD	Roadway shoulder
Data acquisition system 2 (for moisture sensors)	Acclima DataSnap	4 to 5	Location 2 – Part 2	1 or 2	Roadway shoulder
Power supply	Solar panel, battery, and	4 to 5	Location 2 – Part 2	1	Roadside

Sensor type	Potential vendor and model	Potential number of instrumented sections	Location of instrumented sections	Potential number of sensors per section	Pavement layer
	charge controller				

2.4. Determination of Protocols for Monitoring and Data Collection

Various protocols were established for a comprehensive monitoring program aimed at collecting and integrating test section performance data. Protocols were established to: 1) monitor vertical movement of the road surface; 2) monitor the development and extent of distresses on the pavement surface; 3) evaluate test section performance under traffic loads; and 4) evaluate degradation of the base course. Each protocol is briefly discussed next.

2.4.1. Monitoring Vertical Movement of Road Surface

As part of the program to monitor vertical movements of the road surface, total station surveys were considered specifically to monitor changes in elevation of the road surface over time. This technique, used by UT team members on various field sections across Texas, involves marking multiple points of a cross-section of the road using spray paint and then surveying the coordinates of the marked points over time. A schematic of this technique is illustrated in Figure 19.

Total station surveys will be conducted at a minimum of two cross-sections in each of the instrumented test sections. The surveys will be conducted every three months after construction or after extreme weather conditions (e.g., heavy rain, drought). Vertical movement of the road surface will be compared among various points across a cross-section of test sections. Specifically, relative vertical movements between the road edges and center will be investigated and potential correlations with environmental conditions at the project site will be sought. In addition, vertical movement of the cross-sections will be compared among various test sections constructed with different design profiles. This comparison will determine any potential effect of various geosynthetics on vertical movement.

2.4.2. Development and Extent of Distresses on Pavement Surface

The condition of the road surface will be carefully monitored by rigorous visual condition surveys, which will be conducted according to the instructions recommended in the TxDOT Pavement Management Information System Rater's Manual. The distress data from the test sections will be collected and characterized using the 10 recommended categories for flexible pavements found in this manual. Over the past decade, UT team members have utilized a well-established procedure for the collection and interpretation of visual condition surveys data. An example visual condition survey form used by the research team members is given in Figure 20. General test section information, including section number, geosynthetic type, section length, and starting and ending stations, are summarized at the top. The severity and extent of each distress type is detailed in the following rows, and the location of each distress observed is recorded using the distance from the beginning of the section. Picture numbers associated with each distress are documented in the next column followed by road evaluator remarks in the last column.

Figure 20. Example visual condition survey form and data collected as part of the monitoring program of FM2 test sections in Austin district

Although road surface distress data will be collected in all distress categories, the surveys will focus on the characterization of longitudinal cracks, which are the main type of distress resulting from environmental loads. An initial survey of the existing condition of the roadway was conducted to establish a reference for future performance. Additional condition surveys will be conducted every three months after construction or extreme weather conditions (e.g., heavy rain, drought) occurs. The percentage of environmental longitudinal cracks will be compared among various test sections. A comparison between the control and geosynthetic-reinforced sections will determine the potential benefits from geosynthetics in reducing the extent and severity of environmental longitudinal cracks. Additionally, the development of environmental longitudinal cracks will be compared with the vertical movement of the marked cross-sections, to be obtained from total station surveys, and with the environmental conditions at the project site. These comparisons provide evidence for establishing relevant mechanisms that result in the development of the cracks.

2.4.3. Performance of Test Sections under Traffic Loads

Rutting depth in the wheel paths will be considered as the main performance measure to assess the effect of traffic loads in various test sections. At the request of the Performing Agency, TxDOT will measure rutting depth along the test sections. The rutting measurements will be made every three months. A comparison of the rutting depth in the control sections with that in the geosynthetic-stabilized sections will determine potential structural benefits provided by the geosynthetic layer. This data along with the traffic record will be used to establish Traffic Benefit Ratios (TBR) for various geosynthetics used in the test sections.

In addition, the information to be collected from asphalt strain gauges will be used to evaluate the potential effect of geosynthetics on the fatigue strains induced by traffic loads. The strain data measured by the asphalt strain gauges will continuously be recorded by data loggers and will frequently be collected after construction of the test sections. Potential structural benefits from geosynthetics under traffic loads are expected to be observed in reducing elastic and plastic tensile strains in the hot mix asphalt layer. Comparison of the data collected by the asphalt strain gauges over time under public traffic will be used to evaluate the plastic tensile strain. Comparison of the data collected by asphalt strain gauges under specific known loads will be used to evaluate the elastic tensile strain.

2.4.4. Evaluate Degradation of Base Course

Degradation of the granular base course is a main source for weakening roadway structures. Specifically, lateral spreading of particles due to stresses induced by traffic loads results in the loss of confinement of the base course. Geosynthetics used for base stabilization are expected to

maintain confinement of the base course over time through interlocking with aggregates. This mechanism is referred to as lateral restraint. Therefore, a comparatively lower rate of base course degradation is expected in sections stabilized with geosynthetics as compared to control sections.

Degradation of the base course will be evaluated by analysis of the data collected from Falling Weight Deflectometer (FWD) tests to be conducted along the test sections. At the request of the Performing Agency, TxDOT will conduct FWD tests along the test sections every six months. In addition, the data collected from soil extensometers and linear potentiometers will be used to evaluate degradation of the base course in various test sections. The soil extensometers and linear potentiometers measure horizontal strains and lateral movements of base course particles. This data will be continuously recorded by data loggers and collected frequently after test section construction. Comparatively smaller lateral strains and movements are expected in geosynthetic-stabilized test sections.

Chapter 3. Material Characterization

3.1. Introduction to Material Characterization

This chapter summarizes the characterization of various materials used in the construction of the IH10 test sections, including the properties of the base material, subgrade soil and geogrids used in the construction of the westbound and eastbound frontage road test sections. The base material used in the test sections was Cemex Flexible Base Gravel from the New Braunfels Quarry, corresponding to Grade 2 Type B according to TxDOT classification. The subgrade soil was identified in the USGS soil map as Houston Black. Three types of geogrids were used in the test sections including geogrid types I, II and III, classified in accordance with TxDOT Departmental Material Specification (DMS) 6240. The characteristics of the different materials determined are discussed next.

3.2. Characterization of Base Material

The base material identified used for the project is Cemex Flexible Base Gravel. This is a grade 2 flexible base gravel (Type B) material available at the Balcones Quarry, just south of New Braunfels on Interstate 35 (Figure 21). This material was characterized and its properties are listed in this section.
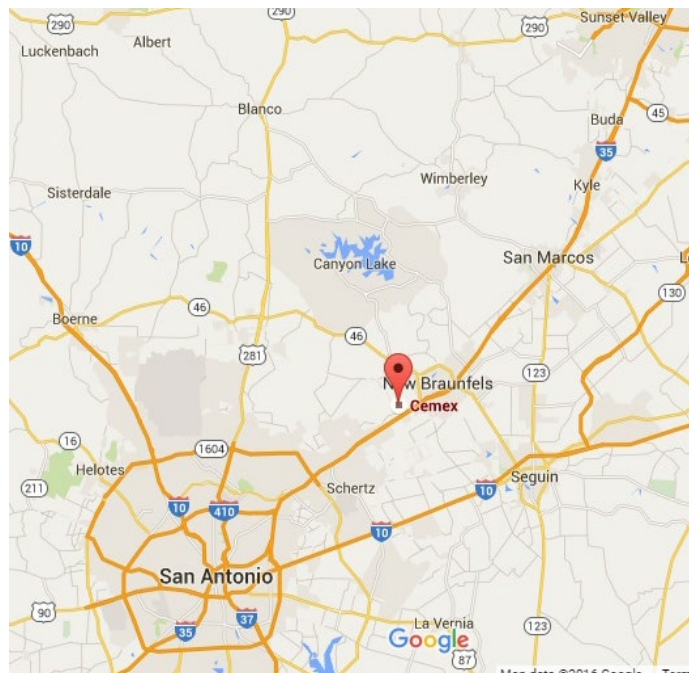
Figure 21: Location where Cemex Flexible Base Gravel was acquired

3.2.1. Grain Size Distribution

Using the standard sieve analysis procedure, the grain size distribution of the Cemex Flexible Base Gravel was determined and is shown in Figure 22. Values for D_{10}, D_{30}, and D60 as well as the uniformity coefficient and coefficient of gradation are listed in Table 4.

3.2.2. Specific Gravity

The average specific gravity (G_s) obtained for the Cemex Flexible Base Gravel was 2.65.

3.2.3. Atterberg Limits

Atterberg limits were determined for the fines of the Cemex Flexible Base Gravel according to ASTM D 4318. The plastic limit, liquid limit and plasticity index values are reported in Table 4.

3.2.4. Soil Classification

Based on the grain size distribution data presented in Table 4 and Figure 22, the values of C_c and C_u were calculated as shown in Table 4. Per ASTM D 2487, the Cemex Flexible Base Gravel is classified as silty clayey gravel (GC-GM).
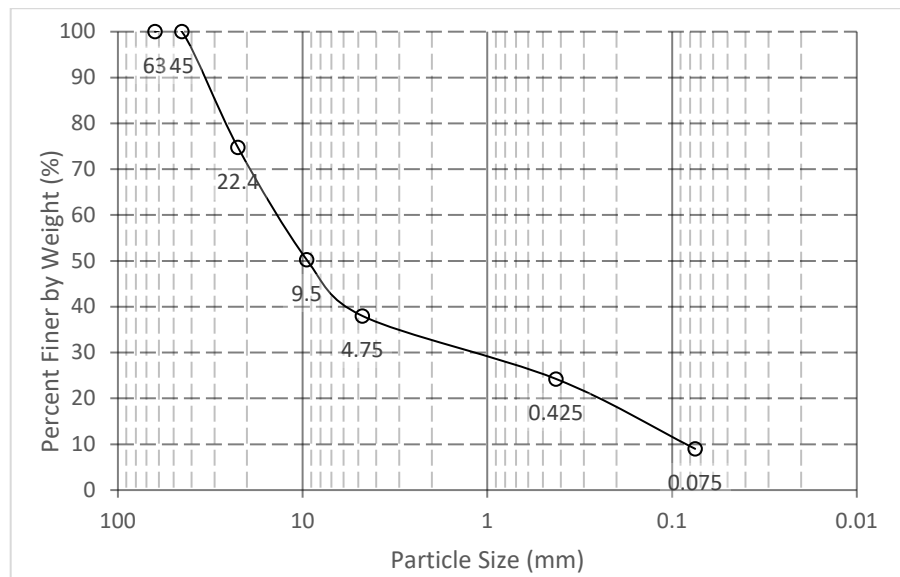
Figure 22. Grain size distribution of Cemex Flexible Base Gravel

3.2.5. Maximum Dry Density and Optimum Moisture Content

Standard Proctor compaction tests (ASTM D 698) were performed on the Cemex Flexible Base Gravel. The results obtained from standard Proctor tests are summarized in Table 4. The curve

46

corresponding to the procedure is plotted in Figure 23. The optimum moisture contents and maximum dry densities are presented in Table 4.

Table 4. Properties of Cemex Flexible Base Gravel

Test	Index parameter	Value	ASTM standard
Soil classification		GC-GM	D 2487
Specific gravity	Specific gravity, G_s	2.65	D 854-14
Grain size distribution	D_{10} (mm)	0.08	D 422
	D_{30} (mm)	1.3	
	D_{60} (mm)	14	
	Cu	175	
	Cc	1.51	
Atterberg limits	Liquid Limit, LL (%)	20	D 4318
	Plastic Limit, PL (%)	15.5	
	Plasticity Index, PI (%)	4.5	
Standard Proctor compaction	Optimum Moisture Content, OMC (%)	7.3	D 698
	Maximum dry density, γ_d (pcf)	137.8	
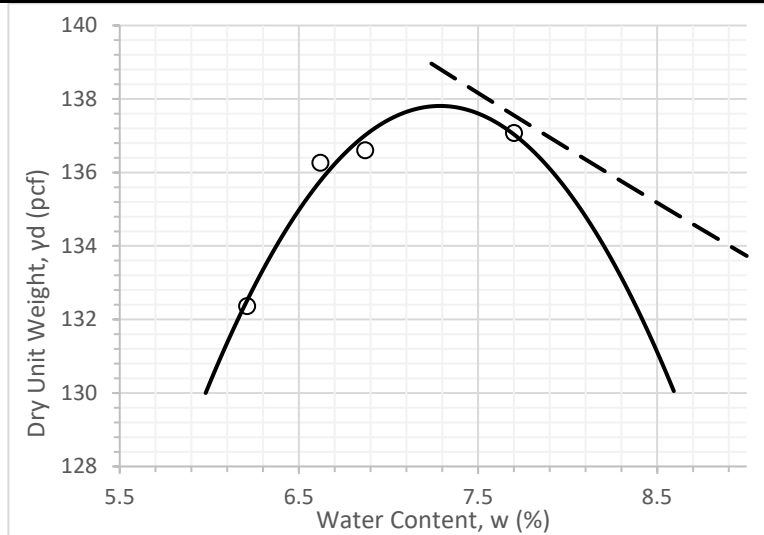
Figure 23. Compaction characteristics of Cemex Flexible Base Gravel

3.3. Characterization of Subgrade Soil

3.3.1. Site Investigation

Location of Borings

A series of borings were collected along an approximately 6-mile corridor between Foster Road and Graytown Road along IH10 in San Antonio. Figure 24 shows the site location in relation to Loop 410 in eastern San Antonio. A preliminary set of borings was conducted by ARIAS Geoprofessionals as shown in Figure 25. Additional borings were requested by the Performing Agency to evaluate the soil profiles and Potential Vertical Rise (PVR) using Direct Measurement of Swelling – Centrifuge (DMS-C) measurements of swelling. The locations of these borings are shown in Figure 26. This section provides a detailed evaluation of these additional borings. Each boring was conducted to a depth of 8 feet, except where Shelby tube sampling was met with refusal by the presence of excessive gravels.

Table 5 and Table 6 summarize coordinates of the borings conducted by ARIAS Geoprofessional and the Performing Agency, respectively.
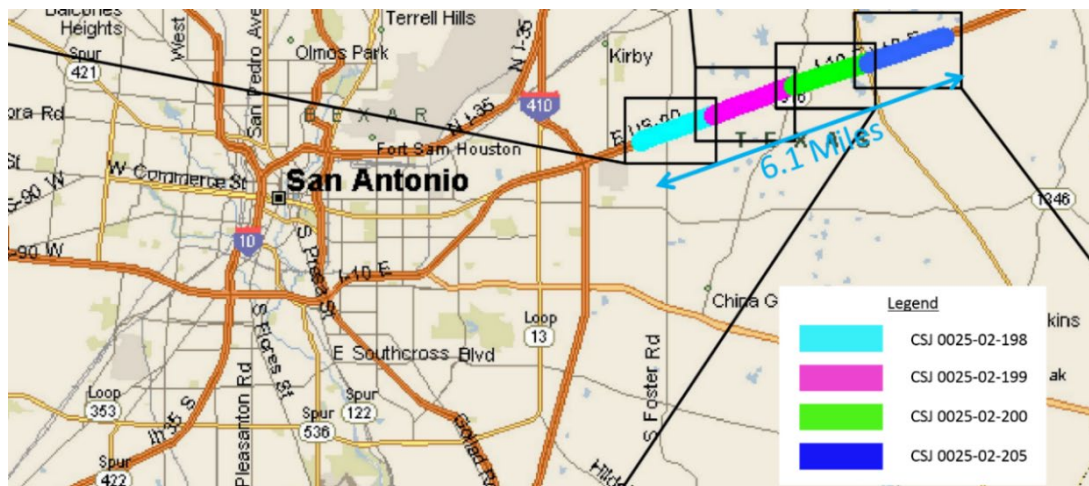
Figure 24. Project locations in relation to Loop 410 in San Antonio
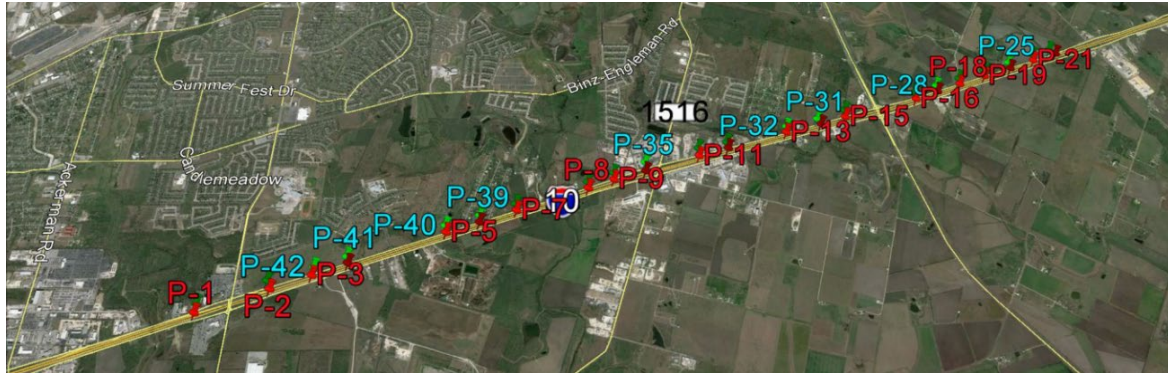
Figure 25. Locations of Shelby tube borings performed by ARIAS Geoprofessionals

Table 5. ARIAS Geoprofessionals eastbound IH10 frontage road sample coordinates and USDA classifications of surface material

Boring	Latitude	Longitude	USDA soil classification	Surface soil horizon
P-1	29°26'36.9"N	98°21'51.5"W	HB	B
P-2	29°26'44.9"N	98°21'25.9"W	HB	C
P-3	29°26'49.9"N	98°21'11.3"W	HB	B
P-4	29°26'53.8"N	98°20'58.7"W	HB	C
P-5	29°27'05.1"N	98°20'23.6"W	HE	C
P-6	29°27'08.8"N	98°20'11.3"W	HB	B
P-7	29°27'13.3"N	98°19'57.5"W	HB	B
P-8	29°27'21.8"N	98°19'30.2"W	HE	C
P-9	29°27'25.1"N	98°19'20.3"W	HB	B
P-10	29°27'28.3"N	98°19'07.9"W	HB	A
P-11	29°27'34.4"N	98°18'46.7"W	HB	A
P-12	29°27'37.6"N	98°18'35.0"W	HB	A
P-13	29°27'44.0"N	98°18'11.4"W	HB	B
P-14	29°27'47.4"N	98°17'58.1"W	TF	-
P-15	29°27'50.4"N	98°17'46.9"W	HB	B
P-16	29°27'58.1"N	98°17'16.9"W	HB	C
P-17	29°28'01.6"N	98°17'07.3"W	HB	C
P-18	29°28'04.7"N	98°16'57.6"W	HB	C
P-19	29°28'08.4"N	98°16'46.5"W	HB	B
P-20	29°28'11.9"N	98°16'34.9"W	HB	B
P-21	29°28'15.5"N	98°16'24.4"W	HB	B
P-22	29°28'18.6"N	98°16'14.2"W	TF	-

49

Table 6. Additional borings conducted for centrifuge PVR analysis

Boring	Latitude	Longitude	USDA soil classification	Surface soil horizon
B-1	29°26'20.94"N	98°22'42.02"W	BR	A
B-2	29°26'22.28"N	98°22'39.17"W	BR	A
B-4	29°26'38.83"N	98°21'44.32"W	HB	B
B-5	29°26'41.58"N	98°21'36.18"W	HB	C
B-6	29°26'44.30"N	98°21'28.70"W	HB	C
B-7	29°26'45.85"N	98°21'23.70"W	HF	D
B-8	29°26'48.27"N	98°21'15.46"W	HF	D
B-9	29°26'49.34"N	98°21'14.26"W	HF	D
B-10	29°26'49.46"N	98°21'12.60"W	HF	D
B-11	29°26'49.98"N	98°21'11.28"W	HB	B
B-12	29°26'50.50"N	98°21'10.01"W	HB	B
B-13	29°26'50.80"N	98°21'08.78"W	HB	B
B-14	29°26'51.29"N	98°21'07.78"W	HB	B
B-15	29°26'51.61"N	98°21'06.41"W	HB	B
B-16	29°26'51.98"N	98°21'04.97"W	HB	B
B-17	29°26'52.46"N	98°21'03.67"W	HB	C
B-20	29°26'54.82"N	98°20'56.09"W	HB	C
B-21	29°26'55.93"N	98°20'52.61"W	HB	C
B-22	29°26'59.22"N	98°20'42.35"W	HB	C
B-23	29°27'32.71"N	98°18'52.05"W	HB	A
B-24	29°27'34.67"N	98°18'45.55"W	HB	A
B-25	29°27'45.32"N	98°18'06.38"W	HB	B
B-26	29°27'50.55"N	98°17'46.36"W	HB	B
B-27	29°27'57.17"N	98°17'20.02"W	HB	C
B-28	29°28'01.63"N	98°17'07.43"W	HB	C
B-29	29°28'04.78"N	98°16'57.64"W	HB	C
B-30	29°28'09.53"N	98°16'42.93"W	HE	C

Figure 26. Locations of new Shelby tube borings performed

3.3.2. Index Properties of Subgrade Soil Encountered in Borings

Moisture contents were measured on samples collected from each of the 30 borings. The results are tabulated in Table 7. Borings 3, 18 and 19 were not sampled at all, and several others met with obstructions at depths less than 8 feet. Atterberg limits were measured for each sampled depth interval using the single point method and are tabulated in Table 7.

Table 7. Atterberg limits of sampled soils from borings B-1 to B-30

Boring	Depth (ft)	W (%)	LL	PI	Boring	Depth (ft)	W (%)	LL	PI
B-1	0-2	22.4	55	35	B-16	0-2	10.9	51	31
	2-4	24.5	62	45		2-4	40.5	114	86
	4-6	12.6	39	21		4-6	51.7	148	130
	6-8	13.4	32	16		6-8	35.9	120	84
B-2	0-2	28.3	62	46	B-17	0-2	16.6	75	56
	2-4	26.7	56	39		2-4	28.8	77	47
	4-6	14.1	33	19		4-6	38.0	97	71
	6-8	19.5	42	31		6-8	36.8	93	70
B-3	0-2	-	-	-	B-18	0-2	-	-	-
	2-4	-	-	-		2-4	-	-	-
	4-6	-	-	-		4-6	-	-	-
	6-8	-	-	-		6-8	-	-	-
B-4	0-2	-	-	-	B-19	0-2	-	-	-
	2-4	22.6	65	44		2-4	-	-	-
	4-6	25.2	87	60		4-6	-	-	-
	6-8	19.5	80	67		6-8	-	-	-
B-5	0-2	18.3	58	40	B-20	0-2	14.4	53	35
	2-4	28.3	99	81		2-4	34.9	95	77
	4-6	25.5	88	70		4-6	37.8	83	63
	6-8	27.2	82	65		6-8	36.8	58	34
B-6	0-2	10.7	54	39	B-21	0-2	30.8	51	31
	2-4	31.7	65	46		2-4	31.7	71	50
	4-6	30.6	94	69		4-6	38.1	88	62
	6-8	20.2	53	39		6-8	37.5	97	72
B-7	0-2	27.8	54	37	B-22	0-2	21.4	65	42
	2-4	26.7	44	24		2-4	42.6	97	62
	4-6	21.9	53	36		4-6	59.4	83	49
	6-8	-	-	-		6-8	39.4	101	69
B-8	0-2	16.0	45	24	B-23	0-2	18.9	66	44
	2-4	26.4	80	61		2-4	10.1	50	33
	4-6	31.1	62	44		4-6	-	-	-
	6-8	32.0	72	54		6-8	-	-	-
B-9	0-2	12.0	64	50	B-24	0-2	14.9	62	37

Boring	Depth (ft)	W (%)	LL	PI	Boring	Depth (ft)	W (%)	LL	PI
	2-4	36.6	78	52		2-4	20.4	57	37
	4-6	38.0	65	37		4-6	12.3	51	33
	6-8	36.0	83	65		6-8	29.3	70	52
B-10	0-2	34.3	45	30	B-25	0-2	24.6	61	41
	2-4	37.4	88	62		2-4	-	-	-
	4-6	35.7	84	66		4-6	-	-	-
	6-8	35.6	80	62		6-8	-	-	-
B-11	0-2	39.2	76	55	B-26	0-2	21.4	58	39
	2-4	36.3	79	54		2-4	7.8	38	23
	4-6	35.2	84	60		4-6	5.1	41	24
	6-8	35.9	66	39		6-8	-	-	-
B-12	0-2	27.1	67	49	B-27	0-2	20.4	57	40
	2-4	36.0	89	61		2-4	20.2	60	35
	4-6	36.3	83	57		4-6	-	-	-
	6-8	35.6	88	62		6-8	-	-	-
B-13	0-2	29.3	63	47	B-28	0-2	18.3	61	39
	2-4	34.7	73	54		2-4	14.8	41	24
	4-6	29.2	39	11		4-6	18.2	44	28
	6-8	34.2	87	67		6-8	14.4	52	32
B-14	0-2	45.5	95	73	B-29	0-2	15.8	54	26
	2-4	27.6	54	36		2-4	26.7	109	85
	4-6	22.3	55	28		4-6	26.3	93	70
	6-8	61.6	50	25		6-8	27.4	80	55
B-15	0-2	17.1	59	35	B-30	0-2	25.3	54	32
	2-4	44.4	109	83		2-4	13.5	49	29
	4-6	52.8	132	98		4-6	32.8	87	62
	6-8	21.9	127	100		6-8	34.5	84	59

3.3.3. PVR Calculations at each Boring Location

Stress-Swell Curves and Vertical Rise

The Potential Vertical Rise (PVR) at each boring was assessed using swelling data generated for each 2-ft interval using the DMS-C method. Shelby tube samples were sectioned and allowed to moisture-adjust in an environmental chamber, and then tested for swelling using centrifuge swell testing technology. A total of four specimens were prepared for each 2-ft interval within each boring collected during sampling.

Based on previous research, a log-linear stress-swell behavior was assumed to fit the swell-stress data using the equation:

$$\varepsilon(\sigma') = A \ln(\sigma') + B \qquad\qquad (1)$$

where *A* represents the slope of a log-linear trend, and *B* represents the swelling at unit effective stress. Both *A* and *B* were calculated through ordinary least-squares log-linear regression. It should be noted that when *A* was larger than zero, *A* was set equal to zero, and *B* was set equal to the average of all measured strains for that 2-ft. section. Both *A* and *B* were set to zero when consolidation (instead of swelling) was measured for both the upper and lower set of stresses. Where significant gravel was encountered during sampling, material below the depth of Shelby tube refusal was assumed not to swell.

The expected swell of each 2-ft section was calculated for each layer, in inches, by numerically integrating the positive portion of the swell-stress curve between the stresses expected at the top and bottom of the layer. The PVR at a given location was calculated as the sum of the swelling expecting of the four 2-ft layers at that location. Soil profiles in this study were truncated at a depth of 8 ft and some swelling strain could be expected below that depth based on the swell-stress data.

Centrifuge testing was performed on specimens collected from each boring, and PVR data and calculated PVR values are shown in Table 8. PVR values from the DMS-C approach are shown first, while TEX-124-E values are shown in parentheses for reference. Additionally, the *A* and *B* parameters for each swell-stress curve are shown in the legend for each depth interval.

Table 8. PVR data by boring

Boring	USDA soil series	PVR [in] DMS-C (TEX-124-E)	PVR swell-stress data
B-1	BR	1.39 (0.37)	
B-2	BR	3.23 (0.61)	

54

Boring	USDA soil series	PVR [in] DMS-C (TEX-124-E)	PVR swell-stress data
B-4	HB	3.42 (3.19)	
B-5	HB	2.72 (1.84)	
B-6	HF	3.06 (0.51)	

Boring	USDA soil series	PVR [in] DMS-C (TEX-124-E)	PVR swell-stress data
B-7	HF	4.76 (1.45)	
B-8	HF	4.54 (1.66)	
B-9	HF	6.06 (0.99)	

Boring	USDA soil series	PVR [in] DMS-C (TEX-124-E)	PVR swell-stress data
B-10	HB	7.22 (1.57)	
B-11	HB	6.39 (1.11)	
B-12	HB	6.05 (1.51)	

57

Boring	USDA soil series	PVR [in] DMS-C (TEX-124-E)	PVR swell-stress data
B-13	HB	13.84 (1.30)	
B-14	HB	6.90 (2.27)	
B-15	HB	6.25 (2.80)	

Boring	USDA soil series	PVR [in] DMS-C (TEX-124-E)	PVR swell-stress data
B-16	HB	6.80 (1.74)	
B-17	HB	8.02 (1.63)	
B-20	HB	0.36 (1.07)	

59

Boring	USDA soil series	PVR [in] DMS-C (TEX-124-E)	PVR swell-stress data
B-21	HB	4.77 (1.27)	
B-22	HB	0.85 (0.26)	
B-23	HB	0.70 (0.88)	

Boring	USDA soil series	PVR [in] DMS-C (TEX-124-E)	PVR swell-stress data
B-24	HB	0.85 (1.14)	
B-25	HB	0.32 (1.00)	
B-26	HB	2.31 (2.72)	

Boring	USDA soil series	PVR [in] DMS-C (TEX-124-E)	PVR swell-stress data
B-27	HE	6.53 (0.78)	
B-28	BR	6.25 (2.80)	
B-29	BR	6.80 (1.74)	

Boring	USDA soil series	PVR [in] DMS-C (TEX-124-E)	PVR swell-stress data
B-30	HB	8.02 (1.63)	

3.4. Characterization of Geogrid Reinforcement

3.4.1. Sampling of Geogrids

Samples were collected from the geosynthetic rolls used in the test sections constructed along the Westbound Frontage Road (WBFR) as well as the test sections constructed along the Eastbound Frontage Road (EBFR) at location 2 – part 3 and location 2 – part 2. The geosynthetic materials used in the WBFR and EBFR test sections included a type II geogrid and types I, II and III geogrids, respectively, classified according to TxDOT DMS6240. Figure 27 shows samples collected from various test sections, a portion of which was also sent to the TxDOT material laboratory for independent characterization.

a)

63

Figure 27. Geosynthetic samples collected from various IH10 test sections: a) geogrid type II from WBFR test section; b) geogrid type I from EBFR test sections; c) geogrid type II from EBFR test sections; and d) geogrid type III from EBFR test sections

3.4.2. Geometric Properties of Geogrids

Geosynthetic samples collected from IH10 test sections were characterized in the geosynthetics laboratory at the University of Texas at Austin. Geometric properties of the collected samples were determined and compared with the characteristics reported by the manufacturer. Table 9 summarizes the measured geometric properties of the aperture, ribs and junctions for geogrid types I, II and III, along with the geometric characteristics reported by the manufacturer and TxDOT DMS6240 requirements.

3.4.3. Strength and Stiffness Properties of Geogrids

Unconfined wide-width tensile strength tests were conducted on the geosynthetic samples at a rate of 10%/min in accordance with ASTM 6637. The specimens were approximately 10 in long and 7.9 in wide. A total of five longitudinal ribs and four effective transverse ribs were tested in each specimen. The side longitudinal ribs were cut per ASTM 6637 recommendations. Consequently, the effective width of the tested specimens included three longitudinal ribs. Figure 28 shows an example of the geosynthetic specimens before and after the tensile test.

a)   b)
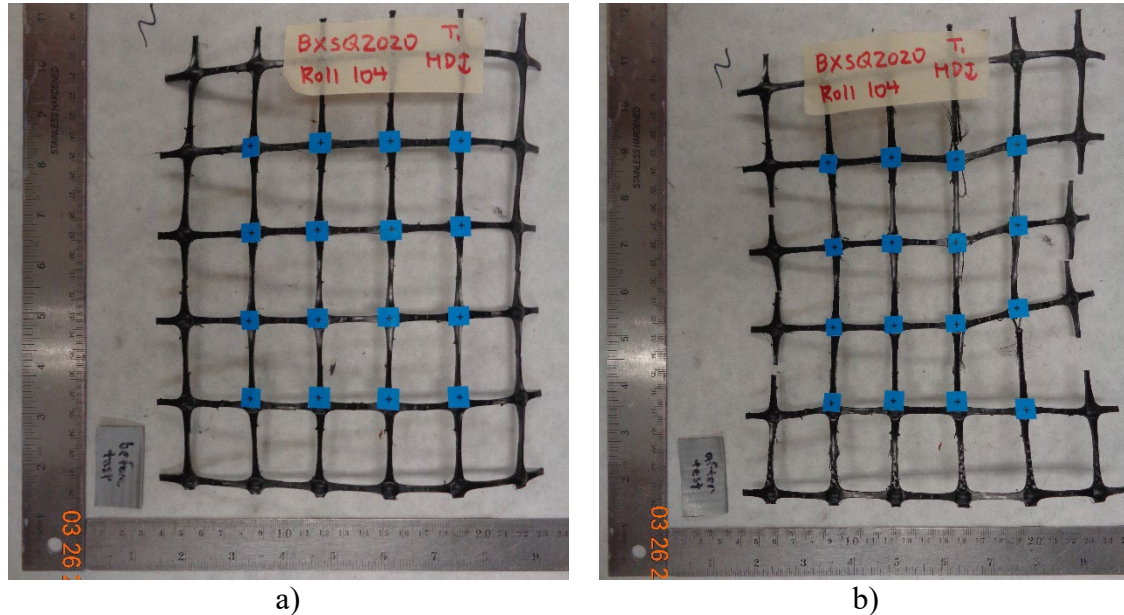
Figure 28. Geogrid type II specimen in tensile tests: a) before test; and b) after test

The tensile tests were conducted at a displacement rate of 0.04 in/min, which is consistent with the displacement rate used in the small soil-geosynthetic interaction test to determine the stiffness of the soil-geosynthetic interaction. Several repeat tests were conducted along the machine and cross-machine directions. Tensile properties were characterized for all three longitudinal ribs in each test using image analysis techniques. Figure 29 shows an example of unit tension-tensile strain data obtained along the machine direction for geogrid type II specimens collected from the WBFR test section.

Table 9. Geometric properties of geosynthetic samples compared to manufacturers' data sheet and TxDOT DMS6240 requirements

		Geogrid type I	Geogrid type II	Geogrid type III
Aperture dimension, mm machine direction*	UT measurement	42.8	42.3	46
		32.8	39.5	39

65

		Geogrid type I	Geogrid type II	Geogrid type III
cross machine direction	Manufacturer's data sheet	38 38	38 38	40 --
	TxDOT DMS6240	25-51	25-51	25-51
Mid-rib depth, mm machine direction* cross machine direction	UT measurement	1.0 0.9	1.6 1.1	1.4 1.2
	Manufacturer's data sheet	0.7 0.5	1.1 0.8	1.3 1.2
	TxDOT DMS6240 (min)	0.77 0.64	1.27 1.15	1.27 1.15
Mid-rib width, mm Machine direction* cross machine direction	UT measurement	2.1 2.1	2.3 2.9	1.1 1.4
	TxDOT DMS6240	--	--	--
Junction thickness, mm	UT measurement	3.0	3.2	2.9
	TxDOT DMS6240	1.5	2.54	2.54
Mass per unit area, gr/m^2	UT measurement	147	222	209
	TxDOT DMS6240	--	--	--
Junction efficiency, % of rib ultimate tensile strength	Manufacturer's data sheet	93	93	--
	TxDOT DMS6240 (min)	90	90	90
Aperture stability, m-N/deg	Manufacturer's data sheet	0.32	0.45	--

* Diagonal direction for multiaxial geogrid type III
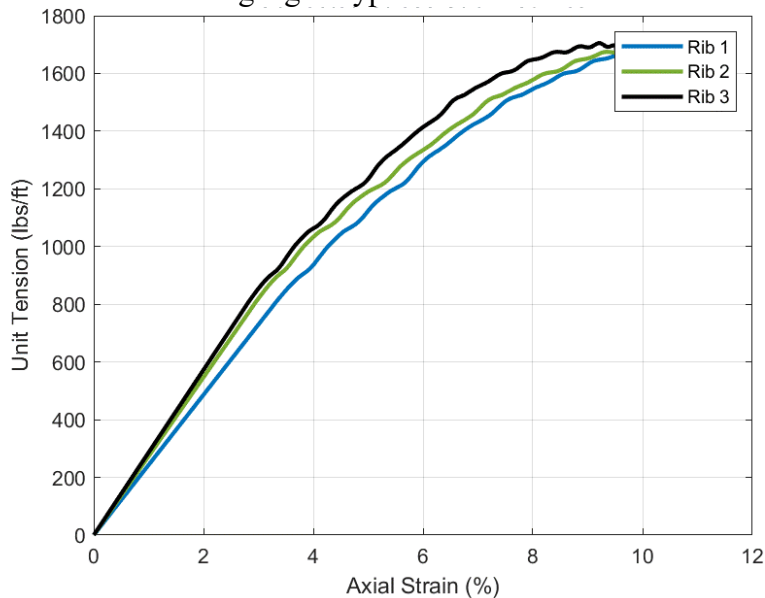
Figure 29. Unit tension versus tensile strain data for geogrid type II specimen along machine direction

Results obtained in the tensile tests were used to determine ultimate tensile strength and unit tension at various strain levels. Table 10 summarizes the measured ultimate tensile strength in both machine and cross machine direction and the unit tensions corresponding to various strain levels for geogrid type II. The minimum values for these tensile properties reported in the manufacturer's data sheet are also presented in Table 10. The measured values were expectedly higher than the minimum values reported by the manufacturer.

Table 10. Ultimate tensile strength and unit tension at various strain levels for geogrid type II specimens

	Machine Direction (MD)		Cross machine Direction (CD)	
	UT measurement	Manufacturer's data sheet	UT measurement	Manufacturer's data sheet
Ultimate tensile strength, lb./ft	> 1700	1370	> 1800	1370
Unit tension at 1% strain, lb./ft	350	--	500	--
Unit tension at 2% strain, lb./ft	575	450	750	450
Unit tension at 5% strain, lb./ft	1200	890	1350	890
Tensile strain at breakage (%)	> 9	--	> 7	--

The measured unit tension at 2% strain was used to calculate the tensile modulus of geogrid type II in the machine and cross machine directions as 28,750 and 37,500 lb/ft, respectively. The obtained tensile modulus was higher than the minimum tensile modulus required by DMS-6240 in the machine and cross machine directions, which are 14,000 and 20,000, respectively.

3.4.4. Soil-reinforcement Interaction Properties (K_{SGC}) of Geogrids

Small Soil-Geosynthetic Interaction (SGI) tests were conducted in accordance with TxDOT standard test procedure Tex-136-E (TxDOT, 2022) for the geosynthetic specimens collected from IH10 test sections. The parameter resulting from these tests is the stiffness of the soil-geosynthetic interaction (K_{SGC}), also referred to as geosynthetic composite stiffness, which captures the tensile characteristics of the confined geosynthetic and shear behavior of the soil–geosynthetic interface (Zornberg et al., 2017; Roodi and Zornberg, 2017). As specified in the Tex-136-E test procedure, the confined dimensions of the geosynthetic specimens were approximately 9.25 in long and 10.8 in wide. Displacement transducers were connected to five different junctions along the confined portion of the geogrid specimens. Metal wires were used to connect the geogrid junctions to displacement transducers. Figure 30 shows the specimen preparation and test setup for SGI tests.

An example data set used to obtain K_{SGC} values for geogrid type III is presented in Figure 31. The K_{SGC} value of each test was determined by linear interpolation of the unit tension squared (T^2) versus displacement (u) data. The K_{SGC} values in the cross-machine direction for geogrid types I and III specimens are summarized in Table 11.

a)

b)

c)
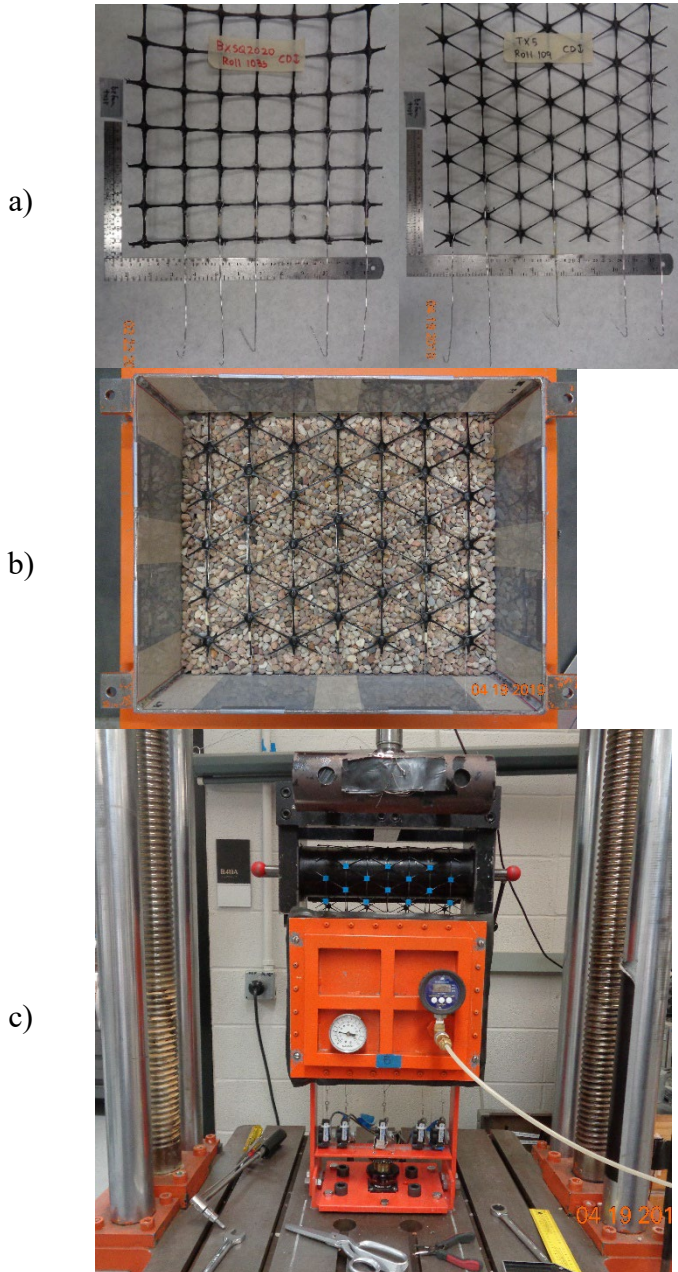
Figure 30. Small SGI test on a geogrid specimen from IH10 project: a) specimens of geogrid types II and III before testing; b) placing geogrid type III specimen in test box; and c) small SGI test setup
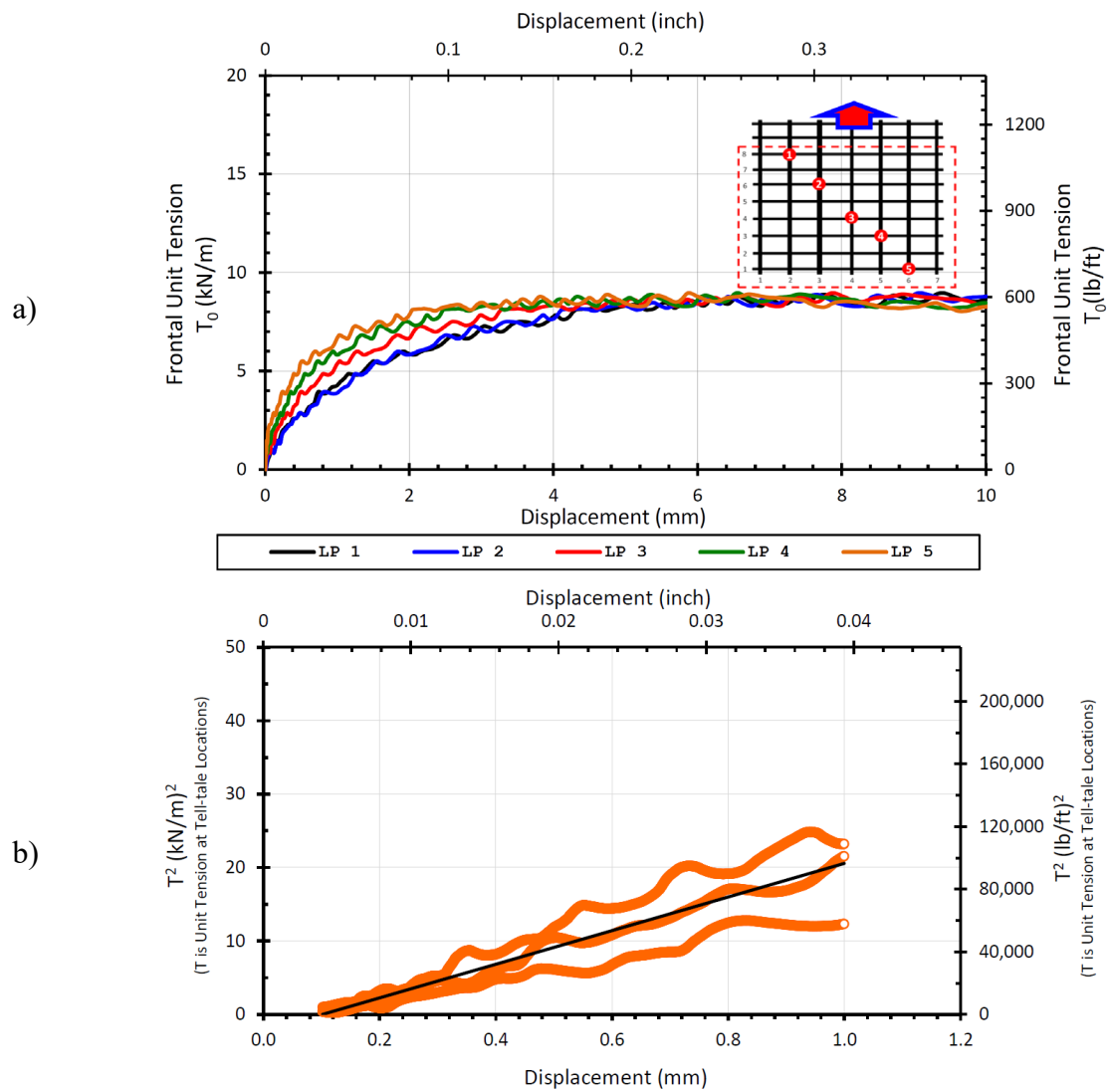
Figure 31. Small SGI test results for geogrid type III specimen along CD: a) unit tension versus displacement data; and b) unit tension squared versus displacement data

Table 11. Initial K$_{SGc}$ in CD, (kN/m)2/mm

	Test 1	Test 2	Test 3
Geogrid Type I from test sections along EBFR	16.3	13.4	16.4
Geogrid Type III from test sections along EBFR	21.5	26.7	24.8

Chapter 4. Instrumentation

4.1. Introduction to Instrumentation

This chapters summarizes the procurement, testing and installation of various materials used in the construction of the test sections along ongoing construction in IH10.

4.2. Instrumentation Layout

Five sets of instrumentation were used for this project (one for each type of geogrid and two in the control section) as shown in Figure 32. The two sets in the control section (No GG) are referred to as section 1a (to the left) and section 1b (to the right). The other sets are referred to as section 2 (type III), 3 (type II) and 4 (type I), respectively, from left to right.
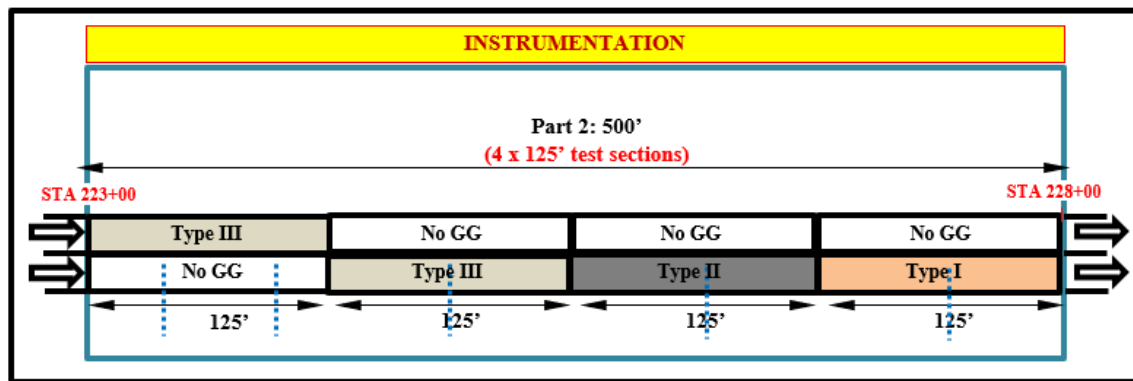
Figure 32. Location of instrumentation within test sections

An overall schematic of the instrumentation layout for each set of instrumentation is shown in Figure 33.
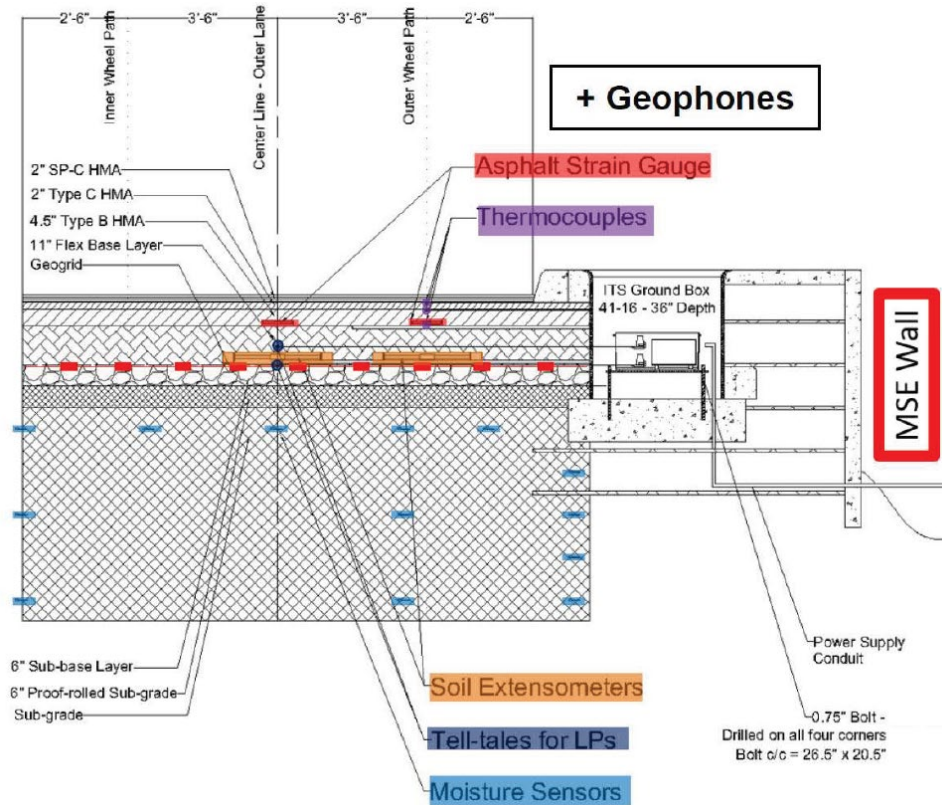
Figure 33. Overall schematic of instrumentation layout

4.2.1. Linear Potentiometers with Tell-tales

Linear potentiometers were used to measure displacements of the geosynthetic reinforcement as well as soil particles close to the geosynthetic and in the middle of the base layer. A schematic of positioning linear potentiometers and tell-tales for connection to the geosynthetic and soil particles are presented in Figure 34.

71
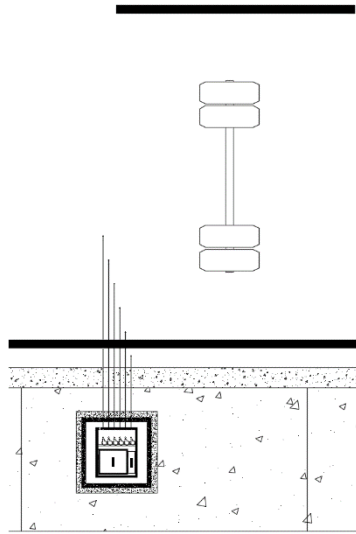
Figure 34. Tell-tales and LP in plan at all sections

4.2.2. Soil Extensometers

Soil extensometers consist of an H-shaped device in which a Linear Variable Differential Transformer (LVDT) is installed between two flanges. The relative displacement between the two flanges is measured by the LVDT. A schematic of the positioning of a soil extensometer relative to the wheel path is presented in Figure 35. Four soil extensometers will be installed in each instrumented section within the control section and two soil extensometers will be installed in each geogrid-stabilized test section.
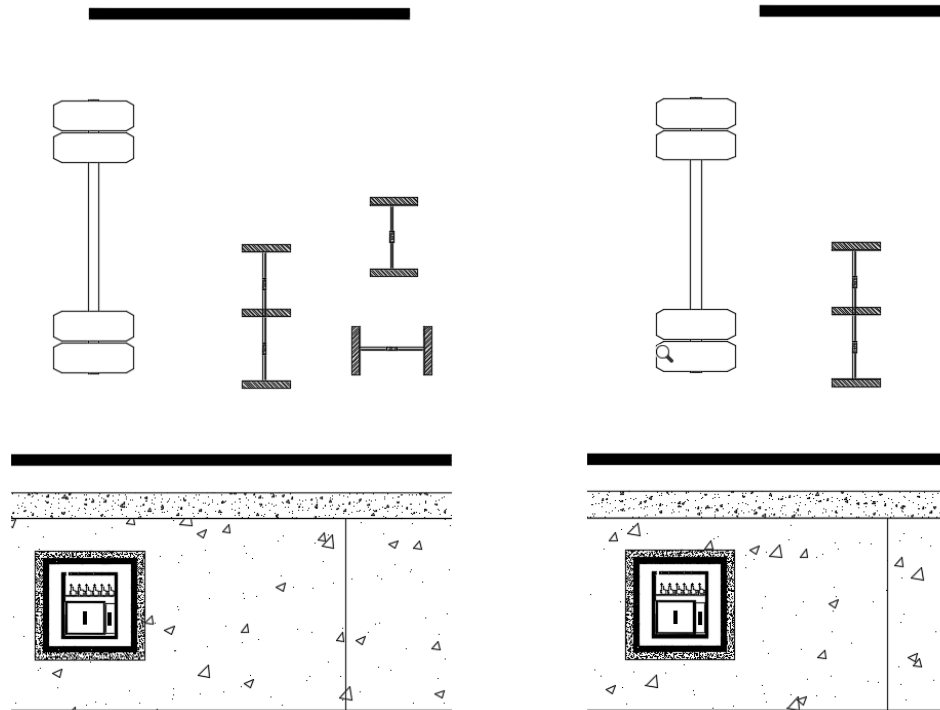
Figure 35. Soil extensometer layout in plan: a) at sections 1a & 1b; and b) at sections 2, 3 & 4

4.2.3. Asphalt Strain Gauge

Asphalt strain gauges will be used to measure tensile strain in the hot mix asphalt layer. They are composed of H-shaped sensors that can be installed in the direction of the traffic or perpendicular to the traffic direction. Figure 36 presents a schematic layout of the location and orientation of the asphalt strain gauges as compared to the traffic wheel path.
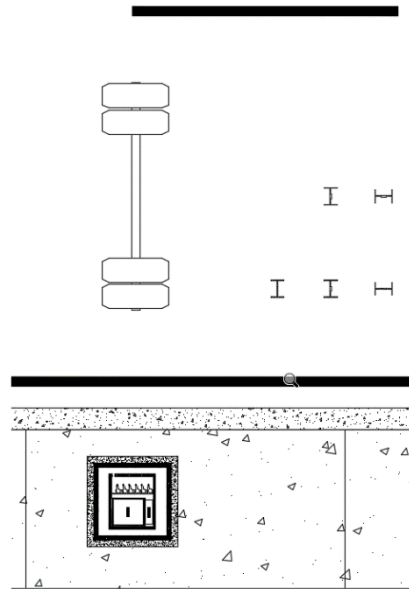
Figure 36. Asphalt strain gauge layout in plan at all sections

4.2.4. Concrete Strain Gauges

An additional type of strain gauges, referred to as concreted strain gauges, will also be used in the hot mix asphalt layer to measure tensile strain. These sensors have been typically been used in a concrete. However, they may also provide useful information in hot mix asphalt pavement. A smaller number of these strain gauges, as compared to the regular asphalt strain gauges, will be installed only in the right wheel path. The data recorded using these sensors will complement the data that will be recorded using asphalt strain gauges. Figure 37 presents a schematic of the layout of these sensors.
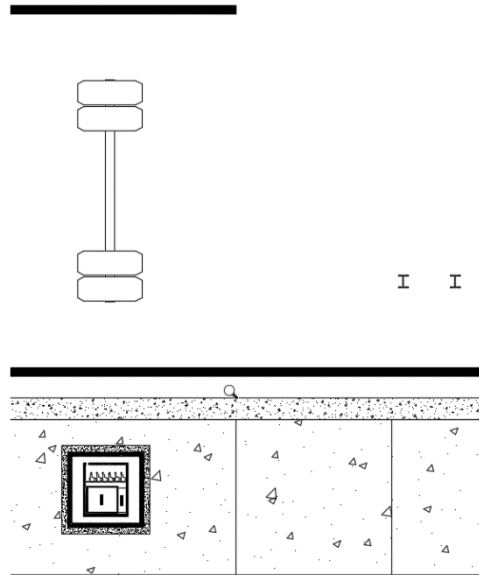
Figure 37. Concrete strain gauge layout in plan at section 2

4.2.5. Thermocouples

The thermocouples are installed with the longitudinal wheel path asphalt strain gauge, and directly above that on top of the first and second Hot Mix Asphalt (HMA) lifts at all sections.

4.2.6. Geophones

Geophones were in several pavement layers including subgrade, sub-base, base, and asphalt layers, to measure deflections in vertical and horizontal directions within the pavement structure. The geophone array consists of a complex 3D layout. Figure 38 shows the overall plan view of geophones in section 1a. Figure 39 shows the positioning of geophones in the longitudinal cross-section of the road along the wheel path in section 1a.
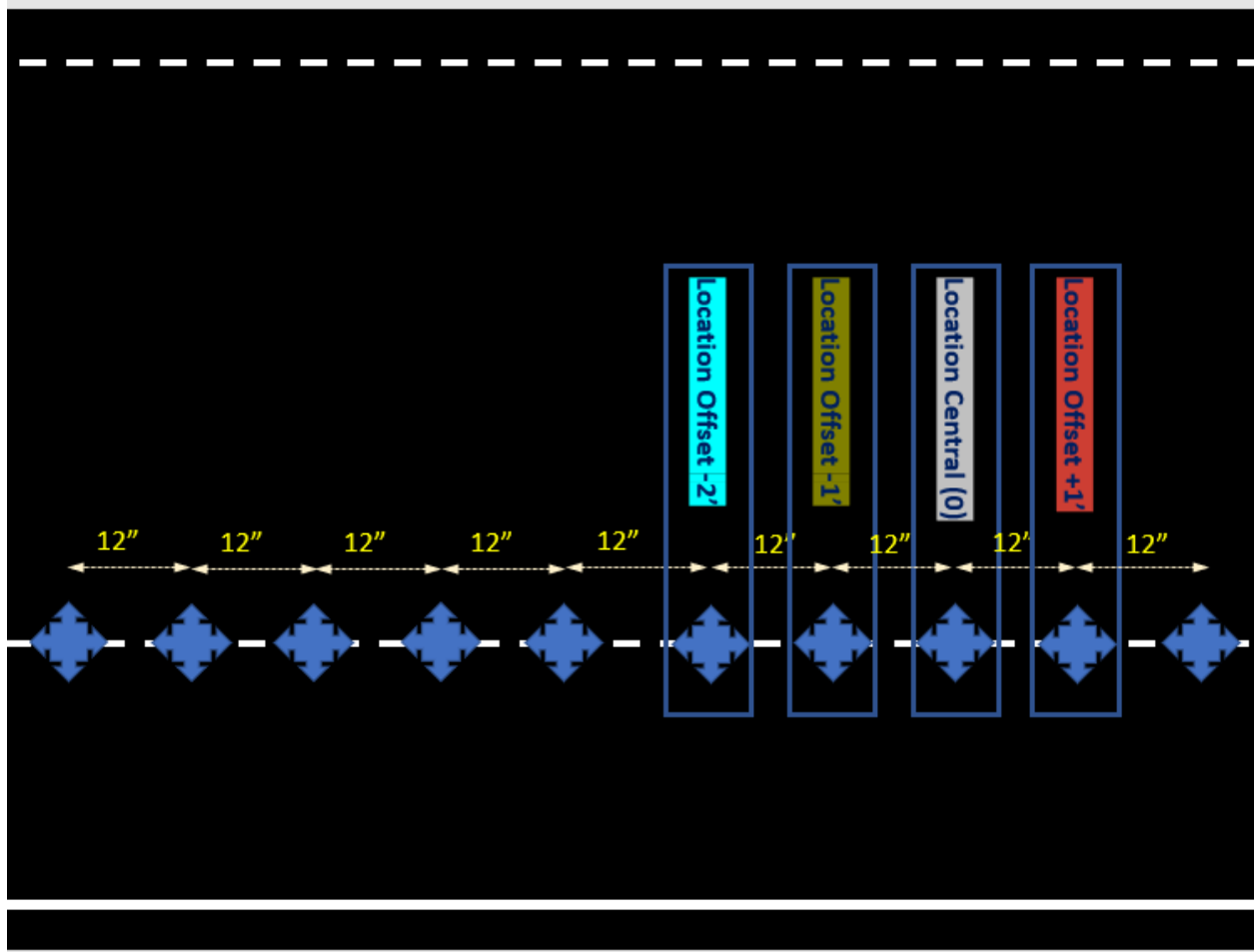
Figure 38. Overall plan view in section 1a

Figure 40 shows the overall plan view of geophones in sections 1b, 2, 3 and 4. Figure 41, Figure 42 and Figure 43 show section layouts of geophones in three cross-sections of the road located at +1, 0, and -1 ft, respectively. Figure 44 shows the positioning of geophones in the longitudinal cross-section of the road along the wheel path.
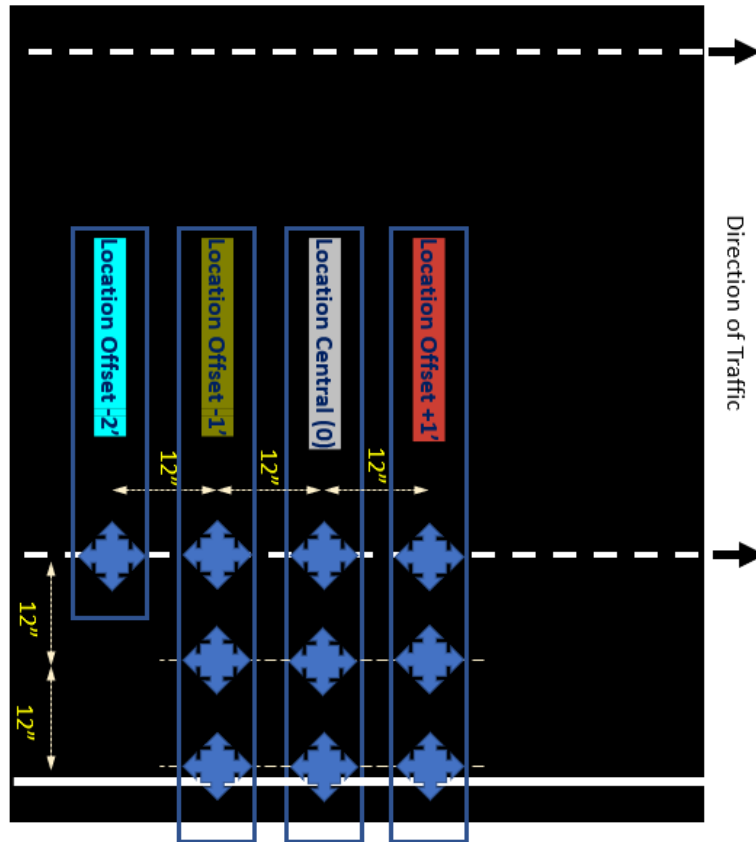
Figure 40. Overall plan view in sections 1b, 2, 3 & 4
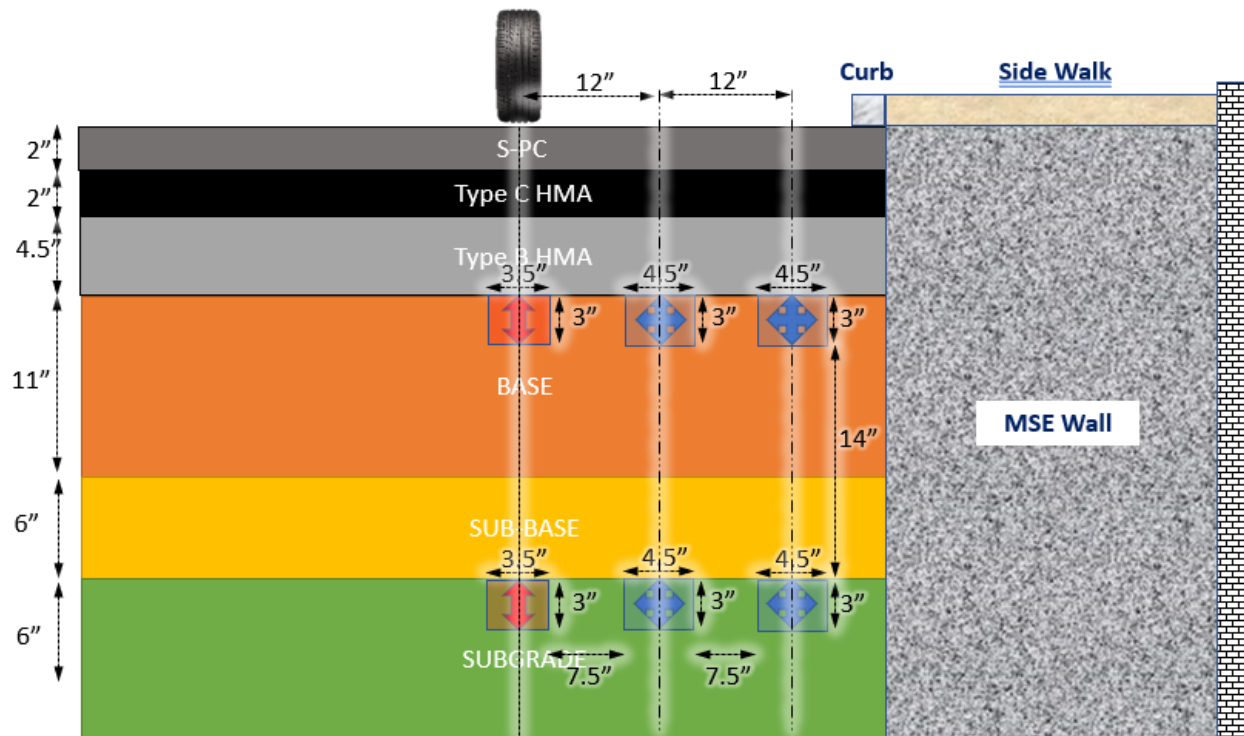
Figure 41. Cross section view at location offset +1' in sections 1b, 2, 3 & 4
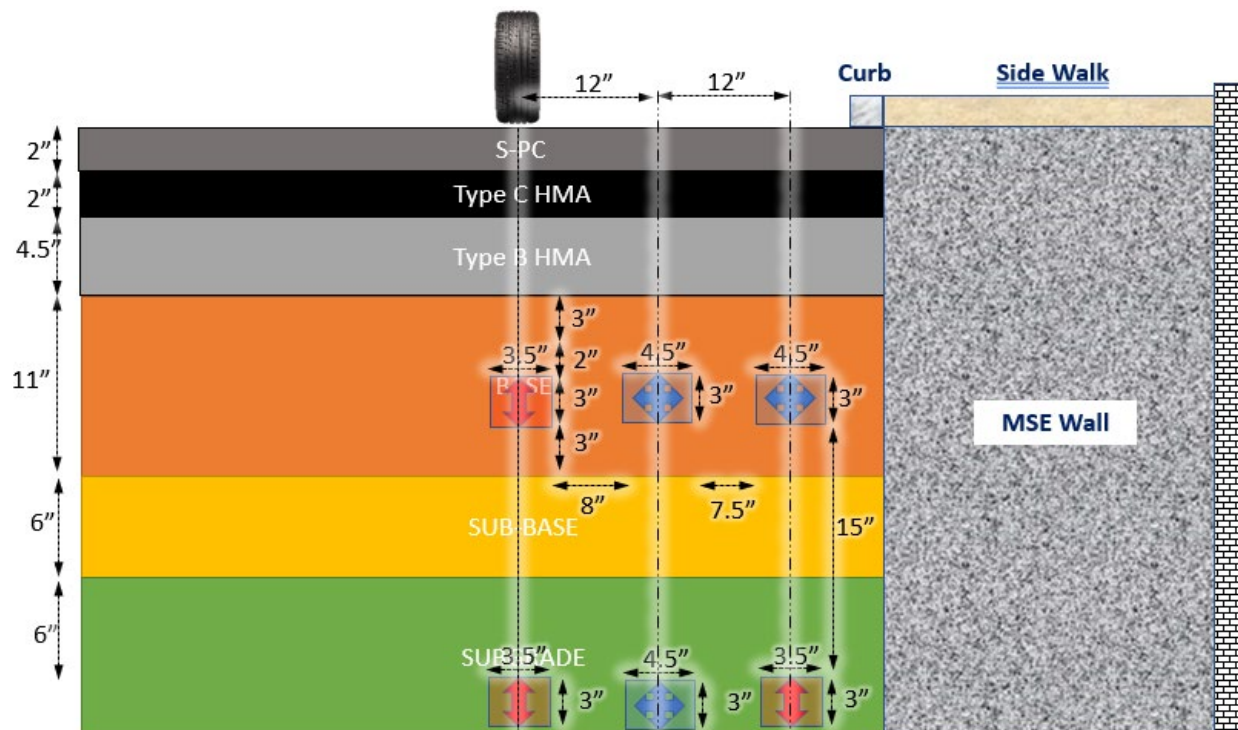
Figure 42. Cross section view at location central (0) in sections 1b, 2, 3 & 4
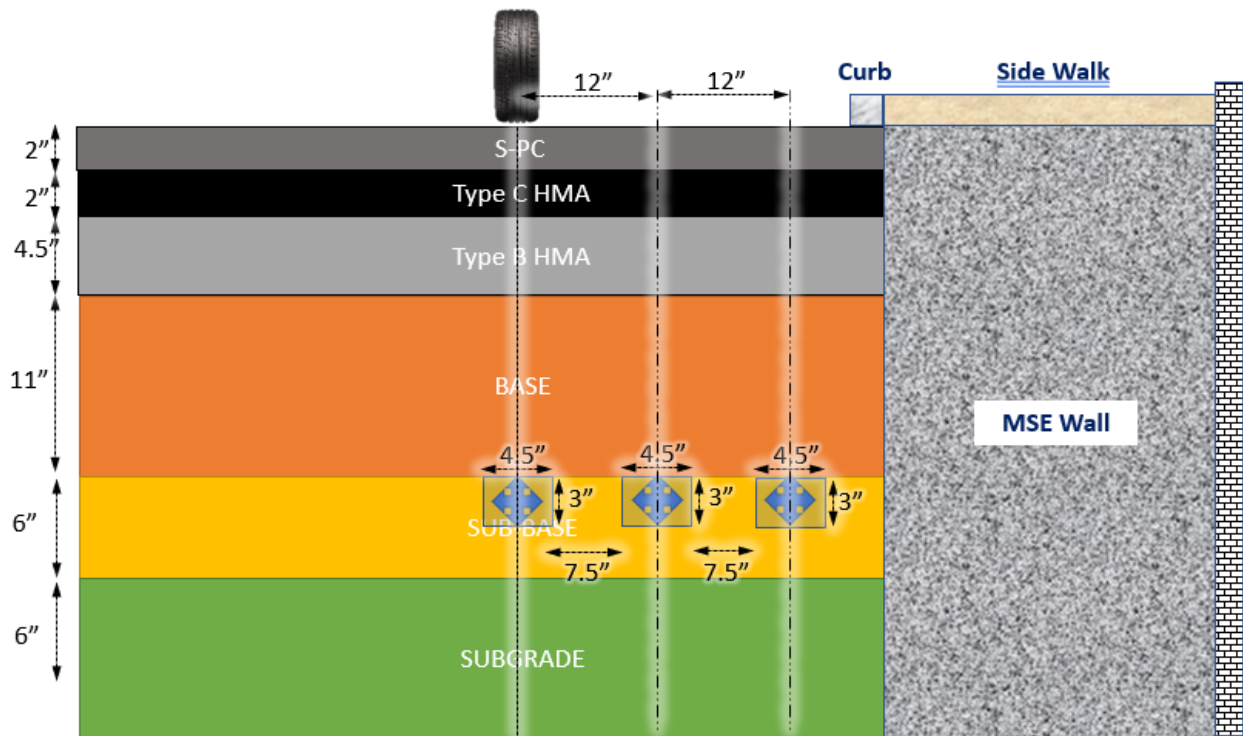
Figure 43. Cross section view at location offset -1' in sections 1b, 2, 3 & 4
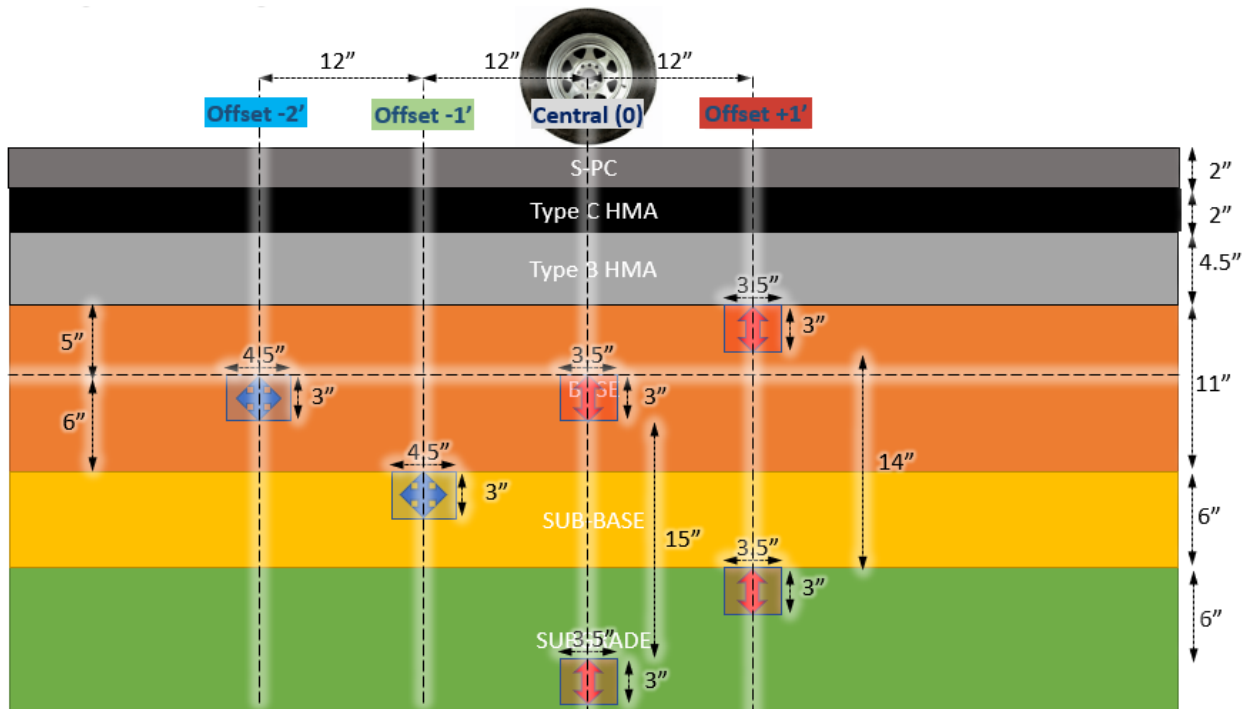
Figure 44. Longitudinal view along the wheel path in sections 1b, 2, 3 & 4

4.3. Specifications

4.3.1. Moisture Sensors

Table 12 summarizes characteristics of the moisture sensors. The maximum sensor length requirement was 5.9 in to allow sensors to be installed horizontally in a reasonably sized borehole. Time Domain Reflectometer (TDR) technology was required to allow additional sensor debugging abilities in the field, and when sensors are installed under marginal sensing conditions.

Table 12. Characteristics of moisture sensors

Maximum Length	15 cm
Volumetric Water Content Resolution	0.1% VWC
Volumetric Water Content Accuracy	± 2% typical
VWC Temp Stability	± 1% of full scale (1C-50C)
Temp Reporting Accuracy	± 0.2 °C to 50 C
Technology	TDR*

4.3.2. Tell-tales

The tell-tales consist of a spring-back 316 stainless steel wire encased in hard nylon tubing, protected inside a reduced-wall aluminum flexible conduit, running from the gravel simulant to the linear potentiometer. The nylon tubing is filled with silica anti-seize grease, which acts as a lubricant and is sealed on both ends with synthetic lubricant-resistant sealant. Various components of the tell-tale system are presented in Figure 45, Figure 46 and Figure 47. The specifications of the various components used in the tell-tales are listed in Table 13.

Figure 45. Components of gravel D50 simulant (from left bolt, nut, washer, assembled simulant)

Figure 46. Stainless steel tell-tale wire and white nylon plastic tubing

Figure 47. Reduced wall aluminum flexible conduit casing of nylon tubing

Table 13. Characteristics of tell-tales

Tell-tale wire	
Material	316 Stainless Steel
Diameter	0.032"
Tensile Strength	222,000 psi
Nylon Sleeve	
Material	Nylon Plastic
Hardness	Rockwell R110
Clarity	Semi-clear
Inner Diameter	7/64"
Outer Diameter	3/16"
Wall Thickness	1/32"
Bend Radius	1.5"
Temperature Range	-40 ^{0}F to 225 ^{0}F
Aluminum Housing	
Trade Size	3/8
Inner Diameter (min/max)	0.375"/0.393"
Outer Diameter (min/max)	0.560"/0.610"
Bend Radius	2"

Lubricant	
Lubricant Type	Grease
NLGI Viscosity Grade	2
Base Oil	Synthetic
Thickener	Silica
Temperature Range	-40 ^{0}F to 450 ^{0}F
Color	Clear
Sealant	
Type	Non-sagging
Formulation	Buna-N
Initial Hardening	10 min.
Final Hardening	24 hrs.
Elongation	100%
Hardness	Durometer 20A
Temperature Range	-30 ^{0}F to 300 ^{0}F
Gravel simulant	
18-8 Stainless Steel Hex Head Screw	3/8"-16 Thread Size, 3/8" Long
18-8 Stainless Steel Hex Nut	3/8"-16 Thread Size
316 Stainless Steel Split Lock Washer	3/8", 0.385" ID/0.550" OD

4.3.3. Linear Potentiometers

The linear potentiometers used are JX-P510 Series – environmentally sealed (IP 65, NEMA 4X) analog output (0 to 5V, 0 to 10V, ±5 V, ± 10 V) – transducers from UniMeasure Inc (Figure 48). They are for use in moderate duty applications in hostile wet or dry environments. The chemical resistant thermoplastic case of the transducer provides IP-65 (NEMA4X) ingress protection for applications where exposure to washdown, rain, oil and other liquids may occur. An integral dust wiper prevents the entry of debris as the wire rope is retracted. The electrical connection methodology includes a sealed bulkhead fitting with an electrical connector. The wire rope exit direction can be adjusted at time of installation. The specifications of the particular sensor chosen are listed in Table 14.

Figure 48. JX-P510 series precision potentiometers from UniMeasure

Table 14. Specifications of JX-P510 precision potentiometer from UniMeasure

General	
Measurement Range	2" (50 mm)
Linearity	±1 %
Repeatability	± 0.02 %
Construction	Thermoplastic Body
Wire Rope	Ø 0.018" (0.46 mm) Jacketed Stainless Steel
Wire Rope Tension	16 oz. (4.4 N)
Weight	6.7 oz. (190 g)
Connections	Plastic Connector
Life	2,000,000 full stroke cycles
Environmental	
Operating Temperature	-25 ^{0}C to 75 ^{0}C
Storage Temperature	-25 ^{0}C to 75 ^{0}C
Operating Humidity	100% R.H.
Vibration	15 G's 0.1 ms max.
Shock	50 G's 0.1 ms max.
Ingress Protection	IP-65
Electrical	
Output	0 to 5, 0 to 10, ±5, ± 10 VDC
Excitation Voltage	4.9 to 30 VDC
Excitation Current	25 mA max
Output Impedance	10 Ω max
Output Load	5KΩ min
Protection	Reversed Polarity
Adjustment Range–0 to 5 or 10 VDC	
Zero	0 to 30% Range
Span	80% to 100% Range
Adjustment Range – ±5, ± 10 VDC	
Zero	40% to 60% of Range

4.3.4. Soil Extensometers

The soil extensometers used are Model 4435 Vibrating Wire Soil Extensometer from Geokon (Figure 49). They are designed to be installed within soil to measure horizontal strains and deformations in roadway embankments. The extensometers work with the vibrating wire technology wherein the vibrating wire element is subjected to increasing tension as the flange separates. This causes the fundamental frequency of vibration (natural frequency) of the element to increase. The changed frequency is transmitted to data loggers which measures and translates the change in frequency to displacement of flanges. The specifications of the soil extensometer used are shown in Table 15.

Figure 49. 4435 vibrating wire soil extensometer from Geokon

Table 15. Specification of 4435 vibrating wire soil extensometer from Geokon

Vibrating Wire	
Range	1" or ±0.5" (25 mm or ± 12.5 mm)
Overrange	115%
Accuracy	0.1% (with polynomial expression)
Resolution	0..025% FSR
Linearity	0.25%
Thermal Zero Shift	0.05% FSR/^{0}C
Gauge Length	24" (610 mm)
Operating Temperature	-40 ^{0}C to +60 ^{0}C
Frequency Range	1200 Hz to 2800 Hz

Vibrating Wire	
Coil Resistance	180 Ω, ± 10 Ω
Cable Type	Two twisted pair (four conductor) 22 AWG Foil Shield, PVC Jacket, nominal OD = 0.25" (6.3 mm)
Diameter	1.05" (26.7 mm) body 1.5" (33 mm) telescoping section 2" (51 mm) flange
Flange	2.5" x 2.5" x 18" (62.5 x 62.5 x 457.5 mm)
Thermistor	
Range	-80 ^{0}C to +150 ^{0}C
Accuracy	± 0.5 ^{0}C

4.3.5. Asphalt Strain Gauge

The asphalt strain gauges used are ASG-152 Black 6/6 nylon cell Full Bridge strain gauges (Figure 50) from CTL Group. The specifications of the strain gauges are listed in Table 16.
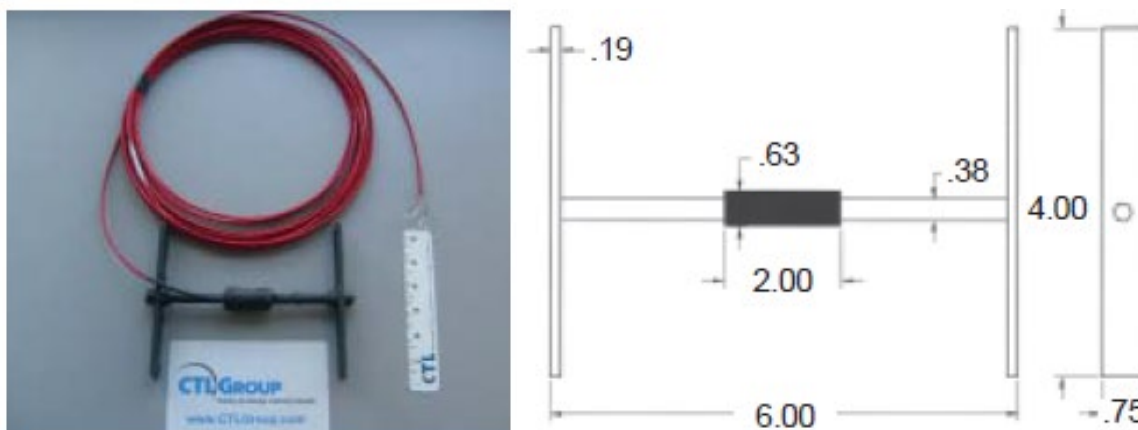
Figure 50. Asphalt strain gauge – 152 from CTL Group

Table 16. Specifications of ASG-152 from CTL Group

Bridge Configuration	Full Bridge
Gauge Resistance	350 Ω
Excitation	Up to 10 V
Output	≈ 2 mV/V @ 1500 με
Grid Area	0.133 cm^2
Gauge Area	1.22 cm^2 overall
Fatigue Life	< 10^5 repetitions @ ± 1500 με
Modulus	≈2,340,000 psi
Cell Material	Black 6/6 nylon
Coating	Two-part polysulfide liquid polymer, encapsulate in silicone with butyl rubber outer core
Temperature	-30 ^{0}F to 400 ^{0}F (-34 ^{0}C to 204 ^{0}C)

Lead Wire	22 AWG, braided shielded, four conductors

4.3.6. Concrete Strain Gauge

The concrete strain gauges used are Model 4200HT Concrete Embedment Strain Gauges based on vibrating wire technology from Geokon (Figure 51). They are commonly used for measurement of strains in concrete. However, in this project, as a pilot study, they are embedded within the asphalt layer of the roads to measure the strains in asphalt concrete. The specifications of the sensor used are as listed in Table 17.
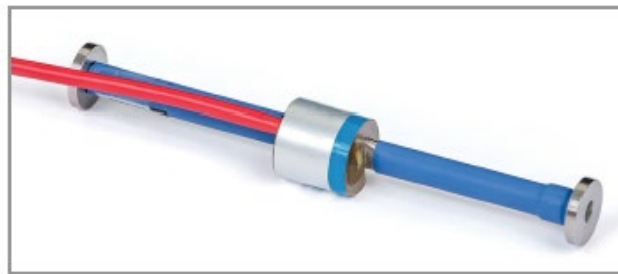
Figure 51. Concrete strain gauge 4200 HT from Geokon

Table 17. Specifications of concrete embedment strain gauge 4200 HT from Geokon

Vibrating Wire Element	
Range	3000 με
Resolution	1.0 με
Accuracy	± 0.1% F.S.
Nonlinearity	< 0.5% F.S.
Coil Resistance	120 Ω
Frequency Datum	800 Hz
Frequency Range	450 Hz - 1200 Hz
Thermal Coefficient of Expansion	12.2 με/^{0}C
Temperature Range	-20 ^{0}C to +200 ^{0}C
Cable Type	4-conductor, 2 twisted pairs, 22 AWG
Cable Jacket	White Teflon 5.20mm Ø
Active Gauge Length	6" (153 mm)
Effective Modulus	596,000 psi
Thermistor	
Range	-80 ^{0}C to +150 ^{0}C
Accuracy	± 0.5 ^{0}C

4.3.7. Thermocouples

The thermocouples used are T-type ready-made insulated thermocouples from Omega Engineering (Figure 52). They have a higher accuracy than other types of thermocouples but come with a limited range. The characteristics of the sensors are as listed in Table 18.

Figure 52. T-type thermocouple from Omega

Table 18. Specifications of ready-made insulated T-type thermocouples from Omega

Model No. @ Omega	5TC-GG-T-20-240
Thermocouple Type	T
Process Temperature Range	32 ^{0}F to 500 ^{0}F (0 ^{0}C to 260 ^{0}C)
Junction Type	Exposed
Accuracy	1.0 ^{0}C or 0.75% above 0 ^{0}C
Number of Wires	2
Cable Insulation	Fiber Glass Braid
Termination Connection Type	Stripped Leads
Cable Length	240" (6 m)
Wire Gauge	20 AWG
+ Lead	Copper
- Lead	Copper-Nickel (Constantan)

4.3.8. Geophones

The geophone array used in this project consists of both one component (1C – one vertical) and three components (3C – one vertical and two horizontal) configurations. The geophone element used for the vertical component in both cases is the HG-6 UB 4.5Hz 375Ω element from HGS India (Figure 53). The geophone element used for the horizontal component is the HG-6 HB 4.5Hz 375Ω element from HGS India. The characteristics of the sensors are as listed in Table 19. Sensitivity and phase-lag curves for these geophones are also presented in Figure 54 and Figure 55, respectively.

Figure 53. Geophones from HGS

Table 19. Specifications of HG-6 from Geophone

Frequency	
Natural Frequency	4.5 Hz
Tolerance	±0.5 Hz
Maximum tilt angle for specified F_n	0º
Typical spurious frequency	140 Hz
Distortion	
Distortion with 17.78 mm/s p.p. coil-to-case velocity	<0.3%
Distortion measurement frequency	12 Hz
Maximum tilt angle for distortion specification	0º
Damping	
Open Circuit (typical)	0.560
Tolerance (open circuit)	±5%
Shunt for 0.60 damping	32960 Ω
Shunt for damping	9090 Ω
Damping for above mentioned shunt	0.70
Resistance	
Standard coil resistance	375 Ω
Tolerance	±5%
Sensitivity	
Open-circuit sensitivity	28.8 V/m/s
Tolerance	±5%
$R_t B_c f_n$	6000 ΩHz
Moving Mass	11.1 g
Maximum coil excursion p.p.	4 mm
Physical characteristics	
Diameter	25.4 mm
Height	36 mm
Weight	81 g
Operating Temperature Range	-40 ºC to 100 ºC
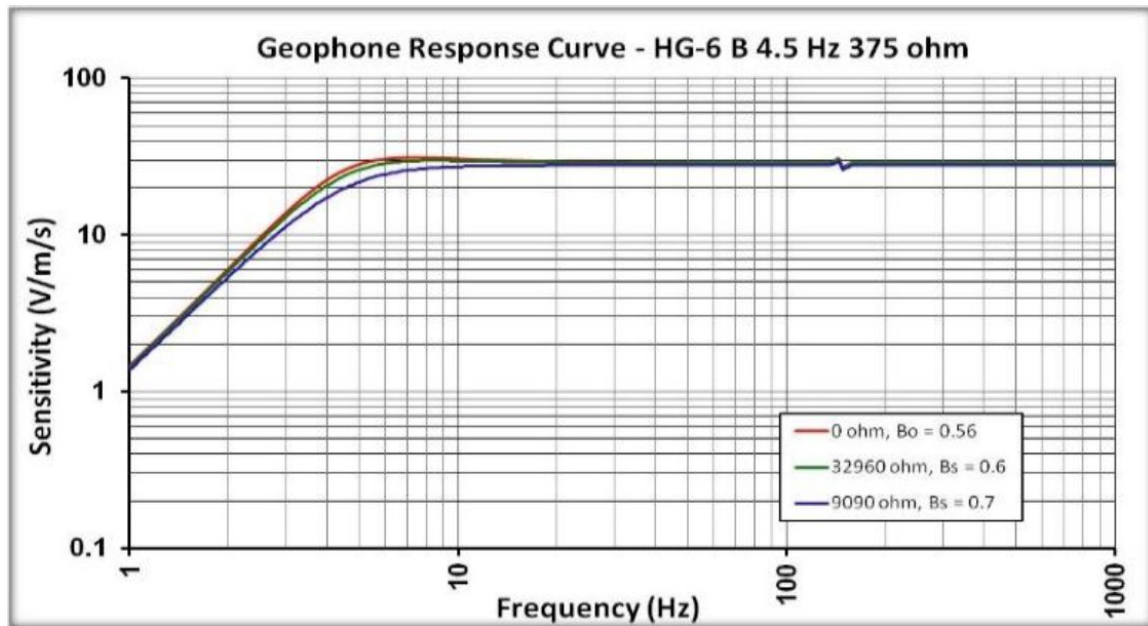
Figure 54. Sensitivity curve of HG-6 B 4.5 Hz 375 Ω
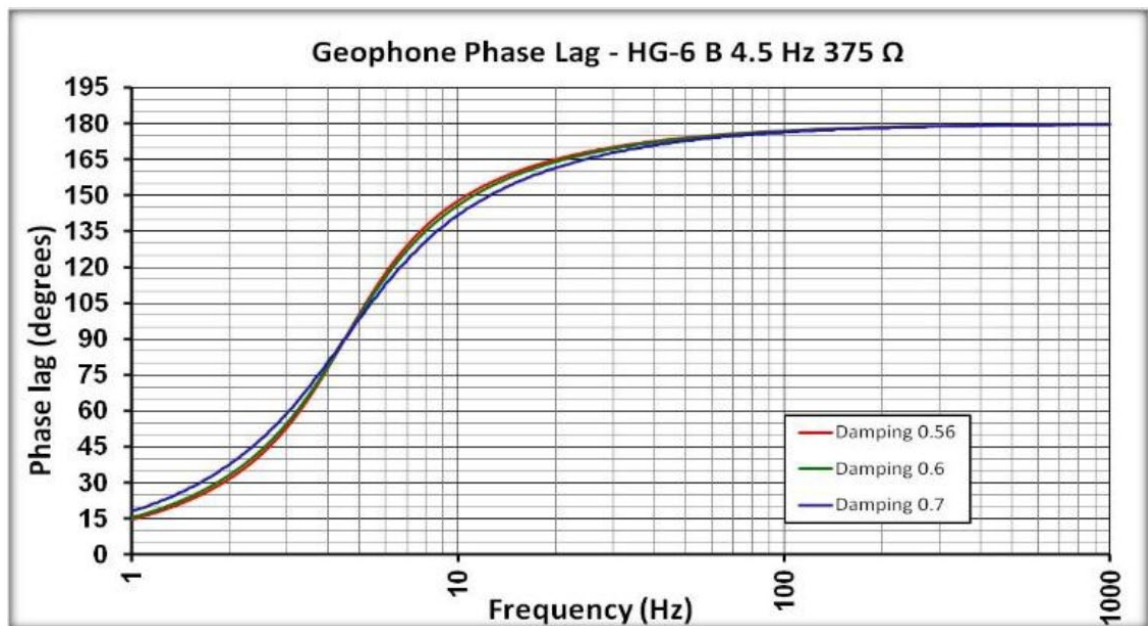
Figure 55. Phase-lag curve of HG-6 B 4.5 Hz 375 Ω

4.3.9. Data Acquisition System

A wide variety of data acquisition systems are used to log data from the different sensors selected for this study. The data acquisition systems differ in the type, accuracy and frequency of

the data measured. The data loggers used and corresponding sensors they record are tabulated in Table 20.

Table 20. Characteristics of data acquisition systems

Data Acquisition System	Sensor logged	Frequency	Accuracy	Stand-alone
DATAQ Instruments 710-ELS	Asphalt Strain Gauge	Low (1S/10 min)	Low	Yes
DATAQ Instruments 710-EHS	Linear Potentiometer	Low (1S/10 min)	Low	Yes
DATAQ Instruments 718B-ES + 8B47T-07	Thermocouples	Low (1S/10 min)	±0.39% ±0.75°C	Yes
Geokon LC-2x4	Soil Extensometer, Concrete Strain Gauge	Low (1S/10 min)	High (1.25 micron)	Yes
Acclima	Moisture Sensors	Low (1S/30 min)	Low	Yes
National Instruments USB-6289	Asphalt Strain Gauge Linear Potentiometer	High (1kS/s)	High	No
National Instruments USB-6255	Geophones	High (1kS/s)	High	No
Campbell Scientific CDM-VW305	Soil Extensometer Concrete Strain Gauge	High (100S/s)	High	No

4.3.9.1. DATAQ Instruments

The DATAQ data loggers offer standalone measurement of asphalt strain gauges, linear potentiometers and thermocouples (Table 21).

Table 21. Specifications of DATAQ data loggers

Parameter	DI-710-ELS	DI-710-EHS	DI-718B-ES
Number of Channels	16 SE or 8 DIF	16 SE or 8 DIF	8 SIG Conditioned
Range	±10V, ±1V, ±100mV, ±10mV	±10V, ±5V, ±2.5V, ±1.25V	0°C to 200°C
Accuracy	±.05%FSR ±50μV	±.05%FSR ±50μV	±0.39% ±0.75°C
Resolution	14 bits	14 bits	14 bits
Max. Sample Rate	1.2 kS/s	1.2 kS/s	4.8 kS/s
Min. Sample Rate	1S/hr	1S/hr	1S/hr
Memory	2 GB	2 GB	2 GB
Interface	Ethernet	Ethernet	Ethernet
Operating Temperature	0°C to 70°C	0°C to 70°C	0°C to 70°C

4.3.9.2. Geokon Data Loggers

The Geokon data loggers are used to measure and log in a stand-alone configuration the signal from the soil extensometer and concrete strain gauge, both of which operate with the vibrating wire technology. The characteristics of these data loggers are as listed in Table 22.

Table 22. Specifications of Geokon LC-02x4 data loggers

Accuracy	±0.05% F.S. (450 Hz – 4000 Hz)
Resolution	1 in 20,000
Interface	USB
Storage Capacity	10,666 Arrays
Temperature Range	-30°C to +50°C
Temperature Measurement	2.0% F.S. Accuracy with 0.1°C Resolution
Power Supply	3 VDC(2 Alkaline 'D' cells)
Scan Interval	10 – 86,400 seconds
Operating Time	8 days to 2 years
Sensor Connection	Hard-wired (Screw Terminal)
L x W x H	260 x 160 x 91 mm

4.3.9.3. National Instruments

The National Instruments data acquisition system offers a higher resolution, accuracy and sampling rate for measurement of elastic response of the asphalt strain gauge, linear potentiometer, and geophones under traffic loading and FWD loading. The characteristics of the data loggers are as listed in Table 23.

Table 23. Characteristics of National Instruments data loggers

Parameter	NI 6289	NI 6255
Number of Channels	16 DIF or 32 SE	40 DIF or 80 SE
Resolution	18 bits	16 bits
Max. Sample Rate	31.25kS/s	9.375kS/s
Range	±0.1 V, ±0.2 V, ±0.5 V, ±1 V, ±2 V, ±5 V, ±10 V	±0.1 V, ±0.2 V, ±0.5 V, ±1 V, ±2 V, ±5 V, ±10 V
Max. Voltage	±11 V of AI GND	±11 V of AI GND
Filter	40 kHz, 750 kHz	750 kHz

4.3.9.4. Campbell Scientific

The Campbell Scientific CDM-VW305 offers a higher sampling rate for measurement of the elastic response of the soil extensometers and concrete strain gauges under traffic and FWD loading. The characteristics of the data loggers are as listed in Table 24.

Table 24. Characteristics of Campbell Scientific data loggers

Number of Channels	8
Vibrating Wire Element	
Range	580 Hz to 6000 Hz / 1150 Hz to 6000 Hz
Accuracy	±(0.005% of reading + effective measurement resolution)
Effective resolution	0.035 Hz RMS / 0.11 Hz RMS
Max. Sample Rate	100 Hz / 200 Hz
Temperature	
Resolution	24 bits on resistance measurement
Rate	1 Hz
Accuracy	0.15% of reading
Resolution	0.002 Ω RMS @ 5kΩ
Bridge Resistor	4.99 kΩ 0.1%
Excitation Voltage	1.5 V
Operating Temperature	–25 to 50 °C

4.4. Installation Protocols

4.4.1. Moisture Sensors

Protocols that were adopted to install moisture sensors in previous field projects were reviewed and refined for the installation of moisture sensors in the subgrade of the IH10 test sections.

Sensors were installed in a horizontal orientation within trenches where possible for horizontal arrays. Sensors will be installed in a horizontal orientation within an 8-in borehole down to a depth of 4 feet, and deeper sensors will be placed vertically in a narrow diameter borehole to allow easy installation at these greater depths using hand tools. The borehole will then be backfilled with a pre-patched sand-bentonite mixture to minimize seepage into the boring, and likewise to minimize shrinkage of the borehole backfill mixture if the subgrade dries out substantially. Figure 56 shows the typical proposed installation plan for the moisture sensors.
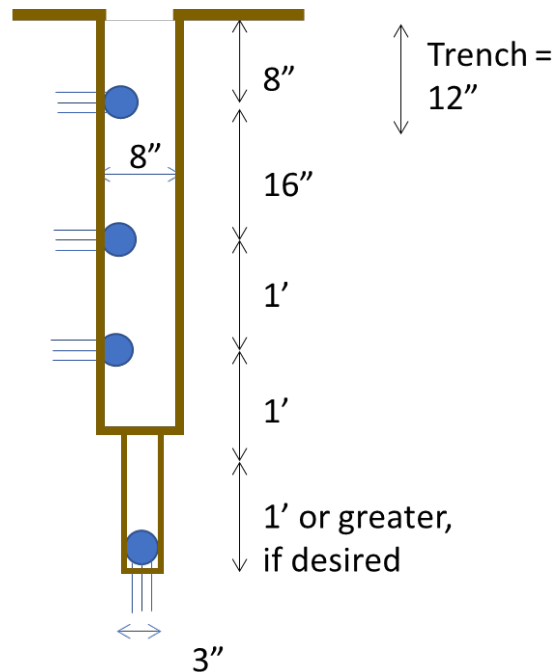
Figure 56. Installation plan for moisture sensors

4.4.2. Tell-tales

Tell-tales are proposed to be installed in the middle of the base layer (six tell-tales) and on top of the geogrid layer (six tell-tales). A brief description of each kind of installation is presented below:

1. Tell-tales embedded in the base layer will be tied to 3/8" stainless steel bolts and nuts (gravel simulant) embedded in the soil mass, representing the D50 grain size of the base.

2. Tell-tales installed on geogrid nodes will be installed at specific nodes of the geogrid. The tell-tales will be attached to geogrid nodes by 1/32" drilled holes and then either crimped.

Materials needed for assembly of the tell-tales are

1. Gravel simulant

2. Stainless steel tell-tale wires

3. Nylon plastic tube

4. Reduced wall aluminum flexible conduit casing

93

5. Wire ferrules

6. Lubricant

7. Sealant

4.4.2.1. Attaching Tell-tale Wires to Geogrid:

Figure 57. Tell-tale installed on a geogrid node

1. Cut the stainless-steel wire with adequate length for the installation.

2. Drill the node on the geogrid where the tell-tale is to be attached with the 1/32" drill bit.

3. Insert the stainless-steel wire into the drilled geogrid node.

4. Bend the inserted end back toward the original wire.

5. Crimp the inserted wire and original wire close to the geogrid node using a ferrule.

4.4.2.2. Attaching Tell-tale Wires to Gravel Simulant:

Figure 58. Tell-tale attached to gravel simulant

1. Cut the stainless steel with adequate length for the installation.

2. Using the ferrule, form a loop at one end (similar to a noose, the end must loop back on to the original wire)

3. Insert this loop between the bolt and nut with the lock washer in between.

4. Tighten the loop around the thread of the bolt by moving the ferrule toward the bolt and nut.

5. Crimp the ferrule as close to the nut and bolt as possible.

6. Tighten the bolt and the nut. The wire must be securely attached to the gravel simulant.

4.4.2.3. Installation of Tell-tales

1. Measure the adequate length of nylon tube required for the installation (2 in short of the end of the tell-tale wire on the geogrid/gravel simulant to 1 in inside the enclosure box). Let X be the length of this tube in inches.

2. Cut the above tailored nylon tube of length X into three pieces of nylon tubes with lengths 8 in, X – 26 in and 12 in. The total length of the three pieces must add up to X – 6 in.

3. Seal one end of the 8- and X – 26-in tubes with 2- and 4-in sealant. Let cure for one day.

4. Fill the 8- and X – 26-in tubes with the lubricant so that the last 2 and 4 in are free of lubricant.

5. Seal the other end of the 8- and X – 26-in tubes with 2- and 4-in sealant. Let cure for one more day.

6. Insert 8-in tube from the free end toward the attached end (geogrid/gravel simulant) falling 2 in short of the end.

7. Cut an adequate length of aluminum conduit required for installation (4 in short of the end of the tell-tale wire on the geogrid/gravel simulant or 2 in short of the end of the nylon tube closer to geogrid node/gravel simulant to the inside of the concrete box)

8. Fish the free-end of the tell-tale wire through the aluminum conduit so that the conduit falls 4 in short of the attached end or 2 in short of the end of the 8-in nylon tube.

9. With some tension in the wire, install the X – 26-in tube from the free end of the wire, all the way into the aluminum conduit.

10. With some tension in the wire, insert the 12-in tube from the free end of the wire. Use this tube to push the X – 26-in tube further down so that only 3 in of the 12-in tube is projecting outside the aluminum conduit.

11. Insert this assembly of wire + tubing + conduit through the side of the concrete box.

12. Insert the grommet through the free end of the wire, over the 12-in tube and screw it onto the aluminum conduit

13. Insert the free end of the wire and the 12-in tube through the cable gland into the Linear Potentiometer (LP) enclosure box.

14. Tighten the cable gland around the 12-in tube.

15. Attach the wire to the eyehole of the LP at the appropriate location in the range of the LP so that there is enough room for movement back and forth.

4.4.3. Linear Potentiometers

The Linear Potentiometers (LP) are mounted onto 8 in x 18 in x 0.25 in aluminum plate (12 LP per plate in two rows of six each). The aluminum plate is mounted onto the enclosure box. The enclosure box is installed inside the concrete box where the free end of the tell tales are inserted into the enclosure box and attached to the LP.

Figure 59. LP mounted on a vertical aluminum plate installed inside the enclosure box
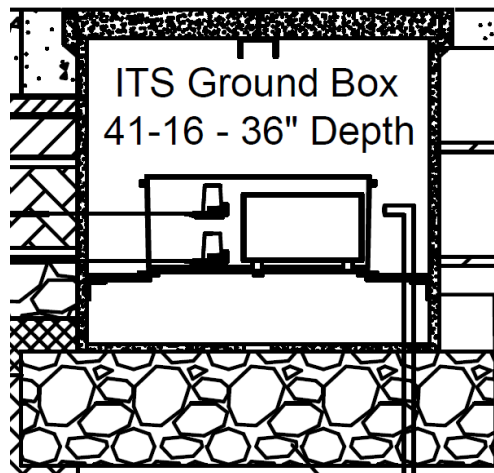
Figure 60. Schematic of enclosure box mounted inside the concrete box using brackets

4.4.4. Soil Extensometers

Soil extensometers were installed on top of the sub-base/geogrid layers (at the bottom of the base layer). The installation protocol is as follows.

Figure 61. Installation of box-outs
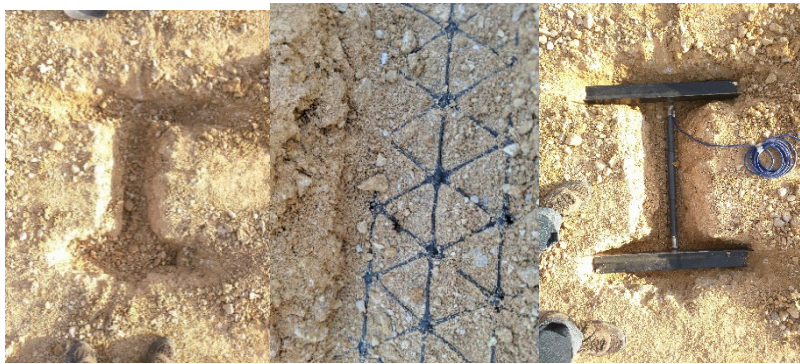
Figure 62. Installation of soil extensometer

1. Allow contractor to place some loose base material on top the completed sub-base/geogrid layers.

2. Carefully excavate the loose base material to the sub-base/geogrid layer at the location of sensor installation.

3. Install box-outs of the soil extensometers at the location of the sensors

4. Run 3/8-in aluminum conduits from each boxout to an electrical junction box on top of the sub-base/geogrid layer.

5. Run ¾-in aluminum conduits from the electrical junction box to the concrete ground box on top of the sub-base/geogrid layer.

6. Hold the conduits in place using staples.

7. Fish wires from the concrete ground box to each soil extensometer through the junction box.

8. Cover the box-outs, conduits and junction box with the loose base material.

9. Allow contractor to place the remaining base material for the first lift and finish construction.

10. Excavate the box-outs by digging through the complete first lift of base material.

11. Install the soil extensometers and fish the sensor cables through the conduits to the concrete boxes.

12. Cover the flanges of the soil extensometers with base material sieved through No.4 sieve.

13. Compact with demolition hammer tamping plate the base material on top of the flanges of the soil extensometers.

14. Remove the nylon screws from the web of the soil extensometer.

15. Cover the web of the soil extensometer with the sieved base material.

16. Compact with hand tampers on top of the web of the soil extensometer.

17. Insert the cables inside the concrete boxes through the cable glands of the enclosure box and feed it into the LC-2x4 Geokon data logger.

4.4.5. Asphalt Strain Gauge

The asphalt strain gauges were installed at the bottom of the asphalt layer. The installation protocol is as follows.

1. After the contractor has constructed the first HMA layer (Type D mix), mark out locations for the installation of the sensors.

2. Cut into the asphalt, to the bottom of the asphalt, using a circular concrete saw (14-in diameter) in the shape of the asphalt strain gauges.

3. Cut out a network of channels in the asphalt to feed the wires to the edge of the pavement.

4. Excavate the cut-outs of asphalt using the chisel tool of the demolition hammer.

5. Run aluminum conduits from the edge of the pavement to the ground box to feed the wires to the edge of the pavement.

6. Place the sensors in the excavated cut-outs.

7. Feed the wires through the network of channels and the conduit into the ground box.

8. Patch the cut-outs with the sensors and network of channels inside them with HMA TOM-A mix.

9. Insert the wire inside the concrete box, through the cable glands into the LP enclosure box.

10. Insert the wire inside the LP enclosure box through the cable glands into the DAQ enclosure box.

11. Attach the wire to the DAQ.

4.4.6. Concrete Strain Gauge

The concrete strain gauges were installed at the bottom of the HMA layer. The installation protocol is as follows.

1. After the contractor has constructed the first HMA layer (Type D mix), mark out locations for the installation of the sensors.

2. Cut into the asphalt, to the bottom of the asphalt, using a circular concrete saw (14-in diameter) in the shape of the asphalt strain gauges.

3. Cut out a network of channels in the asphalt to feed the wires to the edge of the pavement.

4. Excavate the cut-outs of asphalt using the chisel tool of the demolition hammer.

5. Place the sensors in the excavated cut-outs.

6. Feed the wires through the network of channels and the conduit for Asphalt Strain Gauge (ASG) wires into the ground box.

7. Patch the cut-outs with the sensors and network of channels inside them with HMA TOM-A mix.

8. Insert the wire inside the concrete box, through the cable glands into the LP enclosure box.

9. Attach the wire to the LC-02x4 Geokon DAQ.

4.4.7. Thermocouples

The thermocouples were installed at three different depths within the asphalt layer. The installation protocol is as follows.

For the thermocouple at the bottom of the asphalt layer,

1. The exposed end of the thermocouple is tied to the asphalt strain gauge and installed with the gauges.

2. The wire is run along the channels, through the conduit, into the ground box and to the DAQ.

For the thermocouple at the top of the first lift of HMA (Type B mix)

1. After construction of the first lift, a concrete saw is used to make a single cut with the width of the blade to a depth of 0.5 in.

2. The exposed end of the thermocouple is installed at the end of this cut and the wire is fed along the cut to the edge of the road.

3. The wire is then fed from the edge of the road to the concrete ground box through the nylon plastic tube run along the edge of the road for this purpose.

4. The wire is the fed into the two enclosure boxes and to the DAQ.

For the thermocouple at the top of the second lift of HMA

1. After construction of the second lift, a concrete saw is used to make a single cut with the width of the blade to a depth of 0.5 in.

2. The exposed end of the thermocouple is installed at the end of this cut and the wire is fed along the cut to the edge of the road.

3. The wire is then fed from the edge of the road to the concrete ground box through the nylon plastic tube run along the edge of the road for this purpose.

4. The wire is the fed into the two enclosure boxes and to the DAQ.

4.4.8. Geophones

The geophones were installed at six different depths within the pavement section at various locations from and along the wheel path. The installation protocol for the geophones are as follows.

1. After construction of the layer in which the geophone is to be installed, use a core drill to excavate a smooth bore core to the depth at which the geophone is to be installed. Use 4-in core drill for 1C geophone and 6-in core drill for 3C geophone.

2. Mix predetermined weights of water and rapid-set cement-all in a bowl. Weights are determined by the size of the core excavated and the volume of the geophone installed.

3. Pour the cement-all – water mix into the excavated smooth bore hole.

4. Install the geophone to the required depth. Use the level to check if the geophones installed are level.

5. After one hour, back fill the hole with the excavated core materials.

4.5. Final Remarks on Instrumentation

The various sensors were installed within the pavement sections using the aforementioned protocols. Pilot tests were run on the installed sensors to see if the installation was successful and if any of the sensors were damaged during construction process. Excluding three tell-tales and one ASG, all the other sensors were observed to produce meaningful results in the initial testing.

Chapter 5. Field Testing

5.1. Introduction to Field Testing

This chapter reports on field testing conducted during and after construction of the test sections along IH10. The field tests that were initially planned in the project included the Automatic Plate Load Test (APLT) and controlled loading campaigns. However, upon TxDOT request and further evaluation of the suitability of APLT test, the APLT test was replaced by a series of in-situ stiffness characterization tests as elaborated in this appendix. Specifically, a major factor that resulted in replacing the APLT test included the limitations in the number of tests that could be conducted using the APLT equipment. Since conducting the APLT test relied on external capabilities, this test was planned to be conducted only on the base layer and only at a single location in each test section. In addition, considering the load and strain levels induced by the APLT test, this test was not suitable for all pavement layers. Instead, the in-situ stiffness characterization tests, that were adopted to replace the APLT test, utilized the in-house capabilities of the Performing Agency that allowed numerous numbers of tests at all pavement layers and at a wide range of strains.

This chapter elaborates the specifics of various in-situ stiffness characterization tests that were adopted in replacement of the APLT test. Field loading campaigns that involved controlled traffic loading on top of the sensors were conducted upon completion of the construction activities at the instrumented test sections.

Field tests were performed initially during construction of the instrumented test sections. These tests were performed on top of the proof-rolled subgrade, sub-base and base layer as the test sections were being constructed. The tests performed included GeoGauge (GG), Light Weight Deflectometer (LWD), Static Plate Load Testing (sPLT) and Dynamic Cone Penetrometer (DCP). In addition to these tests, Falling Weight Deflectometer (FWD) and vibratory roller tests were also performed during construction on top of the base layer, with responses measured both on the surface and from the geophones buried within the test sections. The details of the various tests performed are reported in the subsequent sub-sections of this chapter.

As part of the four field loading campaigns, LWD, FWD, sPLT, and controlled traffic loading using heavy and light vehicles were performed on top of the completed pavement test sections immediately after construction (first loading campaign conducted on October 21, 2020) and again on March 10/11, 2021 (second loading campaign).

A third loading campaign was conducted on September 09, 2021, after an August loading campaign was postponed due to weather complications. The plan is to repeat these tests once every year post-construction to monitor the change in response of the road with pavement life.

A fourth loading campaign was planned for August 9 and 10, 2022. However, testing was canceled due to unforeseen logistical issues on the first day. The second day of testing was completed successfully, while the first day was rescheduled to Februart 21, 2023, when testing was performed with TxDOT assistance to obtain FWD data.

5.2. In-situ Stiffness Characterization Tests

5.2.1. GeoGauge

The GG is a portable instrument that measures in-place ultra-low strain, lift stiffness or material modulus. It provides a good index measure that may be used to estimate CBR and resilient modulus or the results of plate load tests, laboratory r-value, FWD or DCP. The GG weighs about 22 lb., is 11in in diameter, 10 in tall and rests on the soil surface via a ring–shaped foot (Figure 63).

The GG measures the force imparted to the soil and the resulting surface deflection as a function of frequency. It imparts very small displacements to the ground (< 1.27 x 10-6 m or <.00005") at 25 steady-state frequencies between 100 and 196 Hz. Stiffness (force over deflection) is determined at each frequency and the average from 25 frequencies is displayed alongside the standard deviation and signal-to-noise ratio in accordance with ASTM D6758-18e1.

| (a) | (b) |
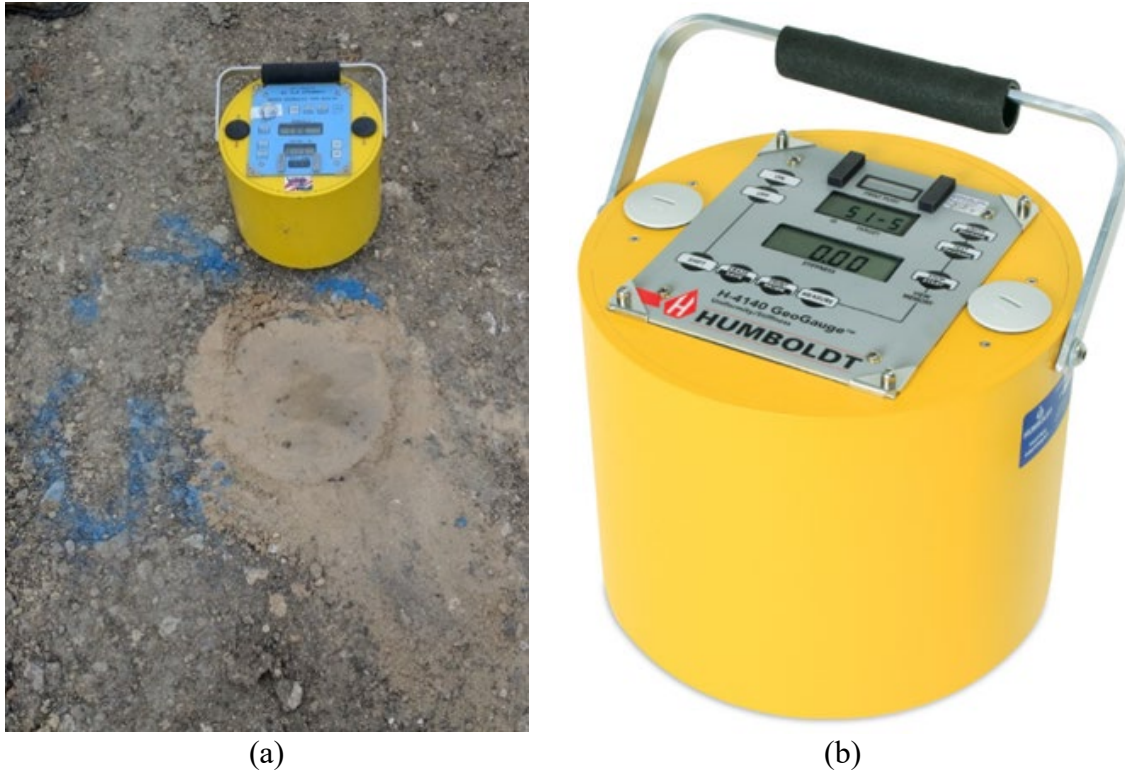
Figure 63. GG equipment for in-situ stiffness characterization: (a) UT's IH10 GG testing; and (b) close-up of GG

The material deflects an amount δ, which is proportional to the outside radius of the ring foot (R), the Young's modulus (E), the Poisson's ratio (υ) (or shear modulus (G)) of the soil. The stiffness (K) is the ratio of the force to displacement as follows:

$$K = \frac{P}{\delta} \tag{1}$$

The GG produces soil stress levels of about 4 psi and soil strain level on the order of 10^{-6}. If a Poisson's ratio is assumed, the modulus may be calculated as follows:

$$K = \frac{P}{\delta} \approx \frac{1.77RE}{1 - \vartheta^2} \tag{2}$$

Table 25. Typical data collected from a GG test

SIG. TO NOISE RATIO	S.D. (MN/M)	STIFFNESS (MN/M)
22.44	1.025	14.88

5.2.2. Light Weight Deflectometer

The LWD is a portable dynamic plate loading device that measures the in-situ stiffness of compacted earth as well as thin asphalt layers. It is predominantly used in quality control

applications similar to the GG. It differs from GG in that it uses an impact load (drop weight) instead of steady-state vibrations to impart deflections on the measured surface. The LWD also applies a higher load (about 12 psi over a 12-in diameter solid plate) and consequently imparts greater deflections (about 700×10^{-6} m) than the GG.
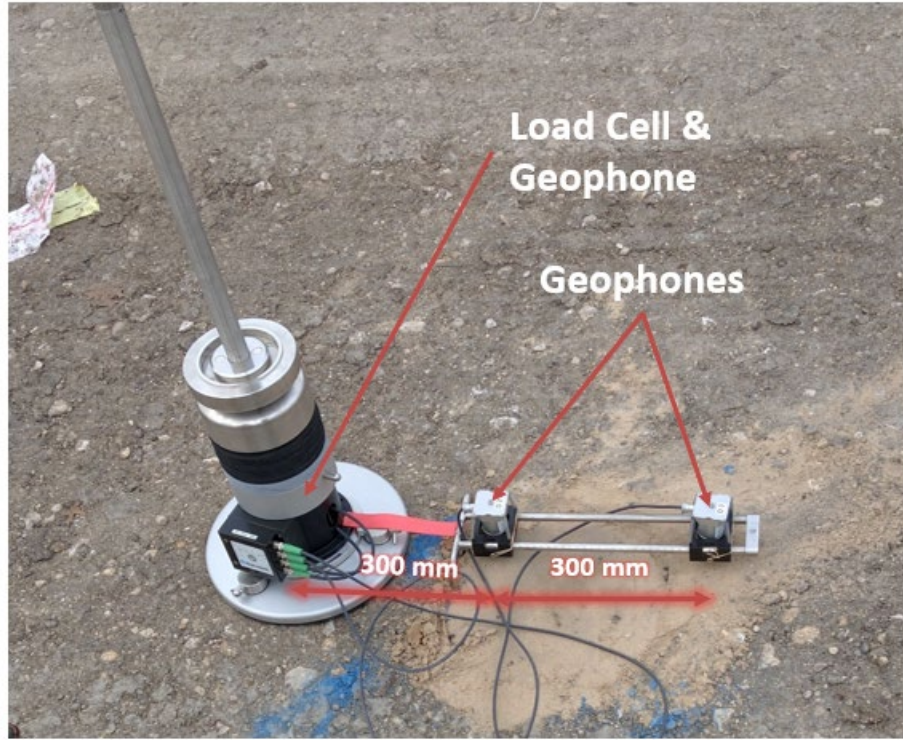
Figure 64. UT's LWD during testing

The apparatus consists of a circular plate at the bottom with a guide rod perpendicular to the plate (Figure 64). The guide rod guides the drop weight to ensure a vertical fall. Weights are dropped from standardized heights (which depends on the soil being tested and stresses needed). A load cell measures the load pulse as the weight falls on the bottom plate. Geophones are used to measure the deflection of the plate and the surrounding surface. If Poisson's ratio (υ) is assumed, the modulus of the layer can be calculated in accordance with ASTM E2583-07(2020) as follows:

$$E = \frac{2F_p(1 - \vartheta^2)}{w_p A r_o} \tag{3}$$

where F_p is the peak force applied; v is the Poisson's ratio; w_p is the peak deflection observed; A is the stress distribution factor (depending on the type of soil and stiffness of the plate); and r_o is the radius of the plate.

Typical data collected from an LWD test drop include the load pulse and deflection pulse as measured from the load cell and geophones in the system (Figure 65).

The equation shown in the figure:

$$\frac{2F_p(1-\vartheta^2)}{w_p A r_o} = E$$

Soil type	Factor (A)	Stress distribution Shape
Uniform (mixed soil)	π	
Granular material (parabolic)	$3\pi/4$	
Cohesive (inverse-parabolic)	4	
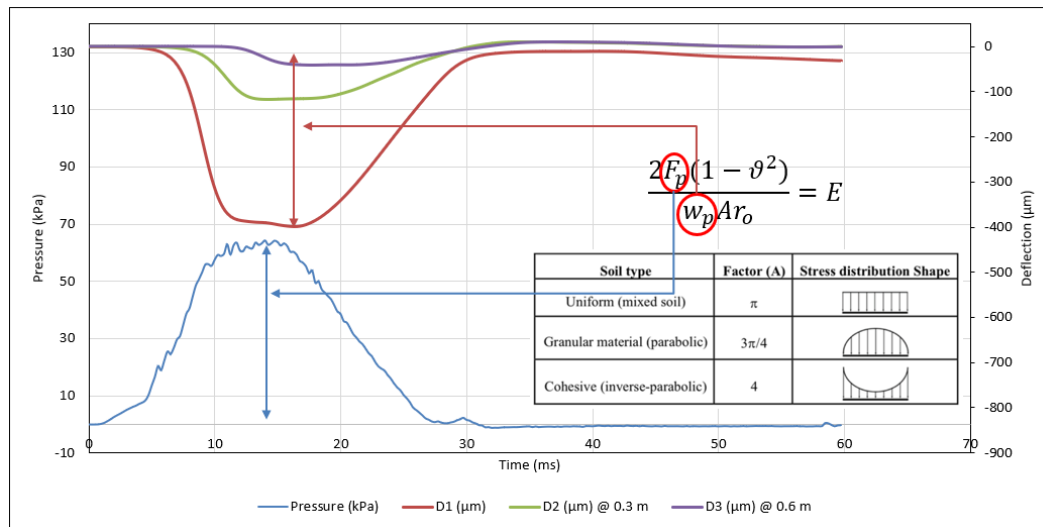
Figure 65. Typical data collected from an LWD drop: load pulse, deflection from geophones at center, 300 mm & 600 mm from center

5.2.3. Static Plate Load Test

The sPLT were used to assess the bearing capacity of the various unbound layers (Figure 66). Tests were conducted according to German Standard DIN 18134-2012 (equivalent to ASTM D1196/D1196M-21 or ASTM D1195/D1195M-09) and involve application of loads to a rigid 12-in-diameter plate. Loads are incremental, from 11.6 psi to 72.5 psi, roughly double with each increment, similar to a consolidation test. The deflection is measured to the nearest 0.008 in.

The typical data collected from the test is shown in Figure 67. As can be seen, the test involves loading the plate from 11.6 psi to the maximum load (blue), unloading back to 11.6 psi (brown) and reloading back to 65.3 psi (green). This enables the calculation of E_v for both the virgin loading curve (blue) and recompression curve (green) using the equation shown in Figure 67. The test subjects the surface to a maximum stress of 72.5 psi and up to 0.2-in settlements. Thus, the test determines moduli at higher strains than LWD or GG.

$$E_v = \frac{1.5r\sigma_{o,max}}{s} = \frac{1.5r}{a_1 + a_2\sigma_{o,max}}$$
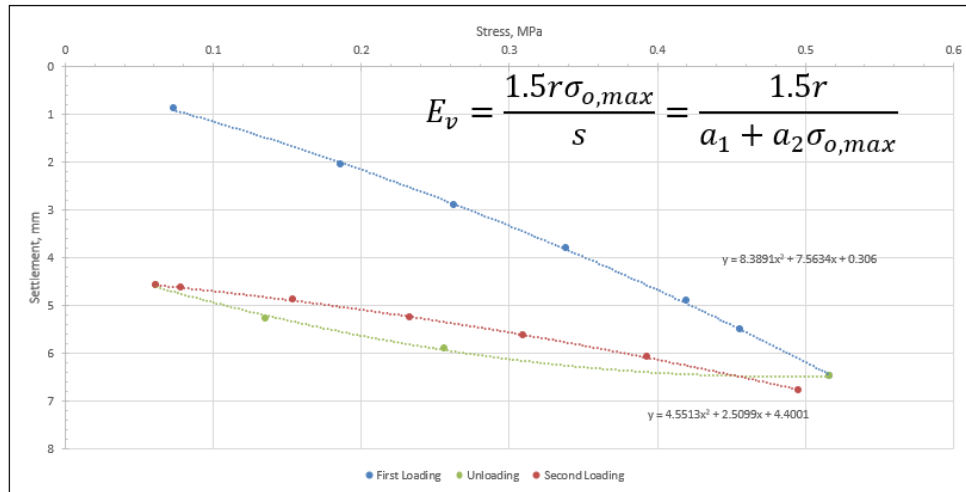
Figure 67. Typical test data from static plate load test

5.2.4. Dynamic Cone Penetrometer Test

The DCP is a destructive index test that combines the conical tip of a static Cone Penetration Test (CPT) with a Standard Penetration Test's (SPT) empirical blow count vs. penetration determination. The US Corp of Engineers developed this test to facilitate quicker determination of CBR especially in clayey soil subgrades. The apparatus at UT conforms with ASTM D6951/D6951M-18 (Figure 68).
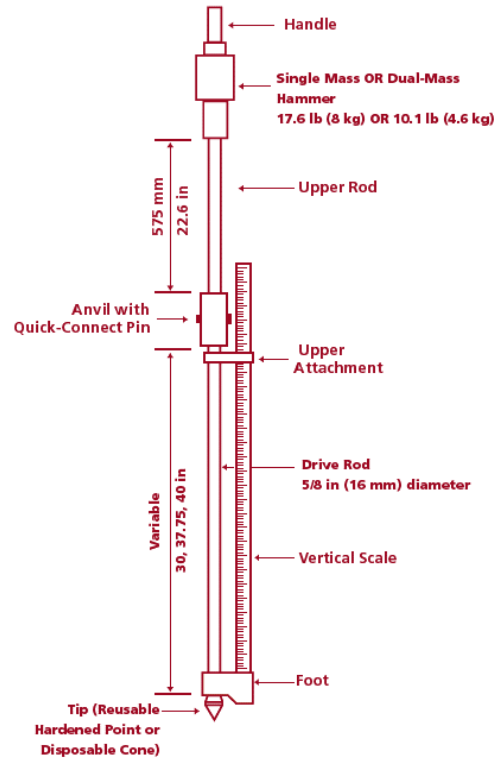
Figure 68. DCP equipment for in-situ stiffness characterization: (a) UT's DCP used at IH10 test sections; and (b) schematic of DCP

The test involves driving a drive rod by dropping a 17.6-lb-mass hammer of through a distance of 22.6 in. The number of drops required to penetrate the ground through 2 in is measured with depth. The resistance to penetration is directly correlated to the CBR or modulus of the soil at a particular depth. The data collected is processed into cumulative blows vs. penetration depth (Figure 69). The slope of this curve is the DCP index, which is converted into CBR or modulus of the soil using correlations.
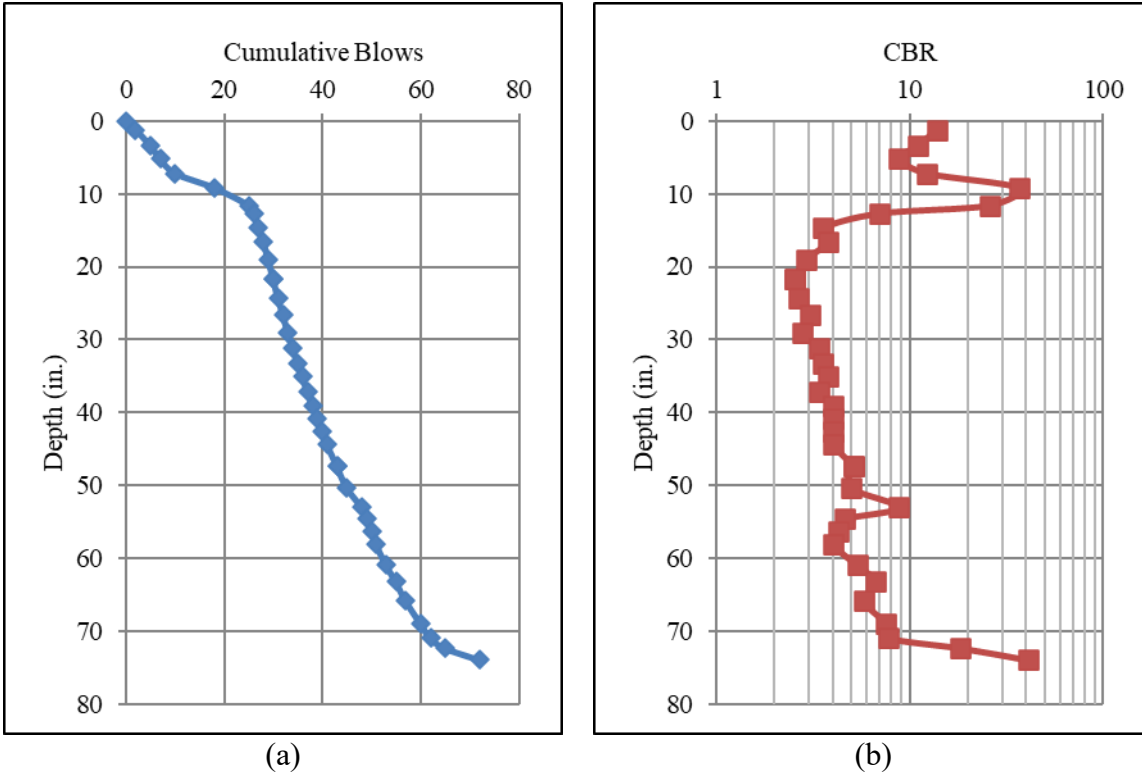
Figure 69. DCP data: (a) cumulative blows vs. depth; and (b) estimated CBR vs. depth based on cumulative blows

5.2.5. Falling Weight Deflectometer Test

The FWD tests were conducted on top of the base layer with help from TxDOT San Antonio, which provided the FWD equipment. This is a dynamic plate load test used to determine the modulus and thickness of multiple pavement layers. The test involves dropping standard weights from standardized heights (which determines the maximum impulse load) and measuring the applied load and deflection bowl surrounding the point of impact of the load itself (Figure 70).
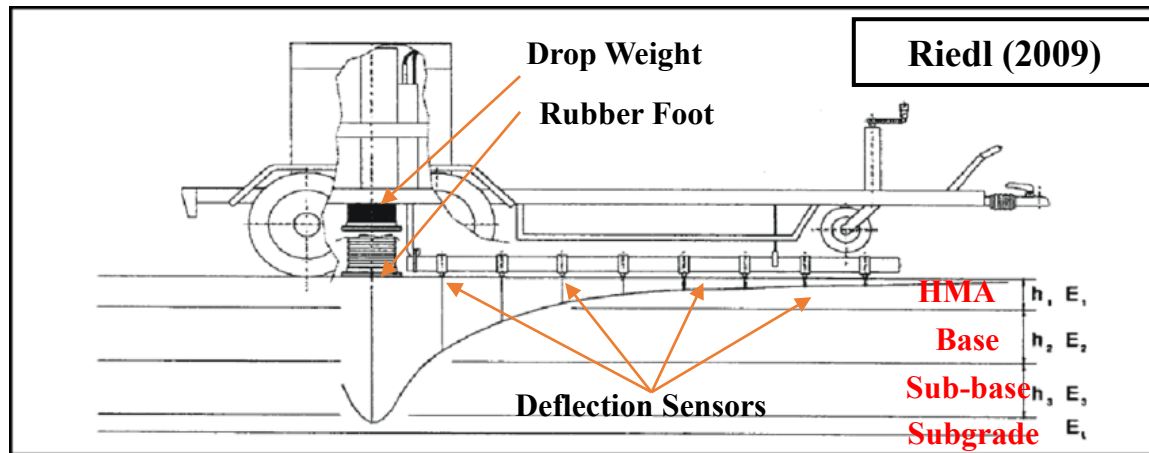
Figure 70. Schematic of FWD test

From this data, the modulus and thickness of the various bound and unbound layers are back-calculated using multi-layer linear elastic analysis. In an FWD test, the loads applied range from 6 to 12 kips that produce deflections up to 60 mils. In addition to collecting data from surface deflection sensors, data was also collected from geophones buried within the instrumented pavement test sections.

The data collected from FWD tests consisted of: (1) the load from the load cell; (2) deflections from surface deflection sensors; and (3) deflections from buried geophone sensors. Figure 71(a) shows the deflection data collected from the FWD equipment at the surface of the base, and Figure 71(b) shows the data collected from one of the 40 geophone channels installed within the base, sub-base and subgrade soil at IH10. The distribution of these 40 geophone channels within the pavement section is shown in Figure 73 for section 1a.
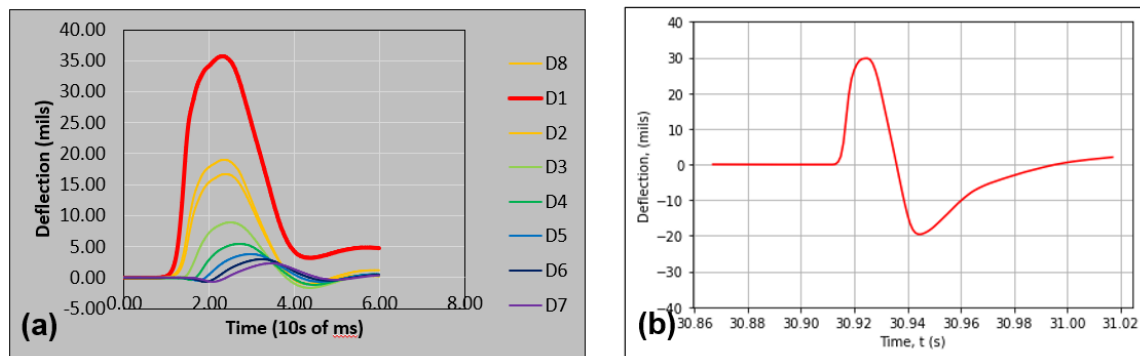
Figure 71. Example data generated from FWD tests at IH10: (a) data from surface geophones; and (b) data from geophones installed within pavement layers

5.2.6. Vibratory Roller Test

The vibratory roller test was specifically designed as part of the in-situ stiffness characterization tests in this project. This test was conducted using a vibratory compaction roller as the vibration source and the geophones installed in the pavement layers as the response of the pavements. The roller used was the BOMAG BW211-50 shown in Figure 72. The roller drum had an axle load of 12,500 lbs with a working width of 83.9 in. The roller was capable of applying vibrations at two different frequencies/amplitudes as shown in Table 2. A schematic of the vibratory roller test is also presented in Figure 73.

Table 26. Characteristics of vibration of BOMAG BW211-50

FREQUENCY VPM (HZ)	AMPLITUDE IN (MM)
1800 (30)	0.077 (2)
2040 (34)	0.039 (1)

Figure 72. BOMAG BW211-50
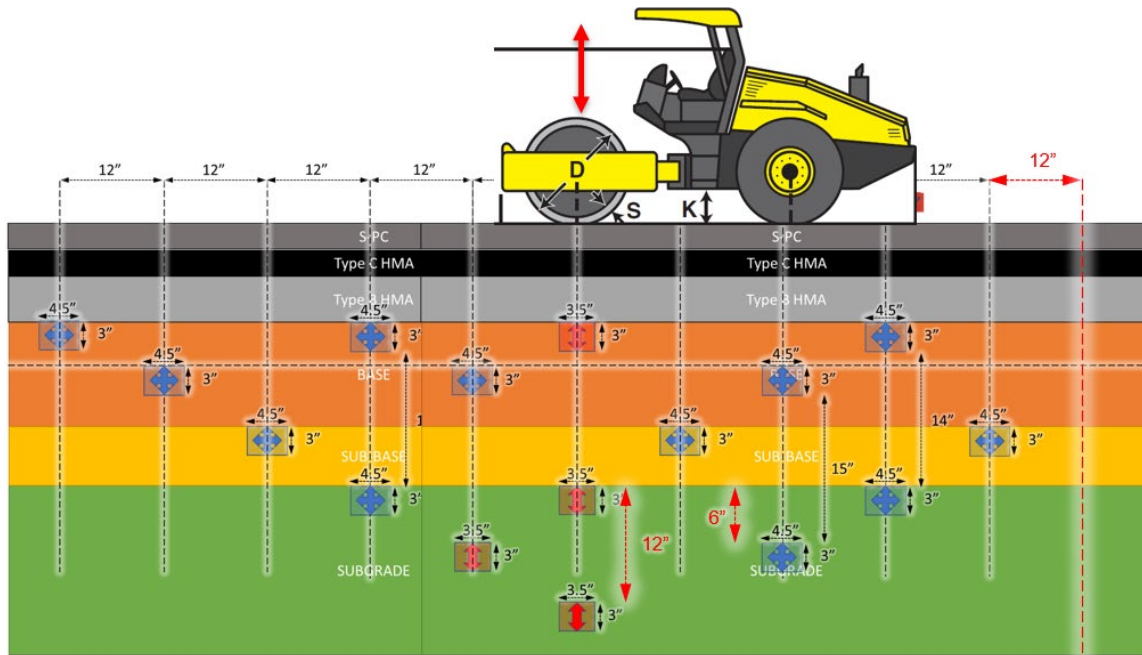
Figure 73. Schematic of vibro-roller over array of buried geophones

The vibratory roller was positioned in various locations on top of the base layer and set to vibrate in the low and high modes. The response of the pavement structure was recorded as deflections within the pavement at the locations of the geophones. A typical data set collected from one geophone under the vibratory roller is shown in Figure 74.
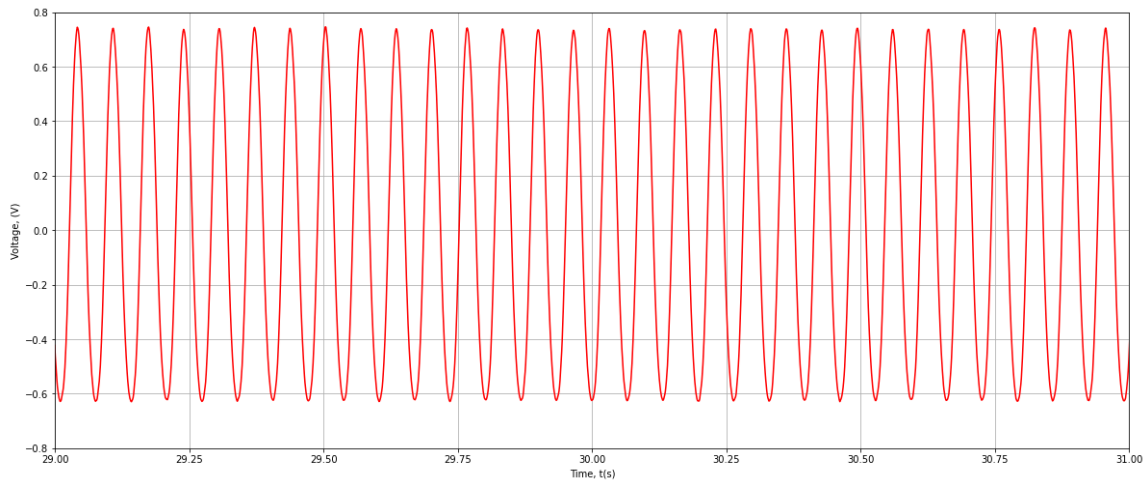
Figure 74. Example data collected from geophones at steady-state condition of vibratory roller test

5.3. Loading Campaign – Post-construction Testing

The first post-construction loading campaign was conducted on October 21, 2020. Although construction of the instrumented test sections concluded in May 2020, the first loading campaign could not be conducted at this point because the inner lane, adjacent to the instrumented sections, was closed for construction, and traffic could not be shut down in the instrumented lane as well. Thus, construction of both lanes had to be completed prior to conducting the first loading campaign. Construction (including the surface HMA layer) was completed in early September 2020 and the first loading campaign was conducted shortly thereafter. This loading campaign served as the basis of comparison for future loading campaigns (performed approximately every four to six months).

The field loading campaign consisted of

1. Controlled traffic loading with a heavy truck and light car

2. FWD tests

    a) over buried geophones

    b) over asphalt strain gauges

    c) at non-sensor locations

3. LWD tests over non-sensor locations

4. sPLT

    a) on the wheel path at non-sensor locations

    b) over the asphalt strain gauges between wheel paths

5. Ground Penetrating Radar (GPR) survey of wheel paths

6. Total station surveys of the horizontal profile of the road

The FWD, LWD and sPLT tests were conducted similar to the in-situ stiffness characterization tests on the base layer. A total of four field loading campaigns were completed under various weather conditions from the time the road was opened to traffic. The four campaigns are as follows:

- October 21, 2021

- March 10-11, 2021

- August 4; September 9, 2021

- August 10, 2022; February 21, 2023

5.3.1. Controlled Traffic Loading

The primary objective of the field loading campaign is to understand the elastic response of the installed sensors under traffic loading. Although the sensors were installed in the expected wheel path, public traffic was not expected to pass over the exact sensor locations across multiple sections. Because of this spatial variability in the applied traffic load from the sensors, their response is affected depending on whether the applied load is closer to or farther away from them. This makes direct comparison of sensor responses across different sections difficult since any differences could be attributed to differences in pavement structures across sections or differences in the locations of load applications.

To overcome this uncertainty in spatial variability of applied traffic load, the sensor response was recorded under controlled traffic passes with vehicles of known weight. This was accomplished by closing the instrumented test sections for public traffic and using vehicles of known weight to perform traffic passes exactly over the sensors. Figure 75 shows the location of the sensors marked with yellow paint and the wheel path highlighted using blue tape.

Figure 75. Photo showing location of sensors marked in yellow and wheel path highlighted in blue to facilitate accurate trafficking of instrumented sections

Two different vehicle classes were utilized to perform the controlled loading: a fully loaded heavy truck provided by TxDOT and a light sedan provided by UT Austin. The wheel load from both vehicles were weighed on the spot using a custom scale designed at UT Austin, in addition to the total gross weight measured on a commercial scale (Figure 76).

(a)   (b)

Figure 76. Custom scale used to weigh wheel load of: (a) light car; and (b) heavy truck

The location of the asphalt strain gauges (Figure 77), and that of the embedded geophones along the wheel path were first determined on the day of the loading campaign. Then, long blue tapes were attached to the road surface marking the outside wheel path that passes these sensor locations (Figure 78). The truck and sedan drivers were then requested to drive on the blue tapes at the specified speed of approximately 25 mph. GoPro cameras were also installed on the truck to capture the specific path that the front and rear wheel passed as compared to the blue tape; thus, the location of the wheel as compared to the sensors' location was determined.

Figure 77. Marking ASG locations

116

| (a) | (b) |
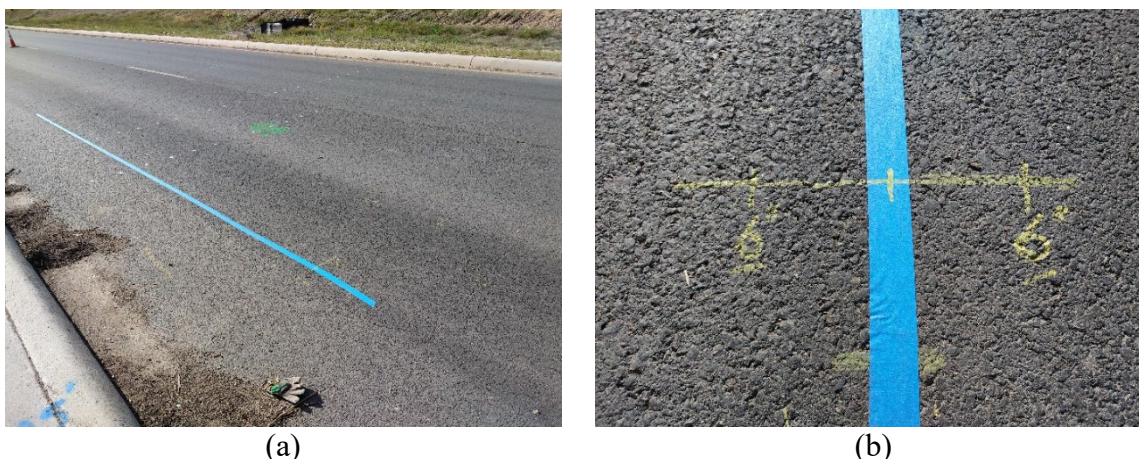
Figure 78. Marking wheel path for controlled traffic loading: (a) length of section; and (b) close-up of markings next to sensor location

The drivers were asked to drive at least 10 passes on top of the sensors while the data loggers were collecting the data from Asphalt Strain Gauges (ASG), Linear Potentiometers (LP) and geophones. The data from each pass in each test section was then carefully analyzed. The first step of the analysis was to determine if the pass was accurately on top of the sensors or it was off. This evaluation was done using the videos captured from the front and the rear wheels of the truck. As presented in Figure 79, snapshots from the videos at the exact moment when the wheel was passing the sensors locations were taken for each pass. As an example, Figure 79a shows the location of the truck front wheel in Pass 1 in Section 1a, as compared to the location of the ASG installed in the wheel path along the transverse direction in the center of the test section (ASG-TWPC). Figure 79b shows the same but for the ASG that was installed as the duplicate of ASG-TWPC (i.e., ASG, Transverse Wheel Path Repeat or ASG-TWPR). Figure 79c shows the snapshot of the truck front wheel as compared to the scale marked on the road surface that indicates ±6" from the blue tape.

(a)
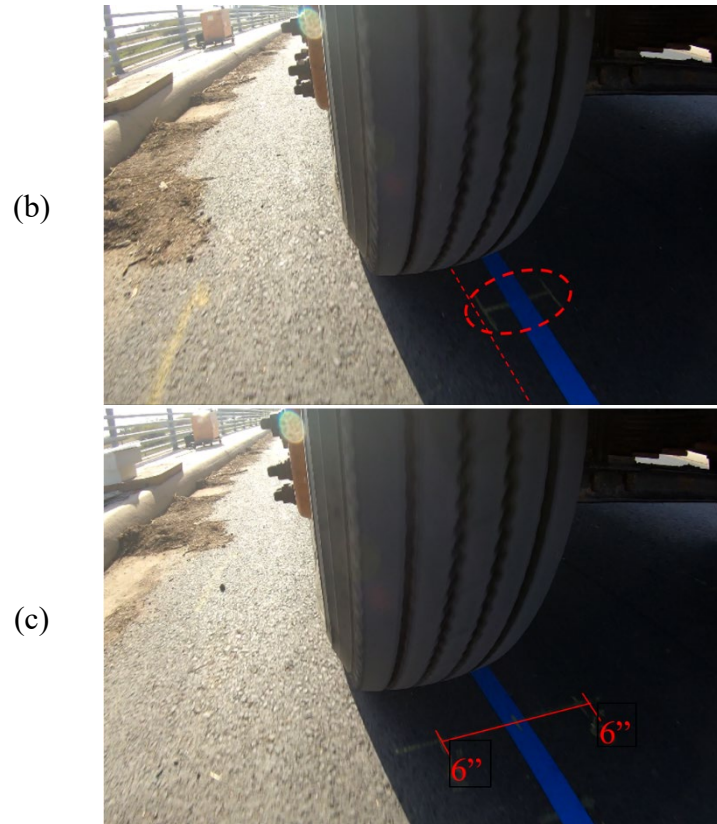
Figure 79. Location of truck front wheel with respect to ASG in wheel path: a) ASG – transverse wheel path center; b) ASG – transverse wheel path repeat; and c) scale photo

After determining suitability of the traffic pass, the next step of the analysis involved filtering the noise from the data. As an example, for the same pass presented in Figure 79 (i.e., pass 1 of the truck in section 1a), Figure 80a and Figure 80b show the original (with noise) and filtered (without noise) data, respectively. Fourier transform was used to transfer the original data from the time domain to the frequency domain; then, a low-pass filter was used to filter the frequencies corresponded to the noise, and lastly, the filtered data were transformed back from the frequency domain to the time domain. The peak values in the filtered data indicate the maximum strains induced in the strain gauge as the truck passed the location of the sensors. In the next step of the analysis, the peak values will be compared among different test sections to evaluate performance of the sections under the same controlled traffic load.
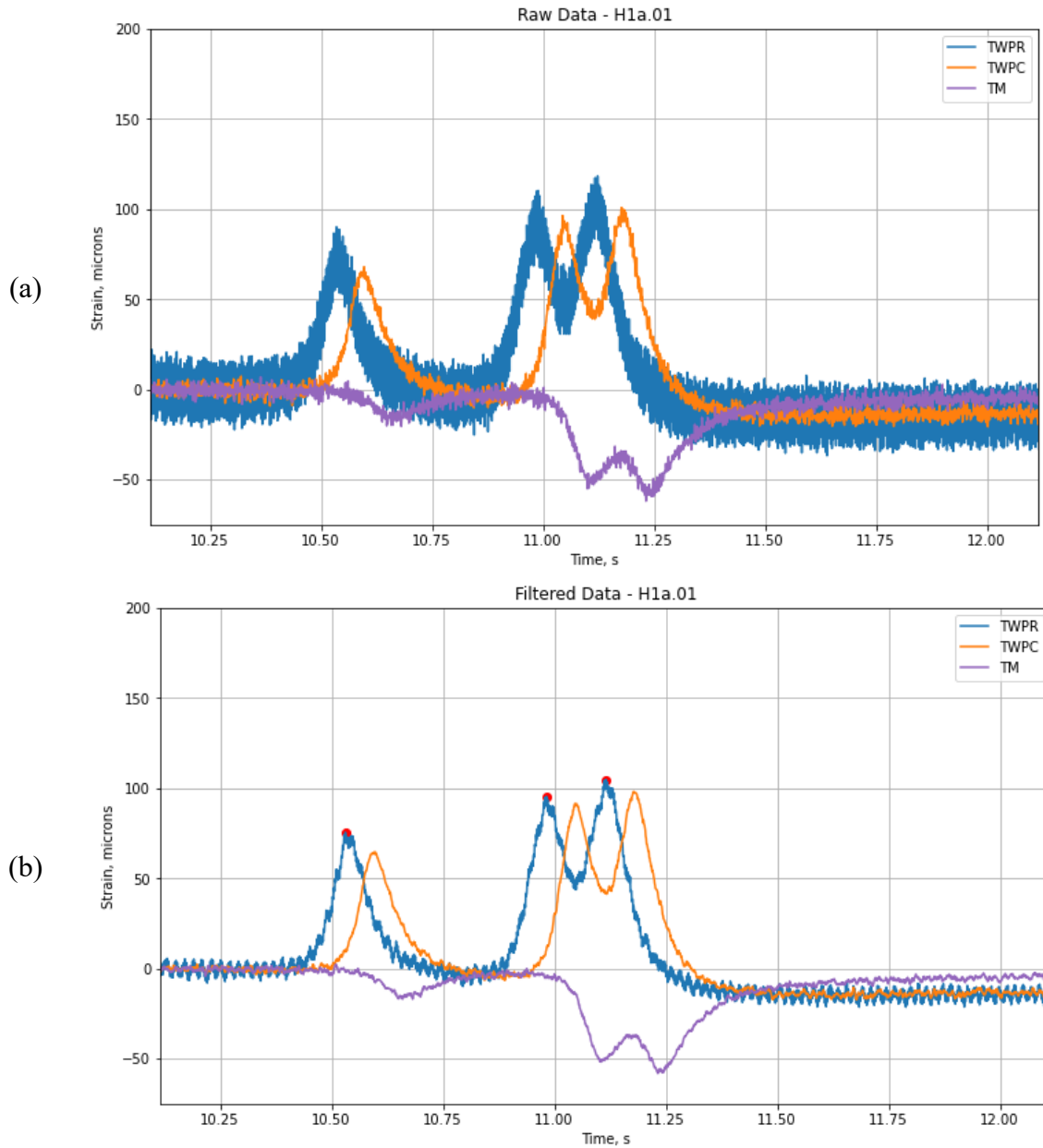
Figure 80. Data recorded under controlled heavy traffic in test section 1 by asphalt strain gauges in pass 1: a) original data (with noise); and b) filtered data (without noise)

The response of the geophones embedded within the pavement structure was also recorded as the heavy truck, and light car passed over the sensor locations. The data obtained from the geophones is a voltage-time history proportional to the acceleration of the coil relative to the magnet within the geophone. This voltage data is then processed to obtain the deflection data from the geophone. As an example, Figure 81a shows the data recorded by the data acquisition system from the geophones as a voltage time-history. Figure 81b shows the same data processed

to translate the voltage time-history into actual internal deflection of the pavement with time at the location of the geophone. Note the similarity in axle distribution annotated in Figure 81 from the geophones and the same peaks in Figure 80 from the ASG. Further analysis of this data as well as a comparison of the stabilized and control sections are presented in Section 7.4.2.

(a)
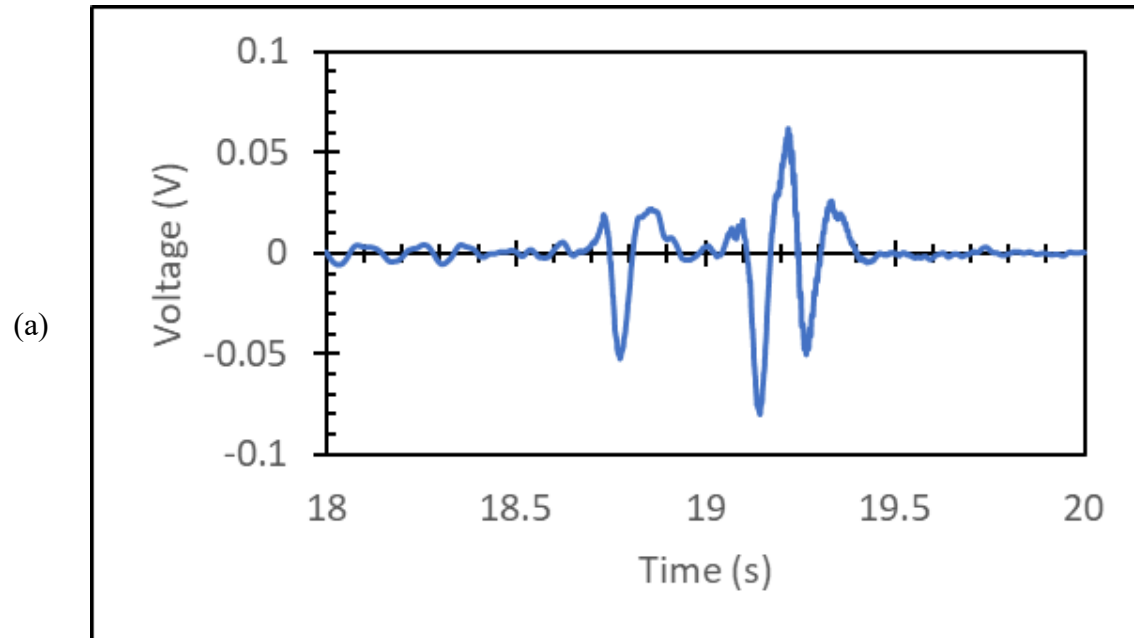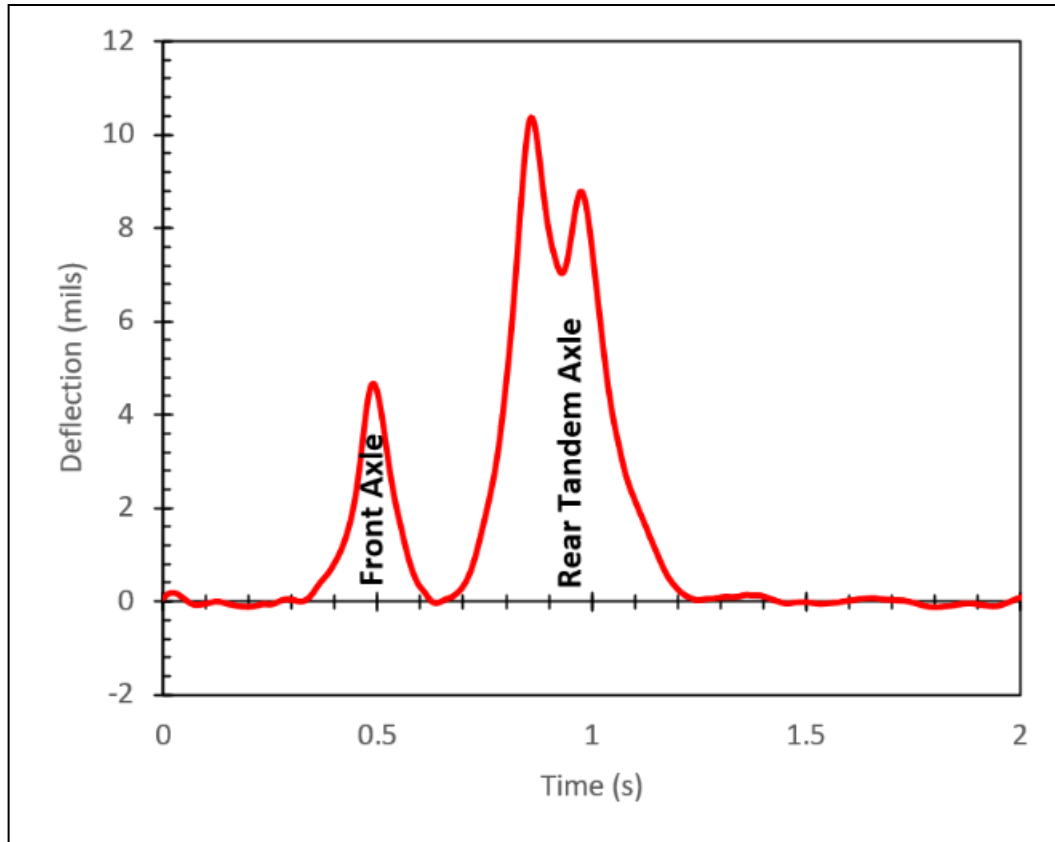
Figure 81. Data from geophones: (a) recorded voltage time-history; and (b) processed deflection-time history

5.3.2. Ground Penetrating Radar

The vehicle-mounted Ground Penetrating Radar (GPR) available at TxDOT San Antonio was used to profile the left and right wheel paths along the instrumented test sections. The system consisted of an air-couple GPR antenna mounted on an extended boom from the front of the vehicle that could swing between the left and the right wheel path.

The data will be primarily used to access the thickness of the various pavement layers as built and also to qualitatively look at the stiffness of the various layers across the test sections.

5.3.3. Total Station Survey

The Sokkia Total Station available with UT Austin was used to profile the test sections. A series of survey points spaced 1 ft apart were marked across the entire cross-section of the test sections as shown in Figure 20. This was repeated for each instrumented test section. This measurement forms the baseline against which future measurements will be compared to determine any relative movement of the pavement surface with time.

121

Figure 82. (a) Sokkia Total Station available at UT Austin; and (b) survey points marked on road (white dots across road)

5.4. Test Locations

5.4.1. Tests Conducted on Top of Subgrade and Sub-base

On top of the subgrade and sub-base layers, four different types of tests were conducted:

1. LWD

2. GG

3. DCP

4. sPLT

These tests were conducted at various locations along the test sections as shown in Figure 83 and Figure 84. The tests were distributed more or less evenly along the length of the test sections to avoid installed instrumentation.

While the LWD and GG tests were conducted along both inner and outer wheel paths, the more intensive tests, such as DCP, were conducted only along the outer wheel path where most instrumentation was installed.

Additionally, one sPLT per section was conducted, with an additional repeat conducted for the control section, to ensure the completion of testing within one day and thus avoid construction

delays.
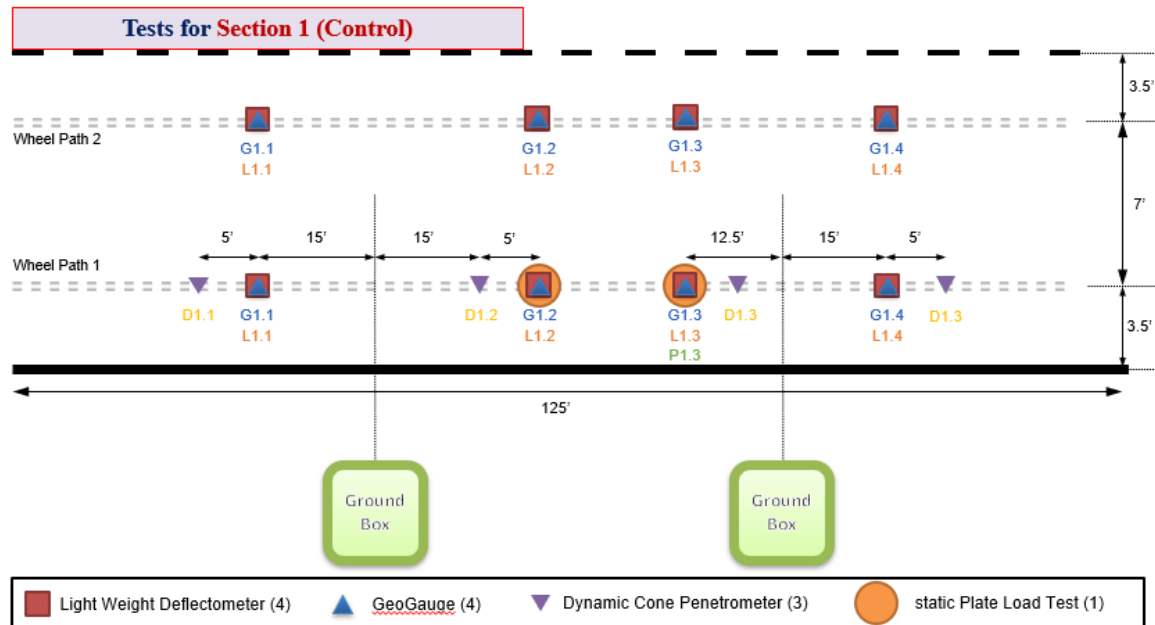
Figure 83. Locations at which tests were conducted on top of subgrade and sub-base in section 1 with reference to ground boxes
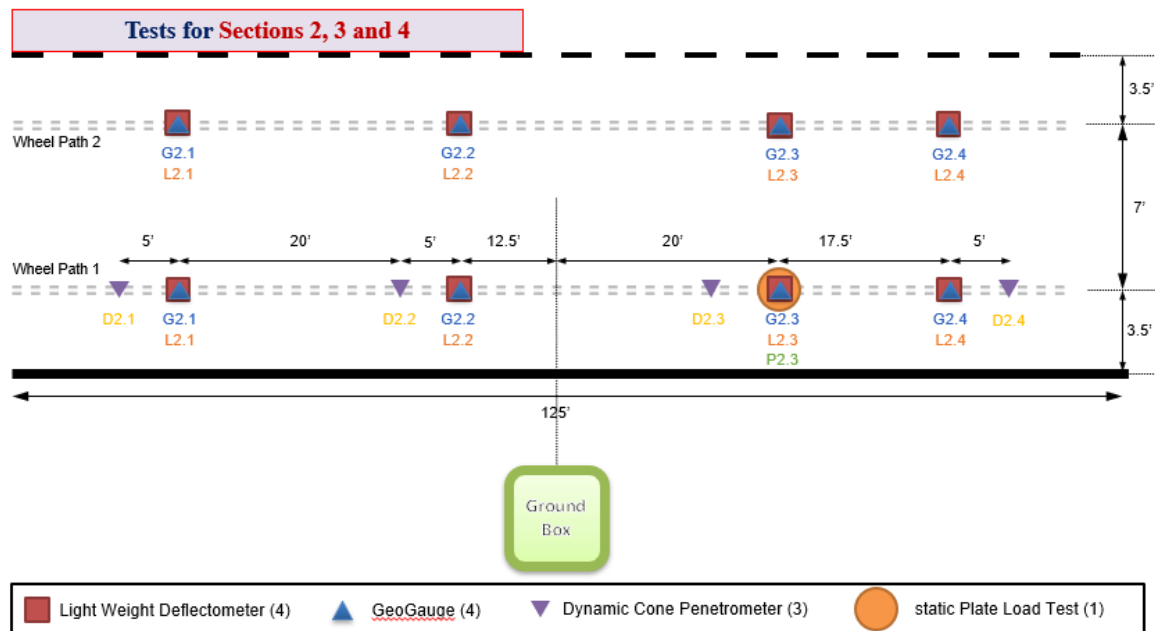
Figure 84. Locations at which tests were conducted on top of subgrade and sub-base in sections 2, 3 & 4 with reference to ground box

123

5.4.2. Tests Conducted on Top of Base Layer

On top of the base layer, in addition to the four types of tests mentioned in Section 5.4.1, two additional types of tests were conducted including FWD and Vibratory Roller (VR) tests. These tests were conducted at various locations along the test sections as shown in Figure 85 to Figure 87. The distribution of the first set of four tests (i.e., LWD, GG, DCP and sPLT) were identical to that observed in the previous section. Consequently, only the latter two tests (FWD and VR) are discussed here.

The test locations for FWD tests are classified into two groups as follows:

- Group A: general locations that conform to the philosophy of evenly distributed test locations along the length of test section

- Group B: sensor-specific locations that are chosen closer to the location of the geophones installed within the pavement layers or prospective locations of ASG.

While the general locations provide data relevant to the overall variation of moduli of pavement layers along the test sections, the sensor specific locations allow the measurement of the response of geophones installed within the pavement layers under FWD loading.

The vibratory roller tests are conducted at locations closer to the geophones (Figure 25) as their response is the only data that is recorded under these tests.
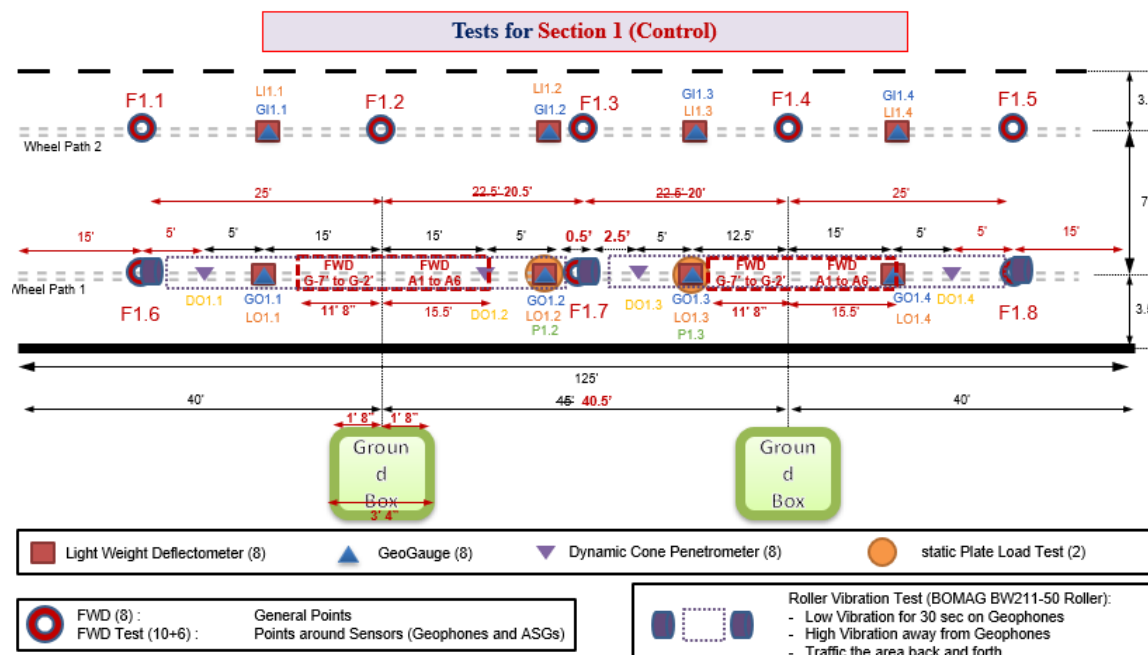
Figure 85. Locations at which tests were conducted in section 1 on top of base
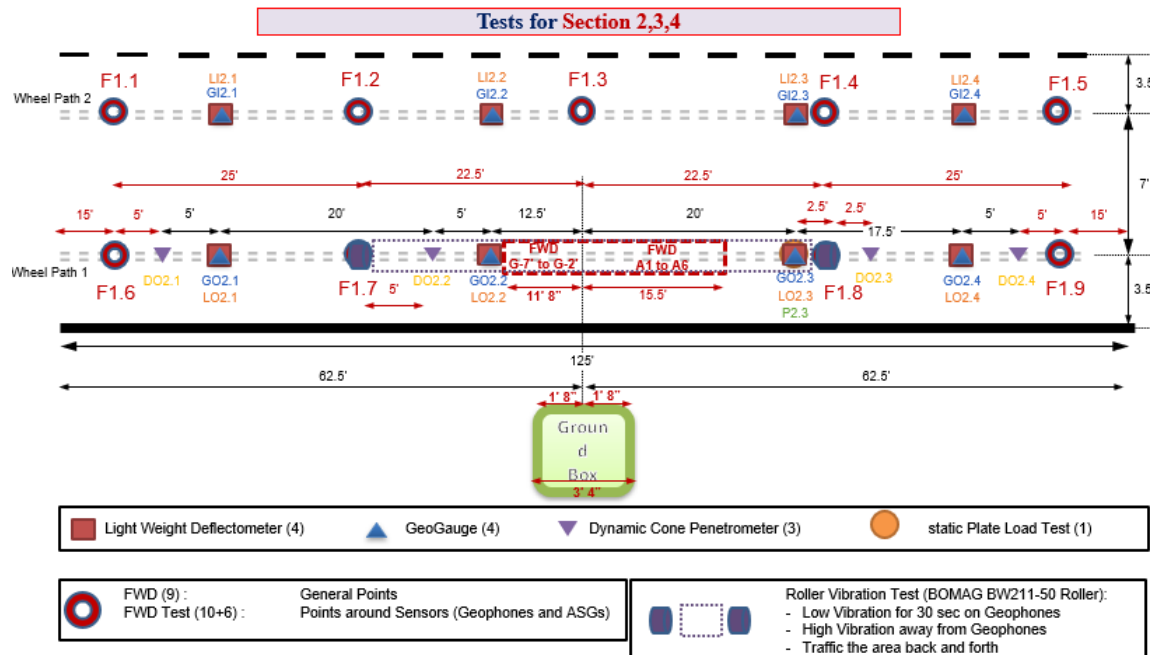
Figure 86. Locations at which tests were conducted in sections 2, 3 & 4 on top of base
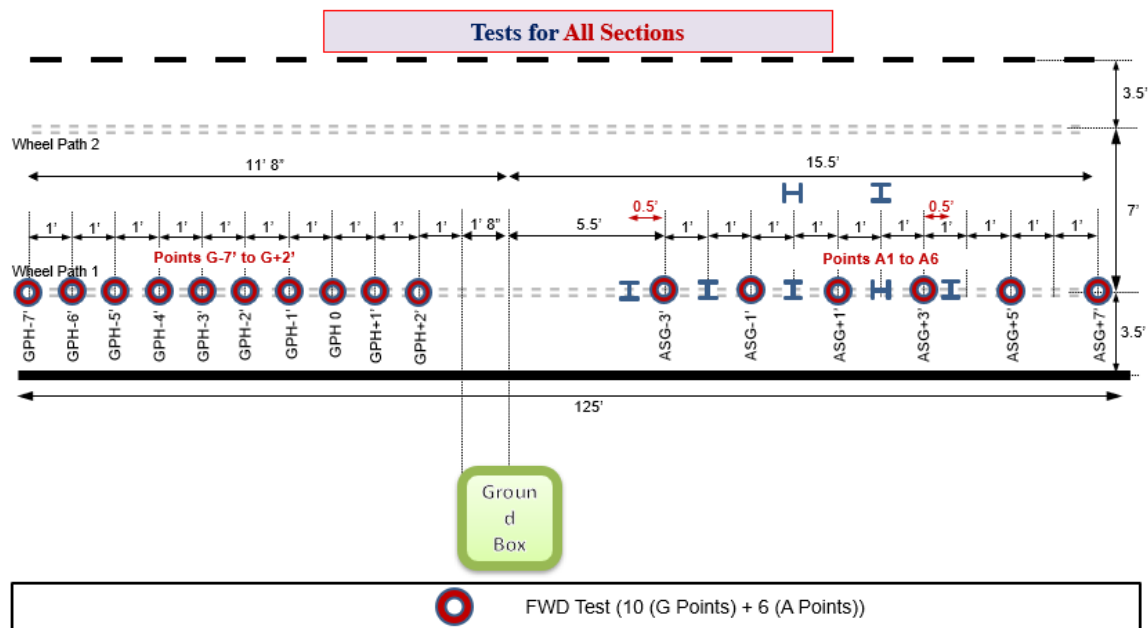
Figure 87. Test locations around prospective sensor locations (geophones & ASG)

125

5.4.3. Tests Conducted on Top of Final HMA Layer

On top of the final HMA layer, the following tests were conducted in addition to controlled trafficking, GPR and total station surveys.

1. FWD

2. LWD

3. sPLT

These tests were conducted at the same locations along the test sections as conducted on top of the base layer (Figure 85 to Figure 87).

In sections 1b, 2, 3 and 4, FWD tests were not conducted on points GPH-7', -6', -5' and -4'. Over the ASG, FWD tests were conducted on top of the ASG instead of between them.

In addition to the locations discussed above, five additional sPLT were conducted on top of the ASG between the wheel paths and oriented in the longitudinal direction (Figure 88).
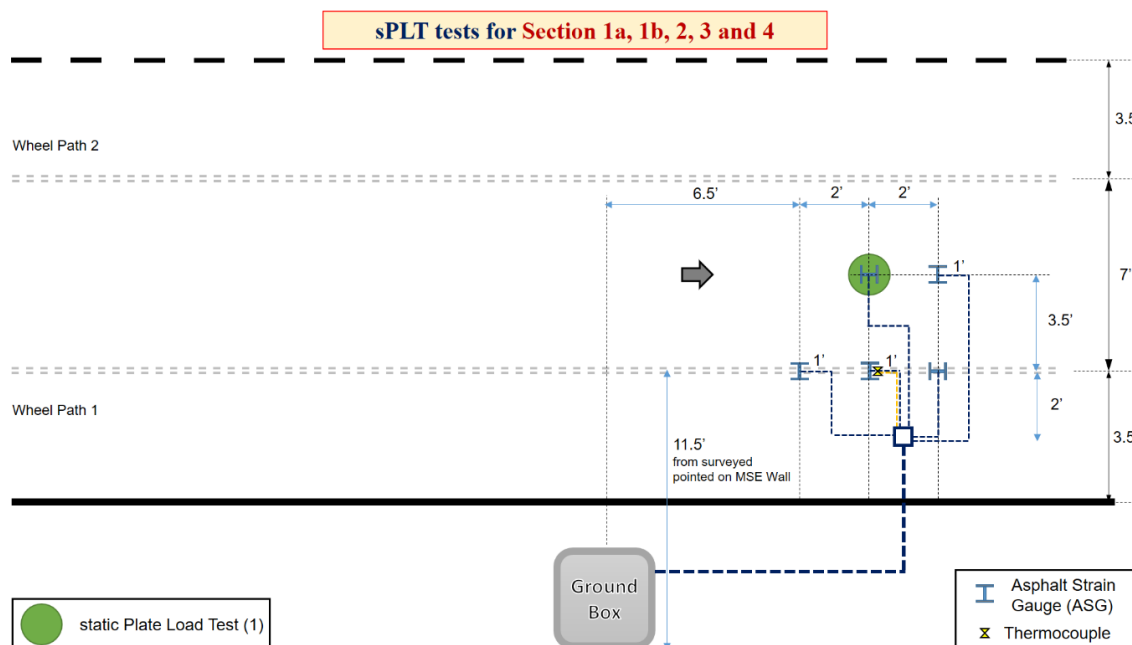
Figure 88. sPLT tests on top of ASG

5.4.4. Summary of Test Locations

Table 27 summarizes the total number of tests conducted in the various layers of the different test sections. A total of 452 tests have been conducted so far at the IH10 instrumented test

sections. This includes a total of 96 GG tests, 96 LWD tests, 15 sPLT, 48 DCP tests, 35 general FWD tests, 80 VR tests and 80 sensor-specific FWD tests.

Table 27. Summary of tests conducted in various layers of test sections

Layer	No. of Tests per Section						
	GG	LWD	sPLT	DCP	FWD	Vibro-Roller Instrumented	FWD Instrumented
Subgrade	8	8	1*	4	0	0	0
Sub-base	8	8	1*	4	0	0	0
Base	8	8	1*	4	9	16	16
HMA Layer (1st)	0	8	2*	0	9	0	9%
HMA Layer (2nd)	0	8	2*	0	9	0	9%
HMA Layer (3rd)	0	8	2*	0	9	0	9%
Total per Section	24	48	9*	12	36	16	43^
Total Overall	96	160	45	48	140	80	233

* 2 PLT tests per layer were conducted in Section 1
 Only 8 FWD tests were conducted in Section 1
^ There are 5 instrumentation sets in 4 sections (Section 1 has two sets)

5.4.5. Timeline of Tests Conducted

Table 28 details the tests conducted at the instrumented test sections from the beginning of the rehabilitation project in Jan 2020 to the most recent loading campaign in Feb 2023. The initial tests, performed during construction, were focused on the in-situ characterization of the stiffness of the various pavement layers as constructed and used for establishing the baseline for the various instrumented test sections. The latter tests, performed after the end of construction, were focused on determining the relative performance of the various test sections against the control section.

Table 28. Timeline of tests conducted at instrumented test sections

Testing Designation	Date	GeoG	LWD	DCP	sPLT	sPLT-ASG	VRT	FWD-NI	FWD-ASG	FWD-GPH	TSS	GPR	CVT-ASG	CVT-GPH
SG	2020-01-15	Y	Y	Y	Y									
SB	2020-02-06	Y	Y	Y	Y									
BL	2020-02-26	Y	Y	Y	Y									
	2020-02-27						Y	Y	Y*	Y				
	2020-02-28											Y		
TC1	2020-10-21		Y		Y	Y		Y	Y	Y	Y		Y	
	2020-11-06											Y		
TC2	2021-03-10		Y		Y	Y		Y	Y	Y				
	2021-03-11										Y		Y	Y
TC3	2021-08-04		Y		Y	Y		Y	Y	Y				
	2021-09-09										Y		Y	Y
TC4	2022-08-10										Y			Y
	2023-02-21							Y		Y				

Notes:

GeoG	=	GeoGauge stiffness measurements	SG	=	Subgrade layer testing
LWD	=	Light Weight Deflectometer test	SB	=	Sub-Base layer testing
DCP	=	Dynamic Cone Penetration test	BL	=	Base Layer testing
sPLT	=	static Plate Load Test	TC	=	Testing Campaign
sPLT-ASG	=	static Plate Load Test at Asphalt Strain Gauge locations			
VRT	=	Vibratory-Roller Test			
FWD-NI	=	Falling Weight Deflectometer test at Non-Instrumented locations			
FWD-ASG	=	Falling Weight Deflectometer test at Asphalt Strain Gauge locations			
FWD-GPH	=	Falling Weight Deflectometer test at Geophone locations			
TSS	=	Total Station Surveys			
GPR	=	truck-mounted Ground-penetrating Radar maps			
CVT-ASG	=	Controlled Vehicular Trafficking - Asphalt Strain Gauge response			
CVT-GPH	=	Controlled Vehicular Trafficking - Geophone response			

5.5. Total Station Measurements

As part of the post-construction monitoring program, vertical movement of the road surface and pavement surface distresses were quantified upon completion of the pavement construction in the test sections using Total Station surveys. This was done five times in total since post-construction measurements started in October 2020.

Five transverse sections were identified, and their elevations have been monitored using the total station. The changes in elevation within the identified transverse sections are evaluated. The width of the road varied between 26 and 28 feet, where vertical movement measurements were done. A prism-less total station system was used in all the site visits, which allowed for the vertical elevation measurements of points without the need for a worker to stand on the roadway. Measurements are taken at 1-ft intervals along the cross-section, where evenly spaced orange points are painted, see Figure 89.

Figure 89. Transverse road section for total station measurement in section 2

5.5.1. Vertical Movements

As expected, a maximum of 0.4 in of vertical movement was detected at any selected point in this road section from the time post-construction total station measurements were first taken. This could be related to the placement of a very thick HMA layer at this site, which prevented the road section from moving, counterweighing/counteracting the swelling soil movements. This was also confirmed by the absence of any longitudinal cracks along the road path.

Vertical movement measurements for all five transverse sections are plotted below in Figure 90 through Figure 94.

The vertical movement plots display the shape of each transverse section, showing that the inner lane has a higher slope than the outer lane. The centerline of each transverse section is taken as the base point and zeroed in all calculations (as shown in the plots).

Although Houston Black (HB) soils are indicated as expansive, no movements were detected over a three-year period.
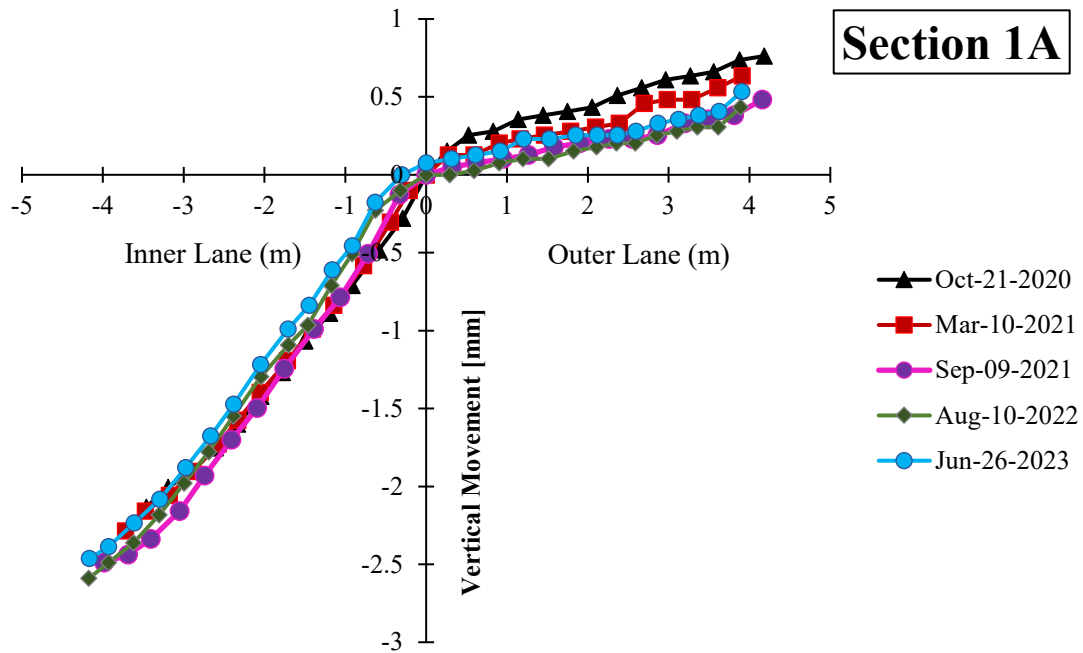
Figure 90. Vertical movement of section 1a
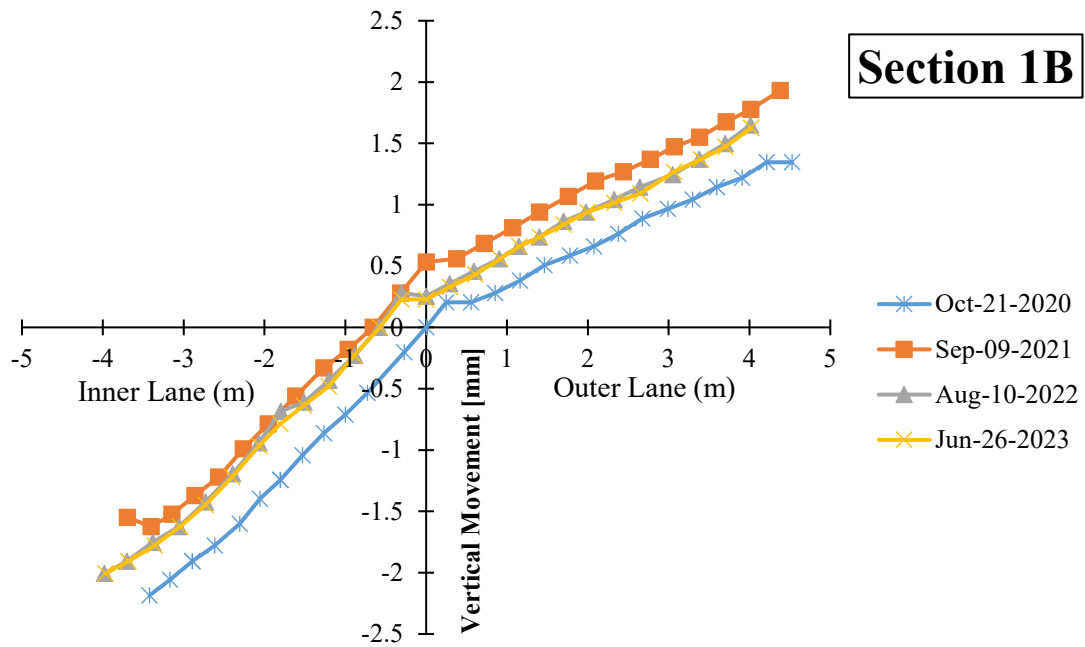
Figure 91. Vertical Movement of Section 1b
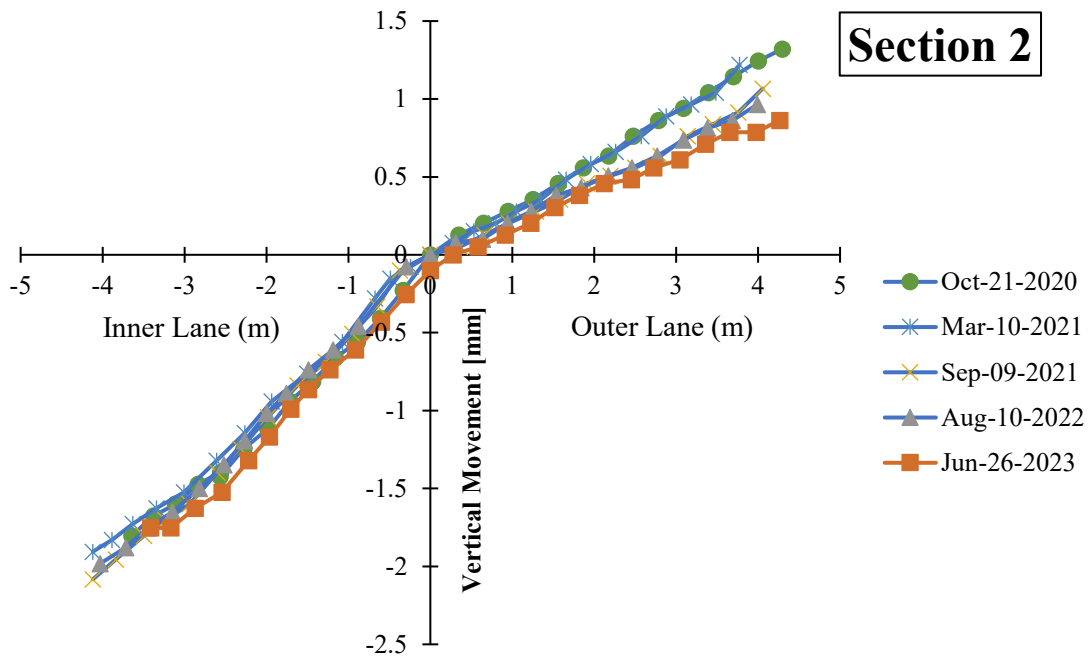
Figure 92. Vertical movement of section 2

131
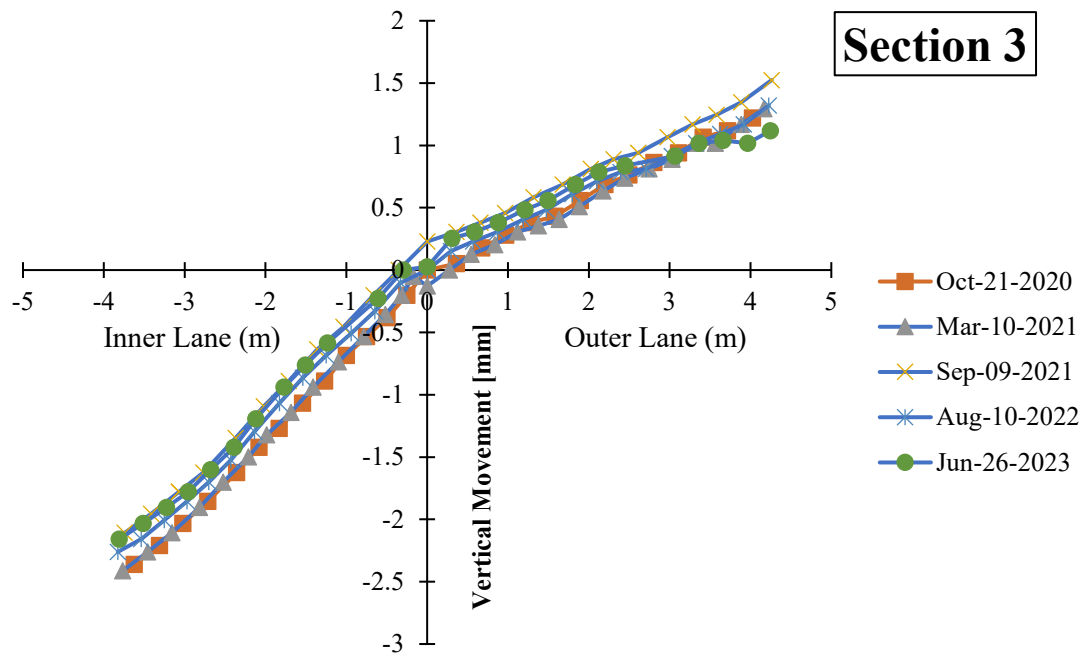
Figure 93. Vertical Movement of Section 3
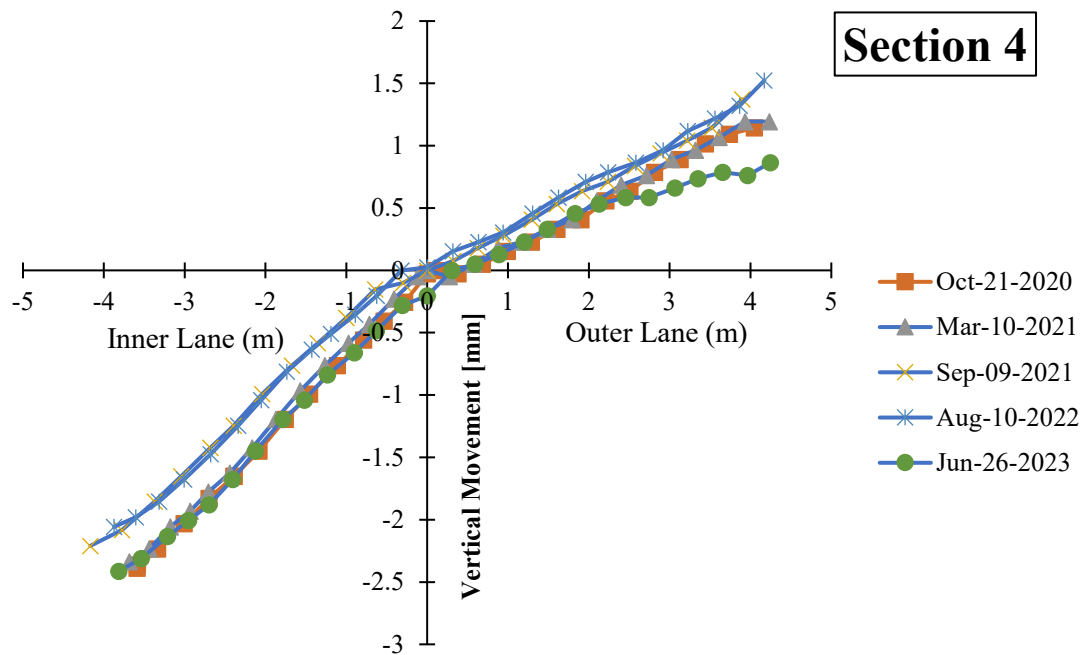
Figure 94. Vertical movement of section 4

132

Chapter 6. Post-construction Monitoring

6.1. Introduction to Post-construction Monitoring

This chapter summarizes the development and execution of a post-construction monitoring program of the field test sections at IH10.

As part of the post-construction monitoring program, vertical movement of the road surface and pavement surface distresses were quantified upon completion of the pavement construction in the test sections using total station surveys. Environmental data in form of precipitation, temperature, and relative humidity has also been collected and were monitored over the life of the project through the nearest weather station. In addition, support from TxDOT was sought for collecting traffic data, and rut depth measurement. However, no significant rut development were observed in any of the control or stabilized sections (instrumented or non-instrumented)

Furthermore, continuous data from the installed sensors were collected to understand the long-term performance of the various test sections. This involves collection of data at very low frequencies (1 sample every 30 min) for extended periods of time (years), which required a permanent data logging system at each test section. The permanent data logging systems were installed in all test sections in early 2020, however, operation of the systems was pending connection of power supply. Eventually, the contractor was able to set up the power supply on November 20, 2020, and since then continuous data has been collected from all sensors installed in all test sections. These include Asphalt Strain Gauges (ASG), Thermocouples (TC) and Linear Potentiometers (LP).

The soil extensometers were monitored using data-loggers supplied by the manufacturer. These data loggers were powered using batteries. It was found that the batteries had run out on some occasions before the period of data collection was over. This resulted in loss of collectable data in some cases and corruption of collected data in other cases. Rectification was sought out from the manufacturer and a solution through the revision of battery replacement protocols was implemented. One of the data loggers (section 1a) experienced a voltage overload, resulting in loss of function for a brief period. The damaged data logger was sent back to the manufacturer for repair and reinstalled at the test section. The data recorded in the data logger before the voltage overload was also successfully retrieved from the damaged logger. However, the data in the period between voltage overload and reinstallation of the repaired logger was lost.

The moisture sensors were also monitored using data loggers supplied by the manufacturer and powered using batteries. A brief transition to the power supply system

setup for ASG, TC, and LP was implemented, however this decision was reversed due to the observed increase of noise in the data collected from the moisture sensors.

Specific activities that have been conducted as part of the post-construction monitoring program are as follows:

6.1.1. Monitor Vertical Displacements of the Road Surface:

- Several cross-sections to be used for monitoring vertical movements were evaluated and identified in each test section.

- Protocols to monitor vertical movement of the road surface were developed, revised, and refined as needed.

- Pavement surface profiles, at predetermined locations, are logged periodically once every six months using total station surveys.

6.1.2. Conduct Condition Surveys of the Road Surface:

- Protocols to conduct visual condition surveys and document surface distresses were developed, revised and refined as needed.

- A visual condition survey of the existing road before reconstruction was conducted to establish a basis for future comparison among test section performance.

- No substantial differences in surface conditions were visually observed between the stabilized and control sections.

6.1.3. Collect Data Recorded by the Installed Instrumentation:

- As previously mentioned, the data acquisition system for most of the installed sensors operates from AC/DC power supply. The performing agency completed the installation of all data acquisition systems for all sensors by March 2020. While initial signal was confirmed and example data were collected from all sensors, continuous collection of data was not possible from most of the sensors because of the lack of power supply at the test sections. This was resolved in late November 2020. Thus, data from all the sensors are being collected as of then.

- Among the sensors that their data logging system had independent power supply were the soil extensometers. The data logging system used with the soil

extensometers operates from batteries. Hence logging of data was started as soon as the installation of the DAQ for these sensors was completed.

- In addition, data loggers used for moisture sensors also operate by batteries. Therefore, continuous data recording by the moisture sensors installed in the subgrade were also initiated upon installation of DAQ for these sensors.

6.1.4. Environmental Data Collection:

- Environmental data, including precipitation, temperature, and relative humidity data has been collected from a nearby weather station.

- Data collection began at the time of construction and has been continued throughout the project construction time.

6.1.5. FWD Testing, Automatic Rut Measurements and Traffic Data:

- As discussed in Chapter 5, FWD tests were conducted on the base layer and final HMA layer upon completion of these layers.

- Additional FWD tests, automatic rut measurements, and traffic counts and classifications passing on the field test sections will be conducted every six months.

- Since support from TxDOT is needed for conducting the above tests, the research team members have been in close coordination with TxDOT regarding the plans for collecting such information upon completion of the construction.

6.2. Status of Data Collection

There are three categories of continuous data collection needed at the project site.

1. ASG, TC and LP – AC power supply

2. Soil extensometers and concrete strain gauges – two D-cell battery powered.

3. Moisture sensors – eight AA battery powered.

6.2.1. AC Power Supply

Out of the various configurations of powering the data loggers, the presence of a reliable AC power supply has worked the best with almost zero interruptions in data collection. The data loggers have been logging data from the ASG, TC, and LP without loss of data to interruptions of power (except for the brief occasional power outages), or data corruptions to erratic supply voltages. The AC power supply with an immediate step-down to 24V DC power at the service pole has been the most reliable data collection setup by far.

6.2.2. D-cell Battery Power for Soil Extensometers

The soil extensometers used in this project are unique sensors working with Vibrating Wire (VW) technology and as such requires a sophisticated data logger to measure the frequency of the vibrating wire with a specific excitation setup. Conventional voltage or current measurement data loggers do not work with these sensors. Therefore, the data loggers, used for this express purpose, supplied by the manufacturer of the sensor are being used log outputs from the sensors. However, the manufacturer-supplied data loggers are powered by two D-cell alkaline batteries.

Figure 95 to Figure 99 show the voltage recorded across these two D-cell batteries from the five data loggers at the project site. The solid red lines indicate the period in which the data from the data loggers were collected and the main D-cell batteries were replaced. As can be seen from the figures, the data loggers did not show any issues with collecting data over a period of six months during the first two data collection windows. The one exception to this observation is in the first window of section 2. The rapid decline in battery in this window may have been due to the interruption of the data collection cycle to install two additional sensors (concrete strain gauges from section 1b). This additional load (starting mid-June 2020) on the data logger, mid-collection, could have caused the battery to die earlier than expected.

The performance of the data loggers (in terms of how long they last) declined, especially in data collection window – 3, for almost all sections. The collapse of the battery voltage in the data loggers has resulted in loss of data due to

1. Interruption to data collection (due to lack of sufficient power) – sections 1b and 4

2. Corruption of the entire dataset in the window – sections 1a and 2

Section 3 seems to have been able to avoid this collapse for some reason, although around the same time (July 2021), the voltage from the data logger had seen a sudden drop but did not collapse.

In addition to this, in some of the sections, a secondary +3V lithium ion clock battery had also failed resulting in time-reset mid-data collection. At the manufacturer's recommendation, it was decided to replace both the clock battery (Panasonic CR2032) and main battery (Duracell Pro-Cell), and this task was completed on Dec 13th, 2021. The research team has decided to replace the main battery every two months to avoid any further loss of data. In addition, the clock battery is also set to be replaced annually starting 2021.
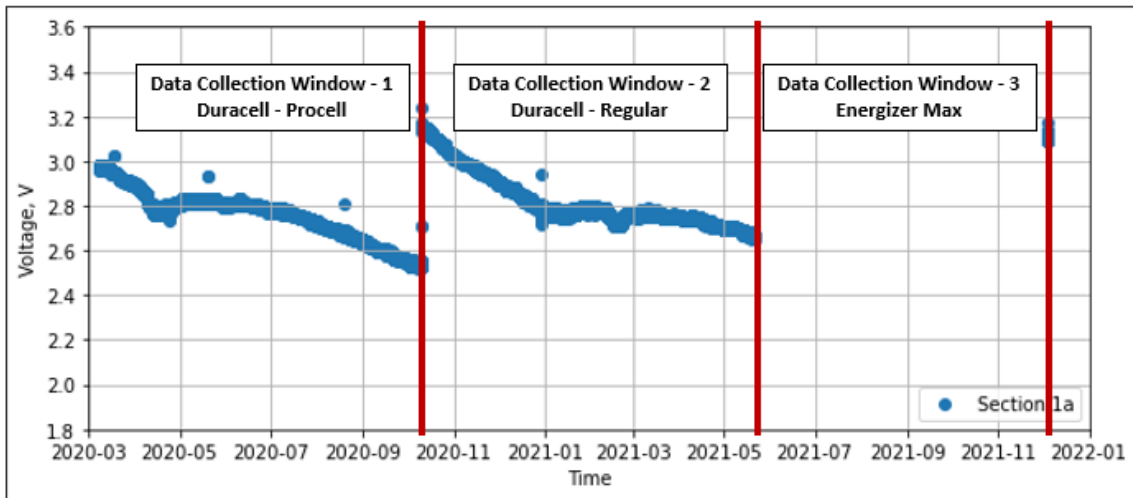
Figure 95. Alkaline battery voltage with time – data logger section 1a
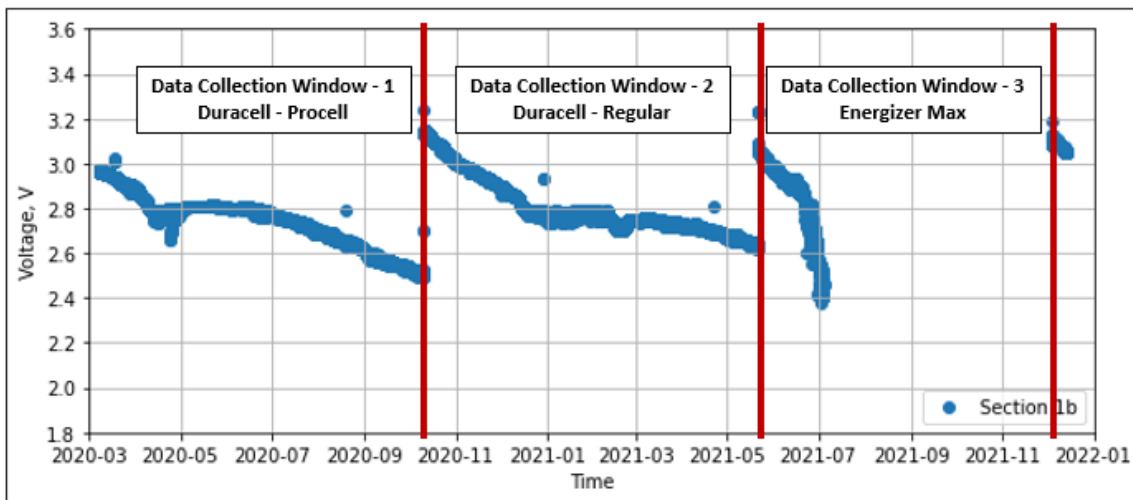
Figure 96. Alkaline battery voltage with time – data logger section 1b
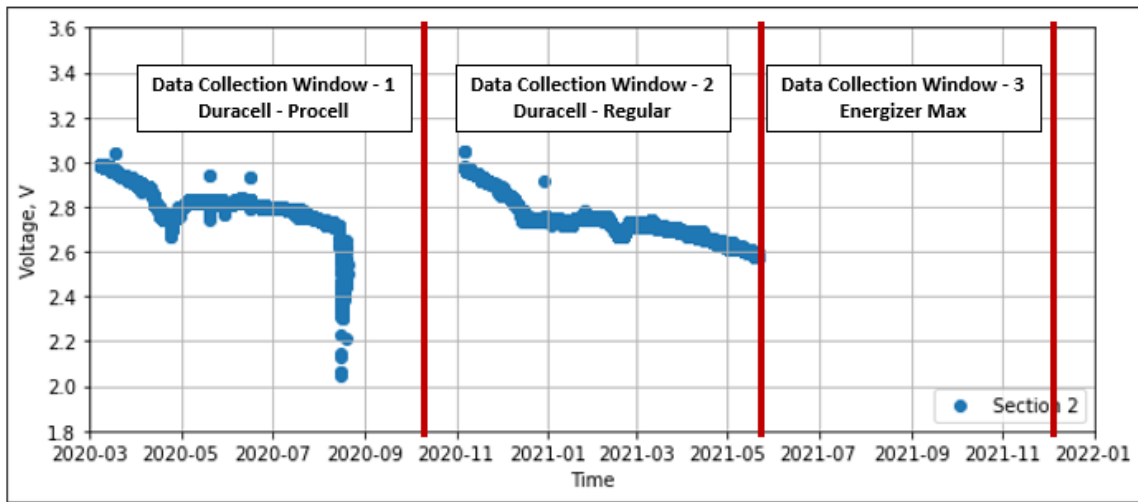
Figure 97. Alkaline battery voltage with time – data logger section 2
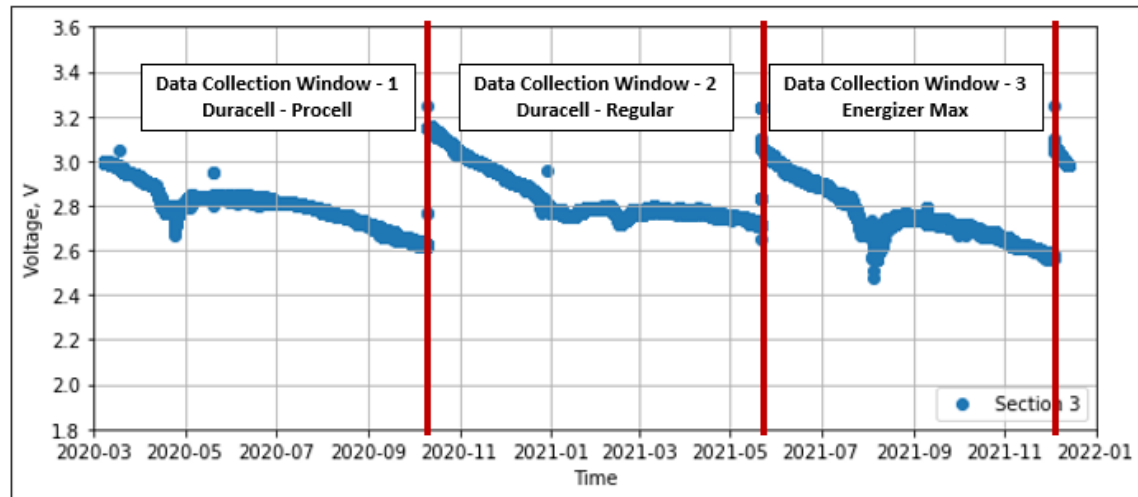
Figure 98. Alkaline battery voltage with time – data logger section 3
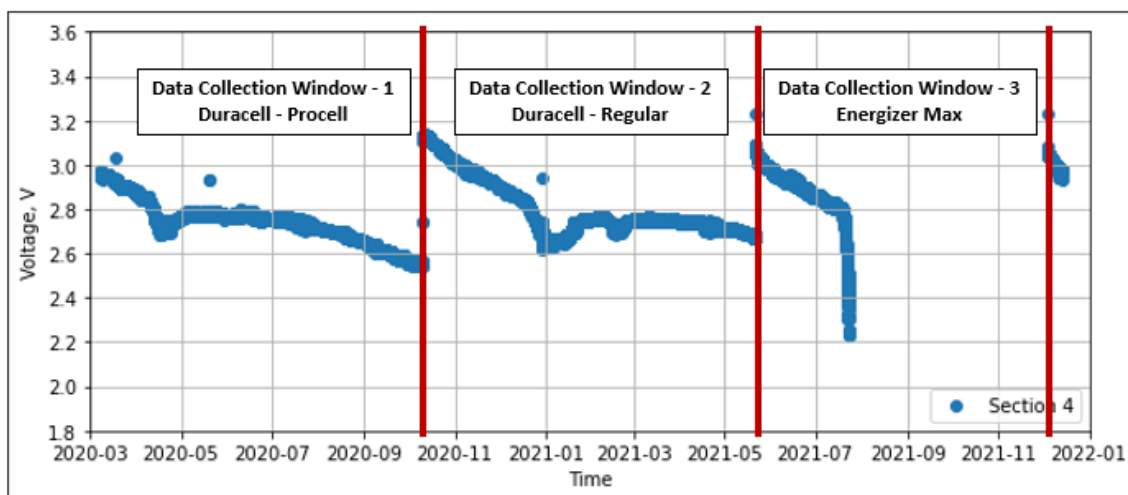
Figure 99. Alkaline battery voltage with time – data logger section 4

Sometime after January 2022, a voltage overload damaged one of the data loggers (section 1A), resulting in a brief loss of data in February and March 2022. The damaged data logger was identified during a routine data collection visit in March 2022. The data logger was sent back to the manufacturer for repair and reinstalled on-site by early April 2022. Although the data logger was no longer functional, the data collected in the logger before the voltage overload (January 2022) was retrieved since the data logger memory was still intact.

6.2.3. AA Battery Power for Moisture Sensors

The moisture sensors are unique sensors that require the manufacturer recommended data loggers which are powered by batteries. So far, we have been able to collect data with minimal data losses. However, given the reduced reliability of batteries, a plan was formulated to transition the power supply for these data loggers from battery to AC power supply. The research team has successfully migrated all five data loggers to AC power in March 2022. The data from these data loggers were monitored in terms of noise levels. It was determined that the noise levels in the moisture data were significantly higher when powered from the AC power. Thus, the power supply was replaced with batteries that were used previously. Details of the noise levels are further discussed in Chapter 7.

Chapter 7. Analysis of Data

7.1. Introduction to Analysis of Data

This chapter summarizes the synthesis, analysis and interpretation of the experimental and field data collected. This analysis focuses on understanding the performance of various sections under public and controlled traffic loads as well as performance under environmental loads.

Various protocols to analyze and interpret the performance data have been established. This includes protocols to analyze data obtained in the characterization of the materials, data obtained from in-situ stiffness characterization tests, and data to be obtained from field loading campaigns and monitoring programs. In addition, the raw data collected from soil extensometers has been processed into meaningful displacement values. Data collected from the tests performed on all unbound layers during construction are also analyzed. Specifically, the data collected at the surface from various tests has been processed, while the data collected from the buried geophones are analyzed.

In addition, the data collected in the first loading campaign conducted on October 21, 2020 has been organized and sorted for evaluation. Specifically, the raw data has been converted to engineering parameters and a preliminary evaluation on the suitability of the collected data has been completed. The same has been done for the data collected in the second loading campaign conducted on March 10/11, 2021, the third loading campaign conducted on August 4 and September 9, 2021, and the fourth loading campaign conducted on August 10, 2022 and February 21, 2023.

The FWD tests conducted at general locations of the instrumented test sections, across four testing campaigns, have been analyzed and used to produce back-calculated moduli of the pavement layers, which is used to compare the difference in results between the stabilized and control sections. An analysis of equivalent sections with increased moduli and reduced layer thicknesses is also performed to quantify the benefits from geogrid inclusion in terms of material savings.

The geophone data collected under FWD tesings were also analyzed. Both the vertical and lateral deflections of the geophone in the control and stabilized sections were processed and compared. It was found that the stabilized sections produced fewer vertical and lateral deflections than the control sections, and this restraining effect appeared to improve with time. A preliminary evaluation of an enhanced FWD back-calculation with data from embedded and surface geophones was also performed.

The soil extensometer data collected since the completion of base layer construction in February 2020 has been analyzed and compiled, showing the relative performance of the stabilized and control sections.

The strain data collected from asphalt strain gauges installed in the transverse direction along the wheel path is used to estimate critical strains at the bottom of the HMA layer relevant to fatigue cracking. The measurements of tensile strains at the bottom of the HMA layer are combined with fatigue cracking performance equations to determine the overall improvement to fatigue life of the HMA layer due to base stabilization.

The vertical deflection data from geophones under vehicular traffic is also evaluated. The deflections under the heavy truck for all stabilized sections were found to be lower than in the control section, and this reduction in vertical deflections increased with time from the completion of construction of the pavement structure.

7.2. Characterization of Stiffness

The stiffness of the various layers of the pavement section was evaluated through tests that allowed for various levels of induced strains. The tests consisted primarily of

1. GeoGauge (GG) testing

2. Light Weight Deflectometer (LWD) tests

3. Static Plate Load (sPLT) tests

4. Dynamic Cone Penetration (DCP) tests

5. Falling Weight Deflectometer (FWD) tests

GeoGauge and DCP testing were conducted on the unbound layers, while LWD tests and sPLT were conducted on all layers (bound and unbound). The FWD tests were conducted on the bound and unbound base layers only. This section summarizes the results of the tests conducted on each layer (as the pavement was being constructed) for section 1b.

7.2.1. GG Testing in Section 1B

The unbound layers of the pavement section were tested using GG to estimate their ultra-small strain modulus over a nominal depth (approximately 6 in). The results from four different test locations along the wheel path of section 1 are shown in Figure 100. As the figure demonstrates, the results of GG testing are repeatable among any unbound layer

and clearly delineate the stiffness of the subsequent pavement layers (i.e., the base is found to be stiffer than the sub-base and stiffer than the subgrade).
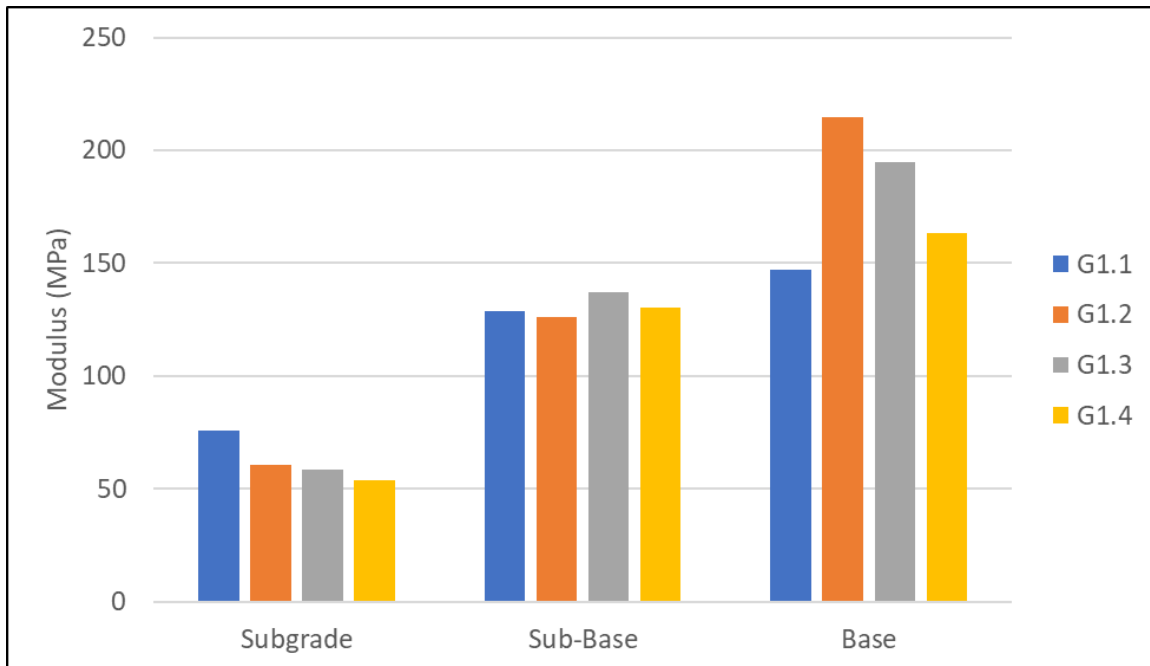
Figure 100. Modulus of unbound layers as estimated using GG

7.2.2. LWD Tests in Section 1B

All pavement layers were tested using LWD to estimate their small strain moduli over varying depths (approximately 6 to 24 in). The depth of evaluation is determined by the deflection data used in the moduli back-calculation. By including the deflection data from geophones placed at different radial distances (12 and 24 in from the center of the plate), the depth of evaluation of the modulus is suitably altered. The results for four different test locations along the wheel path of section 1 are shown in Figure 101 to Figure 103 for increasing evaluation depths. These figures confirm the repeatability of the LWD test results within any layer and clearly delineate the stiffness of the subsequent pavement layers (stiffness increases with additional layers).

Figure 101 shows the modulus for a depth of evaluation of approximately 6 in. These results are consistent with the results from the GG (Figure 100).

Figure 102 and Figure 103 show the moduli evaluated over an intermediate depth (12 inches) and larger depth (24 inches). The reduction in overall moduli with an increase in evaluation depth (number of geophones), especially in the final HMA layers, can be

explained as an artifact of the inclusion of lower layers with significantly lower moduli in the evaluation.

The depths of evaluation are assumed from the half-width of the plate (6 in) and radial distances of the geophones (12 and 24 in). This is only a theoretical approximation.
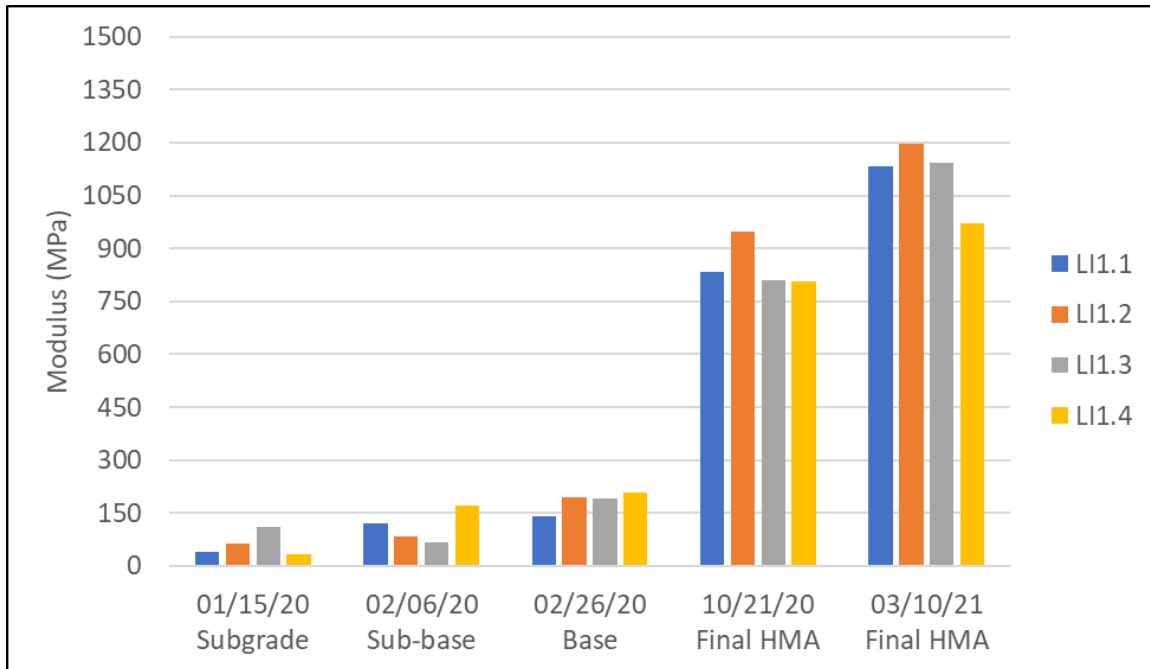
Figure 101. Modulus as estimated using LWD and single geophone deflection data
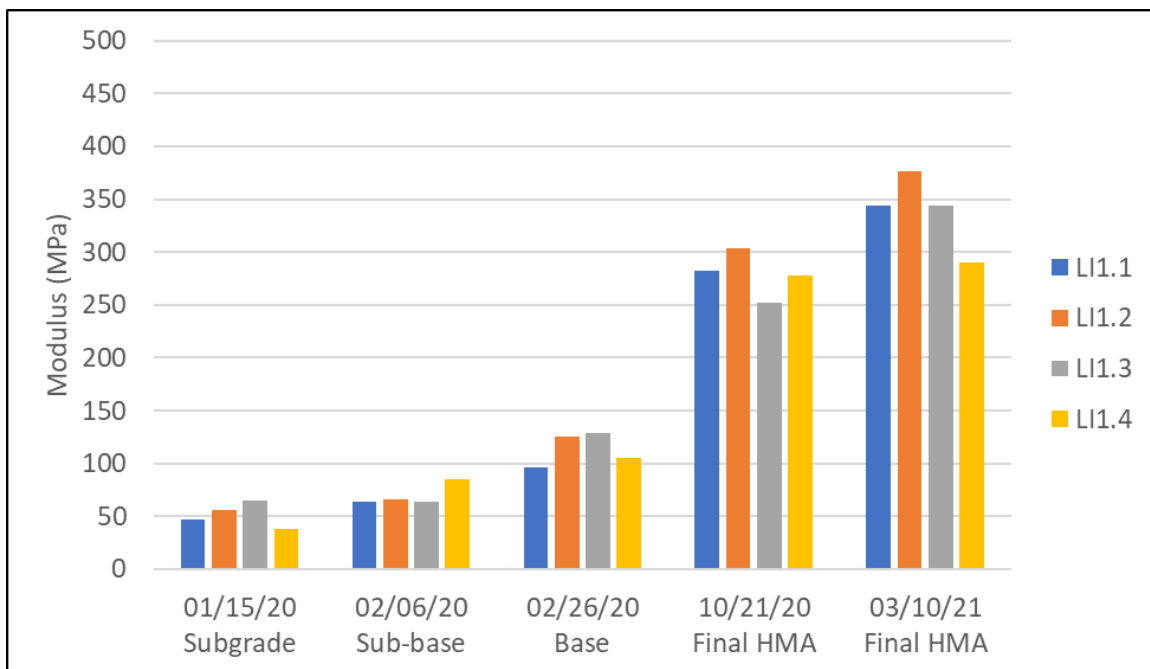
Figure 103. Modulus as estimated using LWD and deflection data from three geophones

7.2.3. sPLT in Section 1B

All layers of the pavement section underwent sPLT to estimate their large strain moduli over a nominal depth. The results of this testing at one location (location 3) along the wheel path of section 1 are shown in Figure 104 to Figure 106. As the figures show, the results of the sPLT delineate the stiffness of the subsequent pavement layers (stiffness increases with additional layers).

Figure 104 shows the maximum settlement achieved during the virgin compression phase under a static plate load of approximately 8,200 lbs. It is seen that with each additional layer constructed, the maximum settlement achieved decreases significantly. This is consistent with the increasing layer moduli as observed during the LWD tests (Figure 101 – small depth).

Figure 105 shows the virgin compression modulus and re-compression modulus under the static plate load. As expected, the trend is inversely correlated to the maximum settlement results presented in Figure 104. The range of moduli from the sPLT are closer to the range predicted from LWD tests (Figure 103 – large depth). This is likely because the nature of the sPLT involves larger strains, which implies a larger depth of influence

144

(deeper stress bulb). Thus, LWD tests that evaluate moduli over a larger depth would be expected to predict this modulus better.

Figure 106 shows the stiffening of the pavement surface following a load-unload cycle. With increasing stiffness of the layers, the stiffening effect is observed to reduce.

Figure 104. Maximum settlement under sPLT
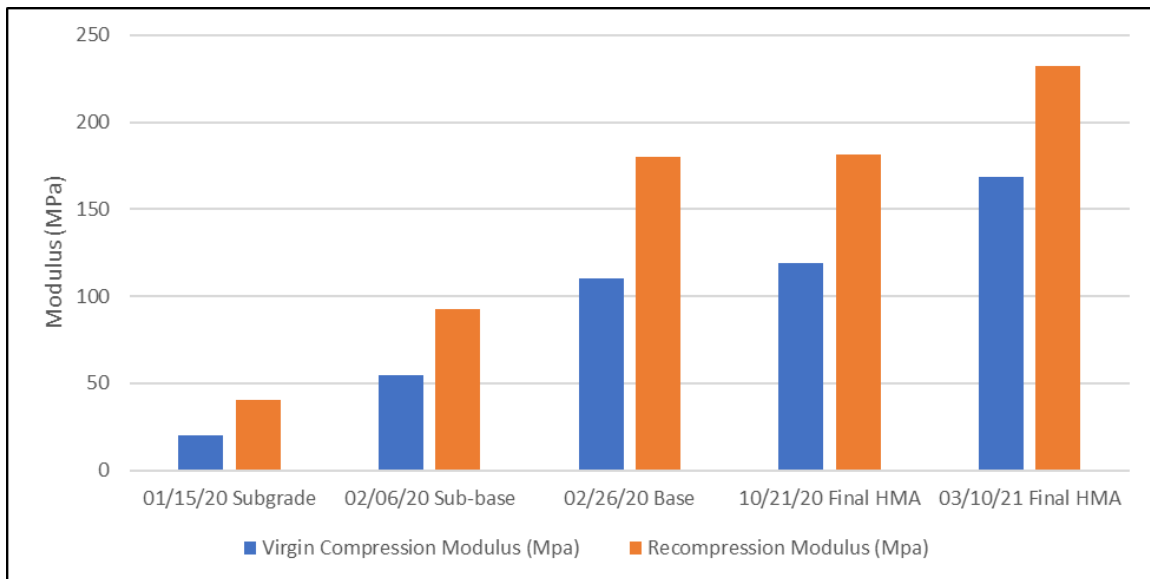
Figure 105. Moduli (virgin and recompression) under sPLT

145
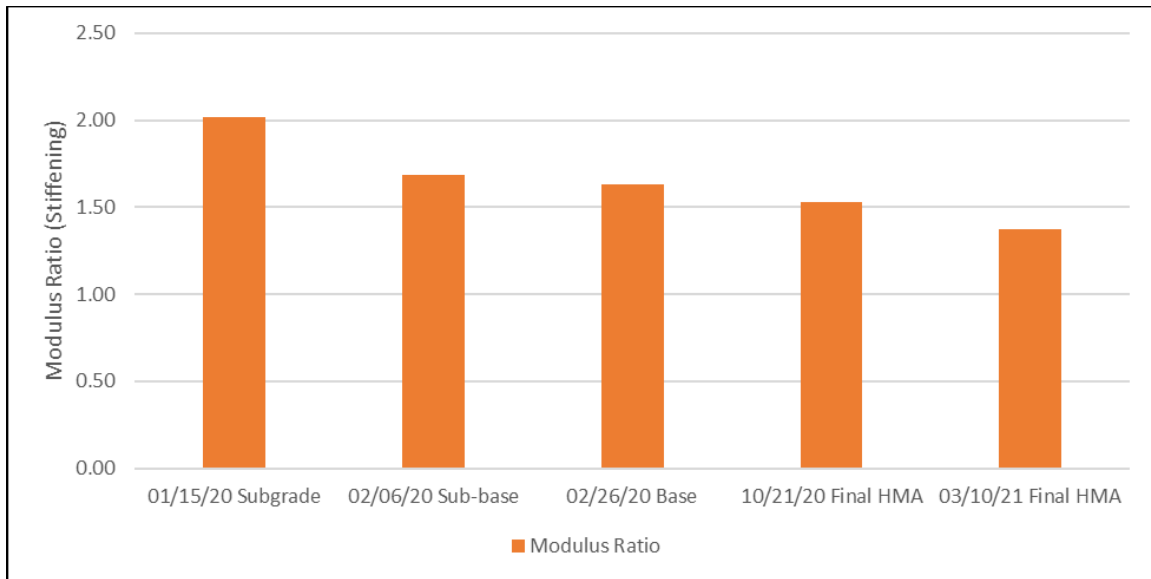
Figure 106. Modulus ratio (stiffening effect) under sPLT

7.2.4. DCP Testing in Section 1B

The unbound layers of the pavement section were tested using DCP to estimate their modulus at failure over a depth of 72 inches. The results for four different test locations along the wheel path of section 1 are shown in Figure 107. The location of the subgrade is marked by an elevation of 0 in. As can be seen in the figure, the DCP test results are repeatable within the unbound layers and clearly delineate the stiffness of the subsequent pavement layers (base layer: -6 in and above; sub-base: 0 in to -6 in; and subgrade: 0 in and below).

146
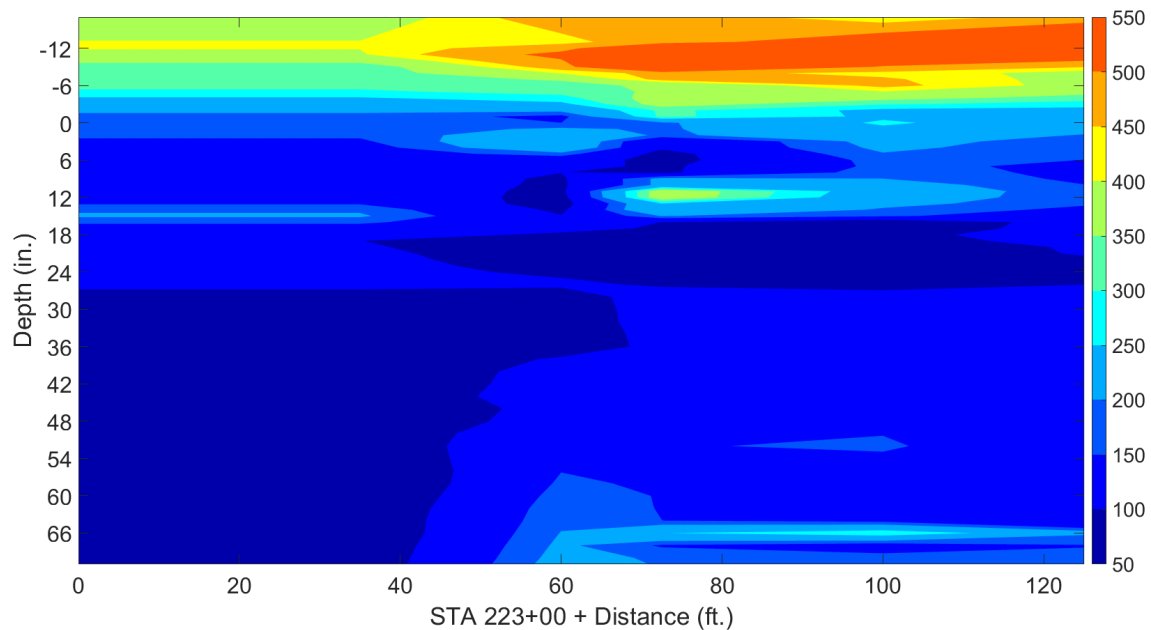
Figure 107. Modulus (MPa) measured from DCP tests in section 1

The modulus predicted from the DCP for the base, sub-base and subgrade layers are found to be higher than those predicted from other tests. This might be due to the nature of the DCP test itself, as the test measures stiffness by inducing shear failure under dynamic loads and is therefore a direct measure of the strength of the material rather than the modulus.

7.2.5. FWD Tests across All Test Sections

In all three testing campaigns and across all four instrumented test sections, FWD tests were conducted at general locations (F points). The location of these non-sensor FWD tests are shown in Figure 85 and Figure 86, labeled with the letter 'F' before the numeric designation of the tests. There are eight 'F' points in the control section, numbered 1.1 to 1.8, and nine 'F' points in each instrumented section, numbered X.1 to X.9 (where X = 2, 3 or 4). Thus, a total of 35 locations are tested during each loading campaign. All FWD tests conducted at the instrumented test sections can be summarized as follows.

- Four loading campaigns (one on top of the base + one on top of the final HMA layer)

- 35 test locations per loading campaign

- Four drops per drop sequence (three different drop heights)

147

The data collected from FWD tests (impulse load magnitude and deflections on the surface) are used to construct a deflection basin as shown in Figure 108. These deflection bowls are then used to back-calculate the moduli of the pavement layers. Thus, the total number of individual back-calculations to be performed = 4 x 35 x 4 =~560
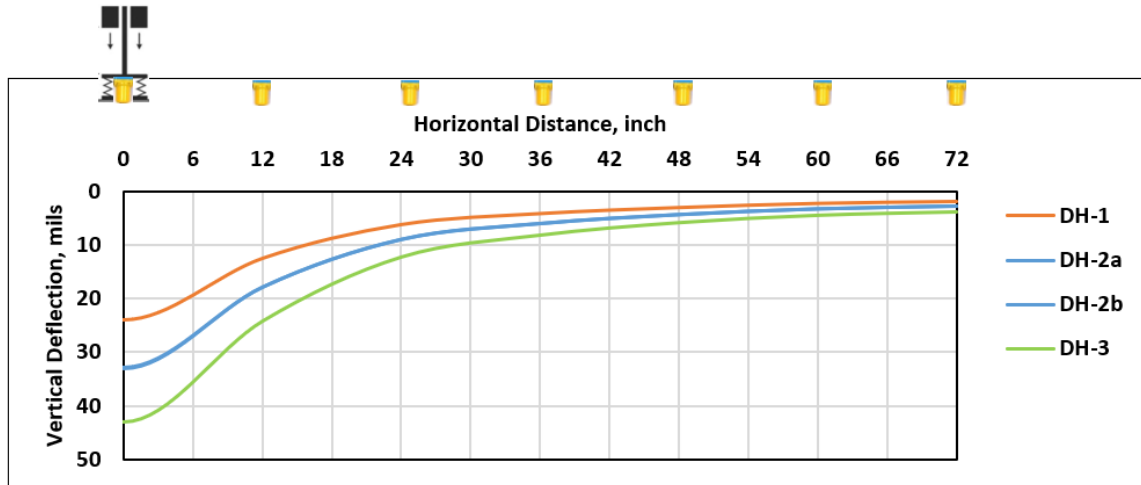
Figure 108. Deflection bowls from FWD tests with three different Drop Heights (DH)

Given the substantial number of back-calculations needed, a Python code was developed to perform a Layered Elastic Analysis (LEA) of pavements, hereafter referred to as UTLEA. The forward calculation engine for UTLEA (layer moduli to deflection bowl shape) was then used, with a differential evolution global optimization algorithm, to back-calculate the layer moduli from the deflection bowl shape recorded from the FWD tests. A simplified flowchart of the back calculation procedure to obtain the layer moduli from the deflection bowl shape is shown in Figure 109. An assumed layer moduli is used to determine the "calculated" deflection basin using the UTLEA forward calculation engine. The calculated basin is compared with the actual basin measured in the FWD test. If the difference between the two basins is within tolerable limits, the assumed layer moduli is accepted as the actual moduli of the pavement layers. However, if the difference between the two basins is significant, the assumed layer moduli is modified, and the procedure is repeated until the difference in the deflection basins is minimum. This modification to the assumed layer moduli is governed by the optimization algorithm chosen for the back-calculation problem, which in this case is the "Differential Evolution" global optimization problem.
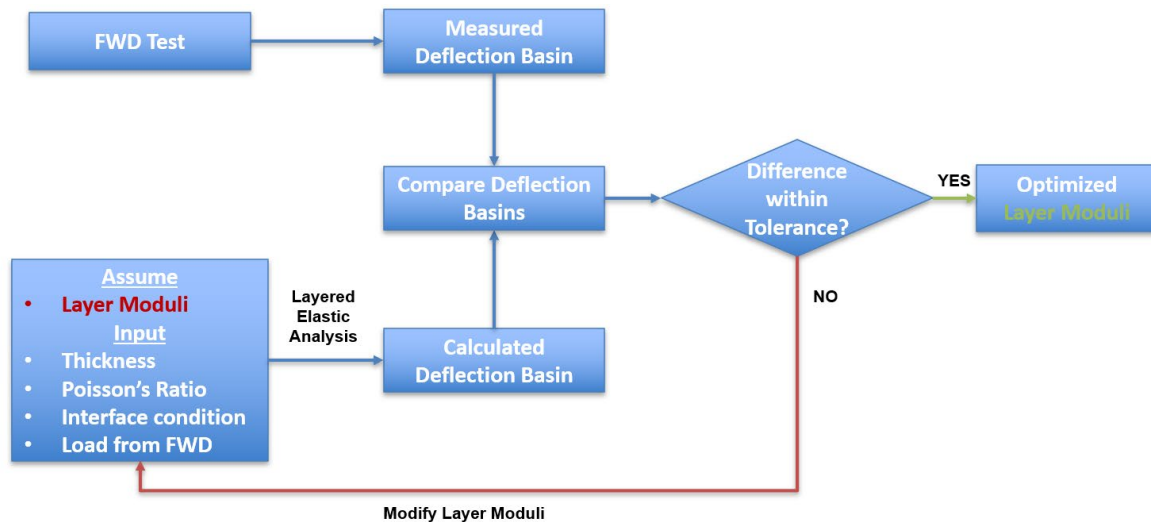
Figure 109. Back-calculation procedure flowchart

Basin-hopping is a stochastic algorithm that attempts to find the global minimum of a smooth scalar function of one or more variables. It is particularly useful when the function to be optimized has many minima separated by large barriers. This is the case with the moduli back-calculation problems where there are multiple local minimums for different combinations of moduli values, separated by a range of moduli values, for which the difference between basins is significant. The algorithm is also particularly suited for problems with higher degrees of freedom (independent variables, in this case the number of pavement layers).

To facilitate comparison between the control and stabilized sections, the back-calculated moduli from the eight to nine drop locations per section and four drops per location (from three different heights), totaling to 32 to 36 back-calculated moduli, are averaged to represent the moduli of the pavement layers of a particular section during a particular loading campaign. For instance, Figure 110 shows the average back-calculated moduli of the base layer for all four test sections during the February 2020 pre-HMA construction testing campaign done on top of the exposed base layer.

149
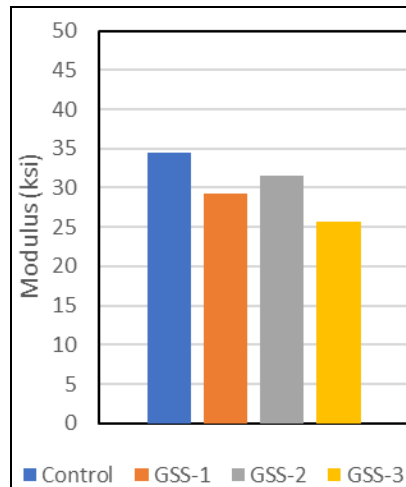
Figure 110. Average back-calculated base moduli from pre-HMA construction tests

7.2.5.1. Comparison of UT Back-calculation Algorithm with TxDOT Modulus 7.0:

Table 29 and Table 30 compare the layer moduli back-calculated using the UTLEA Back Calculation program (UTBackCalc) with the back-calculated values from the Modulus 7.0 program assuming three- and four-layer configurations. The analysis has been done for two randomly selected drops (A and B) from a total of 560 drops. The back-calculated moduli are close to each other (within 10% of each other). The errors in matching deflection bowls are consistent, with UTBackCalc performing slightly better (drop B) and sometimes poorer (drop A) compared to Modulus 7.0. The principal advantages of UTBackCalc appear to be its ability to handle more than four pavement layers and the automated nature of the data processing, which allow for swift processing of thousands of FWD data.

Table 29. Comparison of back-calculated moduli (ksi) – drop A

Drop A	UTBackCalc	Modulus 7.0 - 3 Layer -	Modulus 7.0 - 4 Layer -
E1 (HMA)	614.2	691	713.8
E2 (Base)	47.6	45.2	40.3
E3 (Sub-base)	20.4		25.1
E4' (Pf-SG)	20.4	20.6	20.5
E4 (Subgrade)	20.3		
Error/Sensor (%)	0.1.75	0.87	0.78

150

Table 30. Comparison of back-calculated moduli (ksi) – drop B

Drop B	UTBackCalc	Modulus 7.0 - 3 Layer -	Modulus 7.0 - 4 Layer -
E1 (HMA)	494.7	520.3	536.5
E2 (Base)	39.9	44.1	39.6
E3 (Sub-base)	19.3		23
E4' (Pf-SG)	19.2	18.7	18.6
E4 (Subgrade)	18.7		
Error/Sensor (%)	0.10	0.23	0.33

7.2.5.2. Comparison of Modulus of the Various Pavement Layers

As seen in Figure 110, the average modulus of the base layer in the control section is equal to, if not slightly higher than, the average moduli of the stabilized section. Figure 111 shows a plot similar to Figure 110, except the moduli of all unbound pavement layers are included. The sub-base also shows a higher modulus in the control section compared to the stabilized section. The modulus of the proof-rolled subgrade (the top 6 in of subgrade treated as a separate layer) and semi-infinite subgrade appear to be equal across the control and stabilized sections. Additionally, the modulus of all layers decreases with increasing depth (from the base at the top to the subgrade at the bottom). This is consistent with the expectation of increasingly stiffer layers at the top of the pavement and also with the results from GG, LWD, sPLT and DCP tests shown in Sections 7.2.1 to 7.2.4. In summary, immediately after base layer construction, the control section appears to be performing similar to, if not slightly better than, the stabilized sections. This may be due to the relative immobilization of tension in the geogrids. Similar trends were observed in the data collected from the next three loading campaigns.
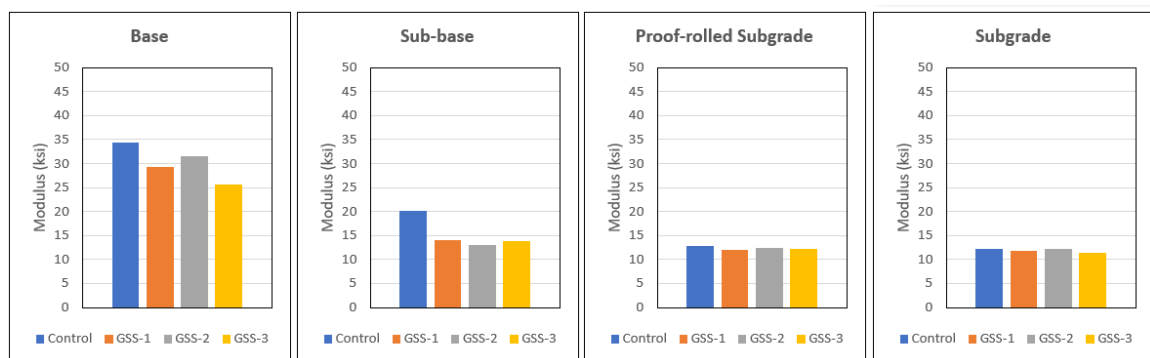
Figure 111. Moduli of all pavement layers from pre-HMA construction tests

To facilitate a better comparison, the moduli of the layers in the stabilized section are normalized with respect to the moduli in the control section. This data is presented in Figure 112. As can be seen, the normalized layer moduli, or moduli ratio, for all

151

pavement layers in the control section is equal to one (since the moduli are normalized to the corresponding layer moduli in the control section). The moduli ratio across all the sections are closer to or less than one.
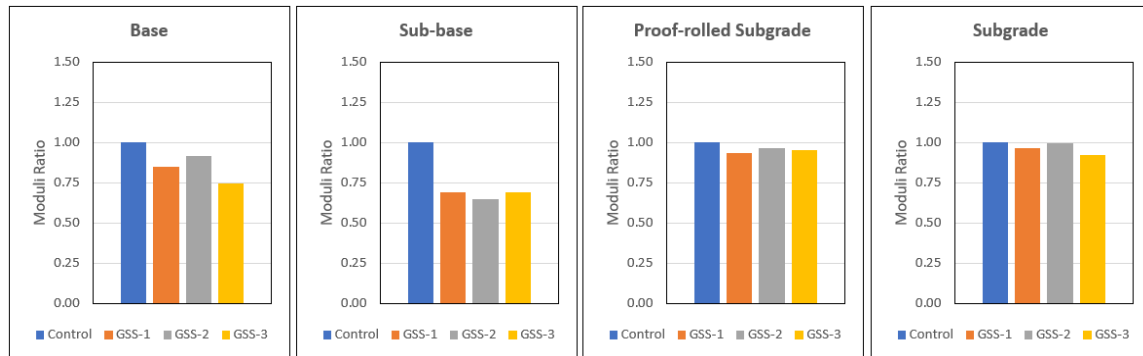
Figure 112. Normalized moduli of pavement layers for control section

7.2.5.3. Modulus of Base Layer over Time

The base layer moduli in all four test sections are compared across the four loading campaigns in Figure 113. The base layer moduli in the control section remain the same or decrease slightly with time. The base layer moduli of all three stabilized sections also clearly increase with time. This is attributed to an increase in tension mobilization, resulting in greater stabilization of the pavement layers over time.
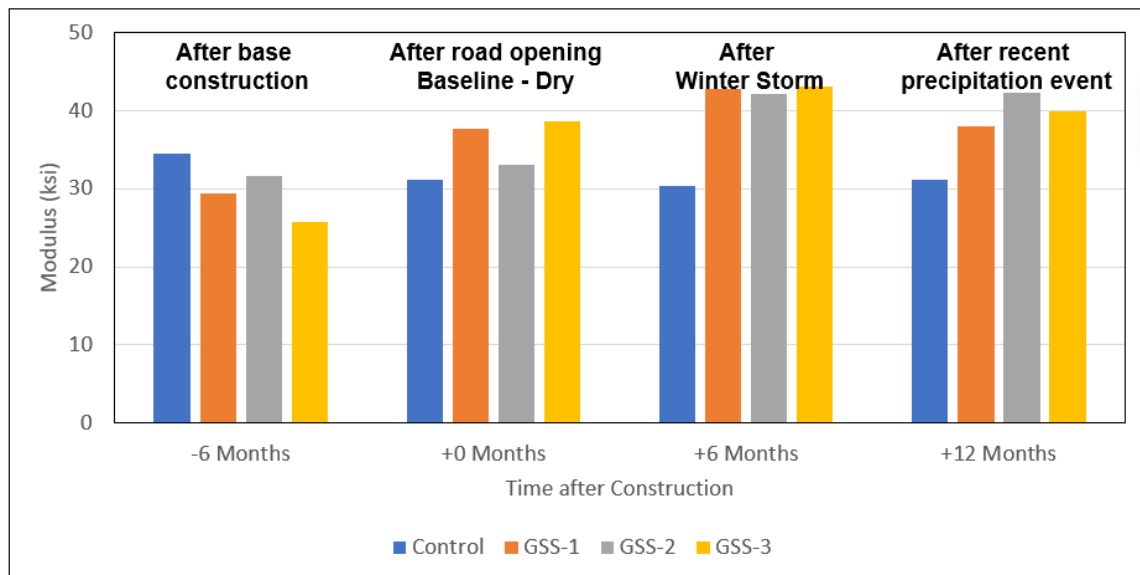
Figure 113. Moduli of base layer with time

Figure 114 shows the data in Figure 113 normalized with respect to the control section moduli across various times. Immediately after base construction, the moduli across test

sections are similar, if not worse, in the stabilized than the control section (as observed earlier). However, with an increase in time, the back-calculated base moduli increase as the geogrids are mobilized, except in the last loading campaign. Longer monitoring is required to determine any trend with time and other environmental variables, such as temperature, moisture, humidity, etc. An improvement in the base layer moduli of the stabilized sections ranged from 10% to as high as 40% when compared to the control section as exhibited in Figure 114.
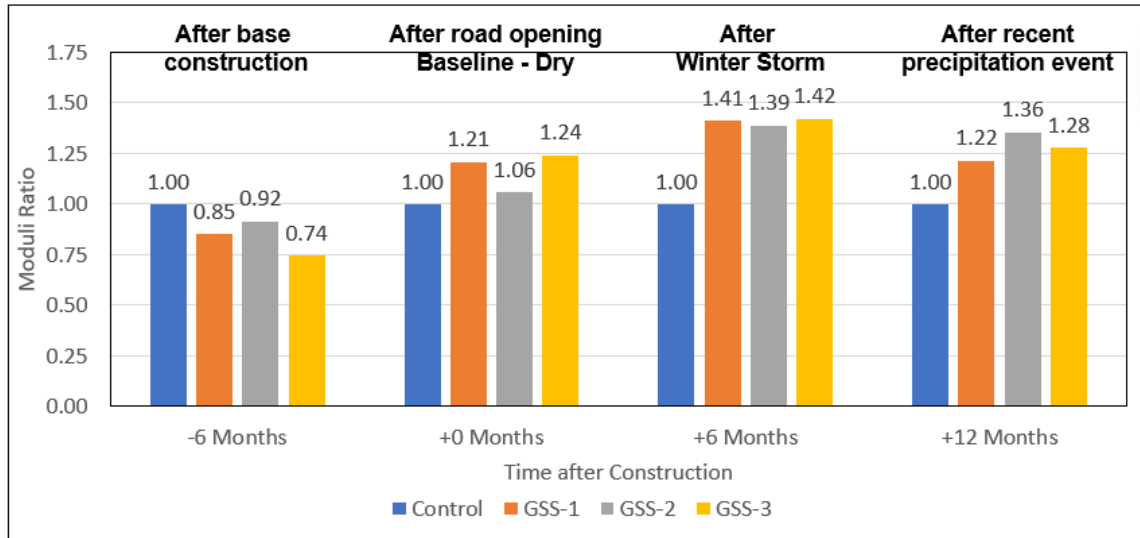
Figure 114. Moduli ratio (normalized modulus) of base layer with time

7.2.5.4. Modulus of Sub-base Layer over Time

Figure 115 shows the moduli ratio of the sub-base layer across the various testing campaigns. The trends are similar to those observed in the base layer. The improvement in sub-base layer moduli ranged from 10% to 45% in the stabilized sections compared to the control.
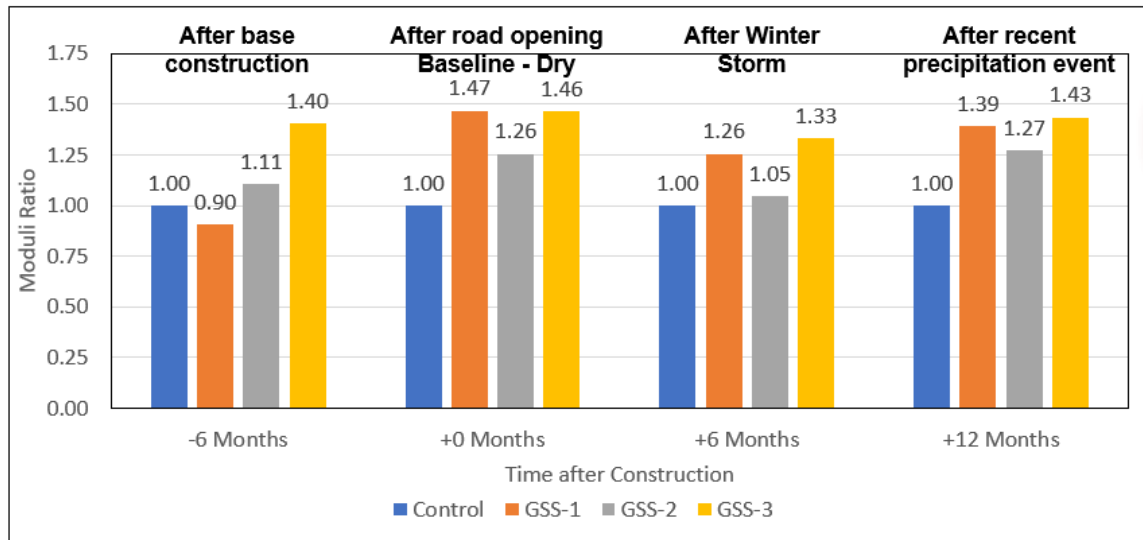
Figure 115. Moduli ratio of sub-base layer with time

7.2.5.5. Modulus of Proof-rolled Subgrade over Time

Figure 116 shows the moduli ratio of the proof-rolled subgrade layer across the various testing campaigns. The trends are similar to those observed in the base and sub-base layers. An improvement of up to 40% is observed in the proof-rolled subgrade moduli of the stabilized sections compared to the control.
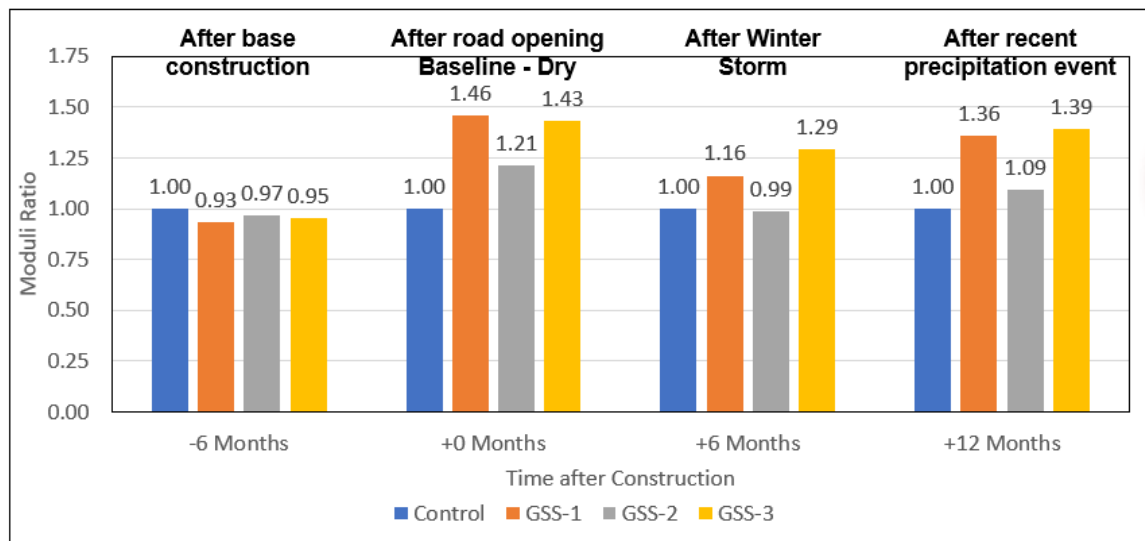
Figure 116. Moduli ratio of proof-rolled subgrade (top 6 in) with time

154

7.2.5.6. Modulus of Semi-infinite Subgrade over Time

The subgrade at the test section locations was found to be over 10 feet deep. Therefore, for the purposes of this analysis, the subgrade is assumed to be semi-infinite. Figure 117 show the moduli ratio of the semi-infinite subgrade (minus the top 6 in) across the various loading campaigns. No improvement in subgrade moduli was observed throughout the one-year testing period, implying the subgrade moduli in all four test sections behaved similarly in all testing campaigns. Given that the construction techniques were similar for all sections, the only reason for the difference in moduli of the other layers is the presence of the geogrid providing lateral restraint. This indicates that the influence of the geogrid in improving layer moduli extends to about 12 in above (11 in in the base layer) and below (6 in in the sub-base + 6 in in the proof-rolled subgrade) its installation depth.
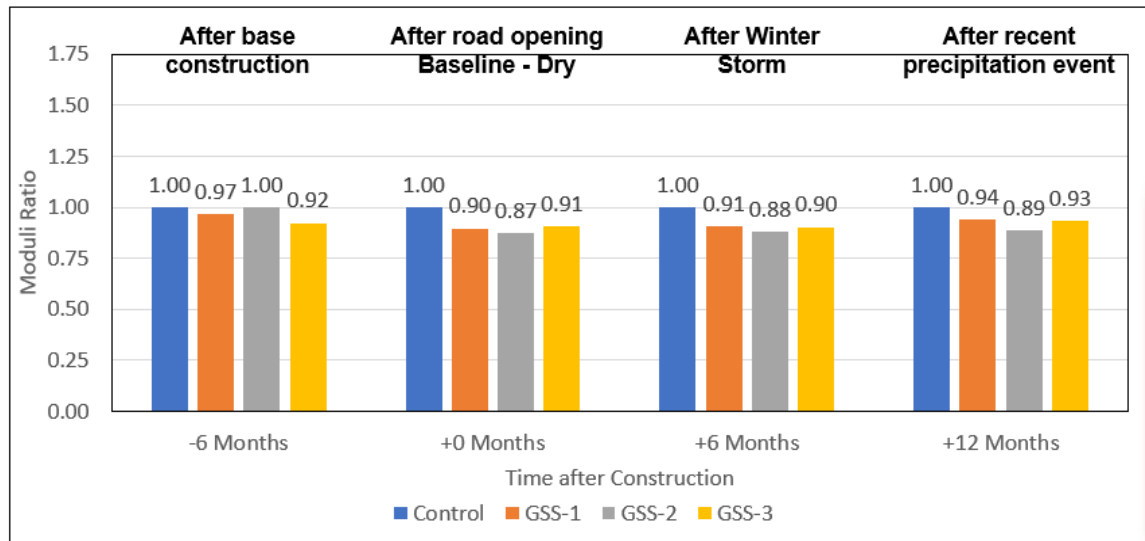
Figure 117. Moduli ratio of semi-infinite subgrade with time

7.2.5.7. Quantification of Benefits

Table 31 provides a summary of the maximum and minimum improvement to the moduli of the stabilized pavement layers compared to the control section. Assuming a typical cross-sectional profile with the design layer moduli and improved layer moduli (minimum and maximum), a layered elastic analysis is performed using the FPS-21 stress calculation tool. Table 32 provides the layer moduli of the typical section, minimum improvement section and maximum improvement section.

Table 31. Summary of moduli ratio range from FWD tests

Layer	Minimum	Maximum
Base	1.22	1.42
Sub-base	1.26	1.47
Proof-rolled SG	1.00	1.46
Subgrade	1.00	1.00

Table 32. Pavement sections with typical and improved layer moduli

Layer	Thickness (inch)	Typical Section (ksi)	Minimum Improved Section (ksi)	Maximum Improved Section (ksi)
HMA	8.5	650	650	650
Base	11	70	85.4	100
Sub-base	6	28	35.3	41
Proof-rolled SG	6	9.5	9.5	14
Subgrade	∞	9.5	9.5	9.5

Table 32 shows the results of the layered elastic analysis of the typical, minimum and maximum improved sections. The analysis is conducted by decreasing the thickness of the base layer in the improved sections so that the deflection bowl and internal stresses within the pavement structure of the improved sections roughly match that of the typical section with higher base thickness. This analysis allows for estimating the savings in base thickness that can be achieved using geogrids to stabilize the unbound aggregate base. The analysis shows that the thickness of the base layer can be reduced, from the 11 in of a typical section, to 9.25 in when assuming minimum stabilization benefits or to 7.25 in when assuming maximum stabilization benefits. In other words, the inclusion of a geogrid aids in shaving off 1.75 to 3.75 in of base material.

7.2.5.8. Lessons Learned from FWD Testing

1. The inclusion of a geogrid to stabilize the base layer resulted in increased layer moduli of all pavement layers within 12 in of the depth of installation of the geogrid (post-construction)

    a. Base (5% - 40%)

    b. Sub-base (5% - 45%)

    c. Subgrade (within 12 in of GG, up to 40%)

2. Such improvements in layer moduli could translate to a reduced base thickness of

    a. 1.75 in at minimum moduli improvement

    b. 3.75 in at maximum improvement

3. These improvements could also translate to a reduced HMA thickness with the same base thickness as a typical design section.

4. These improvements in layer moduli are expected to increase with time as the geogrids mobilize further. Thus, continued tracking of the moduli to observe the stabilized section behavior with time (via future testing campaigns) is critical.

5. Inclusion of a geogrid did not affect FWD layer moduli immediately after construction.

6. Subgrade (12 in and deeper from the geogrid location) moduli remained unaffected by the inclusion of a geogrid.

7. This study does not discuss how deflection bowls are affected from FWD directly due to variations in temperature on a particular day or across different loading campaigns. Instead, the back-calculated modulus from deflection bowls are compared for all layers, except the HMA.

Table 33. Sections with equivalent performance (improved moduli-decreased thickness)

Control Section

Pavement Structure

Name	Thick(in)	Moduli(ksi)	Possion Ratio	Interface
Surface	8.5	650.0	0.35	No Slip
Base	11.0	70.0	0.35	No Slip
SubBase	6.0	28.0	0.35	No Slip
Pf_Subgrade	6.0	9.5	0.35	No Slip
Subgrade	Infinite	9.5	0.40	No Slip

Other Result

Deflections: (by 1 feet space)

Sensor:	1	2	3	4	5	6	7
D(mils)	11.500	9.540	7.810	6.450	5.360	4.500	3.820

Stress & Strain Analysis Result

Layer Location	ID	Depth	Deflection	ε_t	ε_v	σ_t	σ_v
		(in)	(mils)	(Micro strain)		(psi)	
Btm of Surface	1	8.50	11.000	85.30	-105.00	78.0	-13.6
	2	8.50	10.600	69.60	-69.20	57.4	-9.4
Btm of Base	1	19.50	9.590	72.80	-103.00	6.4	-2.8
	2	19.50	9.400	69.10	-92.60	5.9	-2.5
Btm of SubBase	1	25.50	8.850	76.20	-119.00	2.4	-1.7
	2	25.50	8.710	73.50	-111.00	2.3	-1.6
Btm of Pf_Subgrade	1	31.50	7.860	57.00	-144.00	.2	-1.3
	2	31.50	7.770	55.60	-138.00	.1	-1.2
Top of Subgrade	1	31.50	7.860	57.00	-144.00	.2	-1.3
	2	31.50	7.770	55.60	-138.00	.1	-1.2

Min. Improved Section

Pavement Structure

Name	Thick(in)	Moduli(ksi)	Possion Ratio	Interface
Surface	8.5	650.0	0.35	No Slip
Base	9.3	85.4	0.35	No Slip
SubBase	6.0	35.3	0.35	No Slip
pf-Subgrade	6.0	9.5	0.35	No Slip
Subgrade	Infinite	9.5	0.40	No Slip

Other Result

Deflections: (by 1 feet space)

Sensor:	1	2	3	4	5	6	7
D(mils)	11.500	9.520	7.840	6.500	5.410	4.540	3.850

Stress & Strain Analysis Result

Layer Location	ID	Depth	Deflection	ε_t	ε_v	σ_t	σ_v
		(in)	(mils)	(Micro strain)		(psi)	
Btm of Surface	1	8.50	11.000	80.40	-101.00	72.5	-14.6
	2	8.50	10.500	65.40	-65.80	53.4	-9.8
Btm of Base	1	17.75	9.810	73.40	-103.00	7.9	-3.2
	2	17.75	9.600	69.00	-90.50	7.3	-2.8
Btm of SubBase	1	23.75	9.090	80.10	-117.00	3.4	-1.8
	2	23.75	8.940	76.90	-109.00	3.2	-1.7
Btm of pf-Subgrade	1	29.75	8.050	59.10	-150.00	.2	-1.3
	2	29.75	7.960	57.60	-144.00	.1	-1.3
Top of Subgrade	1	29.75	8.050	59.10	-150.00	.2	-1.3
	2	29.75	7.960	57.60	-144.00	.1	-1.3

Max. Improved Section

Pavement Structure

Name	Thick(in)	Moduli(ksi)	Possion Ratio	Interface
Surface	8.5	650.0	0.35	No Slip
Base	7.3	100.0	0.35	No Slip
SubBase	6.0	41.0	0.35	No Slip
Pf-Subgrade	6.0	14.0	0.35	No Slip
Subgrade	Infinite	9.5	0.40	No Slip

Other Result

Deflections: (by 1 feet space)

Sensor:	1	2	3	4	5	6	7
D(mils)	11.500	9.530	7.860	6.510	5.410	4.530	3.840

Stress & Strain Analysis Result

Layer Location	ID	Depth	Deflection	ε_t	ε_v	σ_t	σ_v
		(in)	(mils)	(Micro strain)		(psi)	
Btm of Surface	1	8.50	11.000	77.40	-97.90	69.3	-15.1
	2	8.50	10.500	63.10	-64.00	51.3	-9.9
Btm of Base	1	15.75	10.100	76.50	-108.00	9.5	-4.1
	2	15.75	9.810	70.80	-92.30	8.6	-3.5
Btm of SubBase	1	21.75	9.310	79.80	-117.00	3.9	-2.1
	2	21.75	9.150	76.20	-108.00	3.7	-1.9
Btm of Pf-Subgrade	1	27.75	8.390	67.10	-137.00	.7	-1.5
	2	27.75	8.290	65.10	-130.00	.6	-1.4
Top of Subgrade	1	27.75	8.390	67.10	-137.00	.7	-1.5
	2	27.75	8.290	65.10	-130.00	.6	-1.4

7.2.6. Response of Embedded Geophones under FWD Loading

The geophone measurements under FWD loading were utilized to assess the performance of the geogrid-stabilized sections in terms of lateral and vertical internal deflections. For this evaluation specifically, the FWD tests performed at the embedded geophone locations were taken into account. The data required for this evaluation were obtained during the four FWD loading campaigns performed after the completion of HMA layer construction. A plan view of the geophone layout, which is identical for the control and stabilized sections, is illustrated in Figure 118. Each section includes geophones embedded below the outer wheel path in four offset locations along the direction of traffic (i.e., the central location and offset locations at +1 ft, -1 ft and -2 ft away from the central location) at various depths as shown in Figure 119. In addition, each offset location, except for the "-2 ft offset," is equipped with geophones located 1 and 2 ft away from the outer wheel path as shown in the vertical layout in Figure 120.
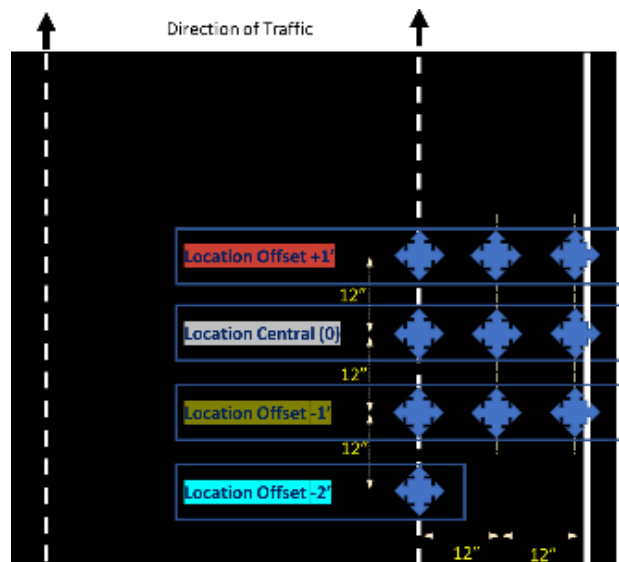
Figure 118. Plan view of geophone layout
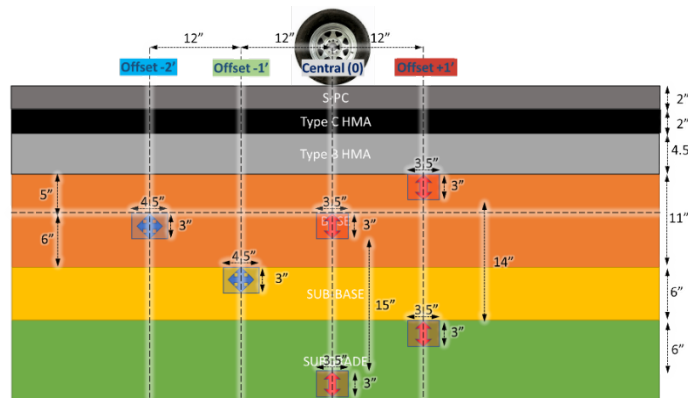
Figure 119. Vertical geophone layout

159
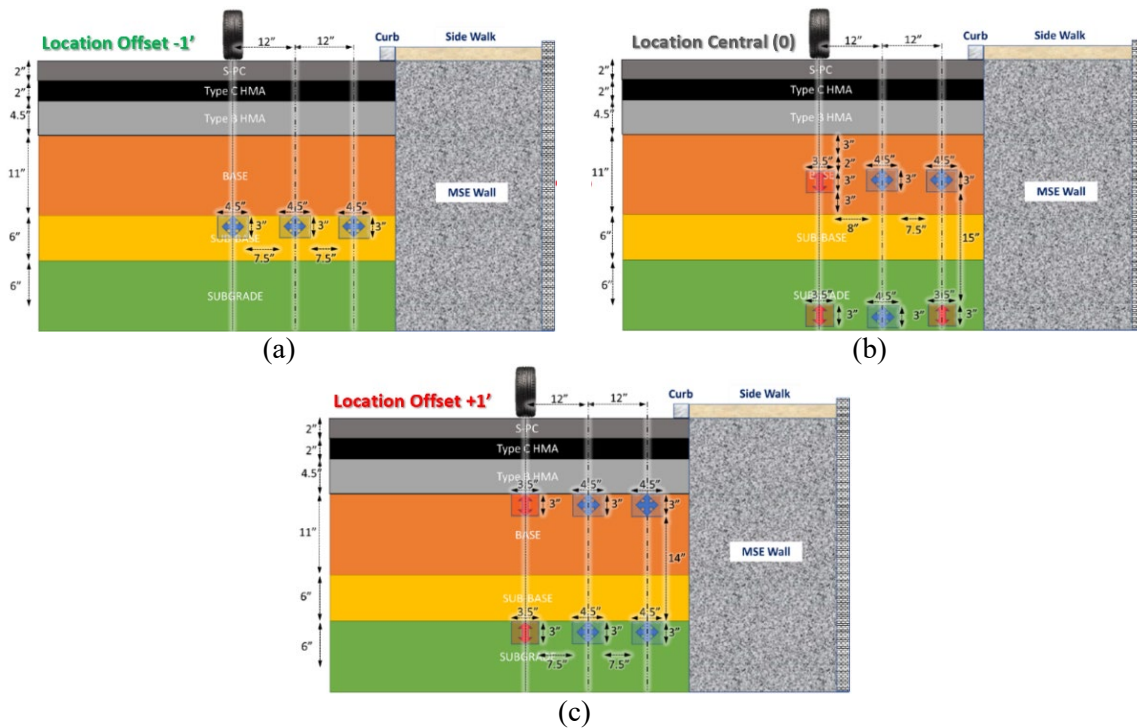
Figure 120. Cross-sectional view of location offsets: (a) location offset -1 ft; (b) central location; and (c) location offset +1 ft

The following subsection summarizes the steps of the geophone data processing procedure. Next, a two-part validation study is presented, where (i) the uniqueness and reliability of the FWD back-calculation results based on surface deflections are investigated and (ii) the geophone measurements are validated using the layered elastic analyses of the pavement profiles resulting from the back-calculated analyses. Lastly, the performance of the stabilized sections is evaluated against the control section in terms of lateral and vertical internal deflections.

7.2.6.1. Geophone Data Processing

The raw geophone data was processed using the frequency domain approach. First, Fast Fourier Transform (FFT) is performed to transform the voltage-time history to a raw voltage spectrum. Next, the frequency response was approximated by a second-order high-pass Butterworth filter, which is used to deconvolve the raw voltage spectrum to get a velocity spectrum. The velocity spectrum is then integrated within the frequency domain to obtain the displacement spectrum. Lastly, the displacement spectrum is converted to displacement-time history through inverse FFT. These steps are summarized in Figure 121.

160
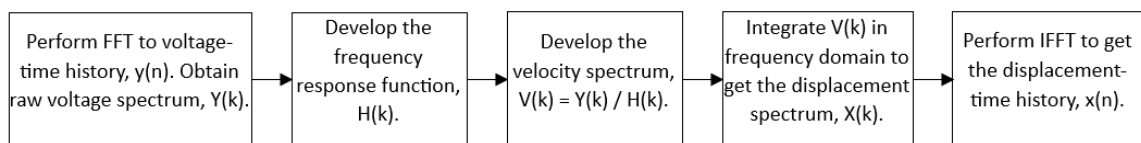
Figure 121. Geophone data processing procedure

7.2.6.2. Validation Studies

To assess the reliability of the collected geophone data and the data processing procedure, a two-part validation study was conducted using the results of the FWD tests performed on the control section. First, the raw geophone data were processed to calculate the peak internal deflections during FWD loading. The internal peak deflections, combined with the surface deflection data, were then utilized in the back-calculation analyses to investigate the reliability and uniqueness of the pavement layer moduli obtained through conventional means of analysis. Following this step, layered elastic analyses were performed using the back-calculated layer moduli, and the results were compared with the calculated geophone deflections. The methodology adopted for this purpose can be summarized with the following steps:

- Process the geophone data and estimate the peak internal deflections during FWD loading.

- Back-calculate pavement layer moduli based on FWD tests.

- Perform layered elastic analysis to estimate the internal deflections at embedded geophone locations.

- Compare the estimated and measured geophone deflections.

7.2.6.2.1. The Uniqueness of FWD Back-calculation Results

Conventionally, FWD-based back-calculation processes only utilize the surface deflection bowls to optimize the pavement layer moduli. However, the results obtained from this process may not be unique as several modulus combinations may yield similar surface deflection bowls. To address this issue, the internal deflections measured by embedded geophones may be integrated into the solution scheme. Accordingly, four alternative solutions are presented in this section. The first alternative (i.e., *Solution 1a*), which can be regarded as the conventional procedure, is based on the methodology described in Chapter 7.2.5 where an initial set of layer moduli is assumed and utilized in layered elastic analysis to produce the surface deflection bowl. The assumed layer moduli are iteratively adjusted by the optimization algorithm to capture the surface deflection bowl measured during the FWD test. The second alternative, *Solution 1b*, adopts the same solution approach as *Solution 1a* except that a different set of initial moduli was assumed. In the remaining alternatives, *Solution 2* and *Solution 3*, the vertical internal deflections calculated for the geophones embedded below the outer wheel path were integrated into the analyses, in addition to the surface deflection bowls. These four approaches are summarized as follows:

- Solutions 1a and 1b: Based on surface deflection bowl only using different sets of initial guesses for layer moduli.

- Solution 2: Based on the surface deflection bowl and the peak vertical deflection obtained for the top of the base layer (i.e., the corresponding geophone is located at "+1 ft offset" below the outer wheel path).

- Solution 3: Based on the surface deflection bowl and the peak vertical deflections obtained for all geophones located below the outer wheel path.

For the analyses, the data obtained during March 2021 campaign for the control section was randomly selected and the relevant tests were identified based on the locations of the geophones, which are mostly installed between "-1 ft" and "+1 ft" location offsets. Among the three load levels applied during the FWD tests, the tests having mid-level loading (i.e., approximately 10-kip impact force) were taken into consideration. The peak loads and the peak surface deflections from these tests are given in Table 34. Considering that the data obtained for these offset locations are highly consistent, it was deemed reasonable to consolidate these tests by averaging the load and surface deflection measurements and to use the resulting values as representative measurements for the control section. A similar approach was adopted for embedded geophone deflections. However, for each embedded geophone, only the tests performed at the same location offset were considered.

Table 34. FWD test results on control section, March 2021

Offset (ft)	Load (lbf)	d_0 (mils)	d_{12} (mils)	d_{24} (mils)	d_{36} (mils)	d_{48} (mils)	d_{60} (mils)	d_{72} (mils)
0	10133	8.11	6.63	5.15	3.92	2.98	2.31	1.93
0	10177	8.16	6.67	5.18	3.92	2.98	2.30	1.91
0	10111	8.04	6.61	5.11	3.86	2.92	2.25	1.87
0	10111	8.03	6.58	5.09	3.85	2.92	2.25	1.84
+1	10166	8.17	6.74	5.22	3.97	2.98	2.33	1.94
+1	10144	8.25	6.83	5.28	4.04	3.06	2.39	2.01
+1	10100	8.11	6.71	5.19	3.93	2.97	2.3	1.91
+1	10078	8.15	6.73	5.22	3.97	2.99	2.35	1.95
-1	10155	8.05	6.59	5.12	3.89	2.97	2.31	1.92
-1	10100	8.02	6.59	5.10	3.89	2.96	2.29	1.89
-1	10122	8.08	6.59	5.09	3.88	2.94	2.29	1.87
-1	10155	8.05	6.59	5.10	3.89	2.95	2.30	1.89
Average	10129	8.10	6.66	5.15	3.92	2.97	2.31	1.91

The results of the back-calculation analyses are presented in Table 35 in terms of layer moduli and Figure 122 in terms of surface deflection bowls. First, it is noticeable that the conventional means of analysis based on the measured surface deflections are sensitive to the initial guesses assumed for the pavement layer moduli. Despite using the same deflection data and achieving similar surface deflection bowls, *Solutions 1a* and *1b* are considerably different from one another and neither one represents a realistic pavement configuration. More specifically, the base

modulus in *Solution 1b* is more than 4 times the value reported in *Solution 1a*. Moreover, the upper subgrade moduli in both solutions are unrealistically high. Meanwhile, *Solutions 2* and *3*, which additionally make use of embedded geophone data, are consistent and more reasonable in terms of the resulting pavement layer moduli. The similarity of these two solutions is particularly interesting as the approach adopted for *Solution 2* only requires one additional embedded geophone as opposed to *Solution 3*, which makes use of 5 embedded geophones. In light of these results, it was seen that the addition of embedded geophones, even in low quantities, has the potential to improve conventional back-calculation procedures.

Table 35. Back-calculated pavement layer moduli

Solution	1a	1b	2	3
Layer	E (ksi)	E (ksi)	E (ksi)	E (ksi)
HMA (t = 8.5")	1431.9	1154.2	1235.2	1236.7
Base (t = 11")	18.7	76.1	49.5	49.0
Subbase (t = 6")	15.3	4.1	16.3	17.1
Upper subgrade (t = 6")	73.4	178.1	9.3	9.3
Lower subgrade (t = ∞)	21.6	23.3	22.2	22.2
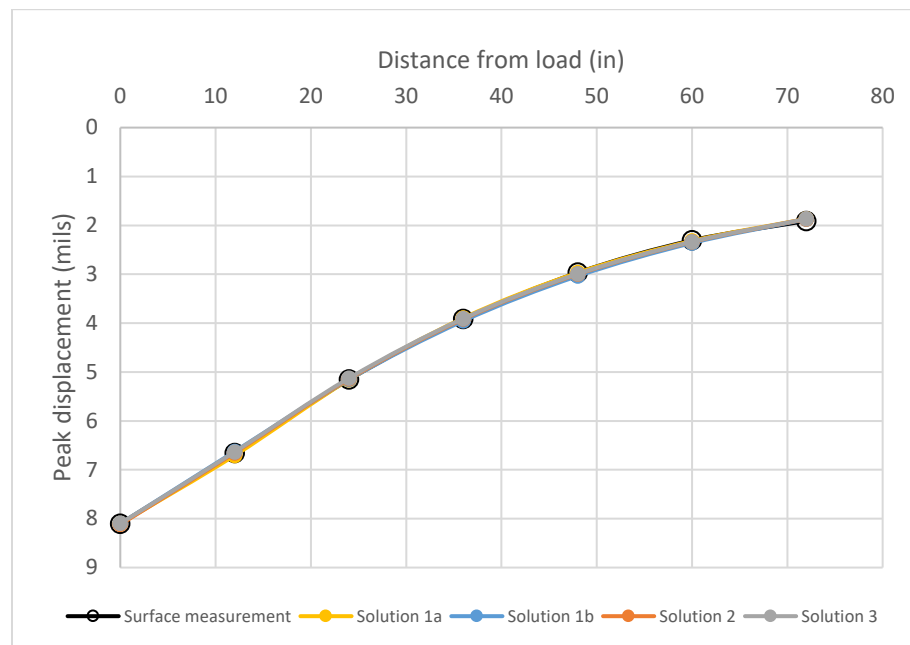
Figure 122. Surface deflection bowls estimated with layered elastic analysis

The back-calculated parameters were utilized in elastic analyses to estimate the internal deflections at the embedded geophone locations. Specifically, the vertical and transverse deflections were taken into consideration. The estimated deflections were plotted against the geophone deflections to validate the sensor measurements as shown in Figure 123. In terms of accuracy and precision, all solutions match reasonably well with the geophone measurements

despite the discrepancies observed in layer moduli. However, the accuracy obtained with *Solutions 2* and *3* is improved compared to *Solutions 1a* and *1b*, which are based on the conventional analysis method.

Solution 1a

Solution 1b

Solution 2

Solution 3
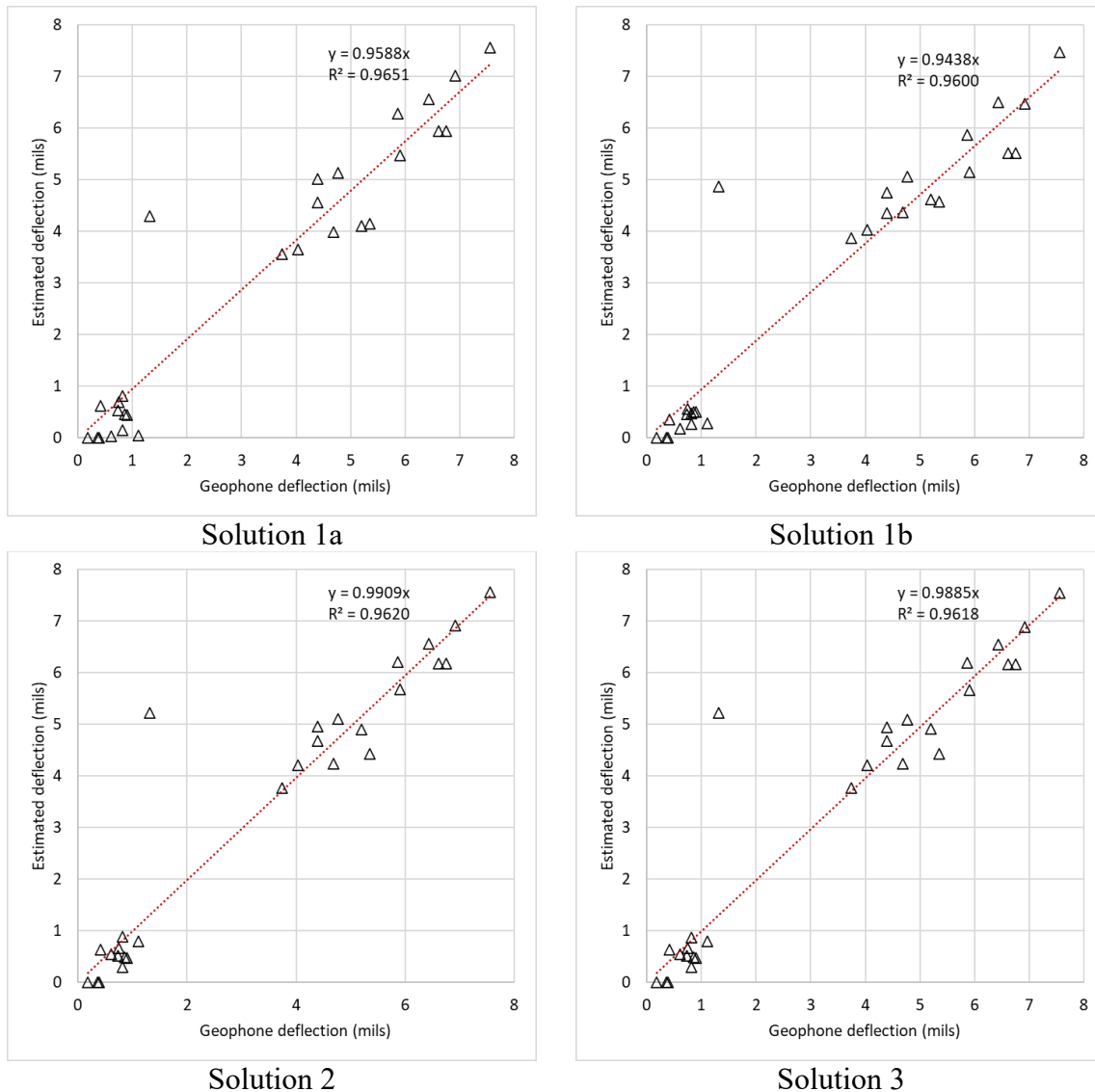
Figure 123. Comparison of measured and estimated geophone deflections

Verification of Geophone Measurements

The integration of embedded geophones into the pavement monitoring program was shown to improve the accuracy and reliability of the back-calculation process based on the outcomes of the previous analyses. Among the two solutions that utilize embedded geophone data, *Solution 2* gives a better trade-off as it yields an accuracy similar to that obtained with *Solution 3* using only one embedded geophone. Therefore, the rest of the validation study was based on this approach. Accordingly, the data obtained during the other loading campaigns were analyzed in a similar manner and the estimated and measured geophone deflections were plotted together in Figure

124. The results suggest a strong correlation, verifying the reliability of the collected geophone data and the processing methods that are utilized.

2020, October	2021, March
2021, August	2023, February
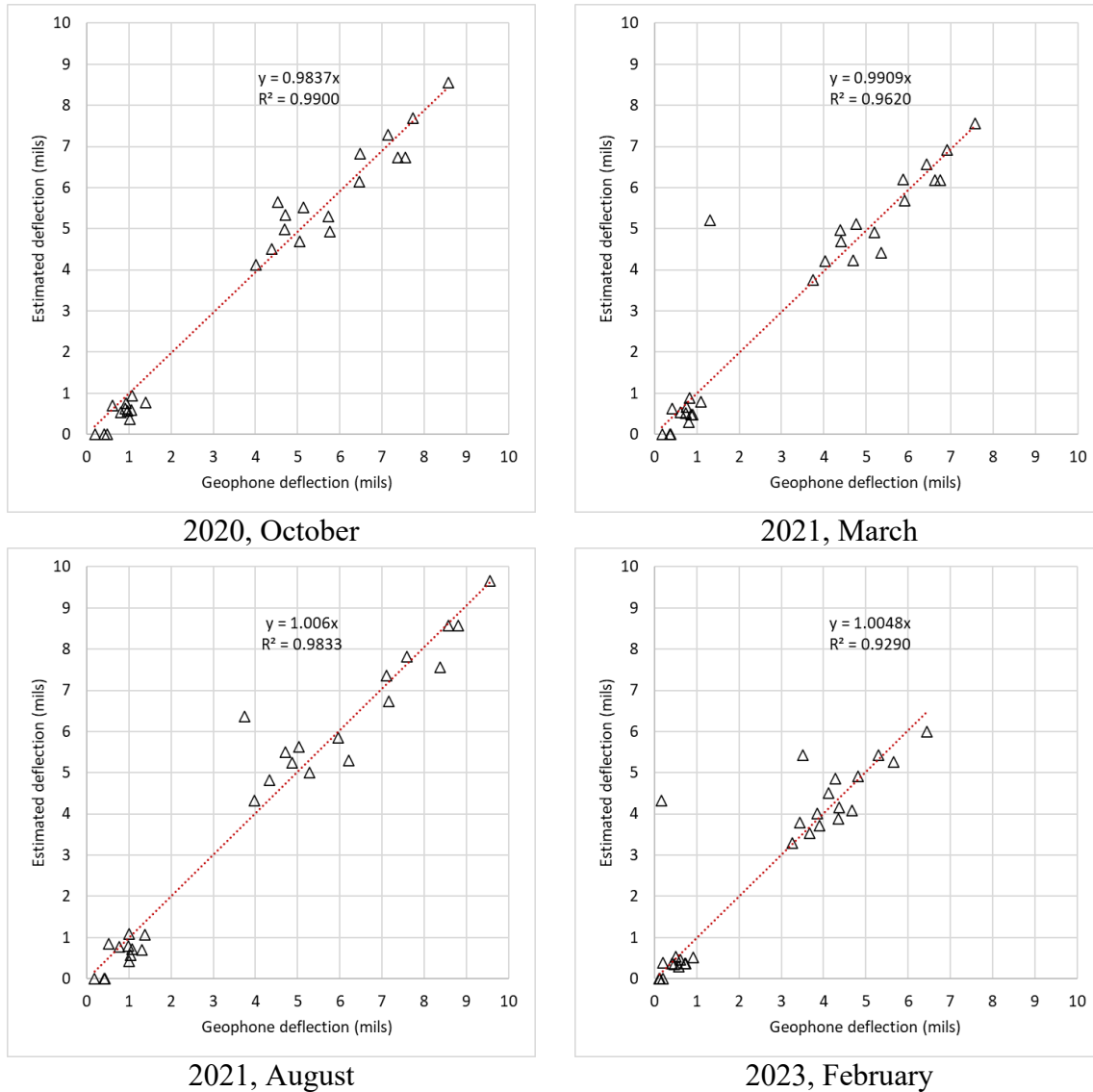
Figure 124. Validation of geophone deflections

7.2.6.2.2. Lateral Deflections under FWD Loading

It is a widely accepted phenomenon that the performance of geosynthetic-stabilized pavement bases relies on the interaction between the base aggregate and the geosynthetic. While unbound aggregates tend to lose stiffness upon repeated loading due to lateral permanent displacements, the inclusion of geosynthetics within the base layer can provide lateral restraint and help reduce modulus degradation over time. To investigate this phenomenon, the lateral deflections of the geophones embedded within the base layer of the control section were compared to those of the stabilized sections in terms of the deflection ratio defined below:

$$Deflection \text{ ratio} = \frac{h_{GSS}}{h_{control}} \tag{4}$$

where h_{GSS}: lateral deflection of the geosynthetic stabilized section, $h_{control}$: lateral deflection of the control section.

The geophones utilized for this analysis are 10 and 15 in below the surface, which correspond to the upper and mid-sections of the base layer. Each of these levels has geophones located 12 and 24 in away from the outer wheel path. The results, given in Figure 125, indicate that the lateral deflection measurements have a continuing trend of increased lateral restraint over time in most cases. Although some of the lateral deflections are higher in the stabilized sections initially, they improve over time and measure below the control section in the last two loading campaigns. This continual improvement is consistent with the argument that geosynthetics mobilize over time as permanent displacements take place.
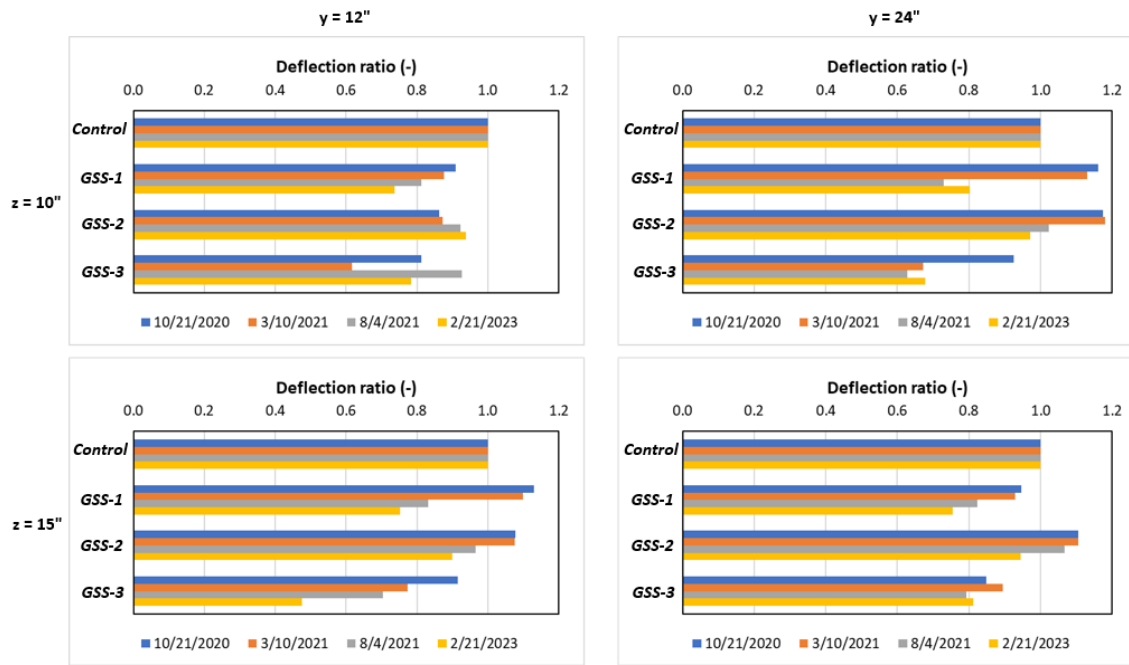
Figure 125. Lateral internal deflections under FWD loading

7.2.6.2.3. Vertical Deflections under FWD Loading

Similar to the previous section, the deflection ratios between the stabilized and control sections were calculated based on the relation given in equation (4). The geophones that are utilized for this evaluation are located directly below the outer wheel path at depths corresponding to the upper and mid-base, sub-base, and lower subgrade. In addition, surface deflection measurements were also utilized to make comparisons.

The vertical displacement ratios obtained from the surface measurements are illustrated in Figure 126 and the results derived from the embedded geophone data are given in Figure 127. From the

166

surface deflection data, it can be seen that the stabilized sections show consistently lower vertical deflections. Similarly, in the base layer, smaller deflections are observed within the stabilized sections in all cases. At these levels, the vertical deflections are reduced by as much as 18% in the last loading campaign. The results are similar for the sub-base layer, showing improved mechanical behavior in the stabilized sections. Lastly, the vertical deflections at the lower subgrade level are reduced in the stabilized sections in most cases. While the vertical deflection is slightly larger in the subgrade layer of GSS-1 compared to the control section in the last loading campaign, GSS-2 and GSS-3 exhibit reductions of 43% and 58%, respectively.
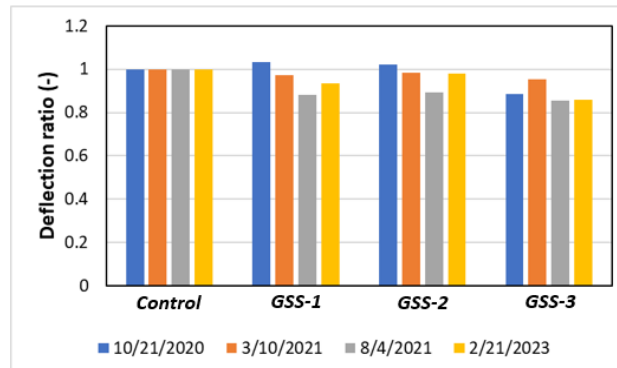
Figure 126. Surface deflections under FWD loading
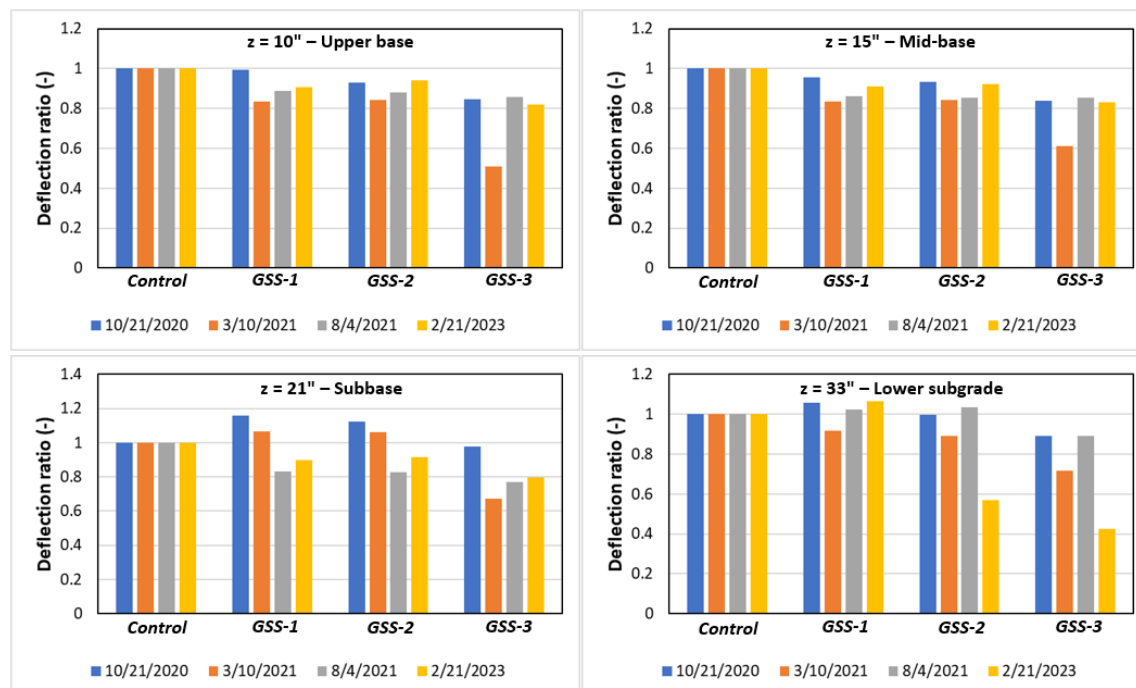
Figure 127. Vertical internal deflections under FWD loading

7.2.6.3. Lessons Learned from the Response of Embedded Geophones under FWD Loading

Verification studies
- FWD back-calculation problems based on surface deflections may not have unique solutions.

- Implementation of embedded geophone data can:

  o Extend the problem definition and yield more realistic back-calculated parameters.

  o Help with convergence.

  o Improve the agreement between measured and estimated deflections.

- The results suggest that geophone-driven internal deflections match reasonably well with the FWD-based layered elastic analysis results.

Lateral deflections
- Lateral deflection ratios between the geosynthetic stabilized and control sections improve over time, indicating that the geosynthetics provide increased lateral restraint as time progresses.

- In all cases, lateral deflections observed for the stabilized sections are smaller than control measurements for the last FWD test campaign.

Vertical deflections
- Stabilized sections show consistently lower surface deflections as the geosynthetics are mobilized over time.

- The base-, sub-base- and subgrade-level deflections are smaller in the stabilized sections compared to the control section.

7.2.7. Back-calculation of Pavement Layer Moduli

The surface deflection measurements along with the embedded geophone data collected during FWD tests were utilized to back-calculate the pavement layer moduli. To simplify the problem and promote convergence, the pavement profile was idealized into three layers as follows:

- Layer 1: 8.5-in-thick asphalt concrete layer

- Layer 2: 11-in-thick base layer

- Layer 3: deep lower layer combining the sub-base, proof-rolled subgrade and natural subgrade.

The flowchart illustrating the back-calculation steps is given in Figure 128. The analyses adopt Nelder and Mead simplex optimization method and a normalized objective function as defined below:

- Objective → minimize $f = \sum \left(\frac{d_m - d_e}{d_m} \right)$

  where d_m: measured deflection and d_e: estimated deflection.
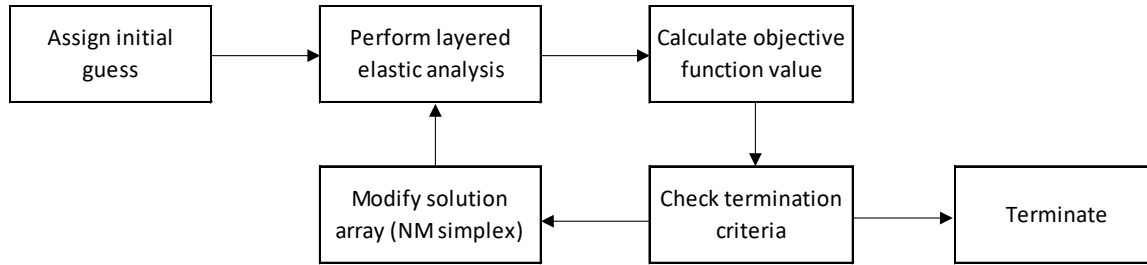
Figure 128. Back-calculation procedure flowchart

As previously shown in Section 7.2.6, the modified back-calculation framework that uses surface and internal vertical deflections from the embedded geophones can improve convergence, agreement between the measured and estimated deflections, and the uniqueness of the solutions. These implications are further supported in the following subsection through an evaluation of outcomes resulting from conventional and modified approaches. Next, the back-calculated layer moduli of the control and stabilized sections are comparatively evaluated using the data obtained from all FWD loading campaigns. Thereafter, the improvement of the stabilized section base moduli over time is evaluated. Lastly, the effect of temperature on asphalt layer stiffness is investigated.

7.2.7.1. Validation Studies

The validation studies involve the back-calculation analyses of the FWD tests performed on the central offset location of each section, illustrated in Figure 118. Using the data collected during the first field campaign after the construction of the asphaltic layers was completed (i.e., the FWD loading campaign was conducted on October 21, 2020), two different approaches were implemented:

- Approach 1: Conventional approach utilizing the surface deflections (i.e., seven surface deflection points).

- Approach 2: Modified approach utilizing the surface deflection and embedded geophone data together (i.e., seven surface deflection points + 16 internal vertical deflection points).

Approach 2 includes the internal vertical deflection data obtained from the embedded geophones surrounding the test section, while the horizontal deflections were not included in the analyses. The resulting base moduli are summarized in terms of statistical parameters in Table 36 and Table 37 for Approaches 1 and 2, respectively. The FWD tests were repeated twice at each analysis location, including 4 load stages per repeat. Accordingly, the statistical parameters were derived from a sample size of 8 analyses for each section.

As given in Table 36, the base modulus of the control section varies between 23.5 ksi and 43.3 ksi with an average value of 31.3 ksi based on the conventional analysis method, Approach 1. The average modulus is observed to be significantly higher in the stabilized sections, showing a 125% to 303% increase compared to the control section. However, the results from Approach 1 have relatively high variability with COV values ranging from 7% to 24%. With the inclusion of the embedded geophone data in Approach 2, the maximum COV reduces to 12% as given in Table 37. In this case, the average base moduli of the control and GSS-2 sections retain similar values, while the difference is more significant for GSS-1 and GSS-3 sections compared to Approach 1. Regardless, the average base module is still notably higher in the stabilized section – showing improvements from 100% to 234% compared to the control section. The main outcome from this evaluation, however, is that the variability of results reduces with the contribution of the embedded geophone data.

Table 36. Variation of back-calculated base layer moduli using Approach 1

	$E_{control}$ (ksi)	E_{GSS-1} (ksi)	E_{GSS-2} (ksi)	E_{GSS-3} (ksi)
Min	23.5	75.1	64.1	80.5
Max	43.3	100.6	80.1	193.3
Ave	31.3	87.1	70.3	126.0
St. dev.	6.0	9.6	5.1	30.5
COV	0.19	0.11	0.07	0.24

Table 37. Variation of back-calculated base layer moduli using Approach 2

	$E_{control}$ (ksi)	E_{GSS-1} (ksi)	E_{GSS-2} (ksi)	E_{GSS-3} (ksi)
Min	29.9	63.7	61.9	88.5
Max	39.2	81.0	74.9	134.1
Ave	34.2	71.7	68.3	114.1
St. dev.	3.1	5.0	3.9	14.0
COV	0.09	0.07	0.06	0.12

The results are further illustrated with the box plot given in Figure 129, which shows similar observations as before. For all sections, the variability of results is lower using Approach 2 and the median modulus values can differ between the two approaches, similar to the average values reported previously.
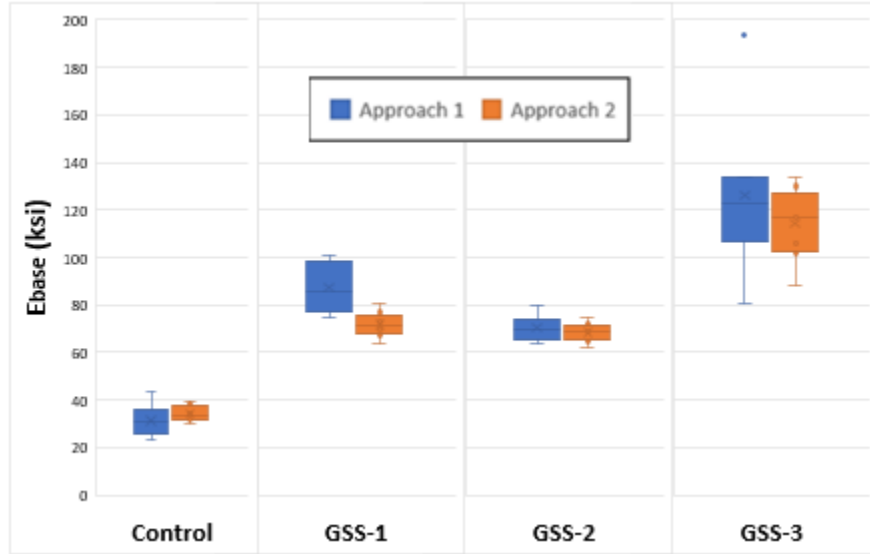
Figure 129. Back-calculated base layer moduli, October 21, 2020

Lastly, the agreement between the measured and estimated deflections at geophone locations was investigated. The results comparing the deflections from Approaches 1 and 2 are given in Figure 130 (a) and (b), respectively. Each figure involves 512 data points based on the analyses of eight FWD drops, four test sections and 16 geophone measurements per case. The slopes of the trendlines indicate that the modified approach results in improved accuracy. Furthermore, the R^2 values show that the precision is also improved. Considering the improved results, the geophone data was included in the back-calculation framework for the rest of the analyses.

(a)   (b)
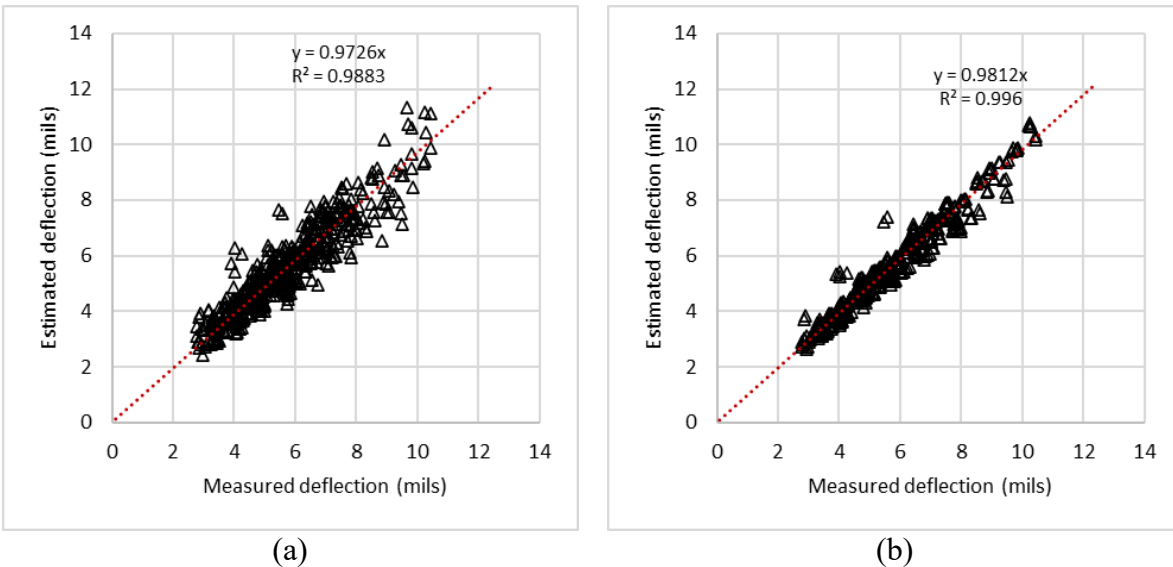
Figure 130. Comparison of measured and estimated geophone deflections: (a) Approach 1; and (b) Approach 2

171

7.2.7.1.1. Comparison of Back-calculated Layer Moduli

Using the modified back-calculation analysis framework, the rest of the data was analyzed to back-calculate the layer moduli of all sections. Differently from the previous section, only the mid-level FWD loading stages (i.e., approximately 10-kip impact force) were included to produce results that are more representative of an 18-kip equivalent single axle load. In addition, the pavement responses (i.e., peak load, surface deflections, and embedded geophone deflections) were averaged across each section to produce representative data sets.

To illustrate the outcomes, the back-calculated pavement layer moduli of the control and the GSS-2 sections are presented in Table 38. Included below, the first FWD campaign, which was conducted on February 26th, 2020, took place before the asphaltic layers were constructed. The rest of the field campaigns were performed after the construction was completed.

Table 38. Comparison of back-calculated layer moduli – control and GSS-2 sections

Date	2/26/2020		10/21/2020		3/10/2021		8/4/2021		2/21/2023	
Section	Control	GSS-2	Control	GSS-2	Control	GSS-2	Control	GSS-2	Control	GSS-2
E_{HMA} (ksi)	-	-	590.6	544.2	880.2	947.9	255.8	230.2	1334.6	1174.8
E_B (ksi)	43.0	34.9	52.7	86.2	59.6	87.1	58.6	117.0	57.5	140.8
E_{SB+SG} (ksi)	13.7	10.8	20.3	18.2	21.0	19.9	18.5	18.5	21.3	19.8
ε_{ave} (%)	11.9	13.5	4.6	3.3	3.6	2.3	4.7	3.4	3.1	3.1
n_{GP}	16	16	16	16	15	16	15	16	15	13

where HMA: hot mix asphalt, B: base, SB: sub-base, SG: subgrade, ε_{ave}: average error between the estimated and measured deflections, n_{GP}: the number of geophones included in the analysis.
It is noticeable that the analyses were not as successful for the first FWD campaign as the others, indicated by the relatively high average errors. The average errors given as 11.9% and 13.5% indicate that the final solutions were not in good agreement with the measured surface and internal deflections. This issue might be attributed to the fact that the roadway section was unpaved at the time, having relatively low structural capacity. Consequently, the measured responses may have included some degree of plastic behavior, which is not accounted for in the analysis framework. However, the rest of the analyses are more successful as the average errors do not exceed 5%.

Comparing the back-calculated HMA layer moduli, the values are similar for the control and GSS-2 sections in all FWD campaigns. However, in between different field campaigns, it is noticeable that the HMA moduli differ significantly. This can be attributed to the effect of temperature as discussed further in the succeeding subsection. As for the lower pavement layer including the sub-base and the subgrade units, the modulus seems to be consistent across all test sections and field campaigns after HMA construction, ranging between 18.2 ksi and 21.3 ksi.

Most significantly, the base layer moduli differ markedly between the control and stabilized sections, which is an expected outcome of geogrid stabilization. Although the base modulus of GSS-2 is lower than that of the control section in the beginning, it increases over time. Starting from a value of 34.9 ksi before HMA construction, the base modulus of the GSS-2 section increases monotonically up to 140.8 ksi in the latest FWD campaign. Whereas, the modulus calculated for the base layer of the control section retains similar values, ranging between 52.7 ksi and 59.6 ksi.

7.2.7.1.2. Modulus of Base Layer over Time

It is expected that the mobilization of a geosynthetic interlay in a base stabilization application could require some time after construction as there needs to be a tensile reaction for a geosynthetic to work as intended. Although some tension can develop in the geosynthetic interlay during construction, it is expected to increase over time due to continual traffic loading and the resulting permanent deflections. Supporting these arguments, Figure 131 illustrates that the base modulus increases over time in the geogrid-stabilized sections. For the GSS-1 and GSS-2 sections, the improvement seems to be monotonic as expected. The exception to this trend is GSS-3, which involves a cement-stabilized subgrade layer. Although the treatment may have resulted in some discrepancies, the outcomes still indicate an increasing trend for the base layer modulus.

Compared to the control section, the stabilized sections show improvements ranging from 138% to 173% in terms of the base modulus as of February 2023. It is apparent that all stabilized sections perform noticeably well with respect to the control section and the base layer moduli continually improve. However, it has not been possible to fully distinguish between the performances of the stabilized sections. It is expected that they are still in the mobilization phase and that they have not reached their full potential yet. Therefore, continued monitoring and future field campaigns are required to derive further conclusions.
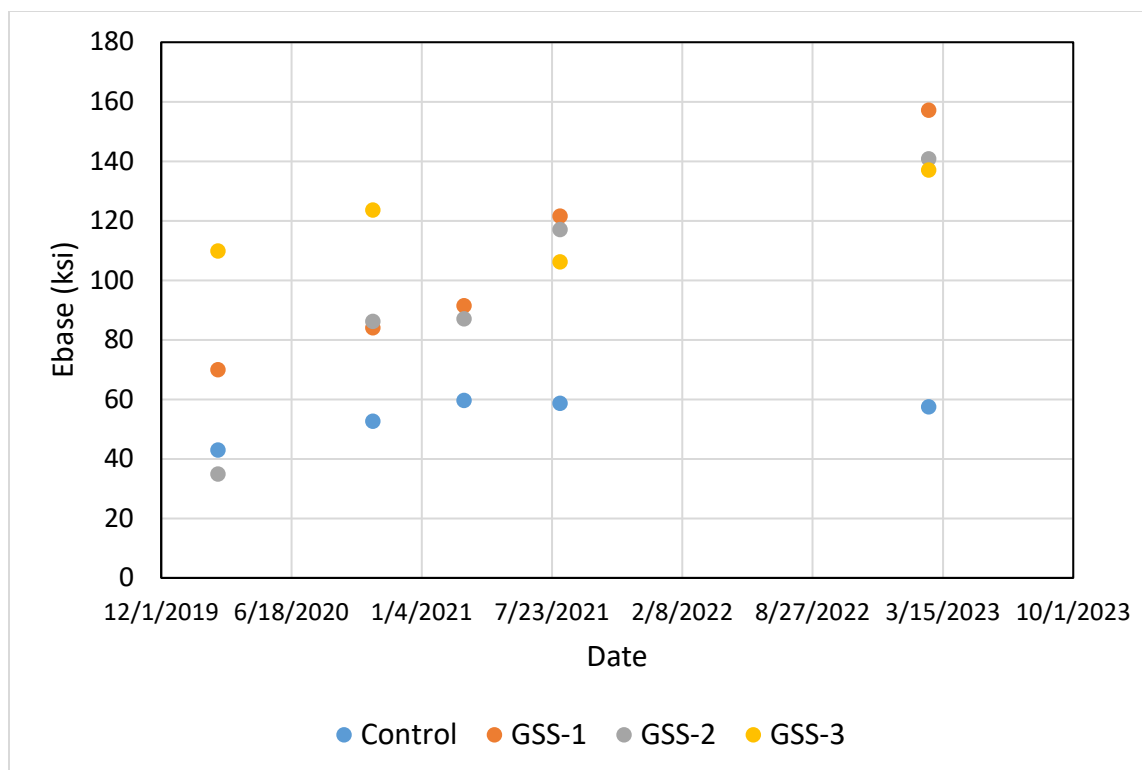
Figure 131. Base layer moduli of all sections over time

7.2.7.1.3. Effect of Temperature on Asphalt Modulus

In this subsection, the effect of temperature on the stiffness of the asphaltic layers is evaluated. As reported previously in Table 38, the HMA modulus varies significantly across the testing campaigns. While there are factors that affect the properties of asphaltic materials over time such as aging, the most significant factor is deemed to be temperature in this case. Using the data acquired from the thermocouples embedded in the HMA layer, it was possible to determine the average layer temperatures at the time of testing. Then, these measurements were coupled with the HMA moduli that were back-calculated using FWD tests performed at different dates and times of the day to build a data set. The results are given in Table 39 for the GSS-2 section. The results suggest an inverse correlation between asphalt modulus and temperature as expected.

Table 39. Temperature vs. back-calculated HMA modulus, GSS-2

Date	Time	T ($^\circ$C)	E_{back} (ksi)
2/21/2023	11:38-11:52	23.1	1334.6
2/21/2023	12:17-12:31	23.7	1174.8
3/10/2021	13:49-14:09	29.4	947.9
3/10/2021	17:15-17:19	30.6	892.2
3/10/2021	15:58:16:18	32.2	880.2
8/4/2021	13:52-14:14	39.6	230.2

174

Date	Time	T (°C)	E_{back} (ksi)
8/4/2021	17:05-17:26	41.9	255.8

To further validate the results, the material models reported in FHWA technical report FHWA/TX-18/5-6622-01-R1 (2019) were utilized to develop master curves for each sublayer. Then, the 8.5" thick pavement layer was idealized based on the properties of the sub-layers consisting of Superpave-C, Type B, and Type C asphalt concrete materials. The variables affecting the asphalt modulus were identified as pulse time and temperature. While the temperature data is already available in terms of thermocouple readings, the pulse time was determined based on the data obtained during FWD tests. In Figure 132, a typical FWD test with four loading stages is illustrated. The duration of a pulse for the surface load can simply be obtained by measuring the width of the pulse. Then, the relation proposed in Barksdale (1971), given in Figure 133, can be applied to calculate an equivalent vehicle velocity. Using this resulting velocity, it is possible to calculate the equivalent pulse times for the asphalt sub-layers which are located at different depths.
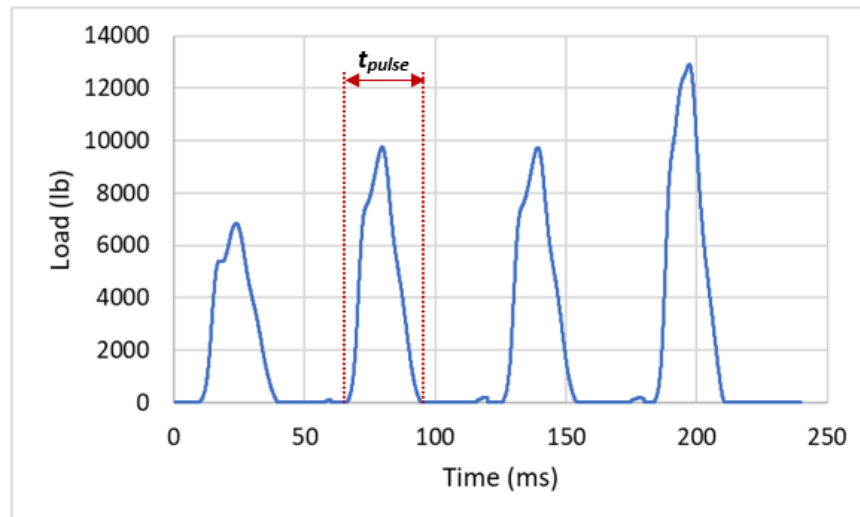
Figure 132. Typical FWD test with four loading stages
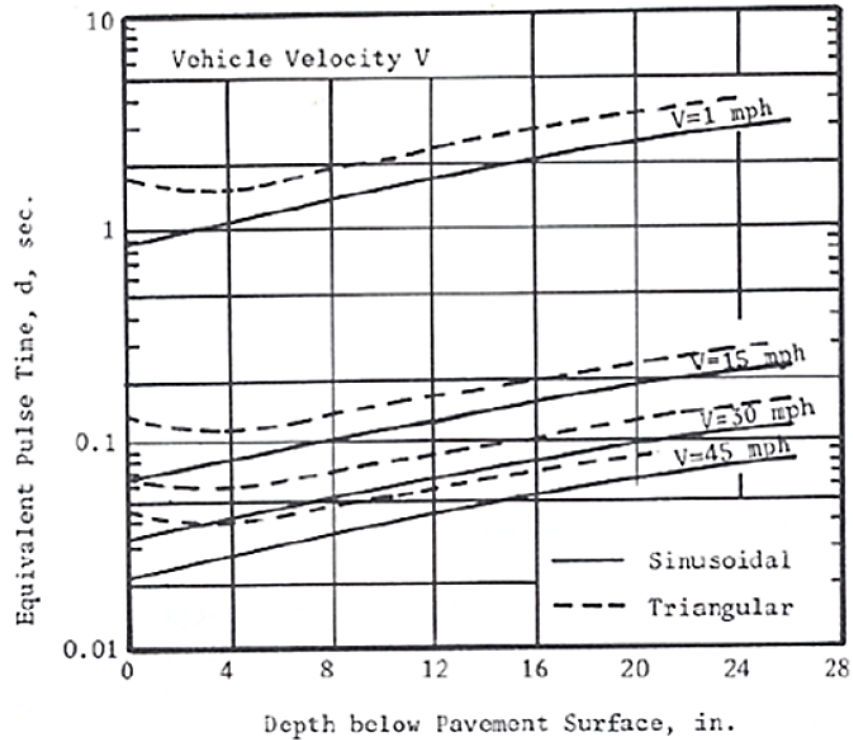
Figure 133. Relation between pulse time, vehicle velocity and depth (Barksdale, 1971)

Using the resulting pulse times, sub-layer moduli were calculated for the range of temperatures representative of the field conditions. Then, the weighted averages of the sub-layer moduli (i.e., based on layer thicknesses) were calculated to develop an idealized modulus vs. temperature curve for the 8.5-in-thick asphalt layer. The results are presented in Figure 134 for GSS-2. The back-calculated asphalt layer modulus and the idealized master curve are in good agreement. Considering that the master curves were developed based on an independent study, the agreement of the two data sets points to the reliability of the geophone-aided back-calculation framework.
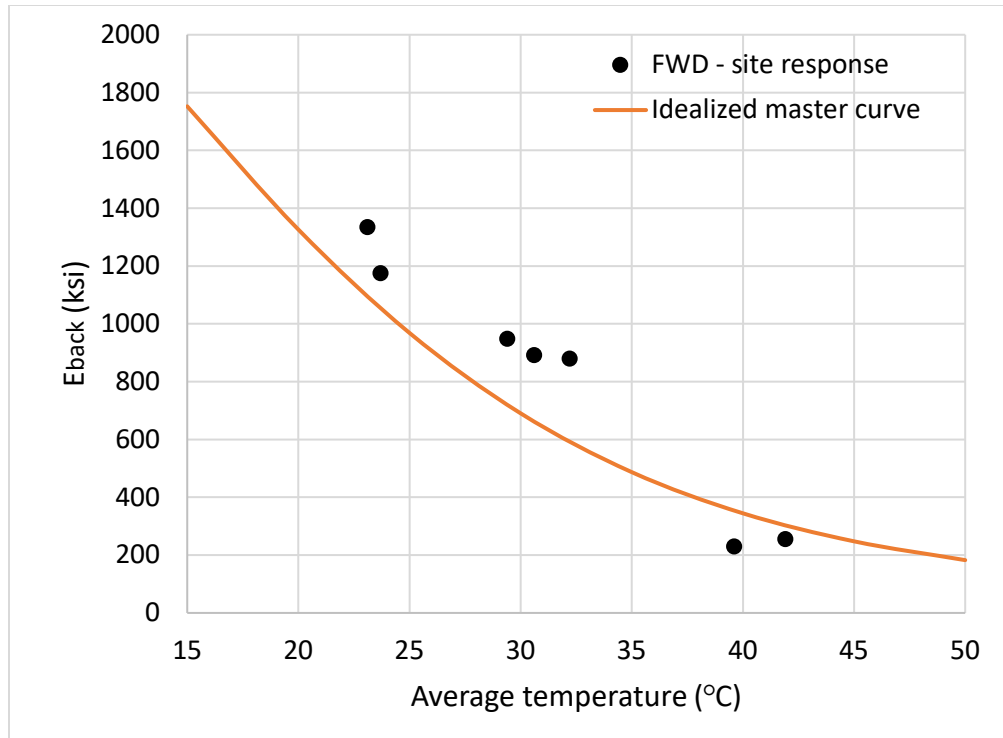
Figure 134. Comparison of back-calculated asphalt modulus and idealized curve for GSS-2

7.2.7.2. Lesson Learned from Back-calculation of Pavement Layer Moduli

Validation studies
The contribution of embedded geophones to the back-calculation processes improves:

- Convergence capability,

- Uniqueness of solutions,

- Accuracy and precision of results.

Improvement of the base layer modulus
- All three stabilized sections perform comparatively better than the control section.

- The base layer moduli of the stabilized sections continually increase over time as the geosynthetics continue being mobilized.

- Further monitoring is required to study the long-term behavior of the stabilized sections to distinguish between the relative performances of the stabilized sections.

Effect of temperature on asphalt modulus
- Based on the back-calculation analyses using the embedded geophone data, an inverse relation was observed between the HMA layer modulus and temperature as expected.

The idealized master curve and back-calculated moduli are in good agreement, which is an outcome that supports the reliability of the geophone-aided back-calculation framework developed as part of this study.

7.3. Characterization of Long-term Pavement Performance

The performance of the pavement over its design life is evaluated from the long-term collection of data from the various sensors used to instrument the pavement section. The sensors from which long-term are primarily collected include,

- Asphalt strain gauges

- Linear potentiometers (displacement sensors)

- Soil extensometers

- Moisture sensors

In this section, the data collected from the above sensors installed in section 1b are analyzed and the results are reported. Analysis protocols for all these sensors were established as part of this project.

7.3.1. Asphalt Strain Gauge (ASG) in Section 1B

Figure 133 shows the transverse strains as measured by the ASG located along the wheel path or Transverse Wheel Path Repeat (TWPR) sensor. The strains measured include those accumulated due to vehicular traffic and those induced by temperature variations over a period from November 20, 2020 to May 20, 2021.
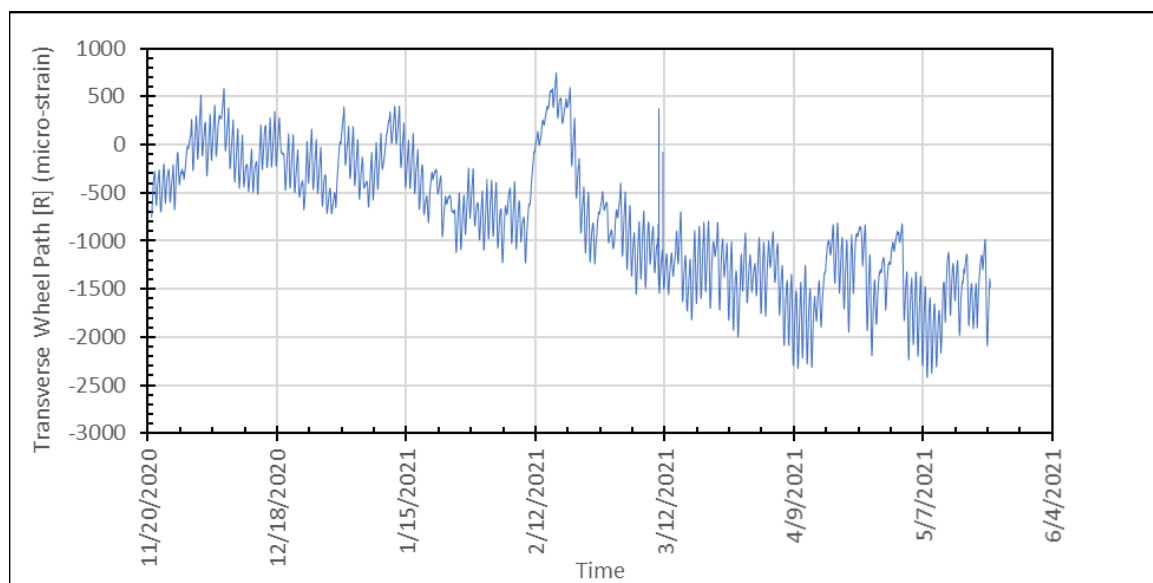
Figure 135. Raw strain values from TWPR sensor in section 1b

Figure 134 shows the data over a week's time. It can be easily inferred that daily variation in temperature results in cyclic straining of the ASG. Thus, it becomes imperative to understand how temperature changes affect the strain values as measured by the sensor. As a first step toward this, the strain data is normalized to begin from zero in Figure 135. It is easier to observe the macro-trends (high and low temperature points) in the strain vs temperature chart than to account for all the daily variations.
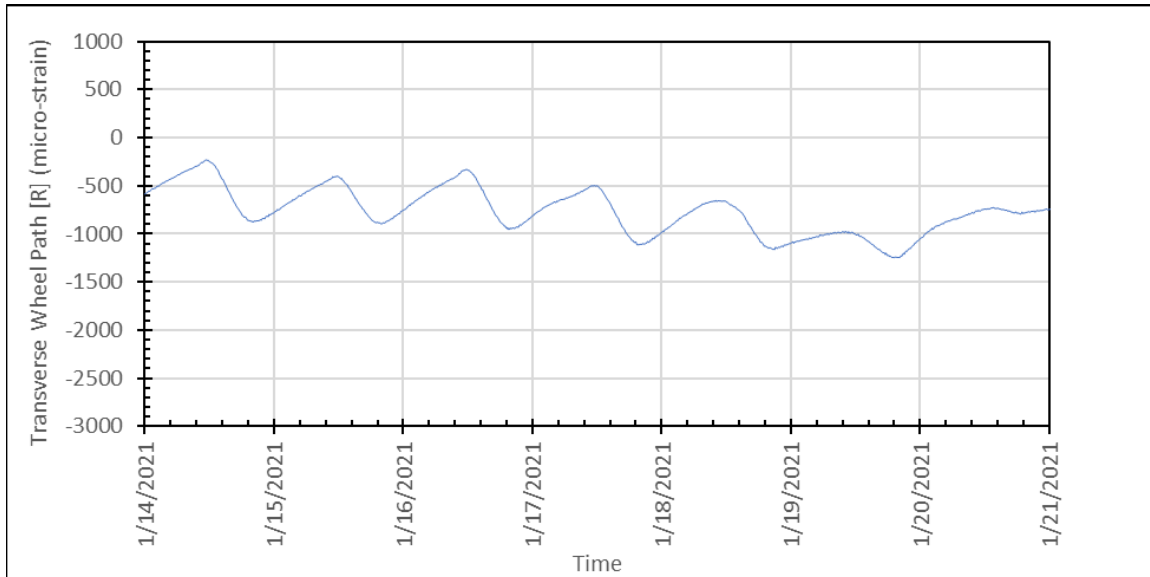
Figure 136. Raw strain values over one week in January 2021
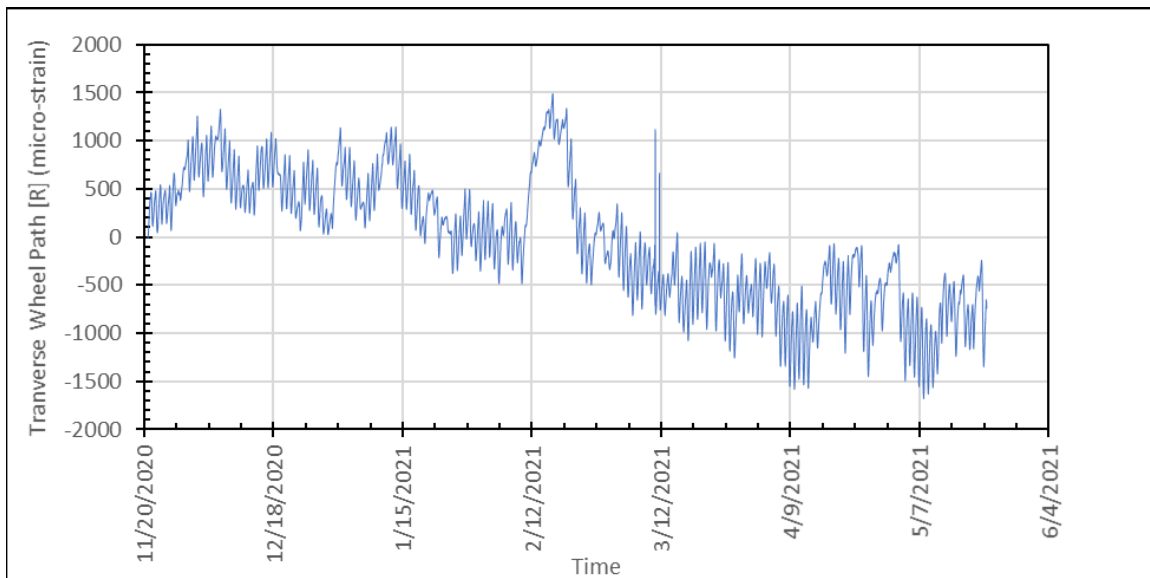
Figure 137. Strain values normalized to zero

With that context, enveloping curves that track the highest and lowest strains in a day are plotted along with the normalized strain values as shown in Figure 136. Finally, a comparison is made

179

between enveloped strains and enveloped temperatures readings as shown in Figure 137. Note that the temperature axis is inverted (higher temperatures are at the bottom of the chart).
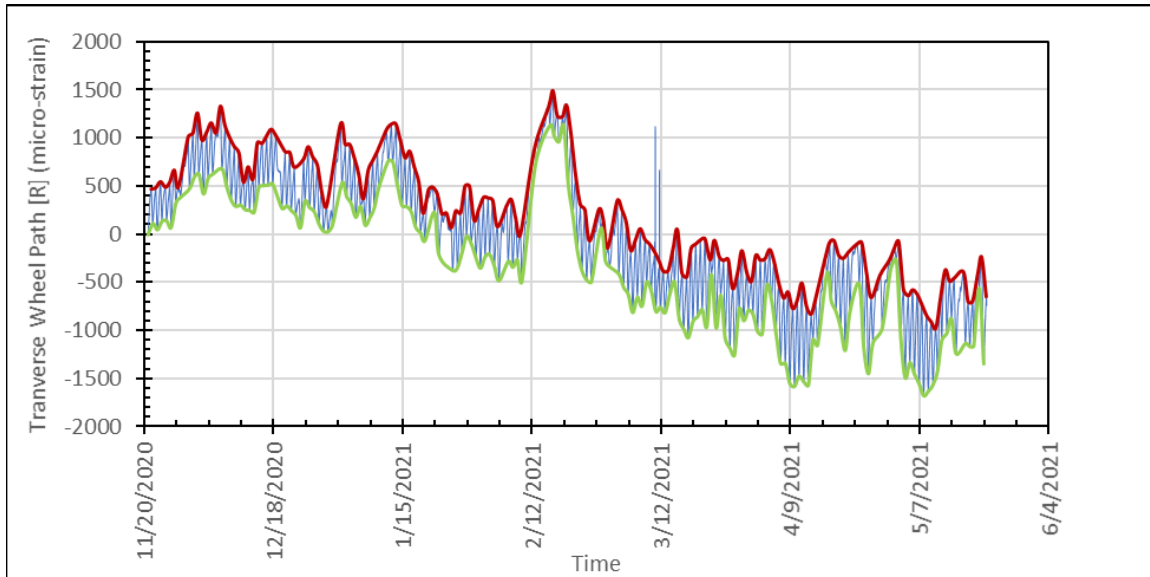
Figure 138. Normalized strain with high and low curves

It can be seen from Figure 137 that the temperatures envelopes track the strain changes very closely. And it is observed that as the temperature decreases, the strain measured by the strain gauges increases (inverse relation). This aspect is more clearly seen in the plot in Figure 138.

Figure 139. Normalized strain and temperature with high and low curves for TWPR
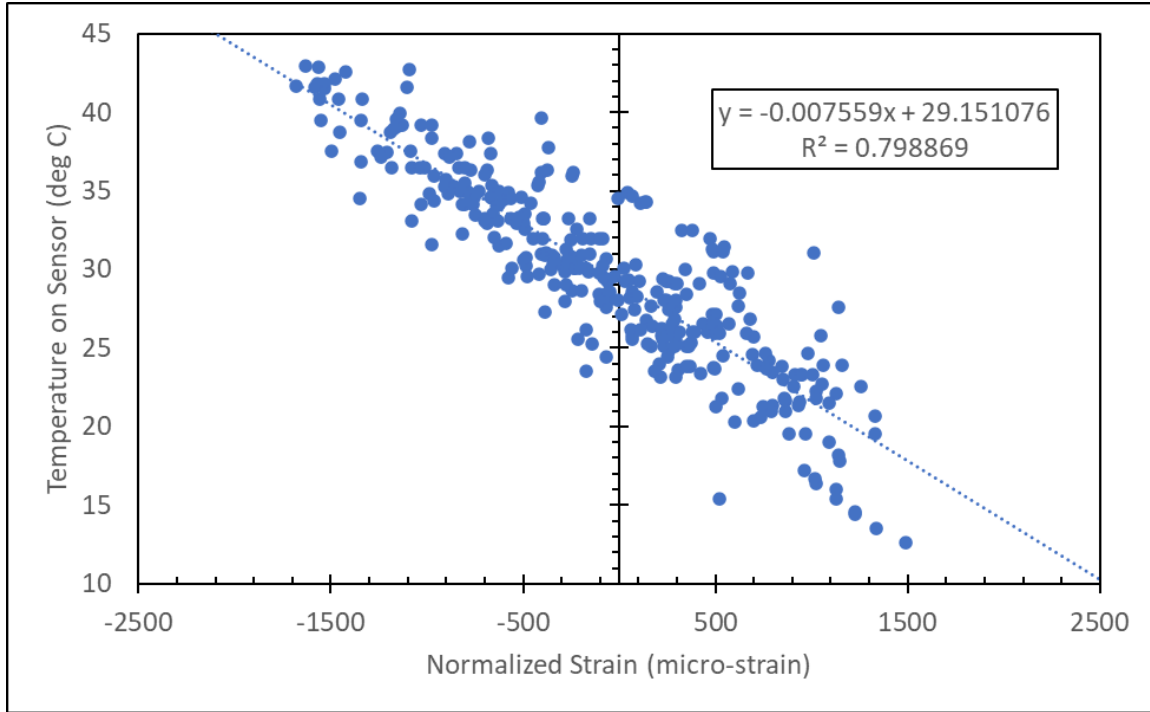
Figure 140. Normalized strain vs. temperature for TWPR

This is counterintuitive for two reasons. The sensor is a strain-bridge in the full-bridge configuration and thus is expected to be compensated for temperature changes. With the increase in temperature, the asphalt layer is expected to expand and thus resulting in increased tension on the strain gauge (increase in strain). However, it is observed that the strain measured from the strain gauge decreases with increase in temperature. This can be explained as follows.

- The ASG's cell material (the block that strains and to which the four resistive strain gauges are attached) is made of Nylon 66 polymer.

- Nylon 66 has a coefficient of thermal expansion and contraction of ~ 90 x 10^{-6} / °C.

- The coefficient of thermal expansion and contraction of HMA is expected to be from 20 x 10^{-6} / °C to 60 x 10^{-6} / °C.

- Since the Nylon 66 has a higher coefficient than the HMA, when a composite of Nylon66 – HMA is subjected to an increase in temperature, the Nylon66 would try to expand more than the HMA.

- Because the material is a composite and cannot undergo two different strains, the net result would be that the HMA would be subjected to tension (resulting in slightly more strain than predicted thermal strain) and the Nylon 66 would be subjected to compression (less strain than predicted thermal strain).

181

- Since the sensor is a full-bridge strain gauge and is compensated for thermal strains in the Nylon 66 cell, the only measured strain is the compression on the cell due to differential straining of HMA and the cell. Thus, an increase in temperature causes a decrease in tensile strains.

Figure 139 to Figure 142 show the final plots from the above analysis on the other four ASG installed in this section. In all these plots it can be observed that the strains track the temperature changes very closely. This behavior is expected to deviate as the accumulation of strains due to vehicular traffic becomes significant enough when compared to thermal strains. At this point (seven months of data collected), the majority of strains observed appear to be thermal strains only. The process of decoupling this thermal strain from the traffic-induced strains requires more data.
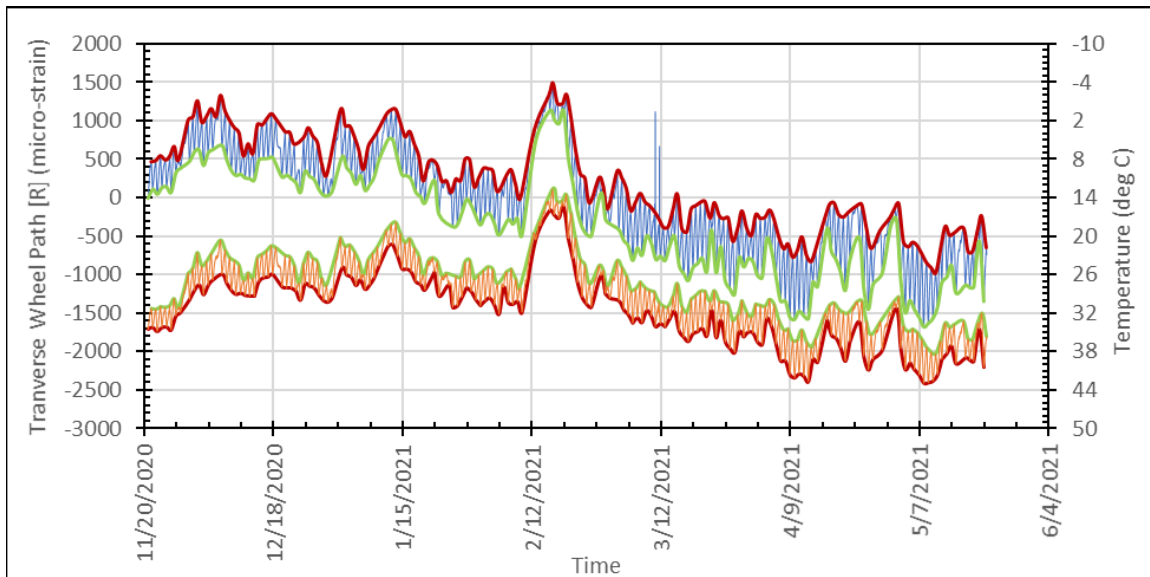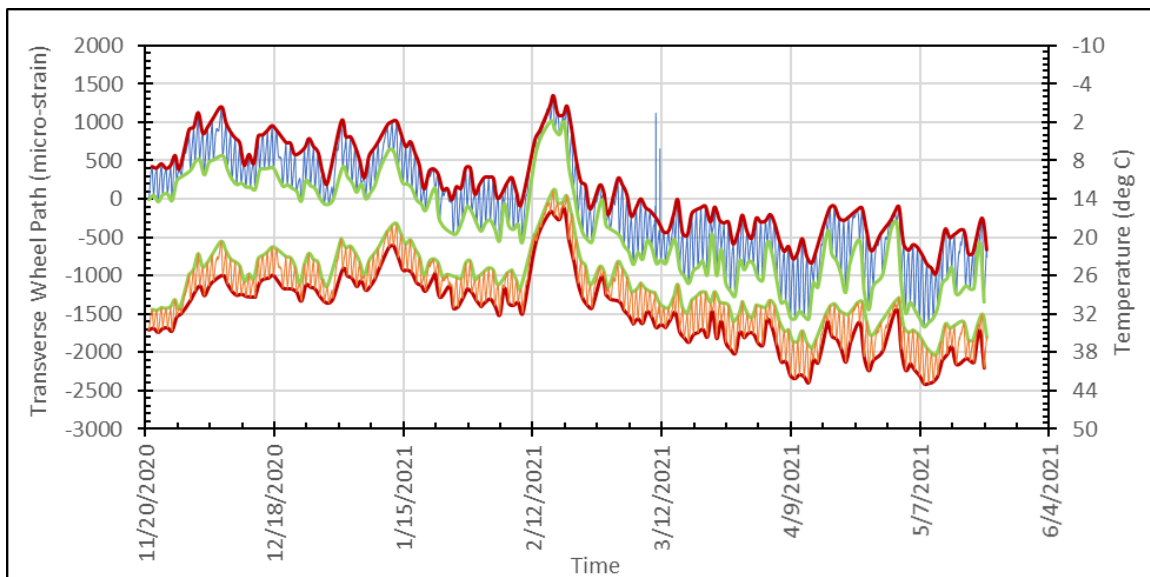

Figure 141. Normalized strain and temperature with high and low curves for TWPR
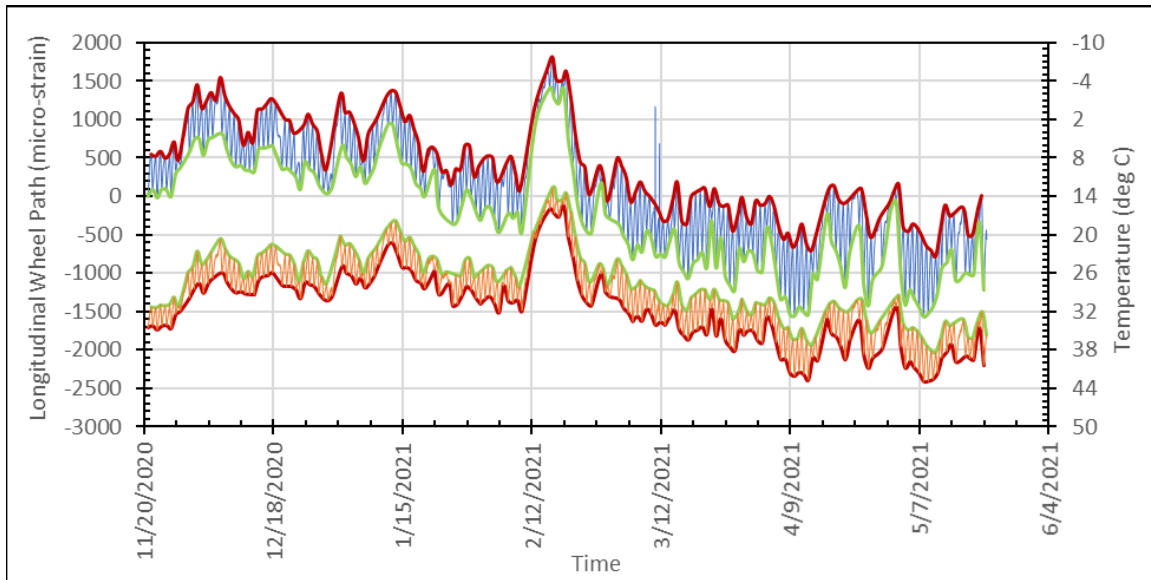
Figure 142. Normalized strain and temperature with high and low curves for LWP
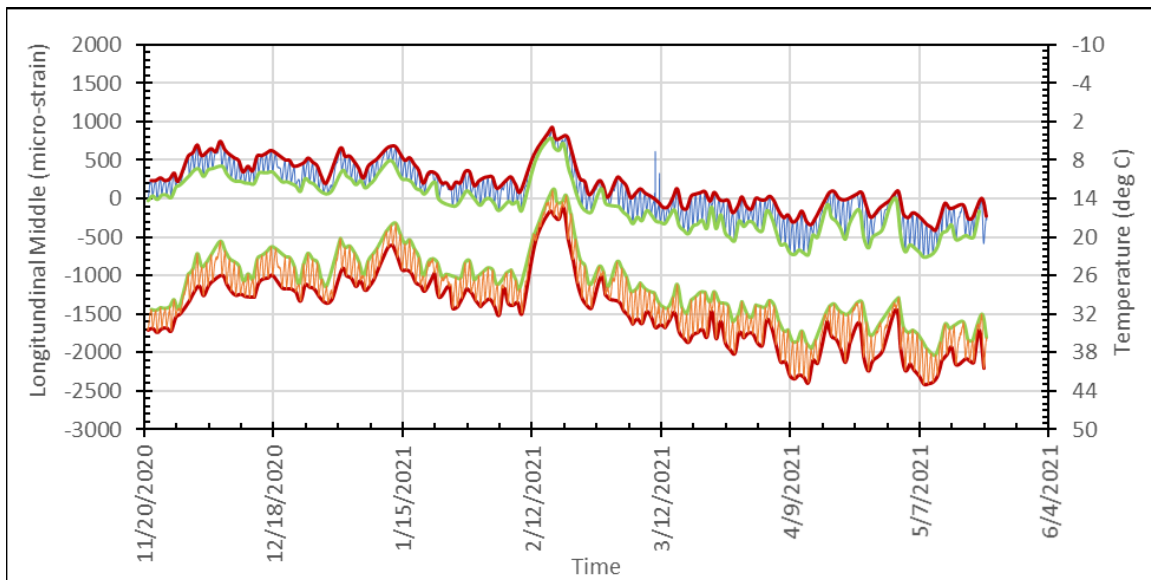
Figure 143. Normalized strain and temperature with high and low curves for LM

183
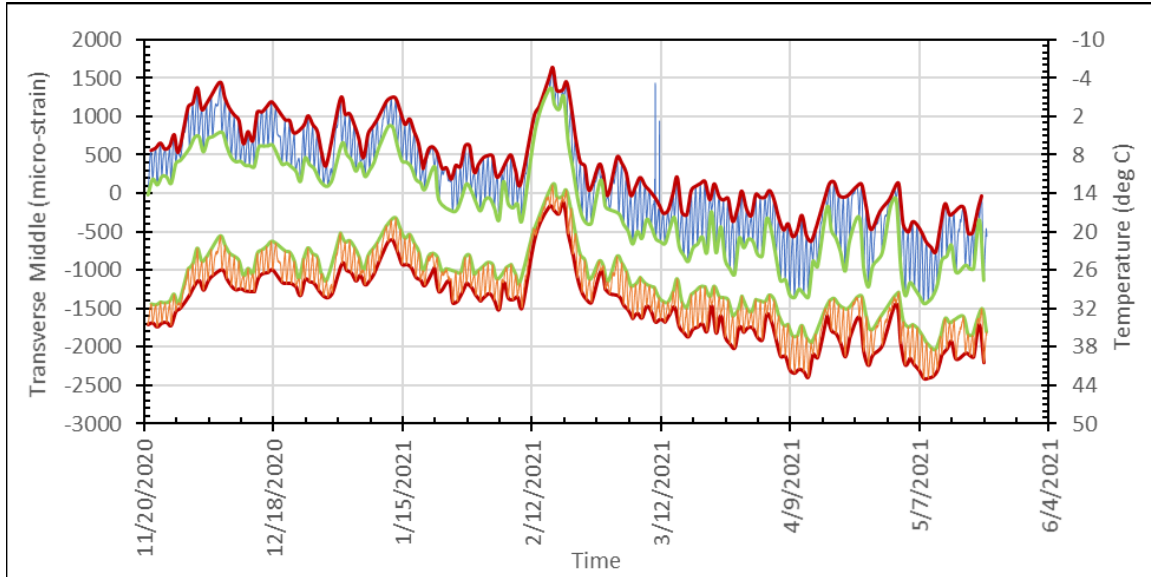
Figure 144. Normalized strain and temperature with high and low curves for TM

7.3.2. Linear Potentiometers in Section 1B

Figure 143 and Figure 144 show the displacement of artificial gravel particles embedded within the pavement at two levels (bottom of the base layer and at mid-depth). The particles were tied to the linear potentiometers housed on the side of the road using tell-tales. At this point, the potentiometers are picking up movement of the tell-tale wires, but the magnitude of the movement has remained quite low (fractions of 1 mm). It is expected to see increased movement as larger permanent deformations are mobilized within the pavement structure as the pavement is trafficked over its design life.
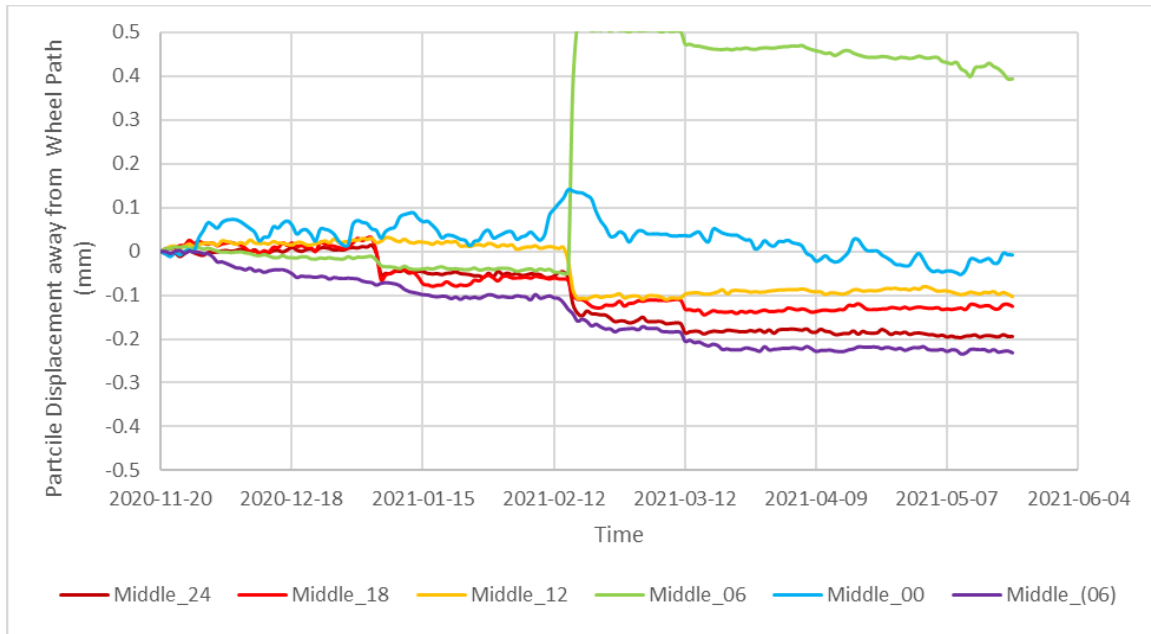
Figure 145. Particle displacements at mid-depth within base layer
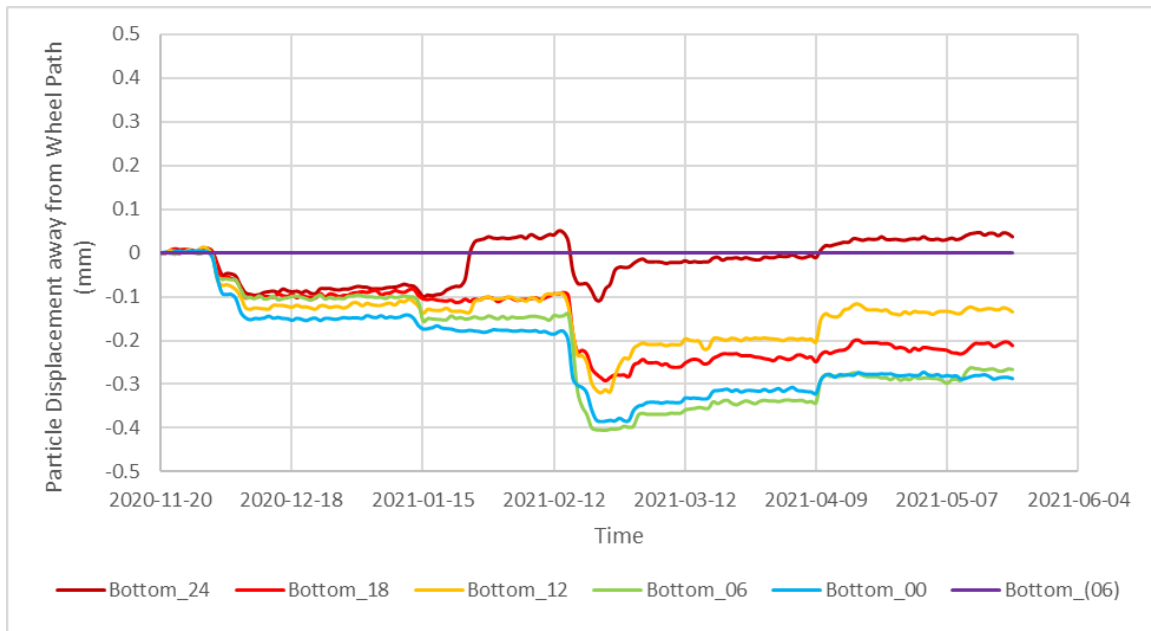
Figure 146. Particle displacements at bottom of base layer

7.3.3. Soil Extensometers across All Test Sections

Soil extensometers are displacement transducers that work with vibrating wire technology used to measure soil displacements/strains within earth structures such as embankments. The research team adopted this instrument to measure lateral displacement and strain in the base layer of the pavement in various test sections. Specifically, these sensors were embedded within the pavement structure at the top of the base layer above the geogrids (Figure 145). Thus, they measure the soil displacement just above the location of the geogrid. These sensors have a gauge

length of 24 inches. Thus, a 24 mils displacement of the flanges would correspond to 1000 micro-strains.
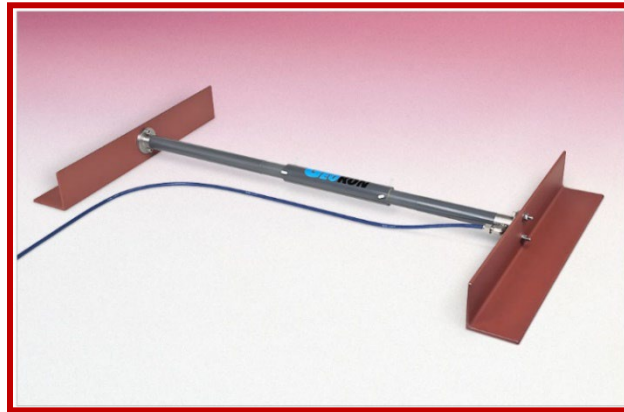
Figure 147. Soil extensometer to measure soil displacement at bottom of base layer

7.3.3.1. Section 1A

The soil extensometers in the control sections (sections 1a and 1b) were installed along the outer wheel path and between the wheel path as well as along the Transverse (T) and Longitudinal (L) directions to measure horizontal displacements in the base layer. Figure 146 presents the plan layout of the soil extensometers installed at the control section. The original plan was to install the sensor DC_WP_T centered over the wheel path with the relative locations of the other sensors being the same. However, a surveying error resulted in all sensors moving toward the outer curb by 6 to 9 inches. This results in the theoretical wheel path running over the sensor in an asymmetrical fashion are shown in Figure 146.

Figure 147 shows the tensile displacement of the flanges of the soil extensometers installed in section 1a. The four curves represent the movement observed in the four soil extensometers in this section.

Maximum movement is registered in the extensometer installed next to the wheel path (daisy-chained), DC_BWP_T. This is contrary to the expectation that the largest movement occurs under the loaded area. It is hypothesized that while the theoretical wheel path still cuts across the DC_WP_T sensor, the actual wheel path (where most traffic travels) may have moved slightly toward the center of the road due to accumulation of debris from the compost plant closer to the outer curb. This lane is also wider than the theoretical one (14 ft instead of 12 ft). This shift in wheel path 1 may have resulted in sensor DC_BWP_T showing greater strains than DC_WP_T.
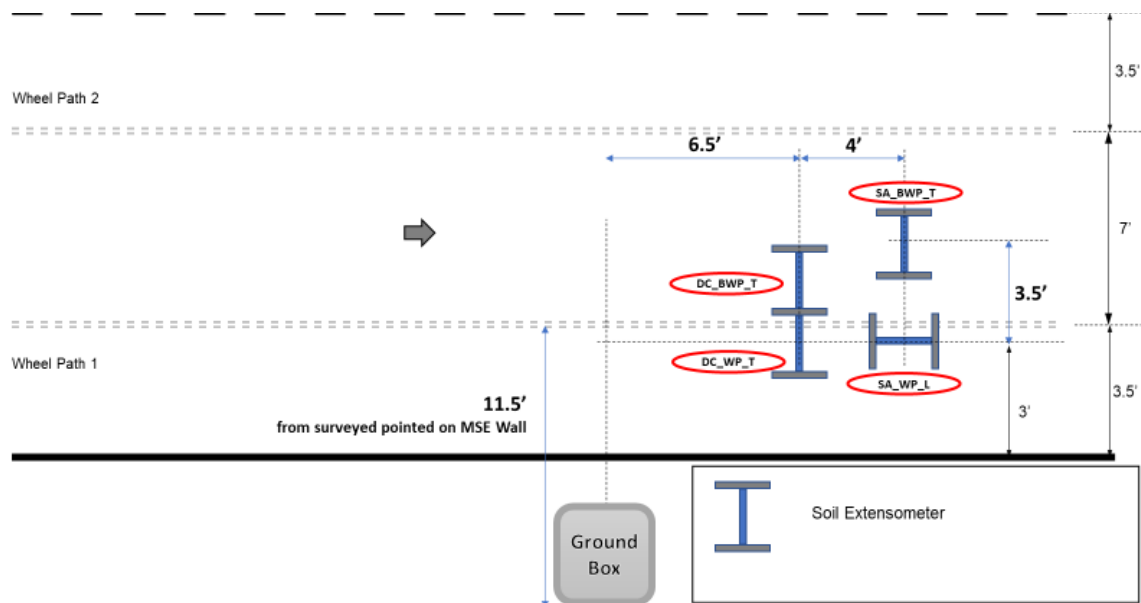
Figure 148. Locations of soil extensometers in control section 1a

Following this is the movement recorded by the sensor placed in the middle of the pavement section. This sensor is usually expected to produce a compressive response, had the sensor ended up being in the middle between the two wheel paths. However, with the actual shift in the location of the sensors and the hypothesized shift in the location of the wheel paths, the inner wheel path may have ended too far away to influence the sensor SA_BWP_T. This results in a possible compressive response. Longer data acquisition may be required to confirm this hypothesis.

The least movement (almost zero) is observed in the sensor installed in the longitudinal direction along the wheel path. This is also consistent with the expectations since the movement in the longitudinal direction is expected to average out to zero over long periods of time.

Another point of consistency would be the order of magnitude of displacements observed from Figure 143 and Figure 144. The data presented in Figure 147 has a greater range than the displacement data from LP. So, a comparison must be made in the appropriate date ranges (Nov 2020 to May 2021).

Figure 149. Tensile strains at bottom of base layer in section 1a

7.3.3.2. Section 1B

Figure 148 presents the plan layout of the soil extensometers installed at the control section 1b.
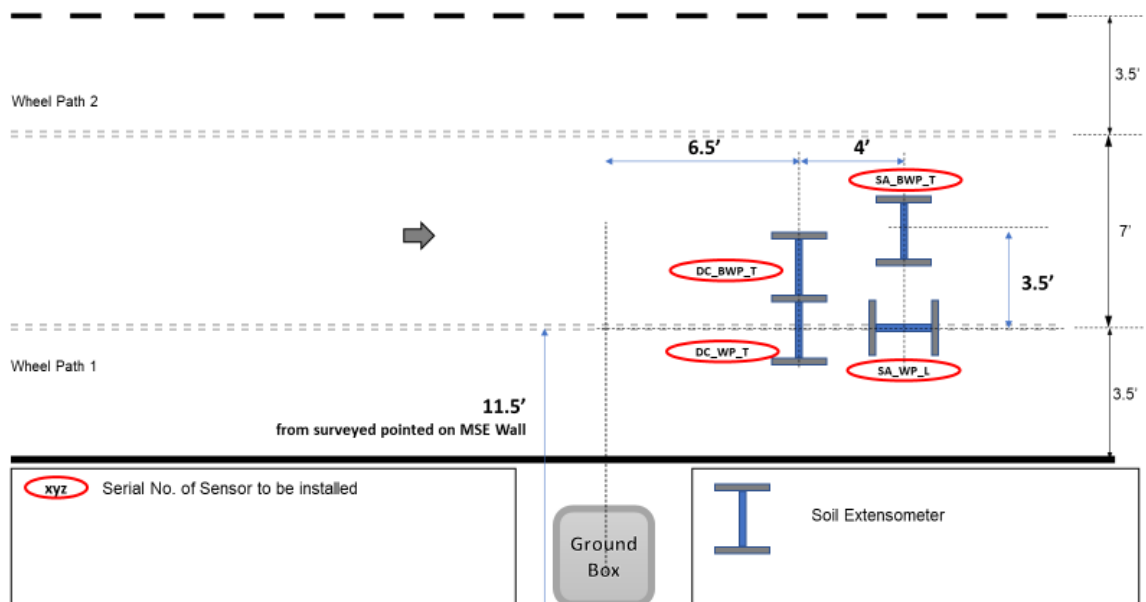
Figure 150. Locations of soil extensometers in control section 1b

Figure 149 shows the tensile displacement of the flanges of the soil extensometers installed in section 1b. The four curves represent the movement observed in the four soil extensometers in this section.

Maximum movement is registered in the extensometer installed within the wheel path. This is consistent with the expectation of largest movement under the loaded area. This is followed by the sensor that is closest to the wheel path (daisy-chained to the first sensor). Since both the

sensors are showing tensile strains, it further supports the hypothesis of the actual wheel paths shifting closer to the center of the road, but still within the DC_WP_T sensor's flanges.

Following this is minimal movement in the compressive direction recorded by the sensor placed in the middle of the pavement section. Since the sensors were installed at the theoretical wheel path (and not off as the case was in 1a), even with the wheel paths being off, the actual wheel path 2 would end up being close enough to the inner flange of SA_BWP_T pushing it inward, resulting in compressive strains.

The least movement (almost zero) is observed in the sensor installed in the longitudinal direction along the wheel path. This is also consistent with the expectations since the movement in the longitudinal direction is expected to average out to zero over long periods of time.
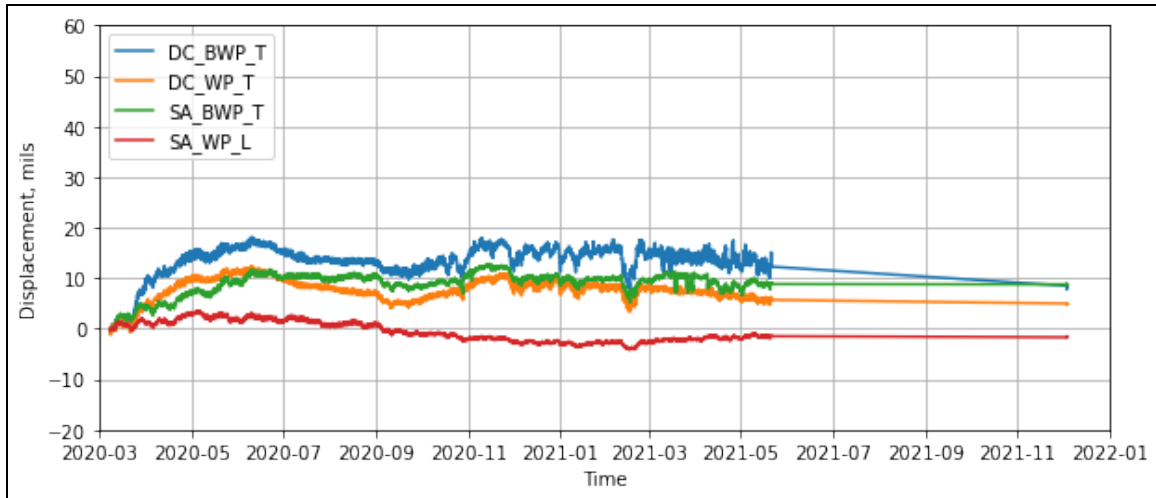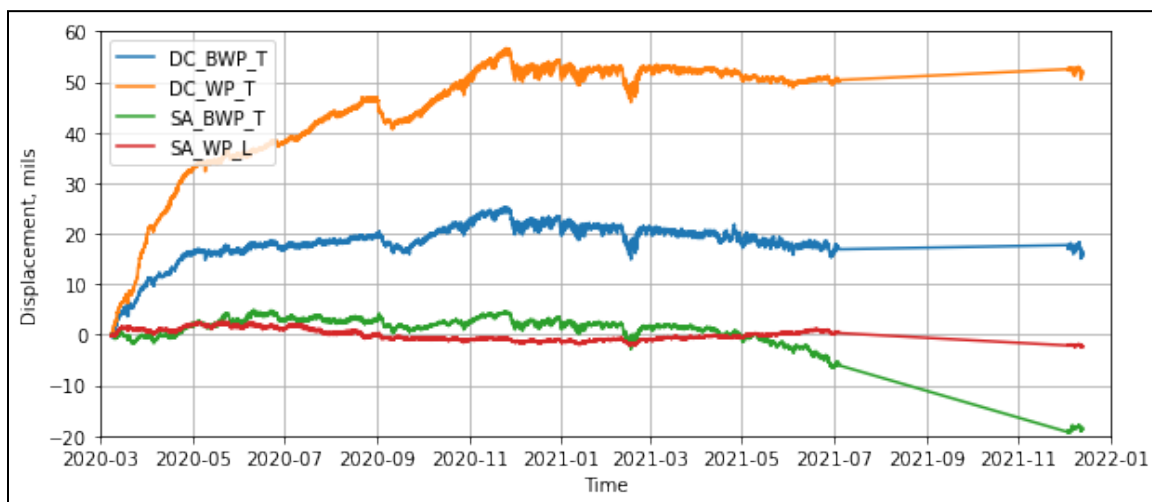

Figure 151. Tensile strains at bottom of base layer in section 1b

7.3.3.2.1. Sections 2, 3 and 4

Figure 150 presents the plan layout of the soil extensometers installed at sections 2, 3 and 4. As can be seen from the figure, only the daisy-chained sensors along the wheel path and adjacent to it are installed. The stand-alone sensors were not included in these stabilized sections.

Figure 151 to Figure 153 show the tensile displacement of the flanges of the soil extensometers installed in sections 2, 3 and 4. The two curves in each figure represent the movement observed in the two soil extensometers in the corresponding sections. Since these sensors were installed at the correct locations, it can be seen that the larger strain occurs under the loaded area similar to section 1b, followed by the off-wheel path sensor. Thus, sections 1b, 2, 3 and 4 are identical in all aspects except for the presence/absence of geogrids for stabilization. Consequently, they are directly comparable as shown in the following section.
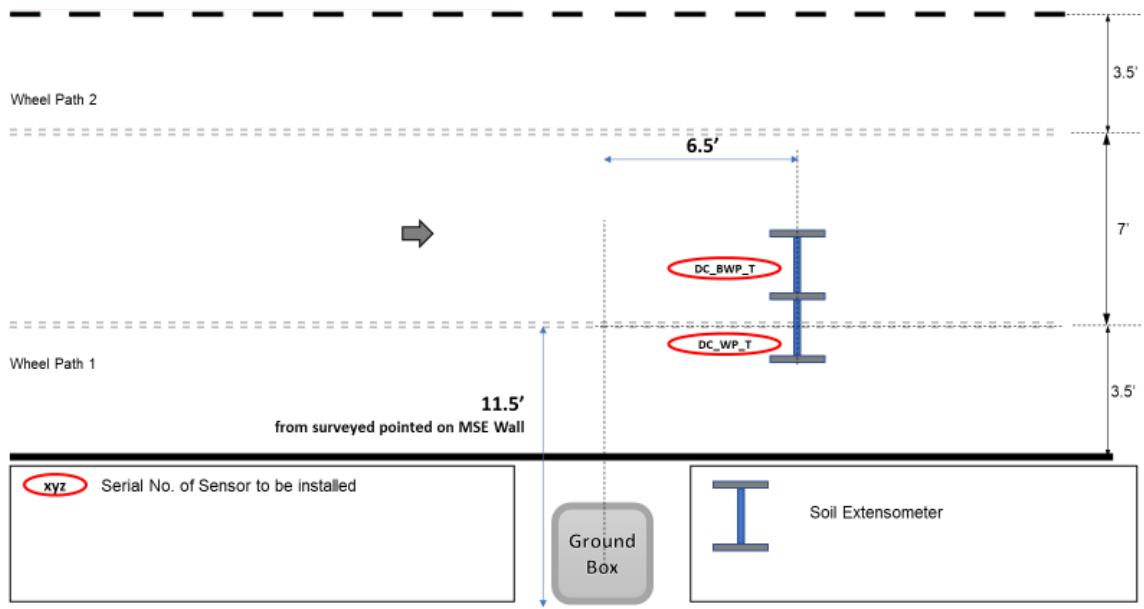
Figure 152. Locations of soil extensometers in sections 2, 3 and 4
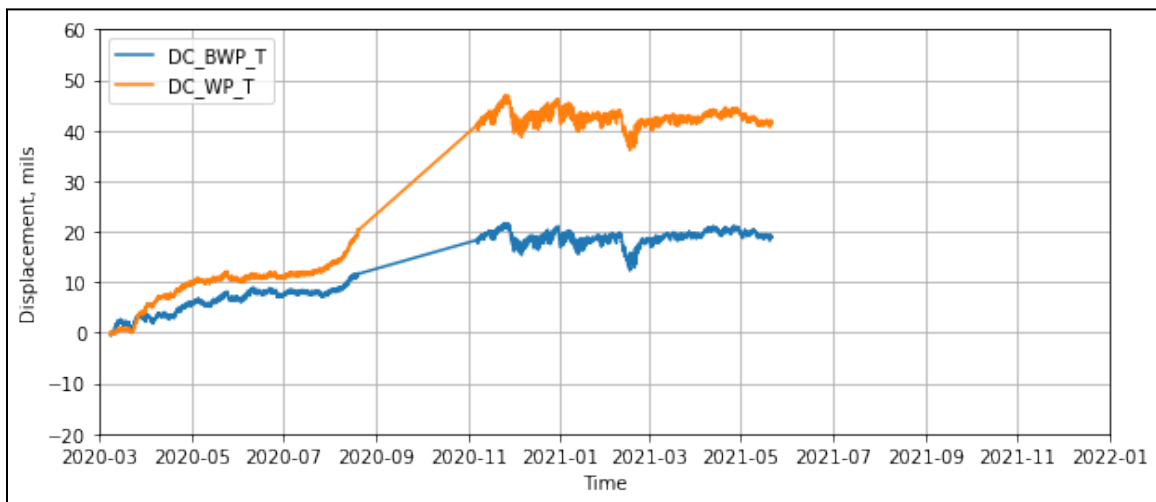
Figure 153. Tensile strains at bottom of base layer in section 2
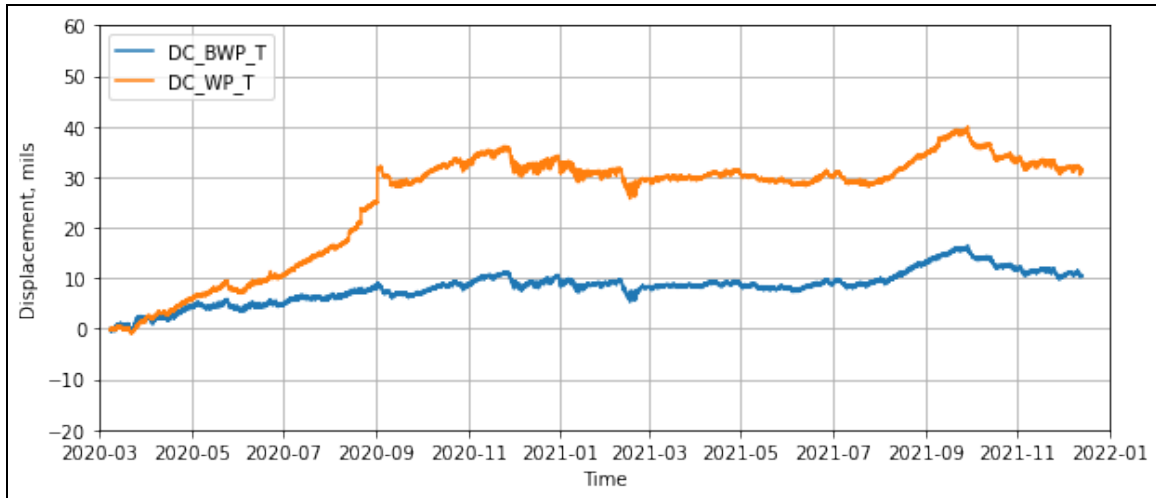
Figure 154. Tensile strains at bottom of base layer in section 3
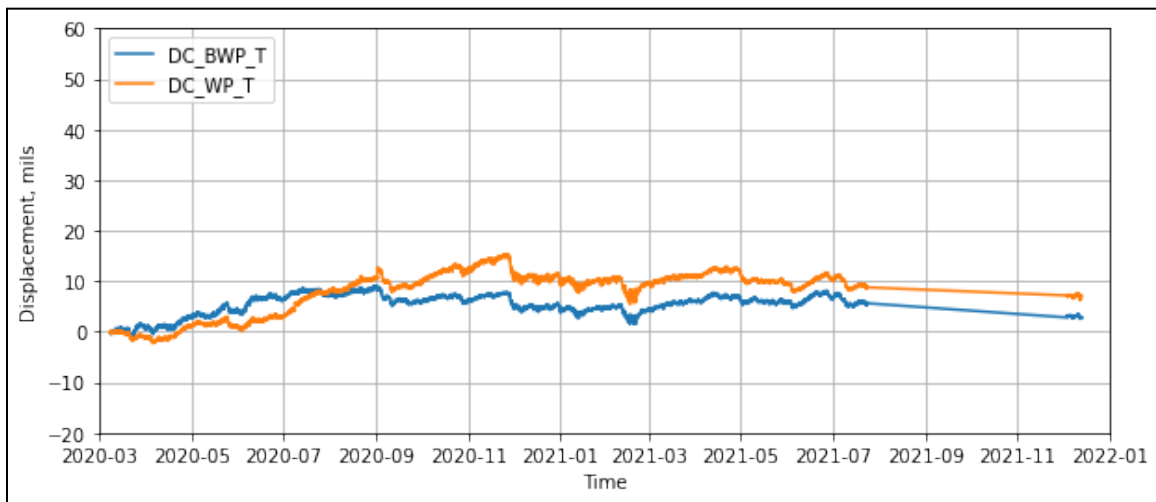
Figure 155. Tensile strains at bottom of base layer in section 4

7.3.3.2.2. Comparisons

As discussed in the previous section, the readings from sections 1b, 2, 3 and 4 are directly comparable with each other, whereas section 1a requires a correction to account for the misalignment of the sensors. This correction was not determined and requires further analysis of the data collected. The subsequent comparisons are limited to sections 1b, 2, 3 and 4.

Figure 154 compares the tensile strains under the wheel path in the control and stabilized sections. There are gaps in data collection due to data logger failure issues. These are battery powered data-loggers. Newer data collection protocol with more frequent collection has been initiated to prevent any future data losses. The control section shows higher strain under the wheel path than all three stabilized sections. Thus, the inclusion of a geogrid within the pavement structure seems to reduce the tensile strains developed in the base layer in the vicinity of the location of the geogrid by 20% to 70%. Most of the tensile strains occur in the immediate

191

months after construction. The initial increase in strain is suspected to be due to construction traffic on the unpaved outer lane, excavation of the inner lane (with some public traffic) and construction of the inner lane. It is hypothesized that the traffic-induced tensile strains are limited at this point in time, owing to a thick pavement section. However, even the strains induced in the construction phase of the roadway have been well-mitigated by the geogrid, which have reduced the lateral expansion of the base layer (this is what we call lateral restraint). Continued long-term monitoring of the pavement section, as the road degrades, will help capture the traffic-induced lateral strains in the various sections.
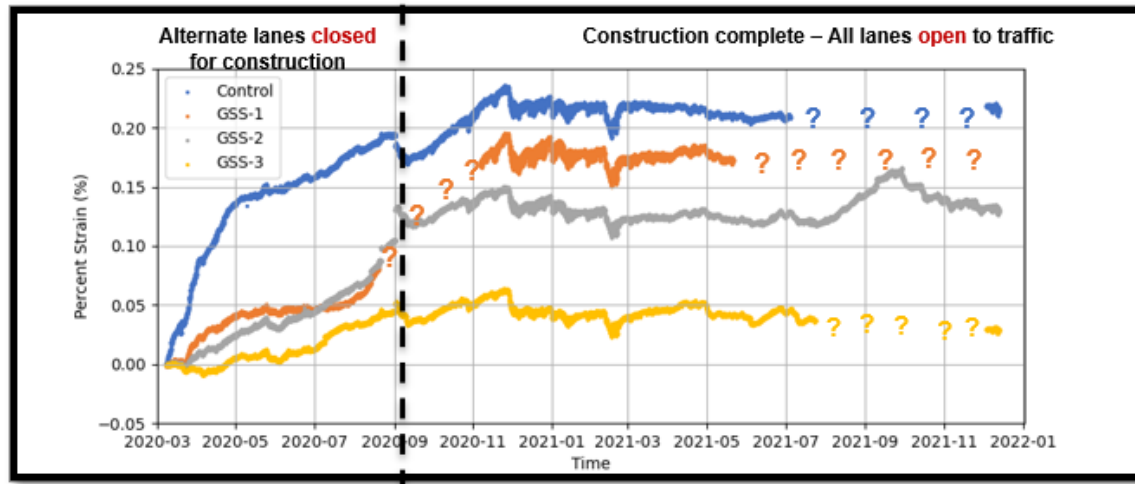
Figure 156. Tensile strains under the wheel path at bottom of base layer

Figure 155 compares the tensile strains 24 in from the wheel path in the control and stabilized sections. Compared with Figure 154, it is clear that maximum tensile strains occur under the wheel path or close to it. Two ft (24 in) inward from the wheel path, the tensile strains are much lower, internally consistent in that the control section shows larger strains than the stabilized sections. It is important to note that most of the deformation takes place in the initial construction period before the road opens (late Aug 2020). Thus, the strains measured are unlikely to be traffic-induced. However, it still demonstrates restrained movement of particles in stabilized sections under construction, excavation of adjacent lane, etc. Continued monitoring of the sections for longer periods of time to see how they respond to traffic loads is critical to understanding the lateral restraint provided by the three grids. The performance of the various sections can be observed to be similar to the sensors under the wheel path but with reduced magnitude. The stabilized sections outperform the control by 5 to 20%. The reduction in improvement may be due to the redistribution of strains by the geogrids.
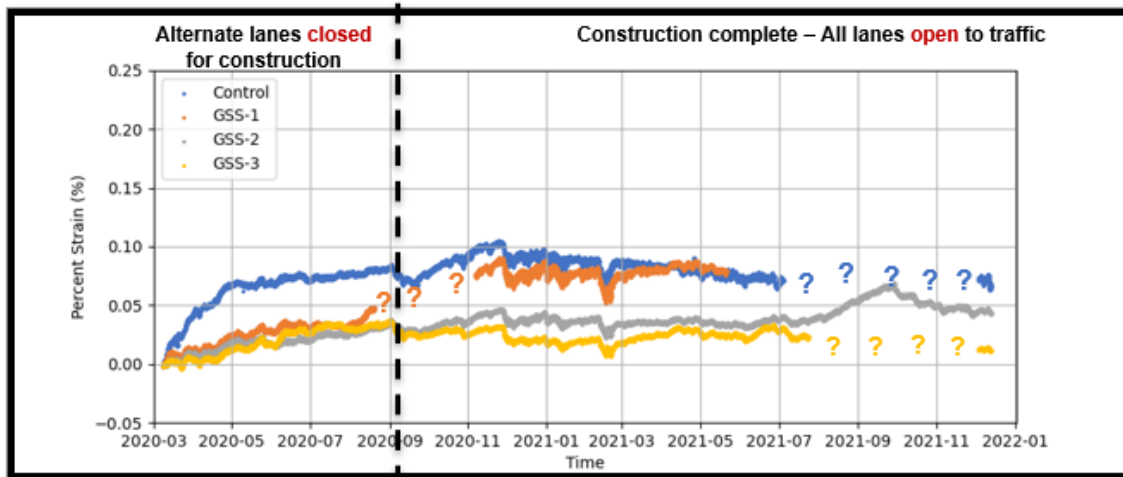
Figure 157. Tensile strains 24 in from the wheel path at bottom of base layer

7.3.3.3. Lessons Learned from Soil Extensometers

- The inclusion of a geogrid within the pavement structure reduced lateral tensile strain development within the base layer under the wheel path (20% - 70%) and adjacent (5% - 55%) to it.

- Reductions in lateral tensile strains are understood to be due to the **lateral restraint** provided by the geogrids.

- The reduced lateral strains are a direct indicator of lower vertical strains, which in turn indicates reduced rutting. Thus, reduced lateral strains due to geogrid inclusion are expected to result in a **reduction in rutting** of stabilized layers.

- This same mechanism of restricted lateral movement of base particles is understood to **prevent modulus degradation**, resulting in higher moduli of stabilized sections (as seen from FWD results in Section 7.2.5)

- These effects are expected to provide increased benefits with time as higher tensions are mobilized in the geogrid. Thus, continued monitoring of the installed sensors and testing of test sections is important in quantifying these benefits.

7.3.4. Moisture Sensors

In this section, a brief analysis has been done to summarize the behavior of Time Domain Reflectometers (TDR) to estimate the volumetric water content of the soils in the different test sections.

Time domain reflectometers measure the dielectric constant of soils, ε, and thus infer from it the Volumetric Water Content (VWC), θ. The equation used to calculate the dielectric constant is shown in Equation (5).

$$V = \frac{c}{\sqrt{\varepsilon}} \rightarrow \varepsilon = \left(\frac{ct}{2L}\right)^2 \qquad (5)$$

7.3.4.1. TDR

The TDR used for this project were models TDR-310S and TDR-305S obtained from Acclima with probe lengths of 3.9 in and 2 in, respectively. An image of a model TDR-310S is presented in Figure 156.

Figure 158. Model TDR-310S from Acclima

7.3.4.1.1. Functionality of TDR

The middle probe of a three-probe TDR sends a wave that is received by the other two shield probes and is then reflected to return to the middle probe. The wave received carries information about the dielectric constant of the soil matrix between the probes. According to equation (5), the dielectric constant is calculated based on two times the length of the probe, and this is because the wave is sent then received for a specific time, t. The waves are sometimes not received due to high salinity or high temperature in the soil, both of which affect the wave received.

In addition to moisture content data, TDR provide information on the electric conductivity of the soil matrix, EC_{bulk}, and thus on soil salinity as well, as the two are linked. The sensors also provide the soil temperature.

7.3.4.1.2. Data Received from TDR

The TDR were programmed to collect data every hour via a data logger obtained from Acclima (model SDI-12 Sensor Reader) pictured in Figure 157. A total of 104 moisture sensors were installed, divided among five sections and placed in a grid. The sensors were installed in the inner and outer lanes, the latter of which has a retaining wall where lower VWC is expected.

Figure 159. TDR installed in section 2 and connected to data logger

Unfortunately, not all sensors were responsive after installation. Only 68 sensors were found to be responsive to the data logger, which was confirmed during the first loading campaign conducted on October 21, 2020, when data from these sensors was extracted. Thereafter, the team visited the IH-10 site every six to 12 months to collect data and reconfirm the responsiveness of the sensors.

In Figure 158, a full timeline of the VWC for all sensors is displayed through March 2022, when the final data collection occurred. Precipitation data is plotted on the second y-axis to give a sense of the VWC measured by the sensors.
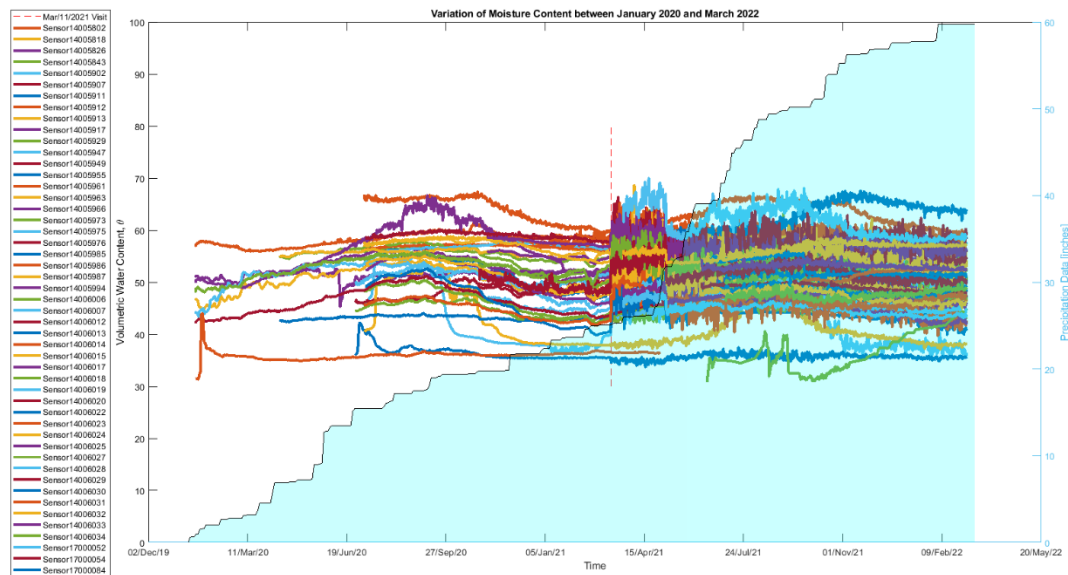
Figure 160. Corrected moisture data for all sensors plotted against precipitation

7.3.4.1.3. Analysis of Moisture Data

Since data from all sensors was collected hourly, data analysis and plotting in Excel would prove difficult. Consequently, a MATLAB script was created to sort, manage and plot moisture data for a better analysis with respect to various parameters like time and temperature.

7.3.4.1.4. Inner vs. Outer Lane

Figure 159 and Figure 160 present plots of VWC against time, VWC against temperature and bulk Electric Conductivity (EC) against temperature for an outer and inner lane sensor, respectively. The second and third plots are displayed with a timeline color map to better understand the data with time. In Figure 159, VWC dropped more significantly than in Figure 160 because of the retaining wall near the outer lane, which provided a drainage path for the group of sensors in the outer lane. The inner lane sensors exhibited fewer fluctuations due to less drainage access.

The fluctuation in VWC with temperature is also presented with time, where it clearly shows how the VWC varied with seasons.

The third graph represents the bulk EC with temperature. This is a very broad topic requiring further analysis in a separate study to determine the effect of salinity on measurements of bulk EC with temperature. For the purposes of this report, the bulk EC should be as linear as possible when plotted against temperature. Hysteresis cycles are an indication of high soil salinity.

196
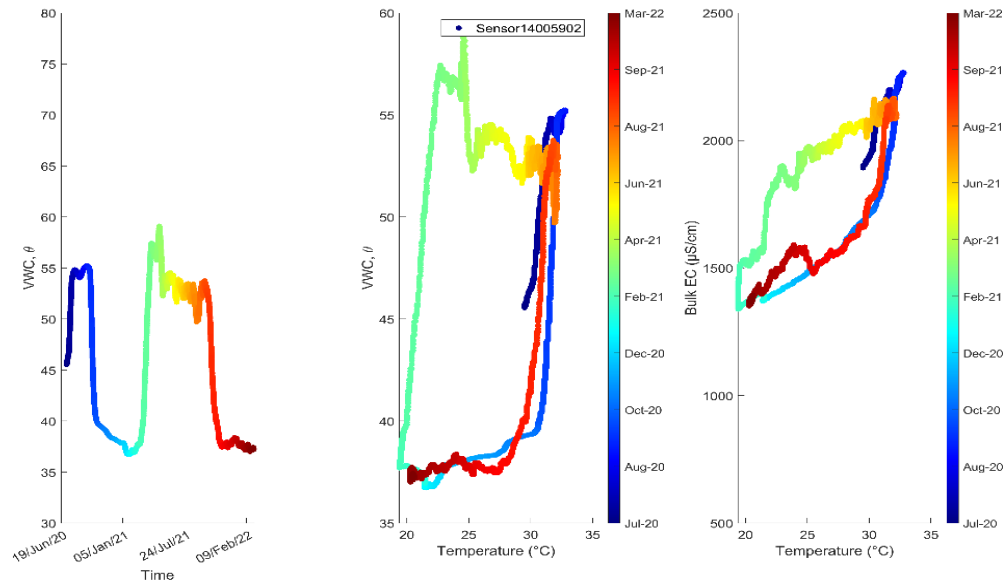
Figure 161. Plots of: (a) VWC vs. time; (b) VWC vs. temperature; and (c) EC_{bulk} vs. temperature for an outer lane sensor
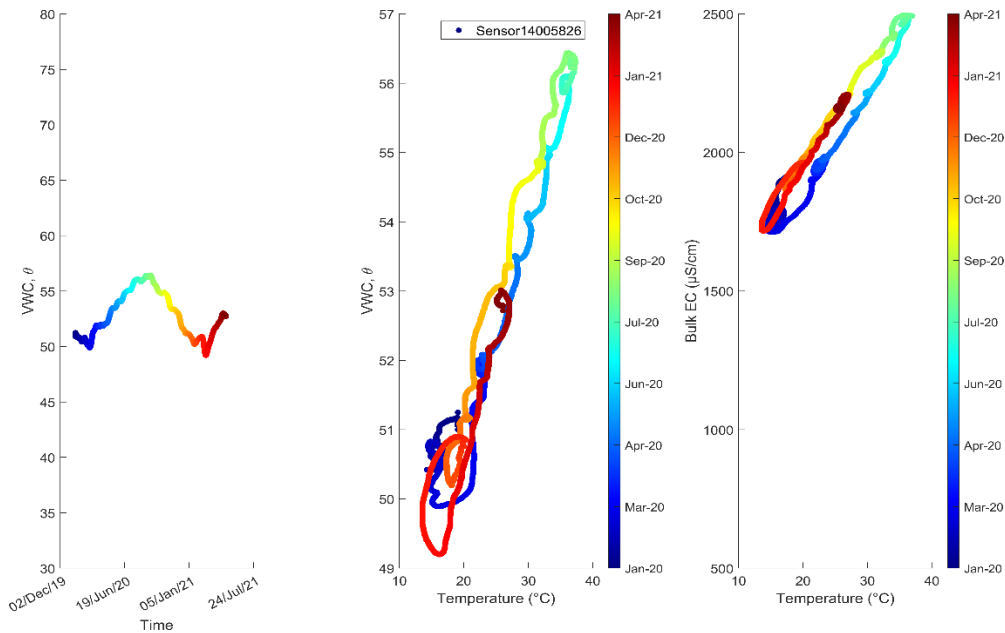
Figure 162. Plots of: (a) VWC vs. time; (b) VWC vs. temperature; and (c) EC_{bulk} vs. temperature for an inner lane sensor

7.3.4.1.5. Shallow vs. Deep Sensors

In an attempt also to compare the output of shallow sensors (0.83 ft) with sensors installed at a deeper level (6 ft), Figure 161 and Figure 162 show the difference in VWC with time for two

197

sensors installed at these depths, respectively. More fluctuation and a higher overall VWC was observed for the deeper sensor, while the shallower sensor exhibited a more fluctuant response and lower overall VWC.
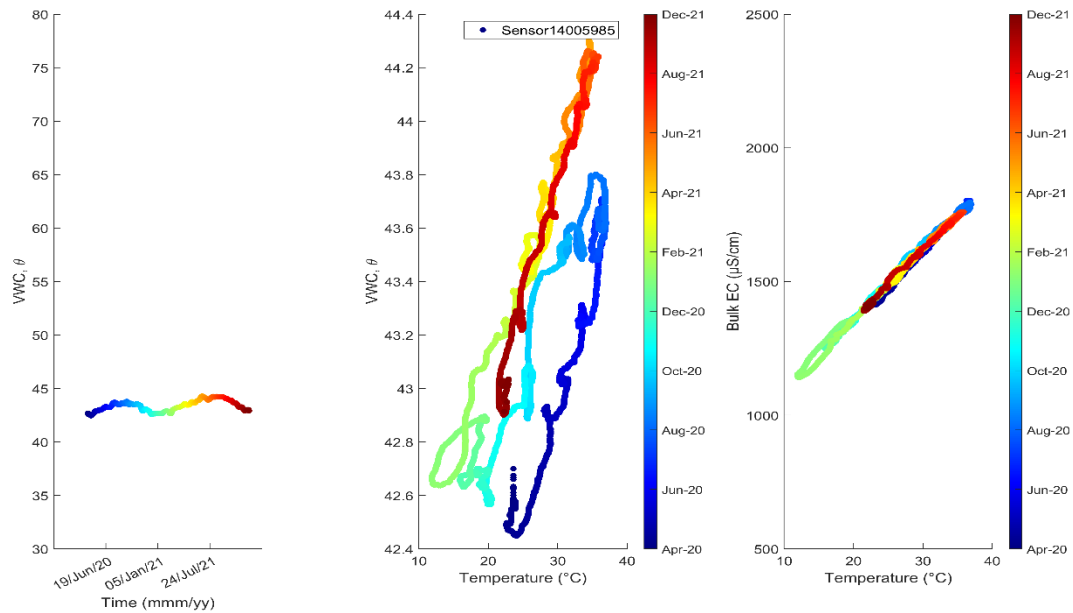
Figure 163. Shallow installed sensor
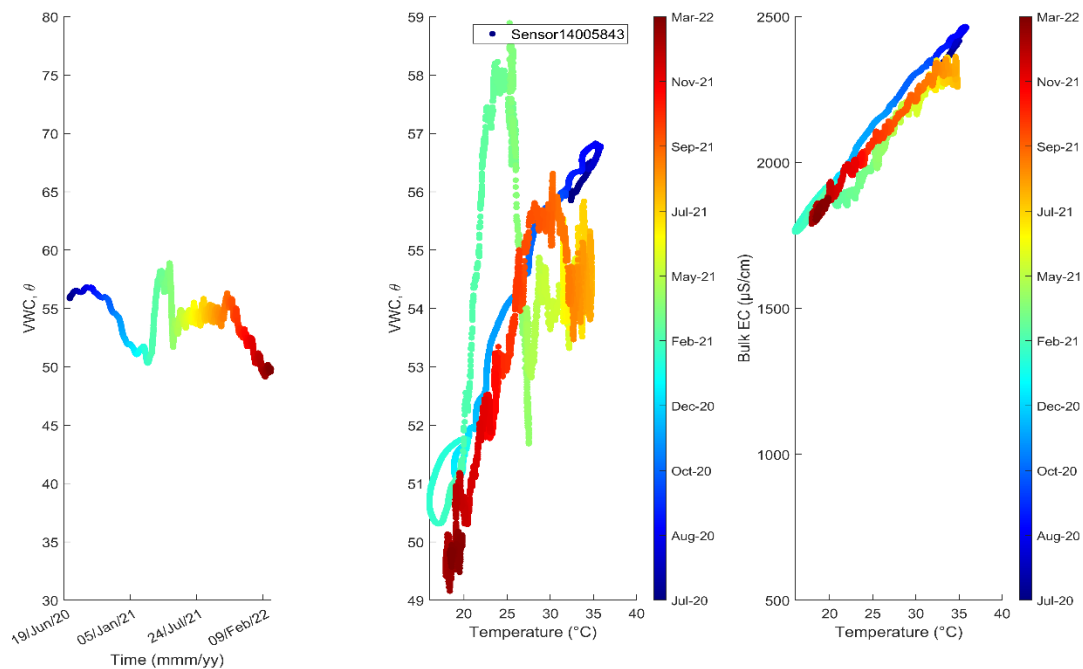
Figure 164. Deep installed sensor

7.4. Characterization of Dynamic Response during Loading Campaigns

7.4.1. ASG under Trafficking

The trafficking of the instrumented sections was undertaken as described in Chapter 5. Figure 163 shows the location of ASG in each of the instrumented test sections. A total of five ASG have been installed to measure the strain at the various locations in both transverse and longitudinal orientations. There are three sensors located along the theoretical wheel path: two are oriented in the transverse direction and referred to as Transverse Wheel Path Repeat (TWPR) and Transverse Wheel Path Center (TWPC); and one is oriented in the longitudinal direction and referred to as Longitudinal Wheel Path (LWP). Two sensors placed midway between the two wheel paths, in the transverse and longitudinal orientations, are referred to as Transverse Middle (TM) and Longitudinal Middle (LM).

A total of 10 passes were conducted at speeds of 25 mph with both the heavy truck and light car. In the section below, the results of these 10 passes at speed under the heavy truck (with three axles) are presented. Figure 164 shows the response of all 10 passes of the five sensors. As can be seen from the figures, the entire loading and unloading of all three axles occurs within a time period of 2 seconds. The time histories of strain response for the 10 passes have been corrected such that the peak from the first axle lines up at the same time (i.e., the first peak from each pass is synchronized with each other). Firstly, this allows for the inspection of the quality of the passes in terms of the magnitude of the first peak. Secondly, this allows for the inspection of the peaks from the rear wheel passes and to judge if all the passes have been conducted at more or less the same speeds.
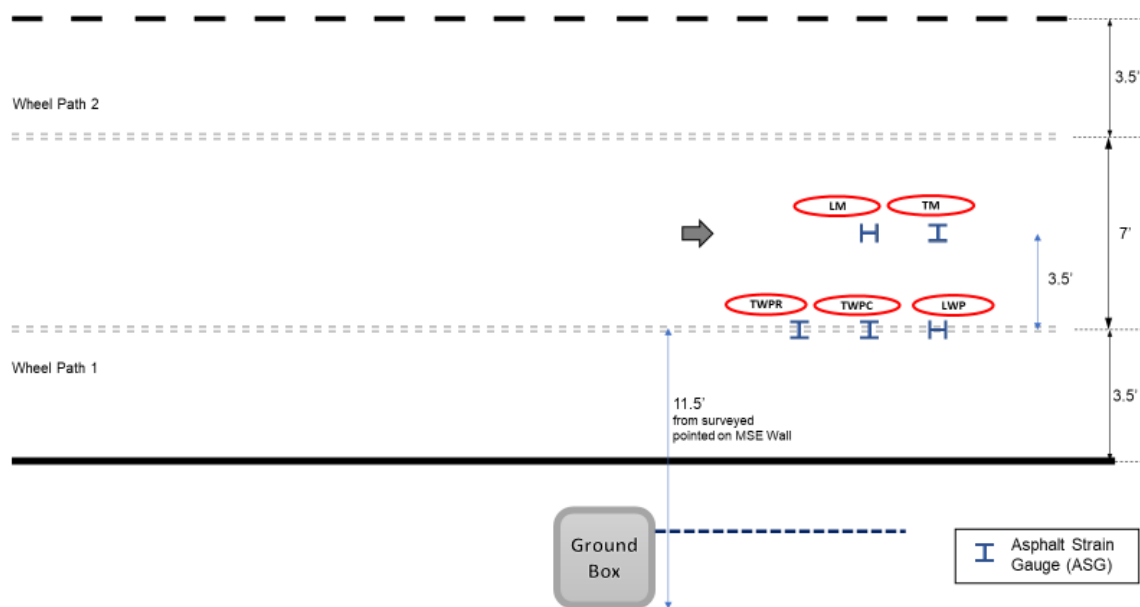
Figure 165. Location of ASG in sections 1a, 1b, 2, 3 and 4

Figure 164 (a and b) shows the response of the ASG in the wheel path measuring strains in the transverse direction (critical horizontal tensile strains). As the figure shows, owing to the spatial variability of the truck passes, each pass produces a slightly different response. Some passes have also been found to produce significantly lower responses. In such cases, GoPro videos of these passes are viewed to verify the location of the passes. If the deviation is beyond acceptable margins, the pass is omitted from further analysis. Another aspect of significance is that because the TWPR and TWPC sensors are repeats, the responses measured from both are also similar in magnitude and characteristics.

(a) **T**ransverse **W**heel **P**ath **R**epeat   (b) **T**ransverse **W**heel **P**ath **C**enter

(c) **L**ongitudinal **W**heel **P**ath

(d) **L**ongitudinal **M**iddle   (e) **T**ransverse **M**iddle
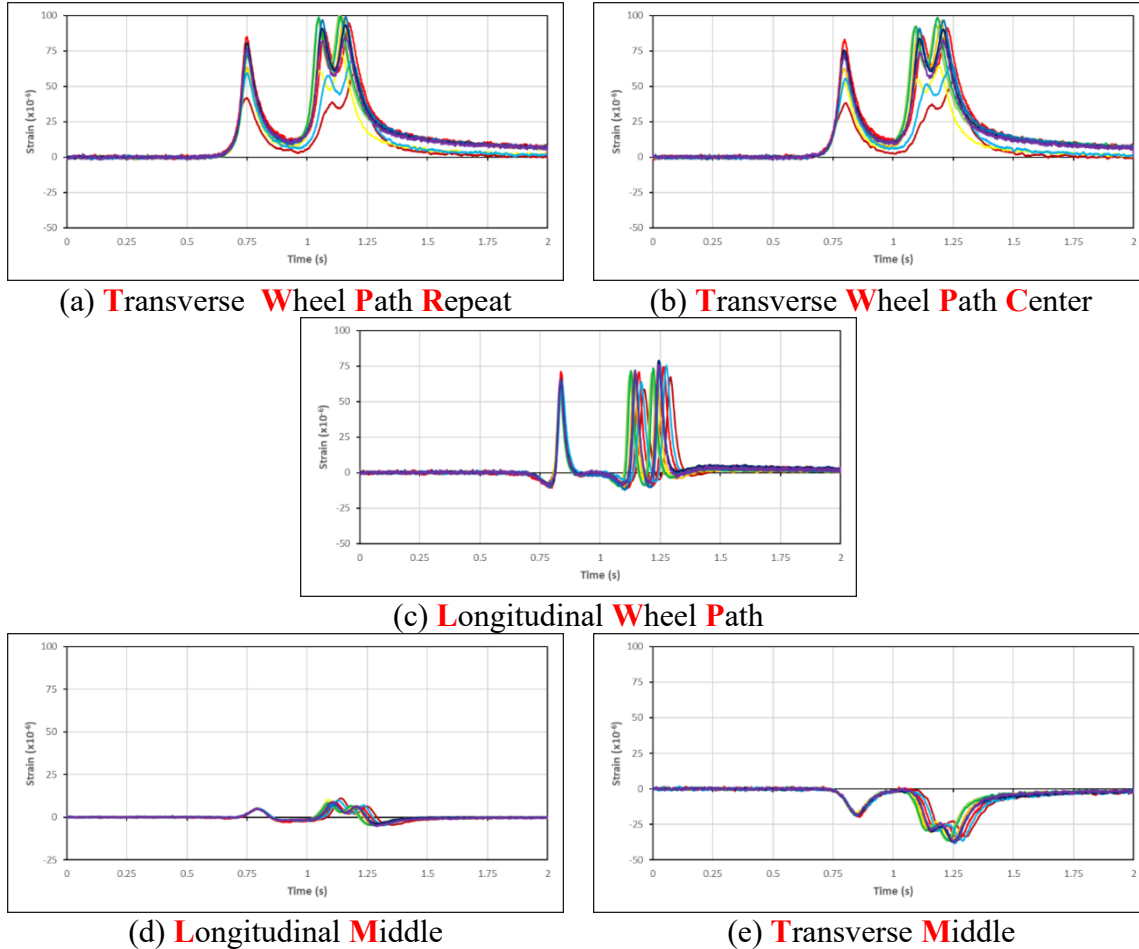
Figure 166. Response of ASG under trafficking

Figure 164c shows the response of the LWP sensor, which is much sharper than those of the TWP sensors. This is due to the transitive nature of the strains produced as the loaded axle approaches the sensor (compression), passes on top of the sensor (tension) and retreats from the sensor (compression again). This causes sharp responses and is thus more sensitive to minor variations in vehicle speed. The effect of vehicle speed is more clearly observed from the rear axle response of the LWP sensor. By contrast, the TWP sensors undergo only tension and hence the response is much smoother and less sensitive to vehicle speed.

Figure 164d and Figure 164e show the responses of the LM and TM sensors, respectively. Sensor TM is subjected to pure compression since both flanges undergo inward stresses from the two wheel loads on either side. The response of the LM sensor is similar to that observed for the corresponding sensor in the wheel path (TWPC) but with a much lower magnitude due to its distance from the two wheel paths.

In the following section, the strain values measured from the TWPC and TWPR sensors across the five sets of instrumentations are compared to establish the relative performance of the various sections.

7.4.1.1. First Loading Campaign – October 2020 – Temperature: Warm

Figure 165 shows the transverse strains in the wheel path (after filtering out the bad passes) as a box plot across four sections (stage A: 1a, 2, 3 and 4). Figure 165a shows the peak strains recorded from the three axles of the heavy truck and Figure 165b shows the peak strains recorded from the two axles of the light car. The data is limited to four rather than five sections due to the number of data acquisition systems capable of simultaneous data collection. The data from the omitted section (1b) is included in the next stage of trafficking (stage B: 1a, 1b, 2 and 3) as shown in Figure 166. All reinforced sections, except section 2, seem to perform better than the control (1a).
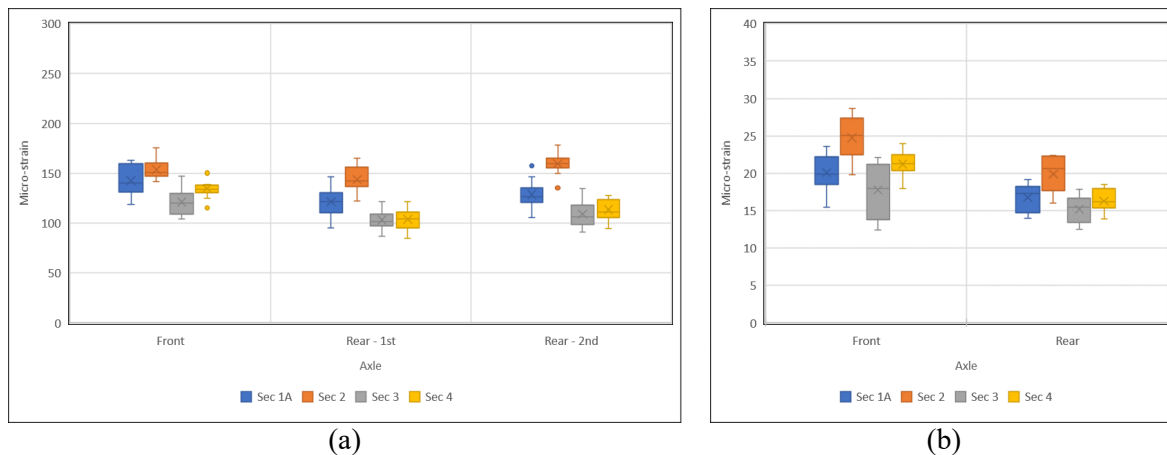
Figure 167. Boxplot of HMA strains in wheel path – stage A: (a) heavy; and (b) light

However, considering the data from stage B as well, we find that section 2 does perform better than control section (1b).
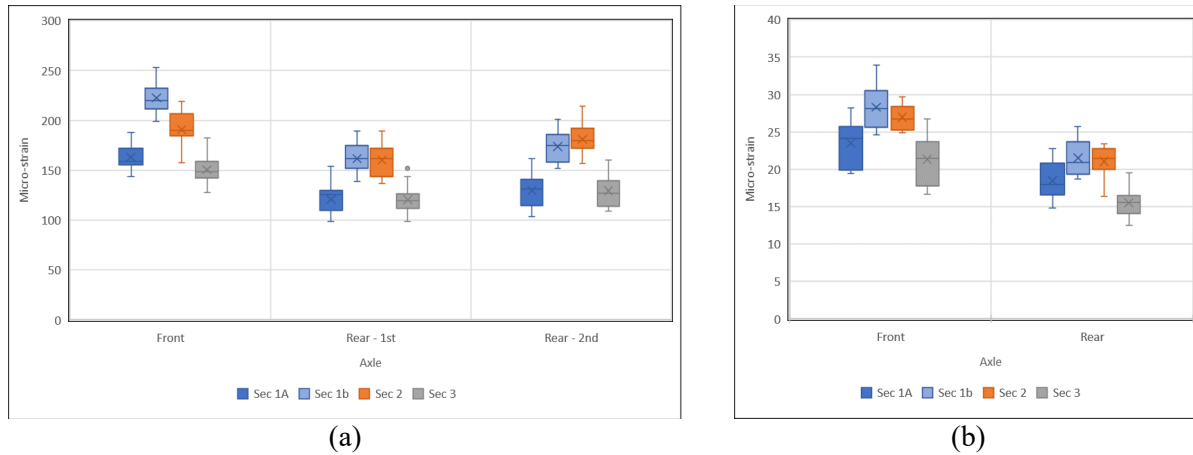
Figure 168. Boxplot of HMA strains in wheel path – stage B: (a) heavy; and (b) light

But, for an unknown reason, section 1a appears to be stiffer than expected (locally), an observation equally reflected in the soil extensometer data (Figure 147 and Figure 149), wherein the soil extensometers at 1a produced lower strains than at 1b by a significant margin, as well as in the LWD data from tests conducted at both locations. The results are shown in Figure 167. As can be seen, location 1a appears to be stiffer than location 1b by about 20%. Thus, any comparisons with section 1a must incorporate a correction factor to increase the local strains at 1a. The sections from stage B data can be directly compared amongst the control, type III and type II. However, the comparable strains are calculated as

$$\varepsilon_{sec1b, \; A} = \frac{\varepsilon_{sec1a, \; A}}{\varepsilon_{sec1a, \; B}} \times \varepsilon_{sec1b, \; B} \tag{6}$$
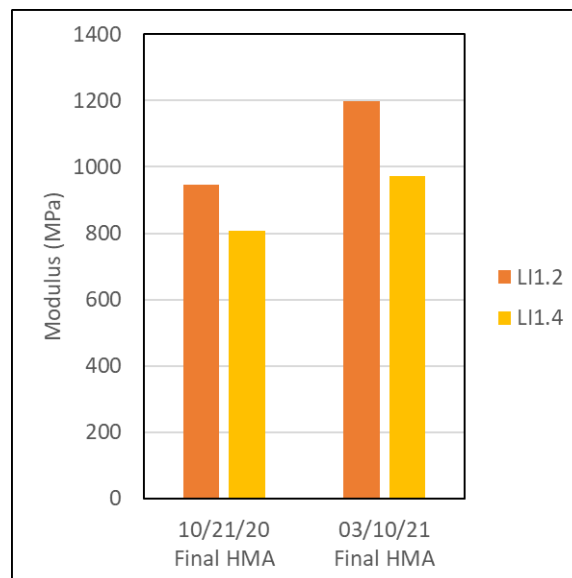
Figure 169. Stiffness of HMA layer at location 1a (1.2) and 1b (1.4) from LWD tests

202

After accounting for the increased stiffness in section 1a, the percentage of transverse strains in various sections compared to those in the control section (100%) is calculated and presented in Table 39. As can be observed from the table, the inclusion of geosynthetic reinforcement results in a reduction in transverse strains by up to 40% (type II). In some cases, especially for the lighter cars, the reduction is substantially lower. This may be due to the inability of the lighter traffic to mobilize the grid effectively.

Table 40. Transverse strains as percentage of those in control section (first campaign)

		Sec 1b	Sec 2	Sec 3	Sec 4
		Control	Type III	Type II	Type I
Heavy	Front	100	79	62	69
	Rear-1	100	88	63	64
	Rear-2	100	93	63	66
Light	Front	100	102	73	88
	Rear	100	102	78	83

7.4.1.2. Second Loading Campaign – March 2021 – Temperature: Cold

A similar analysis was performed for the second loading campaign conducted on March 11th, 2021. The results of the peak strains from three loading stages (A, B and C) are plotted as box plots shown in Figure 168 to Figure 170. The third stage (C) was a repeat of stage A but conducted in the afternoon at higher temperatures.

(a)   (b)

Figure 170. Boxplot of HMA strains in wheel path – stage A: (a) heavy; and (b) light

Figure 171. Boxplot of HMA strains in wheel path – stage B: (a) heavy; and (b) light

The transverse strains in the various section as a percentage of transverse strains in the control section for stages A and C are shown in Table 40. As can be seen from the table, the reduction in strains is much lower (and in some cases, an increase in strain is observed) than was the case during the October (warmer) loading campaign. This may be due to the colder weather, resulting in an overall stiffer pavement, thereby reducing the contribution from the geogrids. However, improvement to the order of about 30% reduction is still observed in some of the reinforced sections.

Figure 172. Boxplot of HMA strains in wheel path – stage C: (a) heavy; and (b) light

Table 41. Transverse strains as percentage of those in control section (second campaign)

			Sec 1b	Sec 2	Sec 3	Sec 4
			Control	Type III	Type II	Type I
Stage A	Heavy	Front	100	101	69	78
		Rear-1	100	111	81	87
		Rear-2	100	108	81	85
	Light	Front	100	124	86	102
		Rear	100	117	84	93

204

			Sec 1b	Sec 2	Sec 3	Sec 4
			Control	Type III	Type II	Type I
Stage C	Heavy	Front	100	104	71	83
		Rear-1	100	102	76	82
		Rear-2	100	100	72	78
	Light	Front	100	104	68	80
		Rear	100	91	63	69

7.4.1.3. Third Loading Campaign – September 2021 – Temperature: Hot

A similar analysis was performed for the third loading campaign conducted on September 9th, 2021. The results of the peak strains from the three loading stages (A, B and C) are plotted as box plots shown in Figure 171 to Figure 173. The third stage (C) was a repeat of stage A but conducted in the afternoon at higher temperatures.
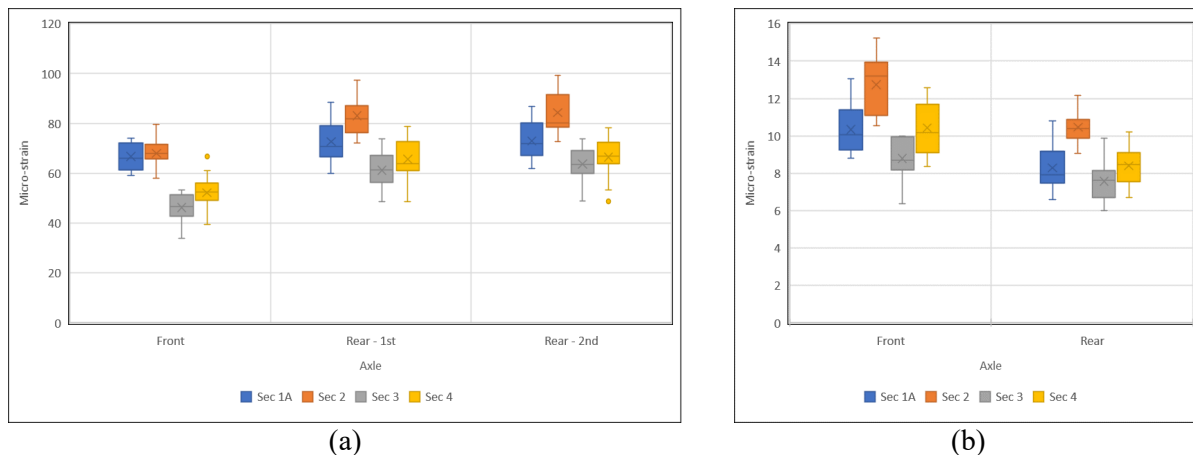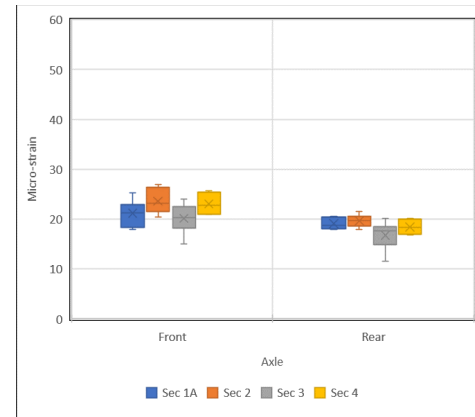

(a)   (b)

Figure 173. Boxplot of HMA strains in wheel path – stage A: (a) heavy; and (b) light
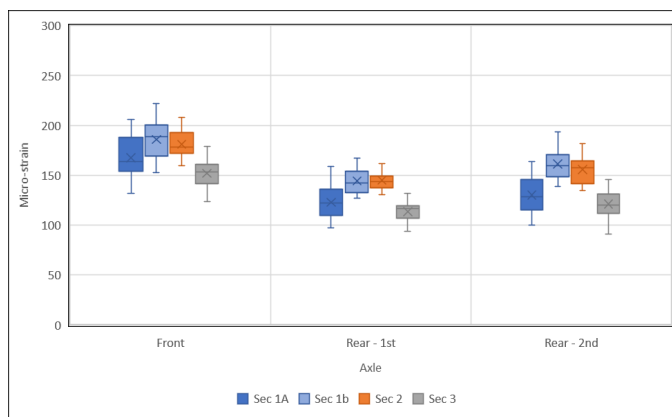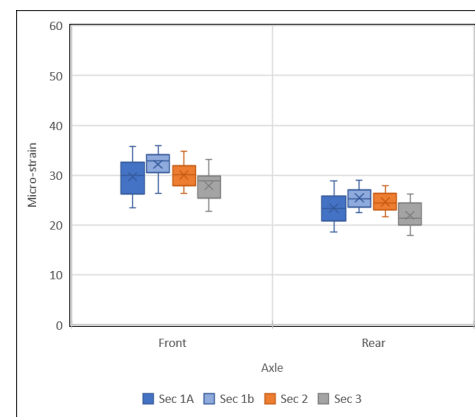
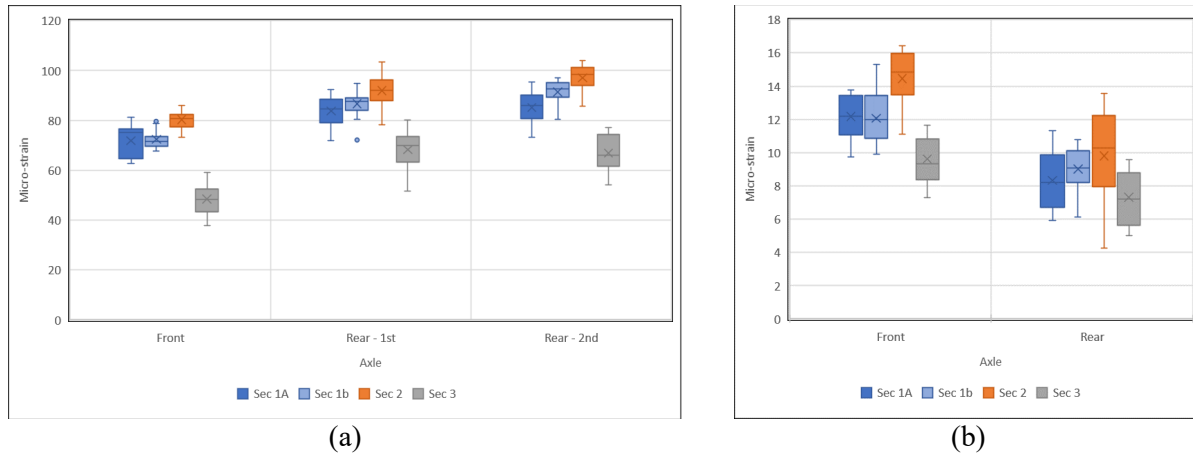(a)   (b)

Figure 174. Boxplot of HMA strains in wheel path – stage B: (a) heavy; and (b) light

The transverse strains in the various section as a percentage of transverse strains in the control section for stages A and C are shown in Table 41. The reinforced sections show strains reduced by 5 to 25%.
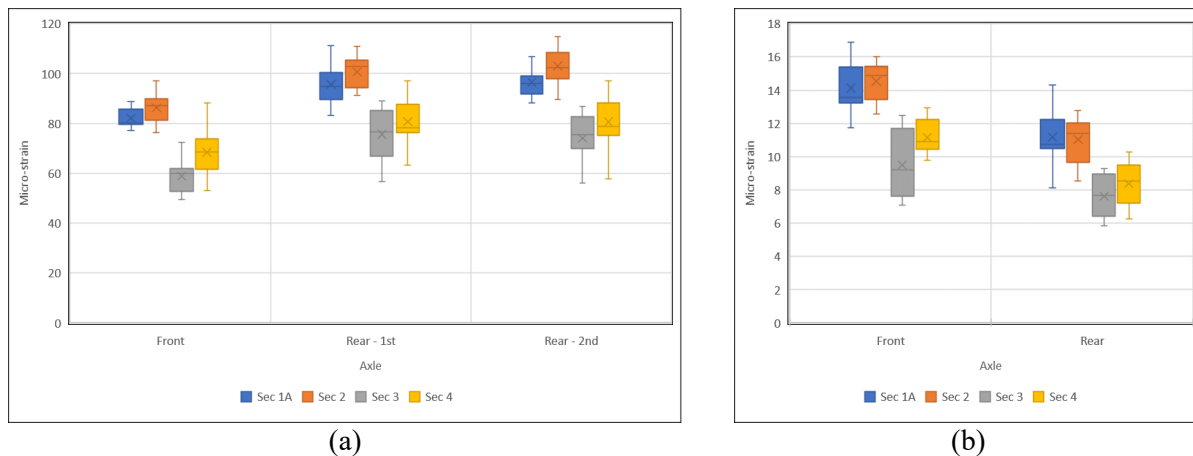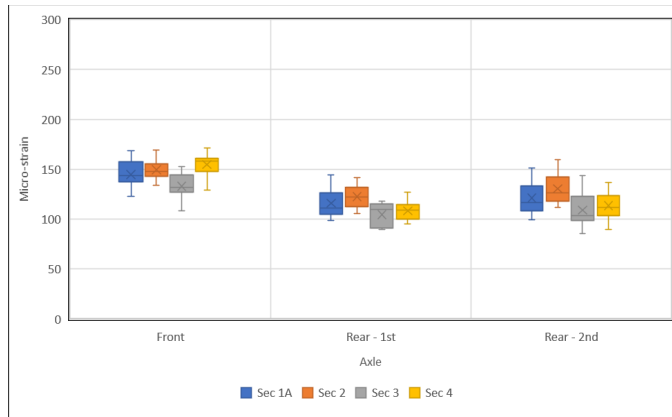

(a)   (b)
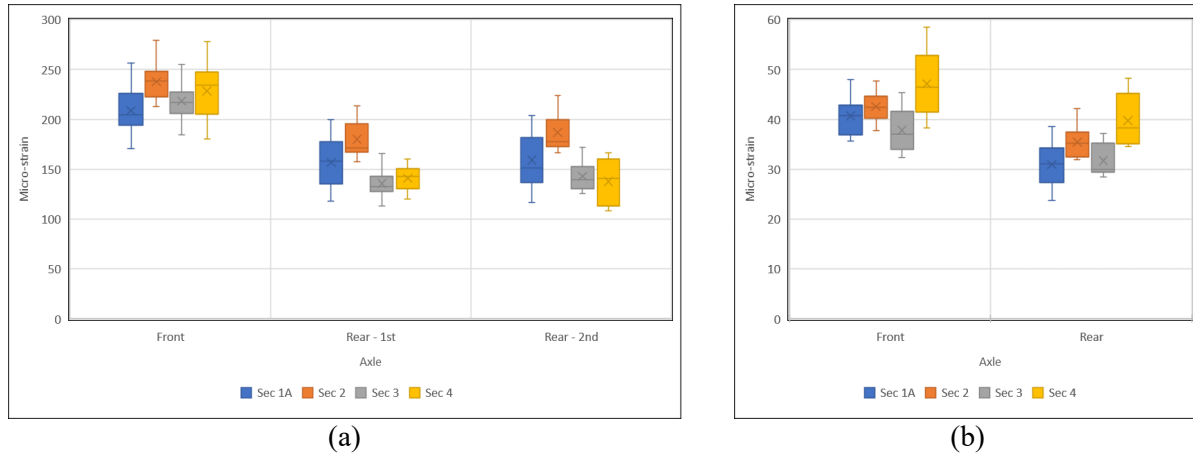
Figure 175. Boxplot of HMA strains in wheel path – stage C: (a) heavy; and (b) light

Table 42. Transverse strains as percentage of those in control section (third campaign)

			Sec 1b	Sec 2	Sec 3	Sec 4
			Control	Type III	Type II	Type I
Stage A	Heavy	Front	100	93	83	97
		Rear-1	100	90	77	80
		Rear-2	100	87	73	76
	Light	Front	100	103	88	100
		Rear	100	97	80	88
Stage C	Heavy	Front	100	103	94	99
		Rear-1	100	98	74	76
		Rear-2	100	95	72	70
	Light	Front	100	96	86	107
		Rear	100	105	94	118

7.4.1.4. Fatigue Life Improvement

The reduction in tensile strains under the wheel path at the bottom of the HMA layer can be used to estimate the improvement in fatigue life of the asphalt layer. One early study into the fatigue life of asphalt mixtures was performed by Monismith et al. (1961) in which a series of four-point bending beam tests were performed on the same asphalt mixture with varying tensile strains. They found that the number of cycles to failure in fatigue (N_f) is inversely proportional to the tensile strain at the bottom of the asphalt beam specimen.

$$N_f = k_1 \left(\frac{1}{\varepsilon_t}\right)^{k_2} \tag{7}$$

where k_1, and k_2 are mix-specific empirical constants. Epps et al. (1969) improved the relation in Equation (7) by including the flexural stiffness of the mix (S_{mix}) to differentiate between the different types of asphalt mixes used, and to account for the effects of temperature and loading frequency. At lower temperatures and higher loading frequencies, the asphalt mixture was observed to be stiffer and demonstrated brittle behavior. Thus, the stiffness of the mix was found to be inversely proportional to the fatigue life of the asphalt beam. They developed the following equation including the stiffness,

$$N_f = k_1 \left(\frac{1}{\varepsilon_t}\right)^{k_2} \left(\frac{1}{S_{mix}}\right)^{k_3} \tag{8}$$

where k_1, k_2, and k_3 are empirical constants independent of the type of mix used, temperature of the asphalt mix and loading frequency, respectively. Finn et al. (1977) expanded the original series of tests by conducting an extensive study of stress-controlled four-point bending fatigue tests on a variety of asphalt mixes to determine the empirical constants k_1, k_2 and k_3, and to recalibrate the data based on the moduli of the asphalt mix instead of the stiffness. The results from the four-point bending beam tests were correlated with the observed performance in the field to determine a field calibration factor of 18.4, corresponding to 45% total cracked area.

$$N_f = 18.4 \times 0.00432 \times \left(\frac{1}{\varepsilon_t}\right)^{3.291} \left(\frac{1}{E}\right)^{0.854} \tag{9}$$

Equation (9) was later modified to include the asphalt mixture properties by the Asphalt Institute Manual MS-1 (1982) as follows.

$$N_f = 18.4 \times 0.00432 \times 10^M \left(\frac{1}{\varepsilon_t}\right)^{3.291} \left(\frac{1}{E}\right)^{0.854} \tag{10}$$

$$M = 4.84 \left(\frac{v_{be}}{v_{be} + v_a} - 0.69\right) \tag{11}$$

where v_{be} is the effective binder content (%); and v_a is the air voids content (%). Equation (10) was recalibrated with the Long-Term Pavement Performance (LTPP) data and to account for the thickness of the asphalt slab in the field for the MEPDG Design Guide (NCHRP, 2004).

$$N_f = K \times 0.00432 \times 10^M \left(\frac{1}{\varepsilon_t}\right)^{3.291} \left(\frac{1}{E}\right)^{0.854} \tag{12}$$

$$K = \frac{1}{0.000398 + \frac{0.003602}{1 + e^{(11.02 - 3.49 h_{ac})}}} \tag{13}$$

where h_{ac} is the thickness of the asphalt layer in inches. The TxDOT pavement design software FPS-21 uses the Asphalt Institute Equation (10) to check for fatigue cracking and assumes an effective binder content of 11% for a typical mix and an air voids content of 5%, resulting in $10^M = 1$. Therefore, the fatigue cracking performance equation according to FPS-21 is given by,

$$N_f = 0.0795 \left(\frac{1}{\varepsilon_t}\right)^{3.291} \left(\frac{1}{E}\right)^{0.854} \tag{14}$$

Since the tensile strain (ε_t) under the wheel path is measured in the IH10 instrumented test sections, this information can be used to determine the fatigue life of the corresponding test section. The asphalt mix used across the various test sections is the same, and the strains are measured under identical conditions of loading magnitude (same truck), loading rate (at the same speed) and at the same temperatures. Thus, the moduli of the asphalt mixtures are the same across all test sections and the improvement in fatigue life (TBR) against fatigue cracking (TBR_f) is determined as follows.

$$TBR_f = \frac{N_{f,stabilized}}{N_{f,control}} = \frac{0.0795 \left(\frac{1}{\varepsilon_{t,s}}\right)^{3.291} \left(\frac{1}{E}\right)^{0.854}}{0.0795 \left(\frac{1}{\varepsilon_{t,c}}\right)^{3.291} \left(\frac{1}{E}\right)^{0.854}} \tag{15}$$

$$TBR_f = \left(\frac{\varepsilon_{t,c}}{\varepsilon_{t,s}}\right)^{3.291} \tag{16}$$

where $\varepsilon_{t,c}$ and $\varepsilon_{t,s}$ are the tensile strains in the control and stabilized sections, respectively. Therefore, the improvement in fatigue life is a function of the ratio of the tensile strains developed under the vehicular load in the control and stabilized sections. These ratios are calculated from the tensile strains measured in the control and stabilized sections during the loading campaigns, and the corresponding improvement to fatigue life for the different vehicle categories and temperatures during the loading campaigns are summarized in Table 42.

Table 43. Fatigue life improvement ratios (TBR$_f$) during various loading campaigns for different vehicles

Heavy Truck			
Temperature	107 F	99 F	85 F
Front	5.58	2.98	1.96
Rear - 1st	5.06	1.80	1.48
Rear - 2nd	5.46	1.81	1.73
Light Car			
Temperature	107 F	99 F	85 F
Front	2.8	1.7	1.7
Rear	2.3	1.8	1.2

The improvement in fatigue life is a function of vehicle speed, temperature of the asphalt mix and axle load of the vehicle. Assuming that the traffic in the test sections follows more or less the same speeds and the distribution axle-loads can be approximated as Estimated Standard Axle Loads (ESAL), then the fatigue life improvement ratios can be determined as a function of temperature only. By dividing the annual traffic over various periods with constant temperatures,

the true improvement in fatigue life across the various temperatures and ESAL may be determined using Miner's Law as follows.

$$\sum_{i=1}^{k} \frac{n_i}{N_{f,i}} = \sum_{i=1}^{k} \frac{n_{design} \times f_i}{N_{f,i}} = 1 \tag{17}$$

where i = $1, 2, \ldots, k$ are the 'k' different periods over which the asphalt temperatures are more or less a constant; n_i is the number of ESAL (traffic volume) in any particular period 'i', such that $\sum n_i = n_{design}$ i.e., the design traffic volume; $N_{f,i}$ is the fatigue life the HMA layer corresponding to the period 'i'; and f_i is the fraction the design traffic volume corresponding to period 'i' such that $f_i = n_i/n_{design}$. From equation (17), the design traffic volume before failure in fatigue (n_{design}) is determined as,

$$n_{design} = \frac{1}{\sum_{i=1}^{k} \frac{f_i}{N_{f,i}}} \tag{18}$$

The overall improvement to fatigue life due to the inclusion of the geogrid across various temperature periods may be determined from equation (18) as follows.

$$TBR_f = \frac{n_{design,s}}{n_{design,c}} = \frac{\sum_{i=1}^{k} \frac{f_i}{N_{f,c,i}}}{\sum_{i=1}^{k} \frac{f_i}{N_{f,s,i}}} \tag{19}$$

Substituting the temperature specific $TBR_{f,i}$ into Equation (19), the overall improvement to fatigue life is obtained as,

$$TBR_f = \frac{n_{design,s}}{n_{design,c}} = \frac{\sum_{i=1}^{k} \frac{f_i}{N_{f,c,i}}}{\sum_{i=1}^{k} \frac{1}{TBR_{f,i}} \frac{f_i}{N_{f,c,i}}} \tag{20}$$

Thus, the overall TBR_f or fatigue life improvement due to base stabilization can be obtained by subdividing annual traffic into different groups corresponding to different temperature levels (T_i) (and corresponding stiffness levels E_i) and obtaining their fatigue lives ($N_{f,c,i}$) and field-obtained TBR ($TBR_{f,i}$). The temperature levels are to be determined from the thermocouples installed in the HMA layer from which the temperature-specific $TBR_{f,i}$ have been determined during the loading campaigns. Ultimately, the overall TBR_f will be determined for the three different types of geogrids and those values can be correlated to the K_{SGC}, base modulus improvement, and other mechanistic parameters to predict stabilized pavement fatigue performance.

7.4.1.5. Lessons Learned from ASG under Trafficking

- Sections with geogrid stabilization showed reduction in transverse tensile strain under the wheel at the bottom of the HMA layer. The reductions ranged from 5% to 40%.

- The reduced tensile strains due to geogrid inclusion is expected to result in reduced fatigue cracking over the course of the life of the pavement sections.

- The benefit of strain reduction from the inclusion of geogrid appears to be a function of the pavement temperature. Pavements at lower temperatures have a stiffer HMA layer resulting in reduced benefits.

- These effects are expected to provide increased benefits with time as the pavement surface layer degrades. Thus, continued controlled trafficking of test sections will aid in validating this hypothesis.

7.4.2. Geophones under Trafficking

As the instrumented sections were trafficked with the vehicle wheels passing on top of the outer wheel path, the data from the geophones embedded within the pavement structure was recorded from the control as well as stabilized sections. Figure 174 shows the location of geophones in each instrumented test section (one control + three stabilized). For this analysis, only the sensors located along the wheel path (four locations highlighted by the blue line) are compared. Figure 175 shows the location of all six geophones within the wheel path at various depths and longitudinal locations with the pavement structure. Although some geophones located along the wheel path could measure deflections at all three axes, for the purposes of this analysis, only the vertical deflections from all geophones within the wheel path are considered. Vertical deflections were measured at the top and middle of the base, top of the sub-base, top of the subgrade and at a 6-in depth within the subgrade. Unfortunately, the geophone on top of the subgrade in the control section failed during construction, resulting in unusable deflection data at this location.
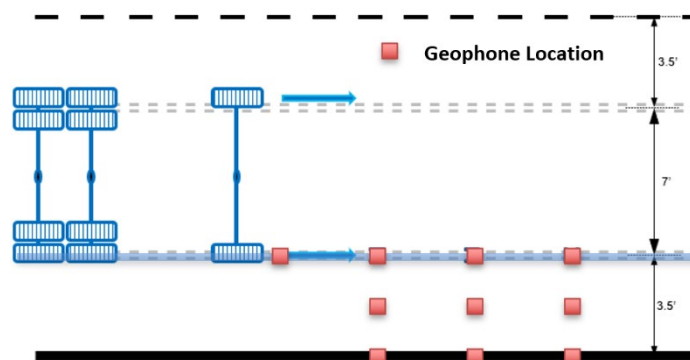

Figure 176. Location of embedded geophones relative to wheel path
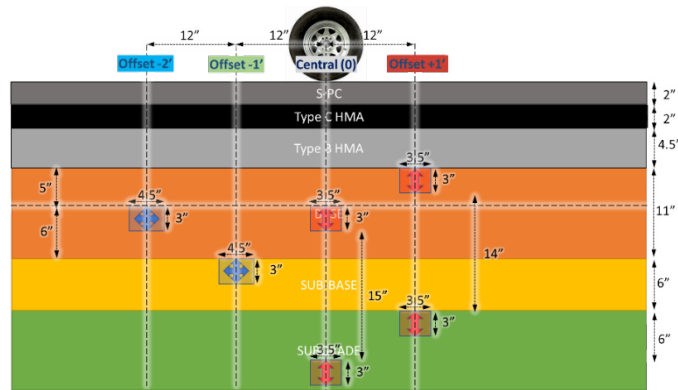
210

Figure 177. Longitudinal section of wheel path

Multiple passes were made with the heavy truck and light car during controlled trafficking, with each pass generating deflection-time history data for each geophone similar to that shown in Figure 71b. To compare the geophones at similar locations between stabilized and control sections over multiple passes, boxplots as shown in Figure 176 are utilized in this report. These boxplots show the mean (x), median (dash) and scatter of the peak deflection data aggregated from the deflection time-history plot for the various axles. Figure 176 shows the peak deflection data collected under multiple passes of the heavy truck in the March 2021 loading campaign from the geophone at the top of the base.
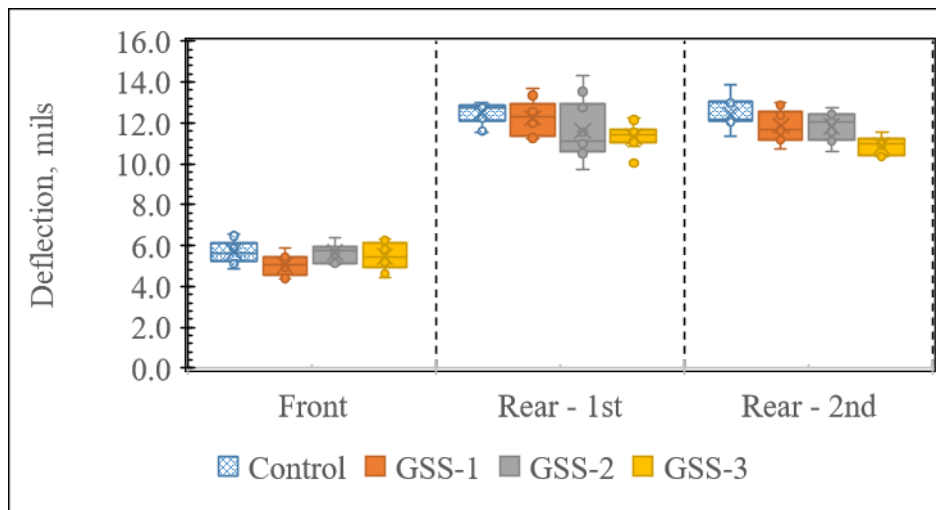
Figure 178. Typical boxplot of peak deflection data from geophones

As can be seen from Figure 176, the peak deflection observed in control section is generally higher than those observed in the stabilized sections, save for some outliers. To better facilitate the comparison between the stabilized and control sections, the deflection ratio is computed for the various sections relative to the control section as shown in Figure 177. The deflection ratio is defined as the ratio of the mean peak deflections of a geophone at a particular location in the stabilized section to the mean peak deflections of a geophone at a similar location in the control section. Consequently, the deflection ratio of the geophones in the control section is equal to 1.0.

Figure 179. Typical deflection ratio plot for comparison across test sections

7.4.3. Third Loading Campaign – September 2021

Figure 178 shows the boxplots of the vertical deflection data under heavy truck passes and the corresponding deflection ratios obtained for geoph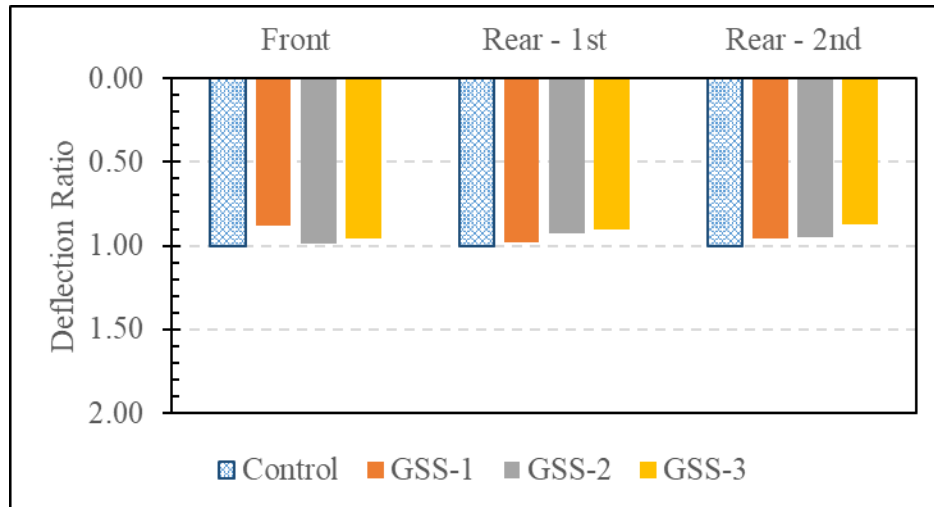ones at various depths within the pavement structure during the third loading campaign in September 2021, one year post-construction. Figure 179 shows data similar to that provided in Figure 178 but obtained later the same day when the pavement had sufficiently warmed up from sunlight. The geophones located deep within the pavement structure did not register a second peak for the tandem axle due to superposition effects. This was especially true for the stabilized sections.

As can be seen from Figure 178 and Figure 179, the internal vertical deflections under the wheel path of the heavy truck is similar in the control and stabilized sections. A marginal reduction in deflection (around 10%) is observed on the top and middle of the base, and top of the sub-base. Also, the reductions were higher for the front axle load compared to the rear axle loads, likely due to the superposition effects from the multi-wheel tandem axles in the rear. The geogrids could have provided greater stress distribution and redistributed the loads from the accompanying axle onto the primary axle.

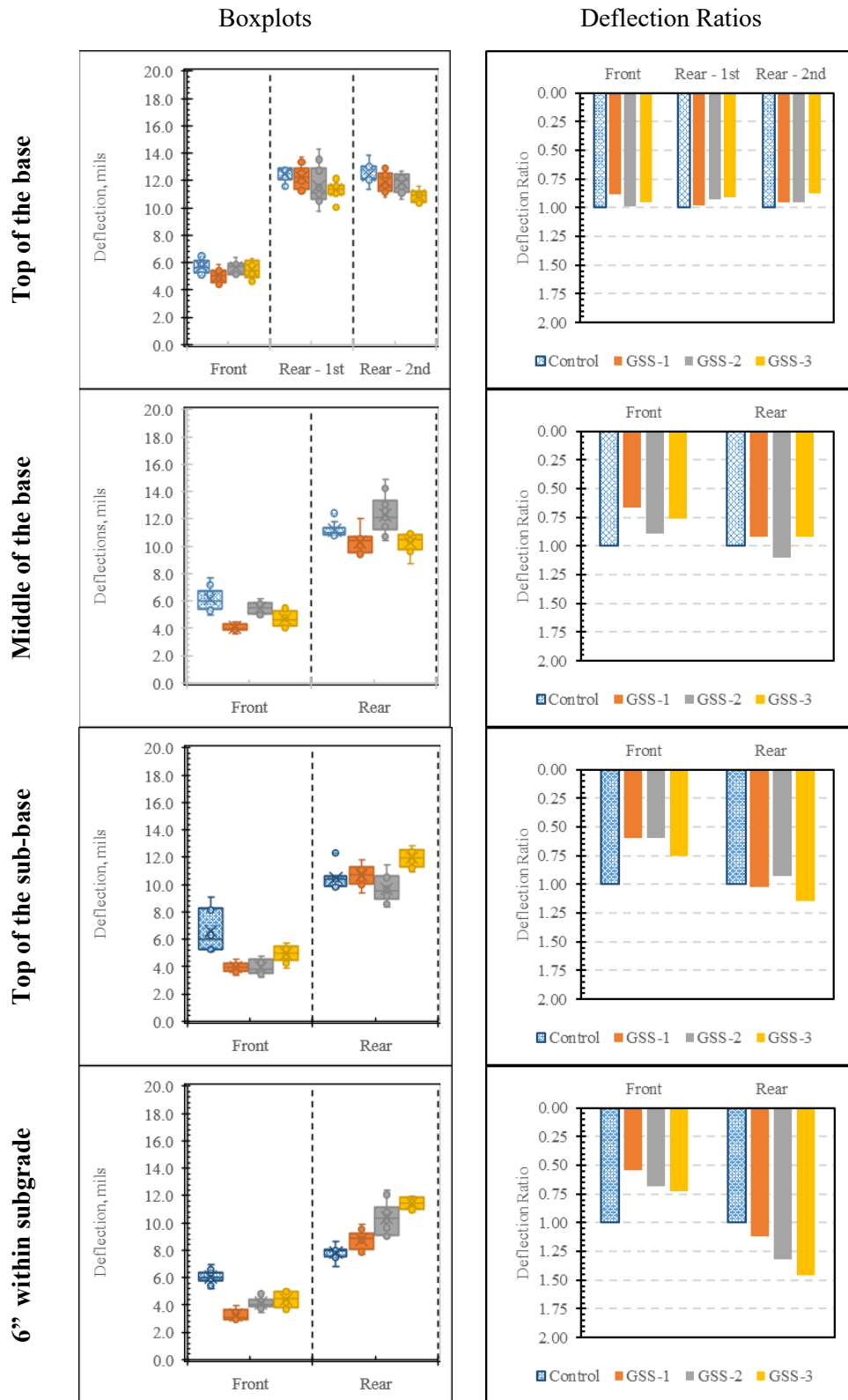The geophone in the subgrade deflected slightly higher in the stabilized sections than in the control.

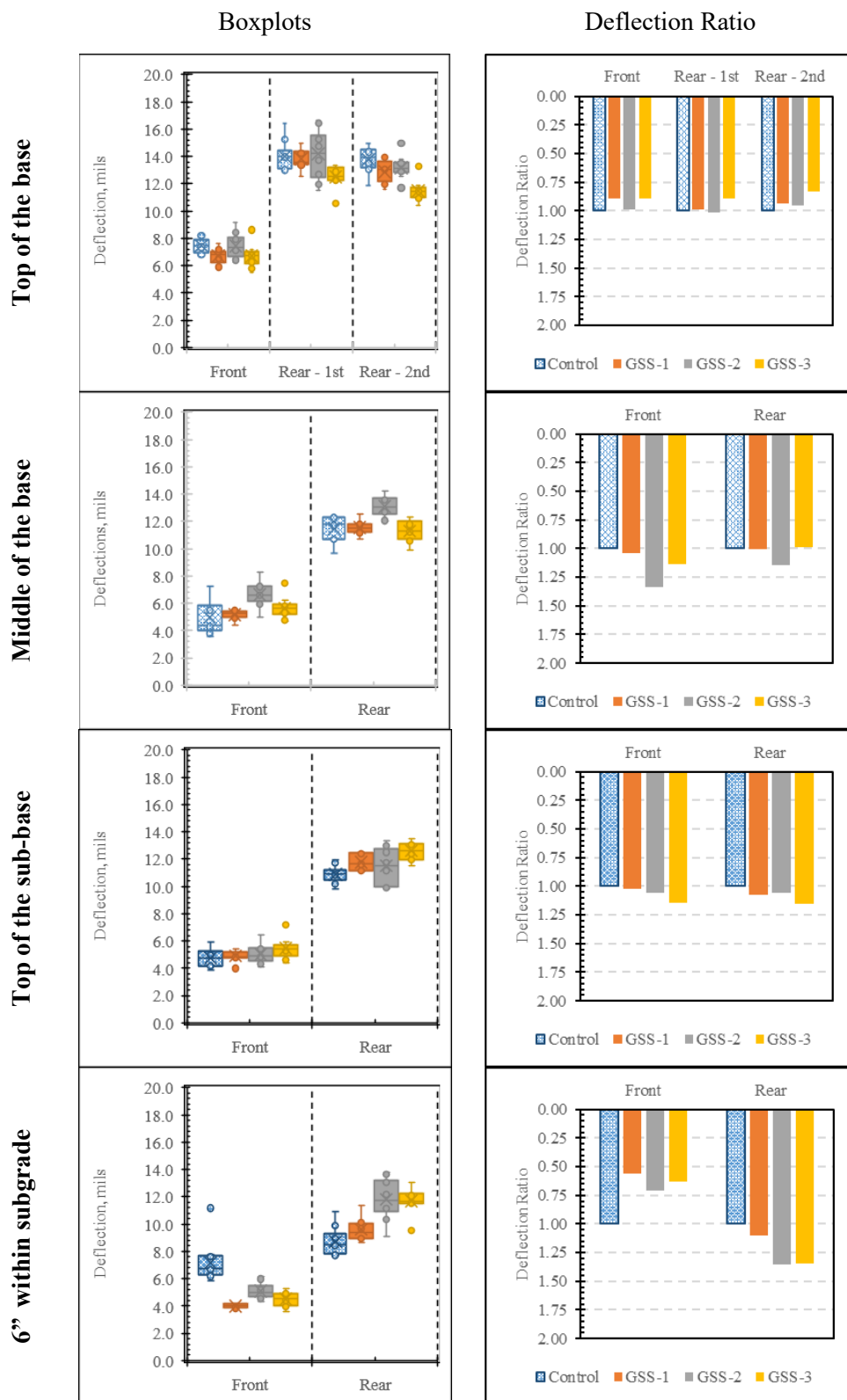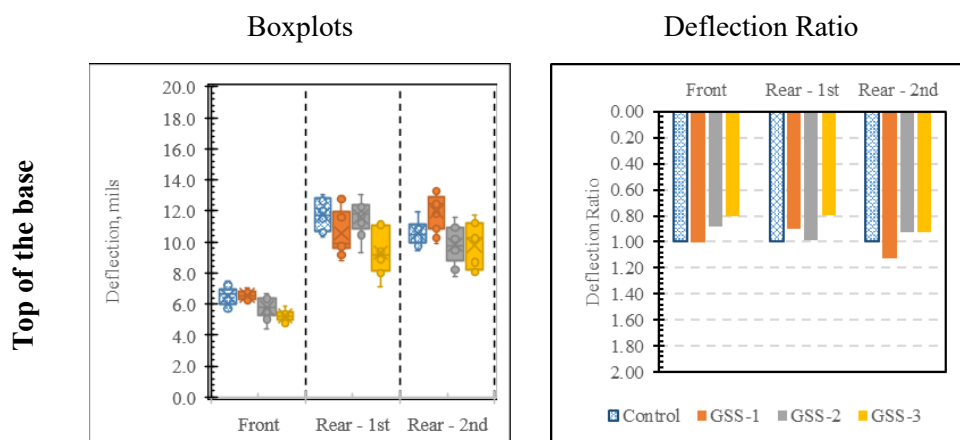*Figure 180. Vertical deflections, September 2021 – lower temperature*

Boxplots   Deflection Ratio

Figure 181. Vertical deflections, September 2021 – higher temperature

7.4.4. Fourth Loading Campaign – August 2022

Figure 180 shows the boxplots of the vertical deflections under heavy truck and the corresponding deflection ratios, obtained during the fourth loading campaign in August 2022, two year post-construction. Figure 181 shows the similar data to Figure 180, but obtained later in the same day under hotter conditions. As can be seen from Figure 180, most, if not all, sensors showed reduced internal vertical deflections under the heavy truck in the stabilized sections compared to the control sections. As evident from Figure 181, this is more evident at higher temperatures, when the pavement top surface is sufficiently weaker to mobilize the geogrids more actively.

The maximum reduction in deflections (up to 25%) occurred in the middle of the base, 4 in above the location of the stabilizing geogrids. Unlike the earlier loading campaign in which the front axles (concentrated loads) exhibited a greater reduction in deflections than the rear axles (distributed loads), the reduction in deflections in the August 2022 campaign was comparable between the front and rear axles, although some effect of load distribution was visible. At deeper locations within the geogrid, the reductions were higher for the front axle load compared to the rear axle loads, likely due to the superposition effect previously discussed.

These reduced internal deflections are a direct measure of the reduced rutting potential of the pavement structure due to the inclusion of stabilizing flexible reinforcements. As is clearly demonstrated from the differences in performance between the testing conducted at the end of the first year compared to the second, it is evident that the mobilization of the geogrid increases with time. Thus, continued monitoring of these test section, with two or more testing campaigns, is likely to yield a more accurate information on the mobilization of the geogrids and how it benefits the pavement structure.
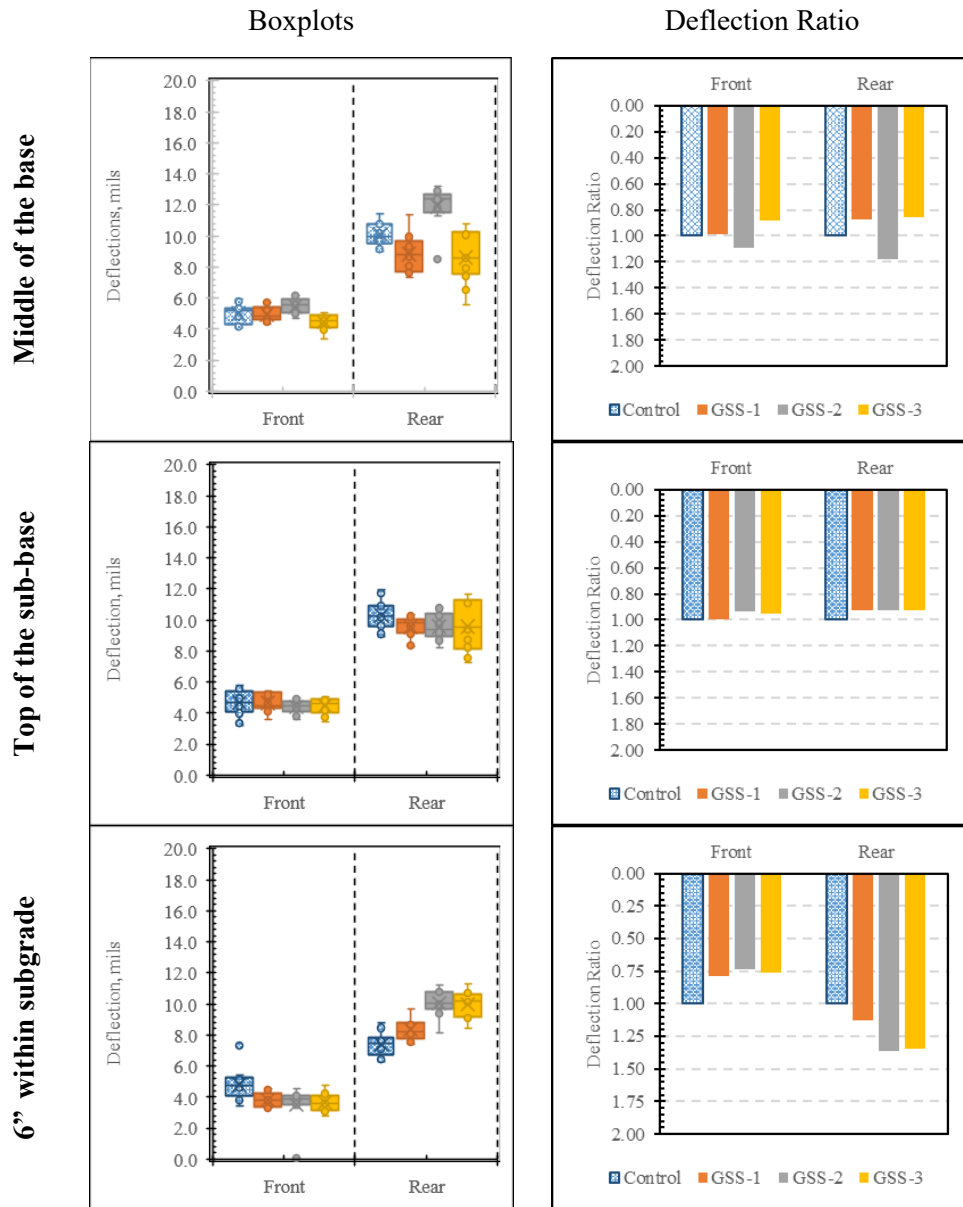
	Boxplots	Deflection Ratio

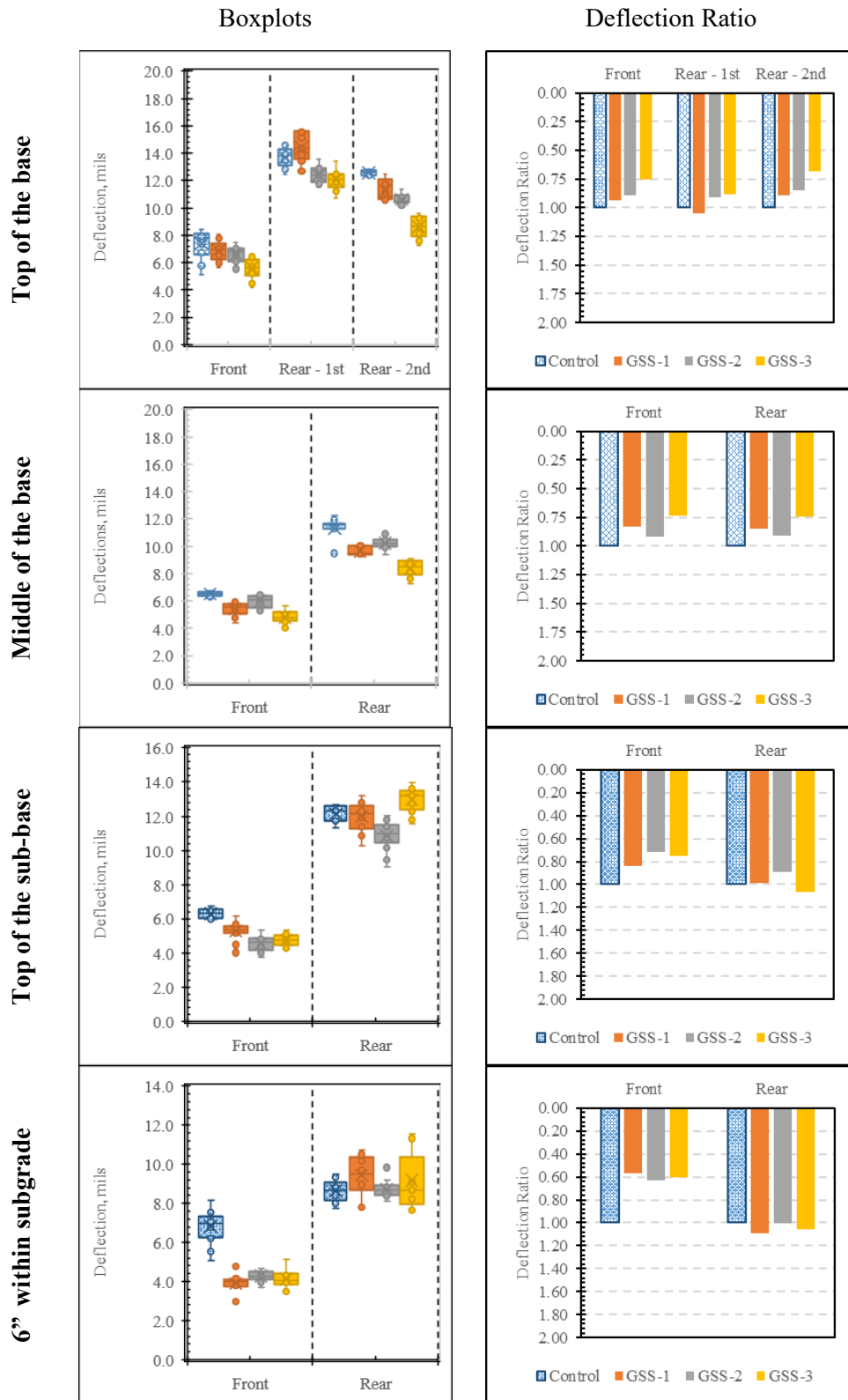*Figure 182. Vertical deflections, August 2022 – lower temperature*

Figure 183. Vertical deflections, September 2021 – higher temperature

Chapter 8. Conclusions

TxDOT project 5-4829-05 involved the instrumentation and monitoring of full-scale field sections of flexible pavement along the frontage roads of IH10 east of San Antonio. The following are key conclusions from the analysis of data collected from the various tests conducted and sensors installed.

- At just one year post-construction, the geogrid-stabilized sections have already shown significant improvements in performance such as increased layer moduli, decreased rutting potential and decreased cracking potential. The data collected so far is categorical, although it represents a lower bound of the actual anticipated improvement, which is expected to increase further over time as the installed geogrid is mobilized with increasing interactions due to lateral strains.

- Falling Weight Deflectometer (FWD) tests showed that the inclusion of a geogrid within the pavement structure increased layer moduli (post-construction) and that such improvements to layer moduli can translate to a reduction in base thickness (or HMA thickness).

- Lateral geophone deflection ratios between the geosynthetic stabilized and control sections improved over time, indicating that the geosynthetics provide increasing lateral restraint. This is consistent with the data observed from ASG under controlled traffic and data from soil extensometers under passive traffic. During the most recent loading campaign, lateral geophone deflections observed in the stabilized sections were consistently smaller than those in the control section.

- Stabilized sections showed increasingly lower surface and base deflections (by as much as 18%) as the geosynthetics were mobilized over time. The vertical deflections were also reduced on the subbase and subgrade levels.

- FWD back-calculation problems based on surface deflections were found to have non-unique solutions in some cases. The inclusion of internal deflection data from the embedded geophones produced more realistic back-calculated layer moduli and helped greatly with convergence to a unique solution. This helped improve the agreement between the measured and estimated deflections.

- The stabilized sections showed consistently higher back-calculated base moduli as a result of the reduced deflections. While all three of the stabilized sections perform comparably better than the control section, further monitoring is required to study the long-term behavior of the stabilized sections to be able to distinguish between the relative performances of the stabilized sections.

- Soil extensometer data under passive traffic revealed that the inclusion of a geogrid within the pavement structure reduced lateral tensile strains within the base layer near the geogrid through lateral restraint and that this leads to a reduced rutting potential for the stabilized layers.

- Transverse asphalt strain gauges under controlled trafficking during loading campaigns indicated that geogrid stabilization of the unbound aggregate base reduced transverse tensile strains induced under the wheel path at the bottom of the HMA layer. This is acknowledged to reduce fatigue cracking over the life of the pavement section.

- Vertical deflections of the geophones under controlled trafficking during loading campaigns showed that the internal (elastic) movements of the pavement under heavy traffic are reduced due to the geogrid inclusion. This is expected to reduce the rutting of the pavement over time.

- Time Domain Reflectometers (TDR) can be used to measure the Volumetric Water Content (VWC) of soils with time. The installation of a grid of TDR sensors indicated a higher VWC at lower depths and locations where little drainage occurs. Deeper sensors and those installed in the inner lane had a higher average VWC over time, while shallower sensors and those installed in the outer lane, where a retaining wall is located, had a lower VWC.

- The long-term monitoring of strains measured by asphalt strain gauges showed that the response is dominated by temperature effects rather than accumulated plastic strains from traffic. This identified the need for an advanced experimental program to quantify these temperature effects and develop a decoupling protocol to assess the long-term plastic strains in pavement test sections.

- The magnitude of displacements observed in linear potentiometers is significantly smaller compared to the noise level of the sensors. Consequently, longer monitoring periods are needed to quantify test section performance and compare the stabilized and control sections.

The information documented in this report corresponds to the initial phase of a more comprehensive monitoring project, as additional cycles of monitoring data are expected. Overall, the results from monitoring the sensors installed under the various tests performed indicated that continued monitoring of the instrumented test sections would be particularly relevant to understand the mechanisms involved in the mobilization of geogrids to provide lateral restraint. The thick pavement sections involved in this study require longer monitoring periods that will facilitate a more complete evaluation of stabilized test sections. Continued monitoring of the instrumented test sections will allow:

- Expanding TxDOT's successful use of geogrids in roadways over expansive clays to geogrids for base course reduction

- Evaluation of the mechanisms governing geogrid stabilization of unbound aggregates

- Differentiating among the performance of different geogrids

- Incorporating stabilized unbound aggregate bases into the design methodologies for flexible pavements

References

Asphalt Institute, 1982. Research and development of the Asphalt Institute's thickness design manual (MS-1) ninth edition. Asphalt Institute: College Park, Maryland.

ASTM Standard D1195M-09, 2015. Standard Test Method for Repetitive Static Plate Tests of Soils and Flexible Pavement Components for Use in Evaluation and Design of Airport and Highway Pavements, ASTM International.

ASTM Standard D1196M-21, 2021. Standard Test Method for Nonrepetitive Static Plate Tests of Soils and Flexible Pavement Components for Use in Evaluation and Design of Airport and Highway Pavements, ASTM International.

ASTM Standard D2487-17, 2020. Standard Practice for Classification of Soils for Engineering Purposes (Unified Soil Classification System), ASTM International.

ASTM Standard D422, 2007. Standard Test Method for Particle-Size Analysis of Soils, ASTM International.

ASTM Standard D4318, 2018. Standard Test Methods for Liquid Limit, Plastic Limit, and Plasticity Index of Soils, ASTM International.

ASTM Standard D6637, 2015. Standard Test Method for Determining Tensile Properties of Geogrids by the Single or Multi-Rib Tensile Method, ASTM International.

ASTM Standard D6758-18e1, 2021. Standard Test Method for Measuring Stiffness and Apparent Modulus of Soil and Soil-Aggregate In-Place by Electro-Mechanical Method, ASTM International.

ASTM Standard D6951M-18, 2018. Standard Test Method for Use of the Dynamic Cone Penetrometer in Shallow Pavement Applications, ASTM International.

ASTM Standard D698, 2021. Standard Test Methods for Laboratory Compaction Characteristics of Soil Using Standard Effort, ASTM International.

ASTM Standard D854-14, 2014. Standard Test Methods for Specific Gravity of Soil Solids by Water Pycnometer, ASTM International.

ASTM Standard E2583-07, 2020. Standard Test Method for Measuring Deflections with a Light Weight Deflectometer (LWD), ASTM International.

Barksdale, R.D., 1971. Compressive stress pulse times in flexible pavements for use in dynamic testing. Highway Res. Rec. 345 (1971) 32–44.

Bender, D.A., Barenberg, E.J., 1978. Design and behavior of soil-fabric-aggregate systems. Transportation Research Record.

Brown, S., Jones, C., Brodrick, B., 1982. Use of non-woven fabrics in permanent road pavements. Proceedings of the Institution of Civil Engineers 73, 541–563.

DIN 18134, 2012-04. Soil – Testing procedures and testing equipment – Plate load test, German Standards.

Epps, J.A., Monismith, C.L., Warden, W.B., Pell, P.S., Kallas, B.F., Terrell, R.L., Busching, H.W., Mcleod, N.W., 1969. Influence of mixture variables on the flexural fatigue

properties of asphalt concrete. Proceedings of the Association of Asphalt Paving Technologists: Vol. 38, pp. 423-464.

Finn, F., Saraf, C., Kulkarni, R., Nair, K., Smith, W., Abdullah, A., 1977. The use of distress prediction subsystems for the design of pavement structures. Proceedings of the 4th Int. Conference on the Structural design of Asphalt Pavements, Vol. 1, pp. 3–38.

Halliday, A., Potter, J., 1984. The performance of a flexible pavement constructed on a strong fabric. TRRL Laboratory Report.

Hu, S., Rahman, A., Zhang, J., Zhou, F., Scullion, T., 2019. Implementation of Texas Mechanistic-Empirical Flexible Pavement Design System (TxME) (Report No. FHWA/TX-18/5-6622-01-R1), Texas A&M Transportation Institute, College Station, TX.

Kinney, T., Barenberg, E., 1982. The strengthening effect of geotextiles on soil-geotextile-aggregate systems. Proceedings of the Second International Conference on Geotextiles: Vol. 2, pp. 347–352.

Monismith, C.L., Secor, K.E., Blackmer, A.W., 1961. Asphalt mixture behaviour in repeated flexure (With discussion and closure). Proceedings of the Association of Asphalt Paving Technologists: Vol. 30, pp. 188-222.

NCHRP, 2004. Guide for mechanistic-empirical design of new and rehabilitated pavement structures, National Cooperative Highway Research Program. Transportation Research Board, National Research Council: Washington, DC.

Roodi, G.H., Zornberg, J.G. (2017). Stiffness of soil-geosynthetic composite under small displacements. II: Experimental evaluation. Journal of Geotechnical and Geoenvironmental Engineering, 143(10).

Ruddock, E., Potter, J., McAvoy, A., 1982. A full-scale experiment on granular and bituminous road pavements laid on fabrics. Proceedings of the Second International Conference on Geotextiles: Vol. 2, pp. 365–370.

TxDOT Standard Tex-136-E, 2022. Test Procedure for Geosynthetic Composite Stiffness Value, Texas Department of Transportation.

Webster, S.L., Watkins, J.E., 1977. Investigation of construction techniques for tactical bridge approach roads across soft ground. US Waterways Experiment Station 2.

Zornberg, J.G., 2017. Functions and Applications of Geosynthetics in Roadways - Part 1. Procedia Engineering 189, 298–306

Zornberg, J.G., Roodi, G.H., Gupta, R., 2017. Stiffness of soil–geosynthetic composite under small displacements: I. Model Development. Journal of Geotechnical and Geoenvironmental Engineering, 143(10).